Understanding Cloud Droplet Size Distributions from Multi-Angle Polarimetric Observations

Veronika Therese Pörtge

München 2024

Understanding Cloud Droplet Size Distributions from Multi-Angle Polarimetric Observations

Veronika Therese Pörtge

Dissertation
der Fakultät für Physik
der Ludwig-Maximilians-Universität
München

vorgelegt von
Veronika Therese Pörtge
aus Kassel

München, den 2. April 2024

Erstgutachter: Prof. Dr. Bernhard Mayer
Zweitgutachter: Prof. Dr. Markus Rapp
Tag der mündlichen Prüfung: 14. Mai 2024

Zusammenfassung

Die Energiebilanz der Erde wird stark von Wolken, Aerosol und Aerosol-Wolken-Wechselwirkungen beeinflusst, die immer noch eine große Unsicherheitsquelle für aktuelle Klimavorhersagen darstellen. Wesentliche mikrophysikalische Wolkenparameter sind die Größenverteilung der Wolkentröpfchen, die die optischen Eigenschaften bestimmt, und die Tröpfchenanzahlkonzentration, die von der Zahl der Wolkenkondensationskerne abhängt. Da die üblicherweise verwendeten passiven Fernerkundungsmethoden zur Ermittlung dieser Parameter große Unsicherheiten aufweisen, ist die Entwicklung neuer Verfahren erforderlich.

Ziel dieser Arbeit ist es, die Tröpfchengrößenverteilung und Anzahlkonzentration aus Beobachtungen des flugzeuggestützten Kamerasystems specMACS (spectrometer of the Munich Aerosol Cloud Scanner) abzuleiten, die während der EUREC^{4}A (ElUcidating the RolE of Cloud-Circulation Coupling in ClimAte) Kampagne gemessen wurden. Daraus sollen die vertikale Entwicklung der mikrophysikalischen Eigenschaften und die Rolle der Einmischung trockener Luft in flache Kumuluswolken in der Passatwindregion untersucht werden. Zu diesem Zweck wurde ein neuartiges Verfahren zur Ermittlung der Tröpfchengrößenverteilung entwickelt. Es basiert auf Messungen des Wolkenbogens, der ähnlich wie der besser bekannte Regenbogen durch die Streuung des Sonnenlichts an sphärischen Partikeln wie Tröpfchen in Flüssigwasserwolken entsteht und sensitiv auf den effektiven Radius (r_{eff}) und die effektive Varianz (v_{eff}) reagiert. Letztere definiert die Breite der Größenverteilung. Da der Wolkenbogen ein Einfachstreuphänomen ist, ist er stark polarisiert und daher in den 2-D-Polarisationsmessungen der specMACS-Kamera sehr gut sichtbar. Das entwickelte Wolkenbogenverfahren kombiniert Messungen derselben Wolke aus verschiedenen Winkeln, die beim Überflug über ein Wolkenfeld aufgenommen wurden. Dadurch wird ein winkelaufgelöstes Signal des Wolkenbogens erzeugt. Eine Lookup-Tabelle von bereits simulierten Polarisationssignalen für unterschiedliche Tröpfchengrößenverteilungen wird an die Messdaten gefittet, um den effektiven Radius und die effektive Varianz bei einer räumlichen Auflösung von etwa 100 m zu bestimmen. Durch die Verwendung von Polarisationsmessungen werden die Anteile der Mehrfachstreuung am Signal und damit die Unsicherheiten des Verfahrens minimiert. Eine Modellstudie zeigt die hohe Genauigkeit der Ergebnisse mit einer absoluten mittleren Abweichung von (-0.2 ± 1.30) µm in r_{eff} und (0.02 ± 0.05) in v_{eff} (Volkmer et al., 2023). Diese hohe Genauigkeit der abgeleiteten Tröpfchengrö-

ßenverteilung erlaubt es, die Tröpfchenanzahlkonzentration unter Verwendung einer Methode zu ermitteln, die üblicherweise auf Satellitendaten angewendet wird und ein subadiabatisches Wolkenprofil voraussetzt, das die Tröpfchenzahl mit der ermittelten optischen Wolkentiefe und dem effektiven Radius verknüpft.

Es wird eine statistische Analyse der während der EUREC^{4}A Kampagne gemessenen Wolkentröpfchengrößenverteilungen präsentiert, die einen mittleren effektiven Radius von $10.2\,\mu m \pm 4.2\,\mu m$ und eine mittlere effektive Varianz von 0.1 ± 0.04 zeigt. Zusätzlich wird untersucht, wie die Tröpfchengrößenverteilung mit der vorherrschenden mesoskaligen Wolkensituation variiert, die in vier verschiedene Wolkenkategorien eingeteilt wird. So finden sich die größten Tröpfchen in den „Fish"-Wolken, die auch mit Niederschlag assoziiert sind, und besonders kleine Tröpfchen in „Sugar"-Wolken. Diese bestehen typischerweise aus flachen Kumuluswolken, in denen sich nur selten Niederschlag bildet. Die hohe räumliche Auflösung der specMACS-Daten ermöglicht es außerdem, die Auswirkungen der Einmischung trockener Luft an den Wolkenrändern auf die abgeleiteten Tröpfchengrößenverteilungen zu untersuchen. Dies ist ein Faktor, der das Wolkenwachstum und die Niederschlagswahrscheinlichkeit beeinflusst. Für diese Studie wurde der Datensatz in Punkte in der Nähe des Wolkenrandes und in Punkte aus dem Wolkenzentrum unterteilt. Die Analyse ergibt, dass das Wolkenzentrum im Vergleich zum Wolkenrand tendenziell größere effektive Radien, geringere effektive Varianzen und höhere Tröpfchenanzahlkonzentrationen aufweist. Diese Beobachtungen stimmen mit theoretischen Überlegungen überein.

Zusammenfassend zeigen die Ergebnisse, dass mit der Wolkenbogenmethode die Tröpfchengrößenverteilung mit hoher Genauigkeit bestimmt werden kann, sodass eine Quantifizierung der Tröpfchenanzahlkonzentration in der Wolke möglich ist und der Einfluss von Mischungsprozessen auf die mikrophysikalischen Eigenschaften von Wolken untersucht werden kann.

Abstract

Earth's energy balance is strongly influenced by clouds, aerosol, and aerosol–cloud interactions, which still represent a major source of uncertainty in current climate predictions. Key cloud microphysical parameters are the cloud droplet size distribution, which determines the optical properties, and the droplet number concentration, which is linked to the number of cloud condensation nuclei. Since commonly used methods that retrieve these parameters from passive remote sensing measurements are subject to large uncertainties, the development of new retrieval techniques is required.

The aim of this work is to derive the droplet size distribution and droplet number concentration from observations of the airborne camera system specMACS (spectrometer of the Munich Aerosol Cloud Scanner) measured during the EUREC^{4}A (ElUcidating the RolE of Cloud-Circulation Coupling in ClimAte) campaign in order to study the vertical development of cloud microphysical properties and the role of entrainment for shallow cumulus clouds in the trade-wind region. For this purpose, a novel droplet size distribution retrieval was developed. The method is based on polarized measurements of the cloudbow, which, similar to the better-known rainbow, is formed through scattering of sunlight by spherical particles such as droplets in liquid water clouds, and is sensitive to the effective radius (r_{eff}) and to the width of the size distribution defined by the effective variance (v_{eff}). Since the cloudbow is a single scattering phenomenon, it is strongly polarized and therefore very well visible in the 2-D polarization measurements of the specMACS camera. The developed cloudbow retrieval involves collecting measurements of the same target on a cloud from various angles when flying over a cloud field, thereby generating an angle-resolved signal of the cloudbow. By fitting a lookup table of previously simulated polarized cloudbow signals for different droplet size distributions to the measured data, the effective radius and the effective variance are determined at a spatial resolution of about 100 m. By using polarized measurements, multiple-scattering contributions in the signal and thus, retrieval uncertainties are minimized. A model-based evaluation demonstrates the high accuracy of the retrieval results with an absolute average difference of (-0.2 ± 1.30) µm in r_{eff} and (0.02 ± 0.05) in v_{eff} (Volkmer et al., 2023). The high quality of the retrieved droplet size distribution allows the droplet number concentration to be derived by a method usually applied to satellite data assuming a sub-adiabatic cloud profile which links the cloud droplet number to the retrieved cloud optical depth and effective radius.

A statistical analysis of the cloud droplet size distributions measured during the EUREC^{4}A campaign is presented, showing a median effective radius of 10.2 µm $\pm$ 4.2 µm and a median effective variance of 0.1 $\pm$ 0.04. In addition, the variation of the droplet size distribution with the dominant mesoscale cloud situation categorized into four patterns is studied. The largest droplets are found in "fish" clouds, which are commonly associated with precipitation, and particularly small droplets appear in "sugar" clouds consisting of non-precipitating shallow cumuli. The high spatial resolution of the specMACS data further allows to study the effect of mixing of dry air at the cloud edges on the derived droplet size distributions, a factor influencing cloud growth and precipitation likelihood. For this study, the dataset was divided into points near the cloud edge, and points from the cloud center. The analysis shows that the cloud center tends to have larger effective radii, lower effective variances, and higher droplet number concentrations compared to the cloud edge, which matches recent theoretical considerations.

In summary, the results demonstrate that the cloudbow method provides the droplet size distribution with an accuracy high enough to quantify the cloud droplet number concentration and to study entrainment effects on cloud microphysical properties.

Publications

Parts of this dissertation are published as first-author publication in:

- Pörtge, V., Kölling, T., Weber, A., Volkmer, L., Emde, C., Zinner, T., Forster, L., and Mayer, B.: High-spatial-resolution retrieval of cloud droplet size distribution from polarized observations of the cloudbow, Atmospheric Measurement Techniques, 16, 645–667, doi:10.5194/amt-16-645-2023, 2023

The text of the original publication was slightly modified to increase the overall readability of the document, and can be found in the following sections:

- Section 1.1.2
- Section 3.1
- Section 3.2.1
- Section 3.2.2
- Section 3.2.4

Furthermore, I actively participated as co-author in the following published or submitted publications. When appropriate, these works will be cited in the following thesis.

- Stevens, B., Bony, S., Farrell, D., Ament, F., Blyth, A., Fairall, C., Karstensen, J., Quinn, P. K., Speich, S., Acquistapace, C., et al. (2021). EUREC^{4}A. *Earth System Science Data*, 13(8):4067–4119.
- Konow, H., Ewald, F., George, G., Jacob, M., Klingebiel, M., Kölling, T., Luebke, A. E., Mieslinger, T., Pörtge, V., Radtke, J., Schäfer, M., Schulz, H., Vogel, R., Wirth, M., Bony, S., Crewell, S., Ehrlich, A., Forster, L., Giez, A., Gödde, F., Groß, S., Gutleben, M., Hagen, M., Hirsch, L., Jansen, F., Lang, T., Mayer, B., Mech, M., Prange, M., Schnitt, S., Vial, J., Walbröl, A., Wendisch, M., Wolf, K., Zinner, T., Zöger, M., Ament, F., and Stevens, B.: EUREC^{4}A's *HALO*, Earth System Science Data, 13, 5545–5563, doi:10.5194/essd-13-5545-2021, 2021

- Dauhut, T., Couvreux, F., Bouniol, D., Beucher, F., Volkmer, L., Pörtge, V., Schäfer, M., Ayet, A., Brilouet, P.-E., Jacob, M., and Wirth, M.: Flower trade-wind clouds are shallow mesoscale convective systems, Quarterly Journal of the Royal Meteorological Society, doi:10.1002/qj.4409, 2022

- Weber, A., Kölling, T., Pörtge, V., Baumgartner, A., Rammeloo, C., Zinner, T., and Mayer, B.: Polarization upgrade of specMACS: calibration and characterization of the 2D RGB polarization-resolving cameras, Atmospheric Measurement Techniques, 17, 1419–1439, doi:10.5194/amt-17-1419-2024, 2024

- Volkmer, L., Pörtge, V., Jakub, F., and Mayer, B.: Model-based evaluation of cloud geometry and droplet size retrievals from 2-D polarized measurements of specMACS, EGUsphere, 2023, 1–22, doi:10.5194/egusphere-2023-2235, 2023

- Emde, C., Pörtge, V., Manev, M., and Mayer, B.: Retrieval of cloud fraction and optical thickness from multi-angle polarization observations, to be submitted, 2024

Finally, I have been and still am involved in co-supervising the theses of the following students. Their work has been very useful for my thesis:

- Scheiderer, A.: Polarisationsbasierte Wolkenerkennung angewendet auf Kameradaten der EUREC4A-Kampagne, Bachelor's Thesis, 2021

- Bünning, M.: Flugzeug- und satellitengestützte passive Fernerkundung des Effektivradius von Wolkentröpfchen im Rahmen der EUREC^{4}A-Kampagne, Bachelor's Thesis, 2021

- Ma, Z.: Cloud Detection based on Polarimetric specMACS Observations over Ocean and Land, Bachelor's Thesis, 2022

- Koppenhofer, S.: Spektrale und radiometrische Kalibrierung der Polarisationskameras von specMACS, Bachelor's Thesis, 2022

- Bernlochner, S.: Bestimmung von Wolkentröpfchengrößenverteilungen mithilfe der Regenbogen-Fourier-Transformation und Anwendung auf specMACS-Daten, Bachelor's Thesis, 2023

- Koppenhofer, S.: Validation of specMACS microphysical products with independent aircraft and satellite observations, Master's Thesis, to be submitted, 2024

Contents

Chapter 1

Introduction

1.1 Relevance of clouds, aerosol and aerosol–cloud interactions for climate

Looking at the sky is usually very rewarding. You can see fascinating cloud shapes, the changing colors of the sky and, if you're lucky, occasionally an atmospheric optical phenomenon. When I look at clouds these days, I have mixed feelings about these celestial formations. Clouds are beautiful objects that can occur at different heights and at different sizes, and I find it fascinating that they appear so light weight and fluffy, but are actually heavy objects and even small clouds can weigh as much as 10 000 kg. How clouds interact with their environment is exciting, and often you can't look closely enough to see the changing parts of the clouds. But despite appreciating their beauty, I also think about the many unsolved problems in the study of clouds. Clouds have a major influence on Earth's radiation balance. Depending on the type, thickness and height of the cloud, they either have a cooling effect on the climate by reflecting large amounts of solar radiation or act like a greenhouse gas in case the absorption and re-emission of thermal radiation dominates. Therefore, they are an important factor that has to be considered *correctly* in climate models. My mixed feelings mainly stem from the "correctly" in the last sentence. The processes that lead to the formation, growth and dissipation of clouds are still not entirely understood, and therefore, remain a challenge for climate models.

A large amount of the uncertainty associated with clouds occurs from aerosol–cloud interactions. Aerosol particles are tiny suspended particles (solid or liquid) in the atmosphere that are emitted naturally, e.g. mineral dust from the soil, sea salt from sea spray or sulphate aerosol from volcanic eruptions. They are also released by man-made processes such as the (incomplete) combustion of fossil fuels. Most aerosol particles efficiently scatter solar radiation, and therefore, counteract the human induced warming by greenhouse gases. But there are also aerosol particles such as black carbon that warm

the atmosphere by absorption of shortwave radiation (Moteki, 2023).

For cloud droplets to form, a cloud condensation nucleus (CCN) is needed onto which the water molecules can condense. Many aerosol particles act as CCN and therefore, play an important role in cloud formation. The interplay between aerosol particles and cloud droplets is complex and cannot be fully represented in climate models. There are various mechanisms that describe how aerosol particles influence clouds and how this affects the radiation budget. An aerosol-rich regime might lead to an increase in droplet number and a reduction in droplet size, which in turn would increase the cloud solar reflectance. This process is called Twomey or albedo effect (Twomey, 1974). Often, the effective radius (r_{eff}) is used as a quantitative description of the droplet size, and the width of the droplet size distribution is characterized by the effective variance (v_{eff}) (Hansen, 1971). Slingo (1990) showed that the radiative effect of a doubling of the atmospheric carbon dioxide concentrations can be balanced by a 15 % to 20 % decrease in the average r_{eff} of clouds which illustrates the potential impact of the Twomey effect on the climate. A reduced droplet size might be accompanied by an increase of the cloud lifetime since the formation of precipitation may be suppressed by the smaller droplets (Warner, 1968; Albrecht, 1989). For low-level clouds that efficiently scatter solar radiation, a longer cloud lifetime would have a cooling effect on climate. On the other hand, smaller droplets may also reduce the cloud lifetime because they evaporate more quickly and cause more mixing of dry ambient air into the cloud which further increases evaporation (Small et al., 2009).

As explained above, the microphysical properties of clouds and their climate response are complex and highly variable, which also makes it challenging to simulate them accurately in numerical models. A cloud's size can be as small as a few meters or as large as hundreds of kilometers. This is an issue for models because they are always limited by their resolution. Although there are cloud-resolving models that substantially help in understanding clouds, such models are computationally very expensive and therefore not used operationally. In addition, they still rely on parameterizations which are subject to uncertainties (Satoh et al., 2019). For example, the effective radius is an important parameter for radiation schemes such as Slingo (1989) or Edwards and Slingo (1996) that are used in climate and weather models like the IFS (Integrated Forecasting System) of the ECMWF (European Centre for Medium-Range Weather Forecasts). To represent the effective radius in such models, a chain of different parameterizations and approximations is used that show a highly simplified picture of cloud processes. For the IFS this is described in a publication by the ECMWF (2023). The parameterization starts with the number of cloud condensation nuclei which is described by a formula that depends on the ground wind speed, as this determines the injection of aerosol into the atmosphere from the surface (Genthon, 1992). As a next step, different empirical formulae are used to describe the transformation from CCN to cloud droplets, which determines the droplet number concentration (Martin et al., 1994). Then, the liquid water

content of clouds is estimated based on the governing equations for water vapour using a so-called single moment bulk microphysic scheme (Forbes et al., 2011). And finally, the r_{eff} is calculated from the liquid water content and the estimated droplet number concentration.

Despite all these difficulties of understanding clouds and representing them in models, the last IPCC report agreed that the scientific understanding of aerosol–cloud interactions is improving (Forster et al., 2021). In contrast to all previous reports, the last one was the first to state with high confidence that "a net negative cloud feedback is very unlikely" (likelihood $\leq 10\,\%$) (Chapter 7, Forster et al., 2021). This means that clouds will amplify rather than suppress global warming in the future. Nevertheless, the uncertainties associated with cloud feedbacks remain the largest contributor to the overall uncertainty in climate predictions and this contribution needs to be reduced. Accurate observations are essential in order to improve the parameterizations used in models.

1.1.1 Challenges in passive remote sensing of clouds and aerosol

This work is based on airborne observations from the passive remote sensing instrument specMACS (spectrometer of the Munich Aerosol Cloud Scanner) (Ewald et al., 2016; Weber et al., 2024). The retrievals that are applied to the airborne measurements are similar to satellite retrievals. While satellite data have the great advantage of a global coverage, using airborne observations is highly beneficial in many applications since they provide a much more detailed insight into cloud processes than is possible with satellite measurements alone. In particular, the spatial resolution of most satellite measurements ($\approx 1\,\text{km}$) is simply not high enough to resolve small scale cumulus clouds and probe the space between the clouds. The aircraft payload is more flexible and airborne instruments have a faster development cycle, allowing the latest technology to be used in airborne measurements. Furthermore, new retrievals for satellite instruments can be developed from airborne remote sensing observations and retrieval uncertainties that arise from, e.g., the satellite's resolution can be investigated. Overall, there are many similarities between retrievals applied to airborne data and retrievals applied to satellite data. The current challenges of such retrievals are summarized in the following section, and the reader is referred to Quaas et al. (2020) for a more detailed explanation.

For studying aerosol–cloud interactions, and determining their effect on climate, the relationship between CCN concentration and droplet number concentration is crucial (Ghan et al., 2016). The first difficulty in satellite retrievals is that a simultaneous retrieval of droplet number concentration and CCN concentration is often not possible. Most of the time, the aerosol optical depth is used as a proxy for the amount of cloud condensation nuclei, which is problematic since the aerosol optical depth not only depends on the concentration of the aerosol particles, but also on their size. In addition, only hygroscopic aerosol particles act as CCN (Hasekamp et al., 2019). Furthermore, there is no direct method to determine the droplet number concentration N_{d}. The most widely used

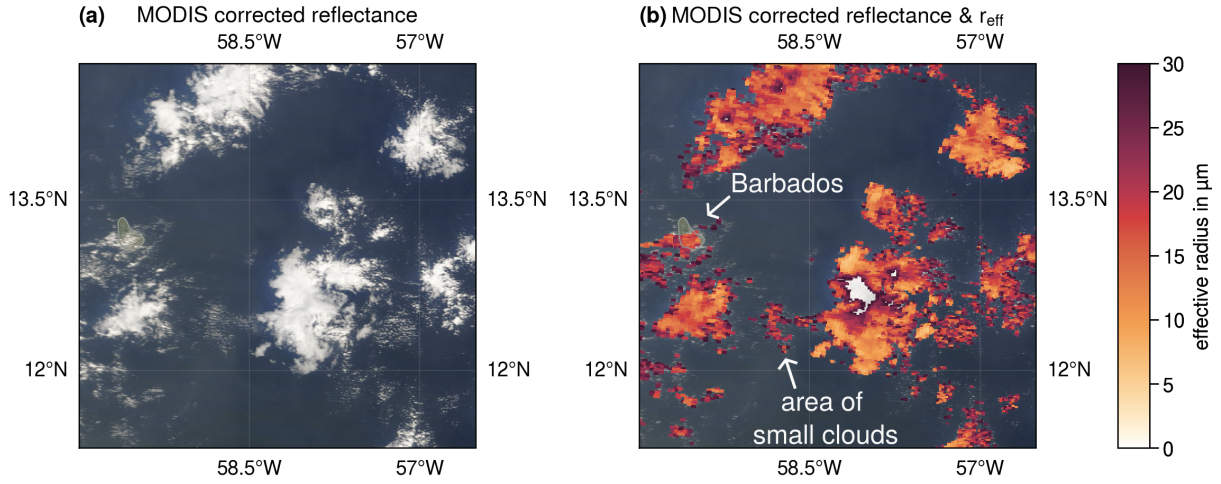

Figure 1.1: Corrected reflectance (panel (a)) measured by MODIS onboard Terra on February 2, 2020 in the region around Barbados and retrieved effective radius on top (panel (b)).

method is to retrieve N_d indirectly from measurements of r_{eff} and the cloud optical depth τ_c (Grosvenor et al., 2018b). This approach is extremely sensitive to r_{eff} ($N_d \sim r_{eff}^{-5/2}$), which is problematic since the determination of r_{eff} (and of τ_c) is subject to uncertainties. These quantities are usually obtained using the two-wavelength or bispectral method described in Nakajima and King (1990). The method simultaneously determines the effective radius and the cloud optical depth by combining reflectance measurements at a wavelength where the cloud absorbs radiation (e.g., at 2.16 µm) with measurements at a wavelength where it does not absorb (e.g., at 0.75 µm). The cloud optical thickness is mainly determined by the reflectance in the nonabsorbing wavelength while the reflectance in the absorbing channel additionally depends on the effective radius. The derived effective radius varies depending on the choice of the absorbing channel. This is explained by the fact that typically the effective radius increases with height inside a cloud. Since different channels have different penetration depths depending on the absorption of the radiation, the effect of the vertical profile of the droplet size is visible within the measurements from different channels (Platnick, 2000).

The bispectral technique is widely used from satellite instruments such as MODIS onboard the Terra and Aqua satellites, VIIRS (on the NPP satellite) or the ABI instrument onboard GOES. However, it is subject to uncertainties which mainly arise from 3-D radiative transfer effects and partial cloud cover effects (e.g. Marshak et al., 2006; Zinner et al., 2008; Zhang et al., 2012). An example of the retrieved r_{eff} using the bispectral technique is shown in Figure 1.1 based on data from the MODIS instrument onboard Terra for February 2, 2020. This figure shows the reflectance measurement in the tropical Atlantic in panel (a) and the retrieved r_{eff} in panel (b) at a spatial resolution of 1 km (Platnick et al., 2003). It illustrates some problems of the bispectral technique. For example, particularly large effective radii are derived for many of the small clouds. This

is unrealistic and can be attributed to a resolution problem. Such pixels are probably subject to subpixel broken cloudiness which means that the pixel is not completely covered by a cloud. If the surface reflection is low (for example above the dark ocean), then the measured reflectance is reduced compared to a pixel that is fully covered by clouds. A reduced reflectance generates large r_{eff} and low τ_{c} in the bispectral retrieval (Platnick et al., 2003). In addition, observations of small clouds are highly influenced by leakage of photons out of the cloud at the cloud sides which also reduces the reflectance compared to the assumption of a homogeneous plane-parallel (1-D) cloud which is considered independent from surrounding pixels. Uncertainties are also caused by subpixel inhomogeneities, and shadowing or illuminating effects for low sun (Marshak et al., 2006). Apart from such 3-D and subpixel effects, the method relies on a very precise calibration of the measured reflectances in order to obtain accurate retrieval results which is challenging. Despite all these uncertainties, it is still the most widely used method.

1.1.2 Polarimetric measurements

Parts of the following section were published in Pörtge et al. (2023).

The last section showed that current methods that derive the parameters (N_{d} and CCN concentration) relevant for aerosol–cloud interactions are subject to various uncertainties which can cause major errors. In particular, more precise retrievals of the droplet size are necessary to increase the accuracy of N_{d}.

For this purpose, the use of polarized measurements for the retrieval of cloud (and aerosol) optical properties has become more and more popular in recent years (e.g., Bréon and Goloub, 1998; Alexandrov et al., 2012a; Diner et al., 2013; Remer et al., 2019; McBride et al., 2020). Unpolarized reflectance measurements, which were previously used for retrievals, are strongly influenced by the signal generated by multiple-scattering of photons, and are therefore affected by 3-D radiative effects. Polarized measurements have the advantage that multiply-scattered contributions are filtered out and single scattering dominates the signal (Hansen, 1971). This greatly reduces 3-D effects, simplifies the analysis and hence increases the overall accuracy of polarimetric retrievals.

Single scattering phenomena that are strongly polarized are the cloudbow and the backscatter glory. The cloudbow is an optical phenomenon that is very similar to the better-known rainbow but forms through scattering of solar radiation by liquid cloud droplets in contrast to scattering by rain droplets as for the rainbow. The glory is formed by backscattering of sunlight by cloud droplets (Laven, 2005). Both phenomena are described by Mie theory (Mie, 1908; Hansen, 1971). Figure 1.2 shows a measurement of the specMACS polarization camera. The total reflectance is shown in panel (a) and the degree of linear polarization in panel (b). The cloudbow and the backscatter glory are visible as rings of enhanced polarization.

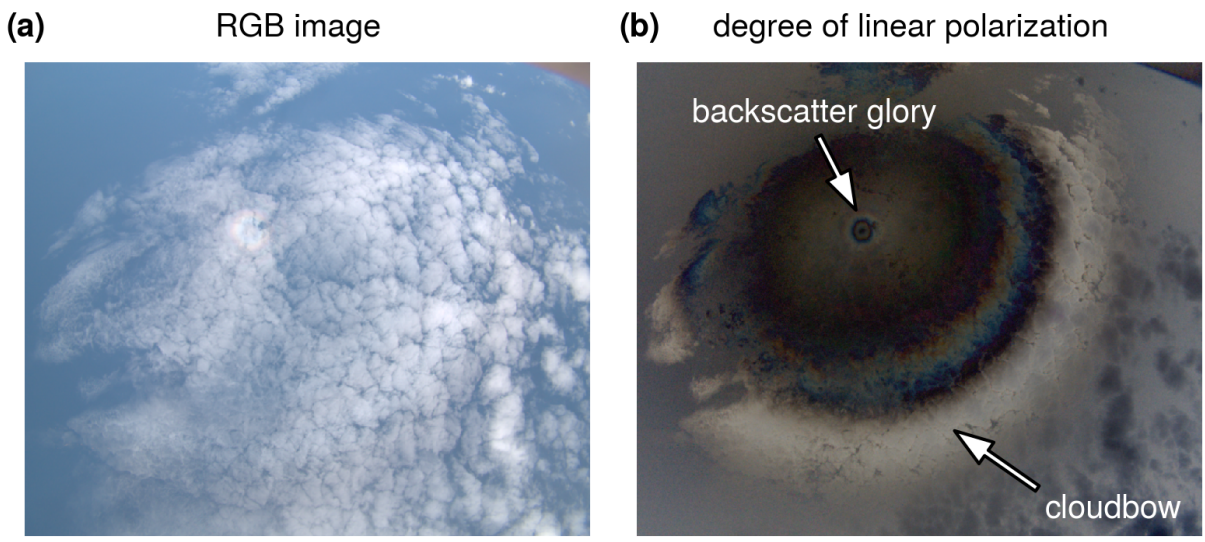

Figure 1.2: Measurement of the specMACS polarization camera. Panel (a): Unpolarized RGB (red-green-blue) measurement; Panel (b): Degree of linear polarization (DOLP)

The polarized radiance of liquid water clouds is sensitive to r_{eff} and v_{eff} in the region of the backscatter glory as well as in the cloudbow or rainbow region. Based on polarized observations of the cloudbow, a new type of droplet size distribution (DSD) retrieval has emerged which will also be the main method of this thesis: the polarimetric cloudbow technique. The polarimetric retrieval fits polarized phase functions to the measured polarized radiance to determine r_{eff} and v_{eff} (Bréon and Goloub, 1998). In general, unpolarized images also show the glory and the cloudbow and have already been successfully evaluated in terms of the DSD (e.g., Mayer et al., 2004; Koren et al., 2022). However, especially for the cloudbow, the contrast in unpolarized observations is usually weak because the signal is dominated by the multiple-scattering background. The use of polarized observations significantly enhances the signal.

The polarimetric cloudbow retrieval has already been applied to data from several instruments which include the POLDER satellite (POLarization and Directionality of the Earth's Reflectances Bréon and Goloub, 1998; Bréon and Doutriaux-Boucher, 2005; Shang et al., 2019), the airborne RSP instrument (Research Scanning Polarimeter; Cairns et al., 1999; Alexandrov et al., 2012a), the airborne AirHARP instrument (Airborne Hyper-Angular Rainbow Polarimeter; Martins et al., 2018; McBride et al., 2020), and the airborne AirMSPI instrument (Airborne Multiangle SpectroPolarimetric Imager; Diner et al., 2013; Xu et al., 2018). A detailed overview of instruments with polarization capabilities that also apply the polarimetric cloudbow technique is given in McBride et al. (2020).

The additional information from polarimetric measurements is also advantageous when it comes to studying aerosol (Remer et al., 2019). Aerosol and clouds have different angular polarimetric signatures (e.g., Emde et al., 2010) that can be exploited to

distinguish between them. Furthermore, theoretical studies have shown that aerosol properties can be retrieved from polarimetric measurements with sufficient accuracy for climate research (e.g., Mishchenko and Travis, 1997; Hasekamp and Landgraf, 2007). For instance, the simultaneous characterization of cloud properties and properties of aerosol above clouds (Knobelspiesse et al., 2011) or of aerosol between clouds (Hasekamp, 2010; Stap et al., 2016a,b) is possible when using multi-angle polarimetric measurements.

In summary, obtaining polarization data is desirable to improve the global picture of the atmosphere concerning both cloud and aerosol properties as well as to quantify aerosol–cloud interactions. For this reason, several satellite missions with polarimetric instruments aboard will soon be launched or are already in space. The PACE (Plankton, Aerosol, Cloud, ocean Ecosystem) mission is a recently launched polar-orbiting satellite with two polarimeters for cloud and ocean retrievals (Remer et al., 2019), the 3MI (Multi-viewing Multi-spectral Multi-polarization Imaging) instrument will be part of the payload of the MetOp-SG satellite (Fougnie et al., 2018), and the MAIA (Multi-Angle Imager for Aerosols) instrument (Diner et al., 2018) will help to characterize particulate matter in air pollution, to name a few of the planned satellite instruments. The various existing polarimetric instruments as well as those under development are listed in Dubovik et al. (2019). The development of polarimetric instruments is an active research focus, and polarimetric airborne instruments are highly useful in investigating appropriate instrument design, satellite mission planning, or retrieval techniques.

1.2 Objective and outline

The scientific objective of the following work is to study the microphysical properties of shallow cumulus clouds in the trade-wind regions. Trade-wind clouds are particularly important for the climate, because they are the most common type of cloud on Earth, and their influence on Earth's radiation budget is a major source of uncertainty in the climate sensitivity across different climate models (Bony and Dufresne, 2005; Zelinka et al., 2020). To advance our understanding of trade-wind clouds and how they interact with the ocean and atmosphere, the EUREC^{4}A (ElUcidating the RolE of Cloud-Circulation Coupling in ClimAte) field campaign took place in January and February 2020 (Bony et al., 2017; Stevens et al., 2021). As a major success, first observational results from the campaign have refuted a long-standing hypothesis from climate models which expected a drying of the cloud layer and subsequent increased warming of the climate. The observations showed that this effect is prevented by mesoscale circulations (Vogel et al., 2022). EUREC^{4}A deployed various measurement platforms (airborne, ground-based, ship-based, ...) to characterize different aspects of the ocean-atmosphere system, and to study the mesoscale organization of convection. One of the platforms was the German research airplane HALO (High Altitude and LOng range research aircraft) which provided large scale observations from dropsondes and remote sensing instruments

including the specMACS cloud camera system (Ewald et al., 2016).

In this work, the polarimetric specMACS measurements are evaluated to study microphysical properties of shallow cumulus clouds. Of particular interest is the cloud droplet size distribution and how it is affected by entrainment and mixing. For this purpose, a polarimetric cloudbow retrieval has been developed and applied to the specMACS measurements. The retrieval involves a sophisticated aggregation of observations from different viewing angles while flying over the cloud to generate angularly resolved polarized cloudbow signals. These signals are used to accurately determine the cloud droplet size distribution at the top of liquid water clouds. In contrast to traditional remote sensing retrieval techniques, the cloudbow retrieval is very well applicable to shallow cumulus clouds since 3-D radiative effects are suppressed. A further highlight is that the specMACS instrument measures 2-D radiance distributions, and thus, the spatial variation of the droplet size distribution can be studied at a high spatial resolution of approximately 100 m. In addition, the highly accurate r_{eff} also allows information on the droplet number concentration to be derived, from which aerosol–cloud interactions can be studied.

This thesis is organized as follows: Chapter 2 explains the theoretical background of cloud microphysical properties and how liquid water clouds interact with solar radiation. It focuses on scattering processes and their effect on the polarization of the radiation. Chapter 3 describes the camera system specMACS and the individual steps of the polarimetric cloudbow retrieval. The retrieved cloud droplet size distributions are presented as 2-D maps illustrating the high spatial resolution of the specMACS measurements. Besides, a case study of small cumulus clouds (diameters of 1 km to 2 km) is presented to discuss uncertainties of the method related to instrument characteristics. The accuracy of the method is validated by an observational comparison study and a study of realistic radiative transfer simulations of shallow cumulus clouds. In addition, a method for deriving the droplet number concentration, which is commonly applied to satellite data, is presented. In Chapter 4, the results of applying the polarimetric cloudbow retrieval to the whole dataset of the EUREC^{4}A campaign are presented. One aspect that is explored is the variation of the droplet size distribution with height which differs for different measurement days. A second scientific study investigates the dependence of the cloud droplet size distributions on the dominant mesoscale cloud pattern. Finally, the influence of entrainment and mixing on the cloud droplet size distribution and the droplet number concentration of a field of shallow cumulus clouds is analyzed, which is only possible thanks to the high resolution of the data and the available 2-D information. The conclusion and possible future improvements of the method are summarized in Chapter 5.

Chapter 2

Theoretical Background

The aim of this work is to investigate microphysical properties namely the droplet size distribution and droplet number concentration of clouds. For this purpose, measurements of clouds taken with a polarization camera are evaluated. To understand the measurements and the retrieval method, basic concepts of radiative transfer and cloud properties will be discussed in the following chapter. The general information about electromagnetic radiation (Section 2.1) is taken from Petty (2006) unless otherwise stated.

2.1 Electromagnetic radiation

Light, or electromagnetic radiation in general, consists of electromagnetic waves. An electromagnetic wave has an oscillating electric field $\vec{\mathbf{E}}$ coupled to an oscillating magnetic field $\vec{\mathbf{B}}$. The two fields $\vec{\mathbf{E}}$ and $\vec{\mathbf{B}}$ are perpendicular to each other and to the direction of propagation of the electromagnetic wave. The first property that characterizes an electromagnetic wave is its wavelength λ, which is connected to the frequency f and the speed v of the wave via

$$\lambda = \frac{v}{f} \tag{2.1}$$

Electromagnetic waves travel at the speed of light c through a vacuum and slow down in a medium depending on the refractive index of the medium. In nature, electromagnetic waves appear at a huge variety of different wavelengths. Over 99 % of the electromagnetic radiation emitted by the sun has wavelengths in the range from 0.1 µm to 4 µm, which are the ultraviolet, visible and near-infrared spectral bands. Most thermal radiation (over 99 %) has higher wavelengths from 4 µm to 100 µm (infrared spectrum). The way radiation interacts with matter crucially depends on the wavelength of the radiation. While radiation at some wavelengths might be absorbed by a certain material or gas, this is not necessarily the case for radiation with a different wavelength. An electromagnetic

wave is further characterized by the intensity of the light. This determines the energy that is transported with the wave. Polarization describes the orientation of the oscillating electric field vector of the electromagnetic wave. Sunlight that enters the atmosphere is unpolarized, meaning that its electric field vector has no preferred direction.

Certain observed properties of electromagnetic radiation cannot be described by the wave nature of radiation. These include the photoelectric effect, which describes the emission of electrons when a material is exposed to electromagnetic radiation. Electrons are emitted only when the frequency of the light exceeds a certain threshold regardless of the intensity of the illumination. This observation disagrees with the classical wave theory of electromagnetic radiation which states that the electrons continuously accumulate energy until they are emitted. To explain these observations, the particle or photon model was proposed which describes a beam of light as consisting of discrete packets of energy called photons. The energy Q contained in a photon depends on the frequency of the radiation. The constant of proportionality is the Planck's constant $h = 6.626\,070\,15 \times 10^{-34}\,\mathrm{J\,s}$ and Q is defined via

$$Q = hf. \tag{2.2}$$

2.1.1 Radiation quantities

Table 2.1: Definitions of radiative quantities. Table as in Mayer (2009).

quantity	symbol	definition	unit
radiant energy	Q		J
radiant power	ϕ	$\frac{dQ}{dt}$	W
irradiance	E	$\frac{dQ}{dAdt}$	$\mathrm{W\,m^{-2}}$
radiance	L	$\frac{dQ}{dA\cos\theta d\Omega dt}$	$\mathrm{W\,m^{-2}\,sr^{-1}}$

In the following, important quantities that are used to describe radiative transfer processes are introduced and summarized in Table 2.1:

- The radiant power ϕ defines the radiant energy dQ per unit time dt and is measured in units of $\mathrm{J\,s^{-1}}$ or W. ϕ is proportional to the squared amplitude of the electric wave.

- The radiant energy per unit time dt and unit area dA is the irradiance, flux density or simply flux E. For a point radiation source, the irradiance is inversely proportional to the squared distance to the source.

- The term radiance or intensity L describes the radiant energy per unit time dt, per unit solid angle $d\Omega$ and per unit area (normal to the direction considered) $dA\cos\theta$. The directional information can be very useful since it provides insights into how radiant energy is distributed in different directions. For example, the way a material reflects radiation can depend on the direction.

For each of these quantities, there is also a wavelength-dependent form which takes into account the contribution of a particular wavelength. For example, a typical unit of a spectral irradiance would be $\mathrm{W\,m^{-2}\,\mu m^{-1}}$.

2.1.2 Polarization

The polarization of an electromagnetic wave determines the direction of the oscillating electric field vector, which can have any orientation that is perpendicular to the wave's direction of propagation.

Stokes vector

A mathematical description of polarization is the Stokes vector $\vec{\mathbf{S}}$ which consists of the four Stokes parameters I, Q, U, and V (Hansen and Travis, 1974):

$$\vec{\mathbf{S}} = \begin{bmatrix} I \\ Q \\ U \\ V \end{bmatrix} = \begin{bmatrix} \langle E_\parallel E_\parallel^\star + E_\perp E_\perp^\star \rangle \\ \langle E_\parallel E_\parallel^\star - E_\perp E_\perp^\star \rangle \\ \langle E_\parallel E_\perp^\star + E_\perp E_\parallel^\star \rangle \\ i\langle (E_\parallel E_\perp^\star - E_\perp E_\parallel^\star) \rangle \end{bmatrix} = \begin{bmatrix} I_{0^\circ} + I_{90^\circ} \\ I_{0^\circ} - I_{90^\circ} \\ I_{45^\circ} - I_{135^\circ} \\ I_{\text{right-handed}} - I_{\text{left-handed}} \end{bmatrix} \tag{2.3}$$

For the definition of the Stokes parameters, the electric field $\vec{\mathbf{E}}$ is split up into a parallel $\vec{\mathbf{E}}_\parallel = E_\parallel \hat{\mathbf{e}}_\parallel$ and a perpendicular component $\vec{\mathbf{E}}_\perp = E_\perp \hat{\mathbf{e}}_\perp$ relative to a certain reference plane. $\hat{\mathbf{e}}_\parallel$ and $\hat{\mathbf{e}}_\perp$ are unit vectors into the parallel and perpendicular directions. In Equation 2.3, time averages are indicated by the symbols $\langle\rangle$ and asterisks indicate the complex conjugates of the fields. Each Stokes parameter has the dimension of radiance. I is the total intensity of the light, and the other Stokes parameters define the linear (Q and U) and circular (V) polarization state. In the atmosphere, there are almost no processes that generate circular polarization. Therefore, the circular polarization can be neglected when it comes to atmospheric studies (e.g., Emde et al., 2015; Hansen and Travis, 1974). The degree of linear polarization is defined by $\mathrm{DOLP} = \frac{\sqrt{Q^2+U^2}}{I}$ and the polarized radiance is calculated by $\sqrt{Q^2+U^2}$. Both quantities are independent of the reference plane of the Stokes vector (Bohren and Huffman, 1998)

In radiative transfer calculations that involve scattering processes, the reference plane of the Stokes vector is often chosen to be the scattering plane which is the plane

containing the incident and scattered directions. Good illustrations of commonly used reference planes are shown in Eshelman and Shaw (2019). Due to symmetries, the Stokes parameter U is equal to 0 within the scattering plane in the case of single scattering. In this case, Q contains all information about the linear polarization of the radiation and the polarized radiance is identical to Q. As shown in Equation 2.3, the Stokes vector can also be determined by measuring the intensities of the light after passing through polarizers of different directions. In this notation, the 0° polarizer direction is parallel to the $\overrightarrow{\mathbf{E}_{\parallel}}$ component.

Müller matrices

Whenever radiation interacts with an optical element, the polarization state of the radiation is changed. This change can be described by a 4×4 Müller matrix $\mathbf{M}$ which relates the incident Stokes vector $\overrightarrow{\mathbf{S_0}}$ to the Stokes vector $\overrightarrow{\mathbf{S}}$ after the interaction (Bohren and Huffman, 1998).

$$\overrightarrow{\mathbf{S}} = \mathbf{M}\overrightarrow{\mathbf{S}}_0 \tag{2.4}$$

A special type of a Müller matrix is the scattering matrix or phase matrix $\mathbf{P}$ which specifies the angular distribution of the Stokes vector after a scattering process (Bohren and Huffman, 1998). Furthermore, a rotation of the Stokes vector by an angle ψ into a different reference plane can also be expressed as a Müller matrix (Bohren and Huffman, 1998):

$$\mathbf{M} = \begin{bmatrix} 1 & 0 & 0 & 0 \\ 0 & \cos 2\psi & \sin 2\psi & 0 \\ 0 & -\sin 2\psi & \cos 2\psi & 0 \\ 0 & 0 & 0 & 1 \end{bmatrix} \tag{2.5}$$

Polarizer

The german term “Polarisationsfilter” might be a little misleading as to what a polarizer actually does. From the term “filter” one might expect that the polarizer selectively transmits light waves of a certain polarization while blocking or attenuating light waves of other polarizations. However, this is not entirely true and will be explained based on an experiment in the following. The description of the experiment can also be found in textbooks like Giancoli (2019) or Sakurai and Napolitano (2020). Unpolarized radiation hits a polarizer. When passing through the polarizer, a portion of the incoming light becomes aligned with the polarizer. Then, a second polarizer is placed at an angle of 90° to the first one and no light is observed after the second polarizer. Finally, a third polarizer at an angle of 45° is placed between polarizer 1 and 2. Surprisingly, a certain amount of light is registered after passing through the whole setup of three polarizers.

The question that comes up is: why do three filters block less light than two?

In fact, a polarizer does not completely block certain components of the light. Instead, it allows the projection of the electric field to the polarizer's axis to pass. This experiment can also be understood in terms of quantum theory, where the photons are thought to be in a linear superposition of photons with vertical and horizontal polarization (Dirac, 1930). The irradiance E passing through a polarizer is defined by Malus's law which relates the outgoing irradiance E to the incident irradiance E_0 and the angle θ_i between the axis of the polarizer and the initial polarization direction of the light (Giancoli, 2019):

$$E = E_0 \cos^2 \theta_i \tag{2.6}$$

2.2 Interaction of radiation with the atmosphere

Electromagnetic radiation interacts with matter by different processes (Petty, 2006):

- Radiation can be *absorbed* by gases or particles. If absorption happens, radiative energy is converted to heat.
- *Emission* generates radiation within a medium from heat energy. The generated radiation depends on the temperature of the medium.
- An elastic *scattering* process results in a redirection of the radiation while the frequency of the radiation is not changed.

Radiation is extinguished if either absorption or scattering occurs. The absorption cross-section σ_{abs} and the scattering cross-section σ_{sca} are measures of the effectiveness of particles or molecules in absorbing or scattering incident radiation. The extinction cross-section σ_{ext} is defined as the sum of absorption and scattering cross-section. σ_{ext} refers to the effective area presented by an individual particle or molecule for interacting with electromagnetic radiation, and therefore, has dimensions of area. The (volume) extinction coefficient (β_{ext}) of scattering or absorbing particles with number density N (unit: m^{-3}) can be written as:

$$\beta_{\text{ext}} = \sigma_{\text{ext}} N \tag{2.7}$$

β_{ext} has the unit m^{-1}, and represents the probability per unit distance that a photon is removed from the beam by absorption or scattering. It is the sum of the absorption coefficient β_{abs} and the scattering coefficient β_{sca}:

$$\beta_{\text{ext}} = \beta_{\text{abs}} + \beta_{\text{sca}} \tag{2.8}$$

The relative importance of absorption and scattering is quantified by the single scattering albedo ω:

$$\omega = \frac{\beta_{\text{sca}}}{\beta_{\text{ext}}} \tag{2.9}$$

Within this work, the main focus lies on the evaluation of scattering processes. The scattering behaviour of a particle with radius r depends on the nondimensional size parameter x. The size parameter is defined as the ratio of the circumference of the scattering particle to the wavelength of the incident radiation:

$$x = \frac{2\pi r}{\lambda} \tag{2.10}$$

2.2.1 Mie scattering theory and approximations

Mie theory is the solution of Maxwell's equations for scattering of radiation by spherical particles (Mie, 1908). Mie theory converges to the Rayleigh approximation for small size parameters x, and can be approximated by the model of geometric optics for large x. Both models are presented in this section.

For size parameters $x \approx 1$, neither the Rayleigh approximation, nor the model of geometric optics is adequate and for a correct description of scattering at such size parameters full Mie calculations are needed. One application is, for example, scattering of visible light by cloud droplets at a typical radius of 10 µm. The scattered light appears white because the light at visible wavelengths is scattered equally. There are methods that determine the Mie coefficients depending on x and on the complex refractive index of the sphere (e.g. Wiscombe, 1980). From the Mie coefficients, the matrix elements P_{ij} of the phase matrix can be computed. The Mie scattering phase matrix for scattering by isotropic homogeneous spheres following Bohren and Huffman (1998) is:

$$\mathbf{P}_{\text{Mie}} = \begin{bmatrix} P_{11} & P_{12} & 0 & 0 \\ P_{12} & P_{11} & 0 & 0 \\ 0 & 0 & P_{33} & P_{34} \\ 0 & 0 & -P_{34} & P_{33} \end{bmatrix} \tag{2.11}$$

Due to the azimuthal symmetry of spherical particles, some terms of the matrix are zero, and the matrix has only four independent matrix elements. The P_{11} element is called phase function and the P_{12} element is the polarized phase function. For single scattering of incident unpolarized light, P_{12} is directly proportional to Q in the scattering plane.

Rayleigh scattering

If radiation is scattered by molecules or particles that are much smaller than the wavelength of the radiation, the scattering process can be described by the Rayleigh approximation. For such cases, the size parameter has a value of $x << 1$. The intensity of the scattered light strongly depends on the wavelength ($\propto \lambda^{-4}$) (Hansen and Travis, 1974), and therefore, Rayleigh scattering is responsible for the blue color of the sky. What we experience as blue is actually sunlight that is scattered by molecules such as nitrogen or oxygen in the atmosphere. The phase matrix of Rayleigh scattering depends on the scattering angle θ which defines the angle between incoming and scattered radiation (Hansen and Travis, 1974):

$$\mathbf{P}_{\text{Rayleigh}} = \frac{3}{4}\begin{bmatrix} 1+\cos^2\theta & -\sin^2\theta & 0 & 0 \\ -\sin^2\theta & 1+\cos^2\theta & 0 & 0 \\ 0 & 0 & 2\cos\theta & 0 \\ 0 & 0 & 0 & 2\cos\theta \end{bmatrix} \tag{2.12}$$

The degree of linear polarization of Rayleigh scattering of incident unpolarized light has a maximum at a scattering angle of 90° and is 0 in the forward (θ =0°) and backward (θ =180°) directions (Hansen and Travis, 1974):

$$\text{DOLP}_{\text{Rayleigh}} = \frac{1-\cos^2\theta}{1+\cos^2\theta} \tag{2.13}$$

Geometric optics

The other extreme ($x >> 1$), defines the limit of geometric optics, where light is scattered according to the projected area of the object. Geometric optics uses the model that light propagates in terms of rays. Full Mie calculations are very time-consuming for large size parameters which is why geometric optics is the preferred method in such cases. Typical examples of scattering events that can be described by geometric optics are the formation of the primary and secondary rainbows by the scattering of sunlight by raindrops, or halo phenomena that occur in clouds containing ice particles (see, e.g., Können, 1985). Geometric optics is a simple approximation and is sufficiently accurate for many purposes but it does not take into account any effects due to diffraction or interference (Liou and Hansen, 1971).

Phase functions of spherical particles for different size parameters

Figure 2.1a shows the unpolarized phase functions (P_{11}) of spherical particles for three different size parameters as a function of scattering angle θ. For the small size parameter $x = 0.1$, the phase function is symmetric in the forward and backward directions and can be approximated by the Rayleigh scattering phase function. This symmetry reduces

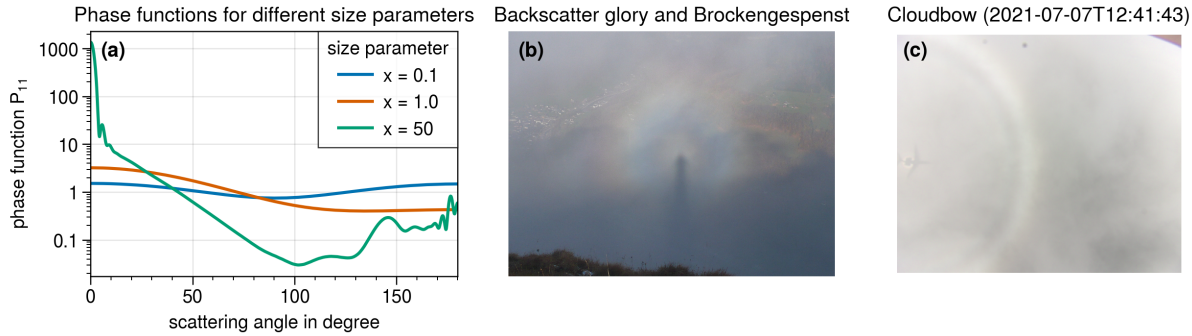

Figure 2.1: (a): Phase functions for different size parameters x calculated from Mie theory. (b): Backscatter glory and Brockengespenst captured by Gotlind Blechschmidt in the Austrian Alps. (c): Cloudbow (and glory) measured with the specMACS instrument on 2021-07-21 during the CIRRUS-HL campaign.

for the phase function with larger size parameter ($x = 1$). Here, an enhancement in the forward direction is visible. For $x = 50$, which corresponds, for example, to a particle with size $r = 5\,\mu m$ and radiation at a wavelength of $0.6\,\mu m$, the phase function is asymmetric and overall very complex. Furthermore, it has a very strong forward peak.

Besides the strong forward peak of the phase function in Figure 2.1a, three other features can be identified in the curve for large spherical particles with size parameter $x = 50$ (Können, 1985). The first is the corona which occurs close to the forward peak ($\theta = 0°$). In nature, a corona can be observed as colorful, concentric rings around the sun or the moon when a thin layer of a liquid cloud is present. At the opposite end of the phase function ($\theta = 180°$) is the backscatter glory which, like the corona, consists of colorful rings and can be observed having the sun in the back during airplane flights or from a mountain as in Fig. 2.1b. The observer's shadow on the cloud may appear to be greatly magnified due to an optical illusion. Due to the movement of the cloud, the shadow is not completely static, which creates a mysterious atmosphere. The shadow is then often called a "Brockengespenst" or Brocken spectre. This name comes from the frequent observations of this phenomenon on the German mountain called Brocken. The third phenomenon is the rainbow or the cloudbow at a scattering angle of approximately 140° (Fig. 2.1c). The main goal of this thesis is to analyze quantitative measurements of the cloudbow because information about the size of the cloud droplets can be obtained from its shape and structure. In the next subsection the benefit of using polarized measurements for this purpose is explained.

2.2.2 The cloudbow and its relation to the droplet size distribution

The cloudbow, introduced briefly in the introduction and the last section of this thesis, serves as the primary focus of this study. Panel (c) of Fig. 2.1 displays an observation of a cloudbow (along with a glory) captured using the specMACS instrument. Unlike rain-

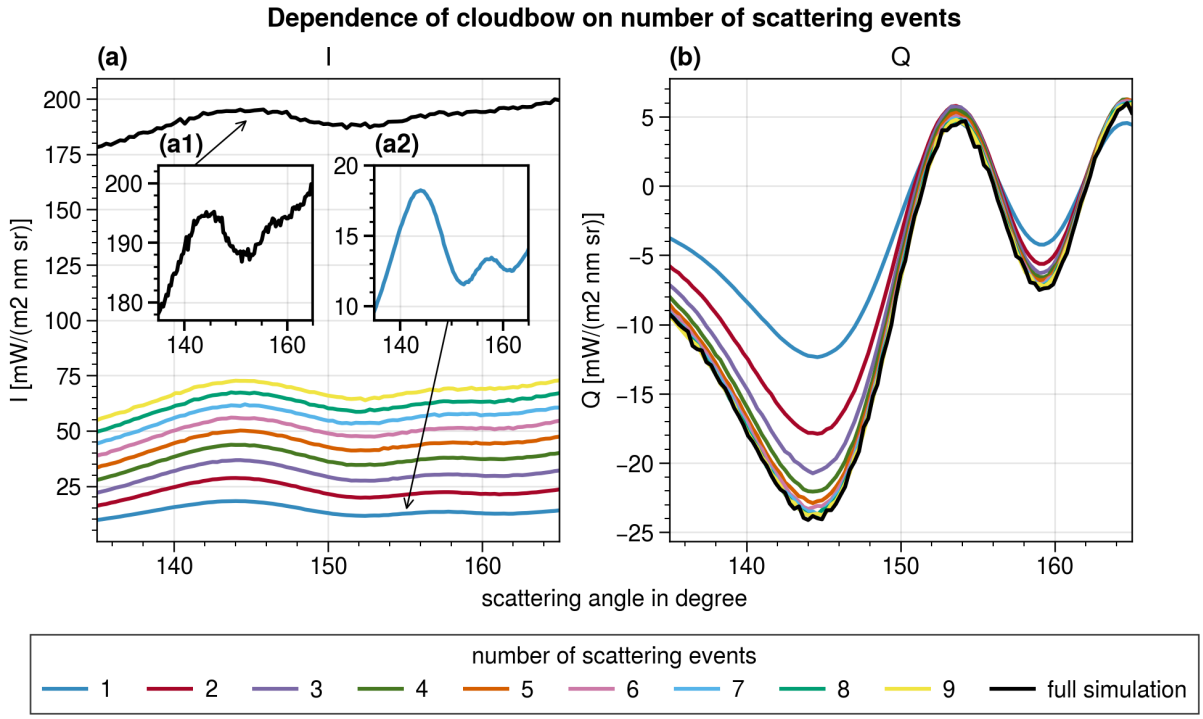

Figure 2.2: Simulated cloudbow for different number of scattering events. Panel (a) shows the I component of the Stokes vector. Panel (b) shows Q. The scattering plane is used as reference plane of the Stokes vector.

bows, which are generated by larger raindrops, cloudbows are formed by much smaller cloud droplets which experience diffraction effects that widen the bow. Consequently, cloudbows exhibit less pronounced spectral dispersion, resulting in predominantly white appearances compared to the strong colors of rainbows. Sometimes it is possible to observe additional bows parallel to the primary bow, called supernumerary bows.

Effect of first and successive scattering events on the cloudbow

In the last subsection, the unpolarized phase function P_{11} was shown in Fig. 2.1a to describe the cloudbow phenomenon. Although the cloudbow is clearly visible in P_{11}, which defines the single scattering properties, its visibility is strongly reduced in actual intensity measurements which are subject to multiple scattering. This is shown in Figure 2.2 which displays simulations of the cloudbow for different numbers of scattering events encountered by each photon. The simulated radiation has the wavelength $\lambda = 620\,\text{nm}$, and a homogeneous cloud layer with $\tau_c = 10$ is considered. The full radiative transfer simulation without a limit on the number of scattering events is plotted as a black line.

The Stokes parameter I is shown in panel (a). The simulation considering only one scattering event has the smallest I and the magnitude of I increases with each additional scattering until it is saturated after being scattered many times. The cloudbow signal is

visible in I but the largest contribution to the signal is generated by photons that were scattered multiple times. This multiple scattering background originates deeper inside the cloud and does not contain any signal from the cloudbow. The figure illustrates that the cloudbow signature, and especially the secondary or supernumerary bows are smoothed out for more scattering events (see also insets in Fig. 2.2).

Panel (b) shows the Stokes parameter Q relative to the scattering plane. Here, the cloudbow with its supernumerary bows is clearly visible in all simulations. What we see in Q is mostly the effect of singly-scattered photons as the Q signal saturates quickly. The simulation considering six scattering events is already very similar to the signal of the full radiative transfer simulation. If light is scattered multiple times, each scattering will change the polarization of the light, and as a result, the light will get more and more unpolarized. The "multiple scattering background" of Q is basically 0 and therefore does not contribute to the total signal of Q. In summary, these simulations show that the best way to analyze the cloudbow quantitatively is to use polarization measurements. More information about the effect of multiple scattering on the cloudbow for different clouds and incident radiation with different wavelengths is given in Hansen (1971).

Dependence of the cloudbow on the cloud droplet size distribution

In this subsection, the polarized phase functions P_{12} of different cloud droplet size distributions are discussed with emphasis on the appearance of the two optical phenomena cloudbow and backscatter glory. To this end, some general properties of the cloud droplet size distribution are introduced here.

The cloud droplet size distribution $n(r)$ defines the number of particles per unit volume with radius between r and $r + dr$ (Hansen, 1971). The droplet formation and the development of the size distribution is explained in more detail in the next chapter, but at this point two characteristic quantities of the cloud droplet size distribution are introduced. The first one is the effective radius r_{eff} which determines the radiative properties of the cloud droplet size distribution. Since the extinction coefficient of cloud droplets is proportional to πr^2, the relevant quantity for radiative properties is the area-weighted average of the droplet radii in a cloud (Hansen, 1971):

$$r_{\text{eff}} = \frac{\int_0^\infty r \pi r^2 n(r) \mathrm{d}r}{\int_0^\infty \pi r^2 n(r) \mathrm{d}r} \tag{2.14}$$

The second quantity is called the effective variance v_{eff} which defines whether the size distribution is narrow, meaning that the individual droplets all have similar sizes, or whether it is broad and the droplet sizes vary strongly (Hansen, 1971):

$$v_{\text{eff}} = \frac{1}{r_{\text{eff}}^2} \frac{\int_0^\infty (r - r_{\text{eff}})^2 \pi r^2 n(r) \mathrm{d}r}{\int_0^\infty \pi r^2 n(r) \mathrm{d}r}. \tag{2.15}$$

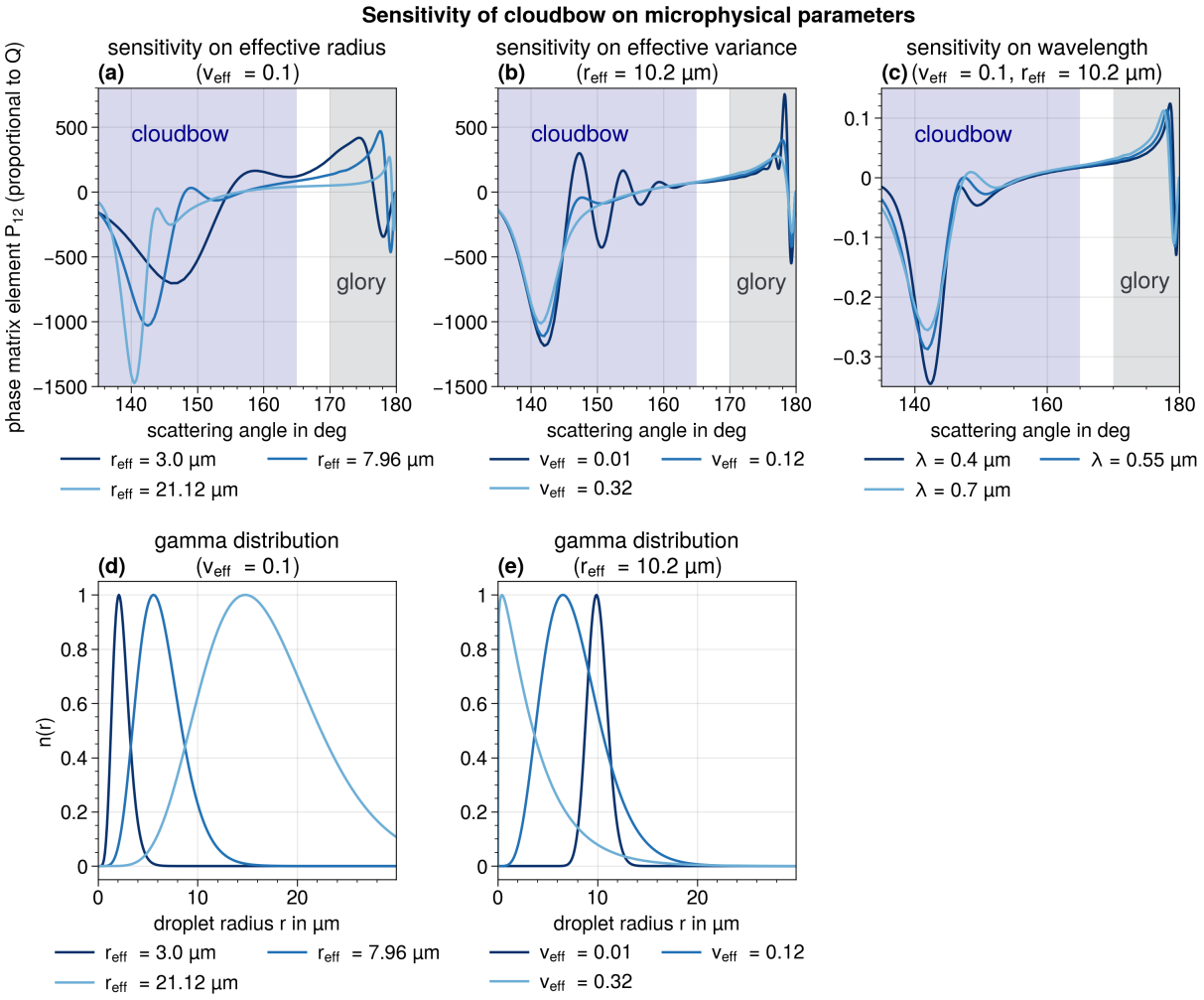

Figure 2.3: Panel (a) shows that the cloudbow signals (P_{12}) vary if r_{eff} is changed while v_{eff} is constant ($v_{\text{eff}} = 0.1$). Panel (b) illustrates the effect of a change in v_{eff} while r_{eff} is held constant ($r_{\text{eff}} = 10.2\,\mu\text{m}$). Panel (c) shows how the cloudbow depends on the wavelength of the radiation. For calculating P_{12}, it is assumed that the DSD has the shape of a gamma distribution. The P_{12} curves shown here are for the green channel of the specMACS cameras. In panels (d) and (e), several gamma distributions for different r_{eff} and a constant $v_{\text{eff}} = 0.1$ (d), and for different v_{eff} and a constant $r_{\text{eff}} = 10.2\,\mu\text{m}$ (e) are shown. Figure adapted with slight modifications from Pörtge et al. (2023).

Figure 2.3 shows the polarized phase function P_{12} within the scattering region from 135° to 180° which covers the cloudbow and the backscatter glory. In this figure, the polarized phase functions P_{12} for six different cloud droplet size distributions are plotted in the panels (a) and (b). Panel (a) shows the P_{12} phase matrix element for different r_{eff} and in panel (b) v_{eff} is varied while keeping r_{eff} constant. The position of the maxima and minima of the polarized phase function strongly depends on the r_{eff} (panel (a)). The v_{eff}, however, determines the amplitudes and widths of secondary minima of the radiance distribution but has only a small effect on the position of the minima. Panel (c) displays how the cloudbow depends on the wavelength λ of the radiation for three wavelengths in the visible part of the spectrum. This shows that the position of the secondary minimum shifts to larger scattering angles for larger wavelengths.

In summary, this figure illustrates that the cloudbow and the glory strongly depend on the cloud droplet size distribution. In Chapter 3, it is explained how this property is used to retrieve information about the cloud droplet size distribution from quantitative measurements of the cloudbow.

2.3 Clouds

In this work, microphysical quantities of clouds are derived from polarized radiance measurements. For this, definitions of the quantities are given in the following sections. Furthermore, the adiabatic model is introduced which defines the maximum possible amount of liquid water inside warm clouds, and thereby, also specifies the theoretically expected droplet radius.

2.3.1 Radiative properties of clouds

Cloud droplet size distribution

Clouds consist of small (spherical) droplets and ice particles. These droplets and ice particles all have different sizes. For liquid water clouds which contain only spherical cloud droplets with certain radii r, we can define the cloud droplet size distribution (CDSD) by $n(r)$. For ice or mixed-phase clouds, this becomes more complicated since ice particles are not spherical and thus do not have a certain radius. Often, the maximum ice crystal dimension is used to define a typical size of the ice particle. This thesis however, focuses on liquid water clouds with small, spherical particles. Larger, non-spherical precipitation particles are not considered either. For small, spherical particles, the droplet number concentration per unit volume (N_{d}) is commonly given in cm^{-3} and is defined by

$$N_{\text{d}} = \int_0^\infty n(r)dr \tag{2.16}$$

It is useful to define a typical radius representative of the CDSD. The volume-mean droplet radius r_v is defined by Martin et al. (1994):

$$r_v = \left(\frac{\int_0^\infty r^3 n(r) dr}{\int_0^\infty n(r) dr} \right)^{1/3} \tag{2.17}$$

The effective radius that was already introduced in Equation 2.14 better determines the radiative properties of the cloud droplets, but it is connected to the volume-mean droplet radius via the empirical factor k (Martin et al., 1994):

$$r_v^3 = k r_{eff}^3 \tag{2.18}$$

Martin et al. (1994) found typical values of the k-factor for continental ($k = 0.67 \pm 0.07$) and for maritime air masses ($k = 0.80 \pm 0.07$) from airborne measurements. Furthermore, measurements show that the CDSD often has the shape of a modified gamma distribution which can be written as a function of r_{eff} and v_{eff} (Hansen, 1971):

$$n_\gamma(r) = n_0 r^{(1-3v_{eff})/v_{eff}} \exp\left[-r/(r_{eff} v_{eff})\right], \tag{2.19}$$

where

$$n_0 = N_d \frac{(r_{eff} v_{eff})^{[(2v_{eff}-1)/v_{eff}]}}{\Gamma\left(\frac{1-2v_{eff}}{v_{eff}}\right)}. \tag{2.20}$$

In Fig. 2.3, several gamma distributions for different r_{eff} (panel (d)) and v_{eff} (panel (e)) are shown. If the CDSD has the shape of a modified gamma distribution, the k-factor can be directly calculated from the effective variance (see derivation in Appendix D):

$$k = (1 - v_{eff})(1 - 2v_{eff}) \tag{2.21}$$

Another frequently used quantity that describes the width of the size distribution is the relative dispersion d. This is defined as the ratio between the standard deviation and the mean radius of a cloud droplet size distribution (e.g. Tas et al., 2015). For CDSDs with gamma distribution shapes, the relative dispersion is connected to the effective variance via the following formula (Alexandrov et al., 2018, Appendix A):

$$d = \sqrt{\frac{v_{eff}}{1 - 2v_{eff}}} \tag{2.22}$$

The liquid water content (LWC) quantifies the amount of liquid water per unit volume (Wallace and Hobbs, 2006) and is usually expressed in $\mathrm{g\,m^{-3}}$. Typical values of the LWC measured from in situ instruments during the EUREC^{4}A campaign range from

$0.05\,\mathrm{g\,m^{-3}}$ to $0.2\,\mathrm{g\,m^{-3}}$ with maximum LWC of around $1.5\,\mathrm{g\,m^{-3}}$ (Bony et al., 2022). For spherical particles, it is defined by:

$$\mathrm{LWC} = \frac{4\pi\rho_\mathrm{w}}{3}\int_0^\infty r^3 n(r)dr = \frac{4}{3}\pi k r_\mathrm{eff}^3 N_\mathrm{d}\rho_\mathrm{w} \tag{2.23}$$

Cloud optical thickness

For a distribution of spherical particles, the extinction coefficient β_ext can be expressed as:

$$\beta_\mathrm{ext} = \pi\int_0^\infty Q_\mathrm{ext}(r)r^2 n(r)dr \tag{2.24}$$

The extinction efficiency factor (Q_ext) can be approximated by 2 for particles large compared to the wavelength (Petty, 2006). In general, β_ext is height dependent and can be expressed in terms of the r_eff and LWC:

$$\beta_\mathrm{ext}(z) = \frac{3Q_\mathrm{ext}\mathrm{LWC}(z)}{4\rho_\mathrm{w}r_\mathrm{eff}(z)} \tag{2.25}$$

The vertical integral of the extinction coefficient between the cloud base (z_base) and the cloud top (z_top) is the unitless quantity called cloud optical thickness or cloud optical depth τ_c (Petty, 2006):

$$\tau_\mathrm{c} = \int_{z_\mathrm{base}}^{z_\mathrm{top}} \beta_\mathrm{ext}(z)dz \tag{2.26}$$

τ_c is an important quantity in radiative transfer studies because it is directly related to the amount of reflected shortwave radiation.

Cloud base height and cloud top height

The cloud base height (CBH) defines the altitude of the lower boundary of the cloud. In this work, the CBH is estimated from the temperature T_L an air parcel would have if lifted adiabatically to its (lifting) condensation level as in Equation 22 in Bolton (1980):

$$T_L = \frac{1}{\frac{1}{T-55\,\mathrm{K}} - \frac{\ln(\mathrm{RH}/100)}{2840\,\mathrm{K}}} + 55\,\mathrm{K} \tag{2.27}$$

Here, T is the temperature of an air parcel at the ground in K, and RH is the corresponding relative humidity given in %. The formula is the iterative solution of an equation derived from the lapse rate of the dew point and the dry adiabatic lapse rate. The cloud base height is then defined as the height where the air has temperature T_L. The publication

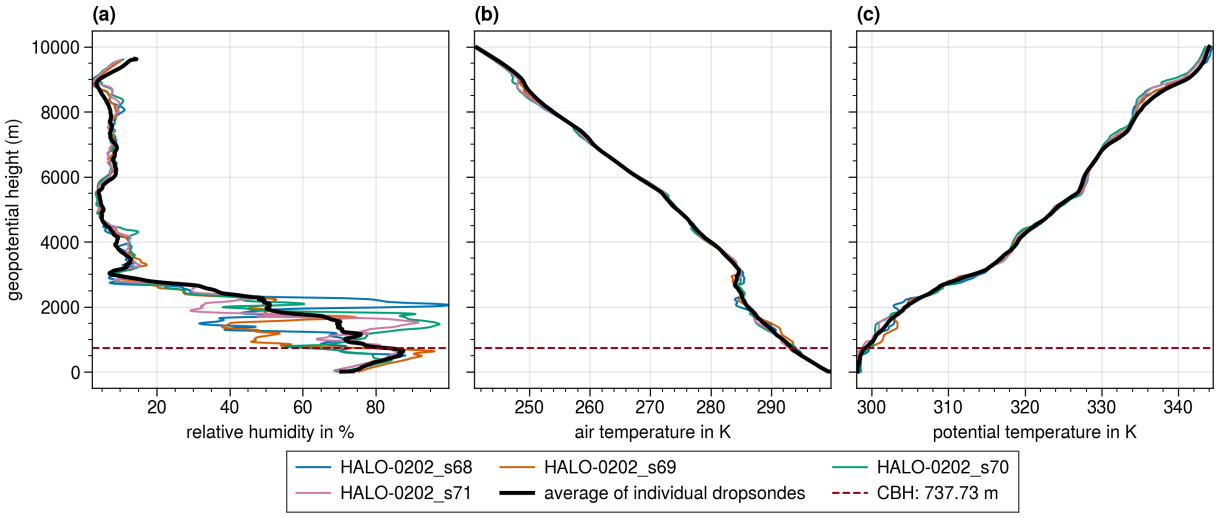

Figure 2.4: Relative humidity (a), air temperature (b) and potential temperature (c) from four subsequent dropsonde measurements indicated by their identifier names starting with "HALO-0202_s". The cloud base height is derived from Equation 2.27 using the air temperature and relative humidity at the surface from the average of the four dropsonde measurements and is shown as dashed line.

by Romps (2017) compares this approximation with an exact, analytic expression of the lifting condensation level and finds deviations of up to 40 m. Furthermore, in real clouds, the actual cloud base height does not necessarily coincide with the theoretically derived lifting condensation level.

The application of Equation 2.27 as used in this thesis is demonstrated in the following. Figure 2.4 shows the relative humidity (panel (a)), air temperature (panel (b)) and potential temperature (panel (c)) of four subsequent dropsonde measurements from the JOANNE dataset (George, 2021). All four dropsondes were launched in the same region within 12 minutes. The relative humidity within the cloud layer is quite variable between the different measurements depending on whether the dropsonde fell through a cloud or not. The measured air and potential temperature however, do not show a large variability from dropsonde to dropsonde. The average T and RH in a 200 m thick layer above ground from the dropsonde measurements are used as input for Equation 2.27 to derive the CBH which is indicated as dashed horizontal line.

The cloud top height (CTH) defines the upper boundary of the cloud. As for the cloud base height, there is no universal definition of the cloud top height and different measurement instruments have different sensitivities to the cloud top (Dauhut et al., 2022). Since this work is based on polarization measurements of the specMACS instrument, the cloud top should be representative of the height from which the polarization signal emerges, which is at a cloud optical depth of $\tau_c \approx 1$ below the top. In Volkmer et al. (2023), it was shown that in the case of specMACS measurements, this CTH (from which the polarization signal emerges) is very close to the CTH derived using a stereo-

graphic reconstruction method applied to the camera measurements (Kölling et al., 2019). Therefore, the CTH from the stereographic retrieval will be used as an approximation of the CTH representative of the polarization signal.

2.3.2 Humidity quantities

The mixing ratio w is the ratio of the mass m_v of water vapor to the mass of dry air m_d (Wallace and Hobbs, 2006):

$$w = \frac{m_\mathrm{v}}{m_\mathrm{d}} \tag{2.28}$$

The mixing ratio w is often expressed in grams of water vapor per kilogram of dry air and ranges from a few $\mathrm{g\,kg^{-1}}$ in the midlatitudes to around $20\,\mathrm{g\,kg^{-1}}$ in the tropics (Wallace and Hobbs, 2006). Using the ideal gas equation, w can also be expressed in terms of the partial pressure of water vapor (e), the pressure of the air parcel (p), and the ratio of the gas constants of dry air (R_d) and of water vapor (R_v):

$$w = \frac{R_\mathrm{d}}{R_\mathrm{v}} \frac{e}{p-e} = \epsilon \frac{e}{p-e} \tag{2.29}$$

Here, $\epsilon = \frac{R_\mathrm{d}}{R_\mathrm{v}} = 0.622$ is introduced. The saturation mixing ratio w_s is defined as the ratio of the mass $m_\mathrm{v,s}$ of water vapor in a certain volume of air that is saturated with respect to a plane surface of pure water to the mass m_d of the dry air (Wallace and Hobbs, 2006). In other words, the saturation mixing ratio determines the maximum amount of water vapor the air can hold at a given temperature. It can be expressed in terms of the saturation vapor pressure e_s:

$$w_\mathrm{s} = \frac{m_\mathrm{v,s}}{m_\mathrm{d}} = 0.622 \frac{e_s}{p-e_\mathrm{s}} \tag{2.30}$$

The liquid water mixing ratio w_l defines the ratio of the mass m_l of liquid water to the mass of dry air m_d:

$$w_\mathrm{l} = \frac{m_\mathrm{l}}{m_\mathrm{d}} \tag{2.31}$$

2.3.3 Adiabatic cloud model

If an air parcel is lifted adiabatically, it expands and cools, but the mixing ratio w of the air parcel is constant. At cloud base, the actual mixing ratio becomes equal to the saturation mixing ratio. The air parcel is saturated and condensation starts. The release of latent heat due to condensation leads to a reduced cooling of the parcel during its

further ascent and its temperature will follow the moist adiabatic lapse rate Γ_S (Curry and Webster, 1999):

$$\Gamma_S = -\frac{dT}{dz} = \frac{g}{c_{p,d}} \frac{(1 + \frac{l_v w_s}{R_d T})}{(1 + \frac{\epsilon l_v^2 w_s}{c_{p,d} R_d T^2})} \tag{2.32}$$

Here, $g = 9.81\,\mathrm{m\,s^{-2}}$ is the acceleration due to gravity, $c_{p,d} = 1005\,\mathrm{J\,kg^{-1}\,K^{-1}}$ defines the specific heat at constant pressure of dry air, and l_v is the latent heat of vaporization. At $T = 0\,^\circ\mathrm{C}$, $l_v = 2.5 \times 10^6\,\mathrm{J\,kg^{-1}}$. In the adiabatic model, the mass of water vapor that is condensed will appear as additional liquid mass in the mass balance. Therefore, the change of liquid water mixing ratio with height $\frac{dw_l}{dz}$ is the negative of the change in saturation mixing ratio with height, and is defined by the following equation (Albrecht et al., 1990):

$$C_w = \rho_d \frac{dw_l}{dz} = \rho_d \left[-\frac{dw_s}{dz} \right] = \rho_d \left[\frac{(\epsilon + w_s) w_s l_v}{R_d T^2} \Gamma_S - \frac{w_s p g}{(p - e_s) R_d T} \right] \tag{2.33}$$

The derivation of this formula using the Clausius–Clapeyron equation is shown in Appendix C. The condensation rate C_w defines the change of LWC with height, and is a constant for a given temperature and pressure. A typical value of C_w is $2.5 \times 10^{-3}\,\mathrm{g\,m^{-3}\,m^{-1}}$ (Min et al., 2012). From Equation 2.33, the adiabatic liquid water content $\mathrm{LWC_{ad}}$ which defines the maximum amount of liquid water within a specific volume is calculated:

$$\mathrm{LWC_{ad}}(z) = C_w(z - z_{base}) \tag{2.34}$$

$\mathrm{LWC_{ad}}$ increases approximately linearly with height. Figure 2.5 shows the adiabatic liquid water content of a cloud having a cloud base temperature of 294.5 K and a cloud base pressure of 951.3 hPa. In real clouds however, the actual liquid water content is usually much lower than $\mathrm{LWC_{ad}}$ since mixing with environmental air reduces the condensation rate (Warner, 1955). The factor f_{ad} relates the actual LWC to the adiabatic LWC and is called adiabaticity or adiabatic fraction (Grosvenor et al., 2018b):

$$\mathrm{LWC}(z) = f_{ad}\mathrm{LWC_{ad}}(z) = f_{ad} C_w (z - z_{base}) \tag{2.35}$$

Integrating the liquid water content with height yields the liquid water path LWP which depends on f_{ad}, C_w and the geometric depth of the cloud H:

$$\mathrm{LWP} = \frac{1}{2} f_{ad} C_w H^2 \tag{2.36}$$

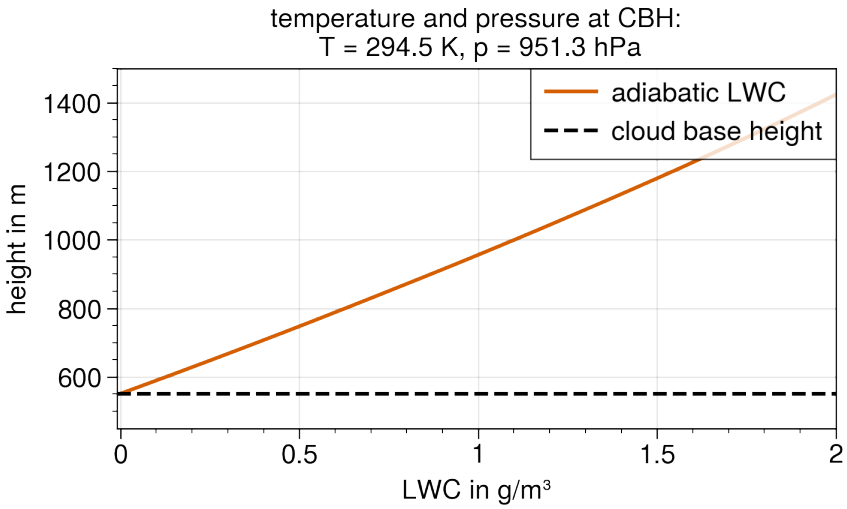

Figure 2.5: Vertical profile of adiabatic liquid water content for a cloud with $T_{\text{base}} = 294.5\,\text{K}$ and $p_{\text{base}} = 951.3\,\text{hPa}$.

Merk et al. (2016) used this equation to determine the adiabaticity from ground-based LWP measurements and found an average $f_{\text{ad}} = 0.63 \pm 0.22$ and a decrease of f_{ad} with height. Similar deviations of f_{ad} from 1 were also found in other studies, e.g. $f_{\text{ad}} = 0.2$ to 1 in Ishizaka et al. (1995). Since the liquid water content depends on the CDSD (Equation 2.23), it is possible to define the effective radius in terms of the LWC as a function of height (Grosvenor et al., 2018b):

$$r_{\text{eff}}(z) = \left(\frac{3\text{LWC}(z)}{4\pi\rho_{\text{w}} k N_{\text{d}}} \right)^{1/3} \tag{2.37}$$

This represents the assumption of the adiabatic model that all droplets grow from the CBH during their vertical ascent. Combining the $r_{\text{eff}}(z)$ equation with the definition of the cloud optical depth allows to define the droplet number concentration N_{d} as follows (Grosvenor et al., 2018b) (see Appendix A):

$$N_{\text{d}} = \frac{\sqrt{5}}{2\pi k} \left(\frac{f_{\text{ad}} C_{\text{w}} \tau_{\text{c}}}{Q_{\text{ext}} \rho_{\text{w}} r_{\text{eff}}^5} \right)^{1/2} \tag{2.38}$$

Here, r_{eff} is the effective radius at cloud top, and it is assumed that N_{d} is constant with height. And although it is not explicitly mentioned in Grosvenor et al. (2018b), also k and C_{w} are assumed to be constant with height for the derivation. The assumption of a vertically constant N_{d} is supported by aircraft observations (e.g. Brenguier et al. (2000) or Miles et al. (2000) for stratocumulus clouds, or Gerber et al. (2008) for small cumulus clouds).

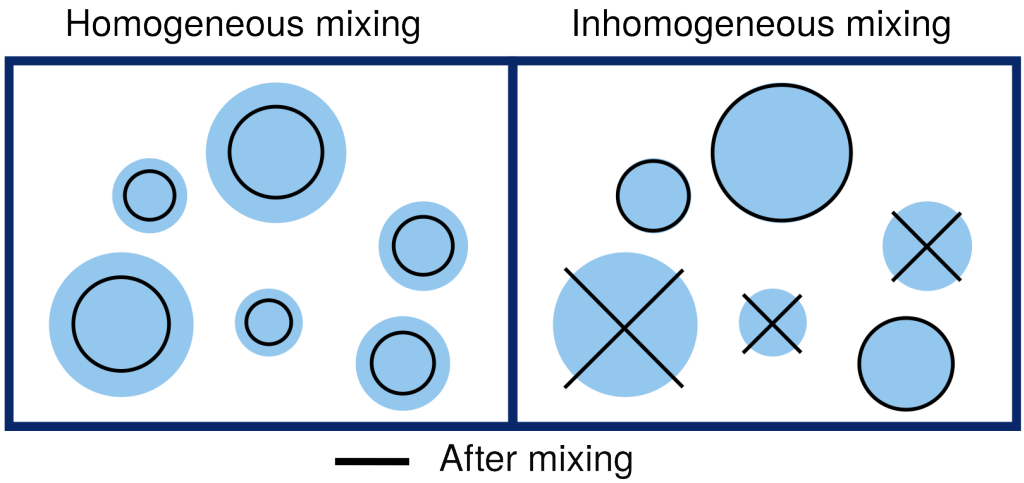

Figure 2.6: Effect of homogeneous (left) and inhomogeneous mixing (right) on the droplet size distribution. Figure adapted from Figure 5 in Karset et al. (2020).

2.3.4 Mixing and entrainment

When a parcel of cloudy air is rising, mixing with the environment will happen through its boundaries. The environmental air is generally cooler and drier as the parcel, and will (partially) cause evaporation of cloud droplets. As a result, the buoyancy and mixing ratio of the air parcel are reduced (Yau and Rogers, 1996). If entrainment happens at cloud top and if a certain volume of the cloud is cooled by the evaporation of droplets, then this volume will begin to sink. While sinking, the parcel will now mix with air inside the cloud. This mechanism can form penetrative downdrafts within the cloud which slowly dry the cloud from the top (Wallace and Hobbs, 2006).

There are two extreme types of mixing which are illustrated in Figure 2.6 which is adapted from Karset et al. (2020). The first case is called (extreme) homogeneous mixing and describes a mixing process that occurs on a short timescale. Short means that the time during which the mixing takes place is much shorter than the time needed for the parcel to adapt to the new situation, i.e. to re-establish vapor equilibrium (Yau and Rogers, 1996). All droplets at a given level in the cloud are exposed to the same, *homogeneous* subsaturation conditions and all droplets evaporate until saturation is reached (Yau and Rogers, 1996; Baker and Latham, 1979). In terms of the CDSD, this is expressed as an overall reduction in droplet size while the droplet number is constant (Figure 2.6 left).

In the second case, turbulent mixing is relatively slow. The turbulent eddies transport some droplets into the dry environment, and these droplets completely evaporate while other droplets remain unchanged (Baker et al., 1980; Khain and Pinsky, 2018) (Figure 2.6

right). This (extreme) *inhomogeneous* mixing will decrease the droplet concentration, but the characteristic droplet radii of the size distribution such as r_v and r_{eff} are conserved. Inhomogeneous mixing might be a crucial mechanism in warm rain formation. Within the so-called size gap between 15 µm to 40 µm, the classical cloud droplet growth mechanisms (diffusional growth or growth by collision-coalescence) are not efficient, and how droplets grow within this size range is still an open research question (Grabowski and Wang, 2013). If an air parcel experiences inhomogeneous mixing and then continues to rise, it could even form larger cloud droplets because of the reduced number of droplets that compete for the available water vapor (Baker et al., 1980). These large droplets could trigger collision and coalescence in warm clouds from which first raindrops could form.

In reality, both mixing processes are observed in clouds (Lehmann et al., 2009). Furthermore, model results also predict a narrowing mixing scenario which occurs if the DSD is broad with many small-size droplets (Lim and Hoffmann, 2023a). Small droplets completely evaporate while large droplets do not change. This scenario reduces the width of the CDSD and increases r_v (Lim and Hoffmann, 2023a).

Mathematical description of entrainment

The strength of entrainment is quantified by the fractional entrainment rate ϵ which depends on the mass flux M (de Rooy and Siebesma, 2010)

$$\epsilon = \frac{1}{M}\frac{\mathrm{d}M}{\mathrm{d}z}. \tag{2.39}$$

Measuring the fractional entrainment rate is very difficult but it can be estimated from the difference of a conserved variable ϕ between inside the cloud (ϕ_c) and the environment (ϕ_e). In this case, a conserved variable is a variable which is constant in adiabatic motions, such as the total water mixing ratio or the equivalent potential temperature. A change in these variables is directly related to an entrainment process and is described in Betts (1975) by

$$\frac{\mathrm{d}\phi_c}{\mathrm{d}z} = -\epsilon(\phi_c - \phi_e). \tag{2.40}$$

The study of Gerber et al. (2008) used this equation to determine the fractional entrainment rate from in situ measurements of the total water mixing ratio. They found an average $\epsilon = 1.30\,\mathrm{km}^{-1}$ and observed a decrease of ϵ with height. A study on the basis of LES simulations by Siebesma et al. (2003) found $\epsilon = 2\,\mathrm{km}^{-1}$. In early works of laboratory water tank experiments, a quantitative description of ϵ was found to be inversely dependent on the radius r of the plume or in our case of the cloud (Morton et al., 1956; Turner,

1963; Takahashi et al., 2021):

$$\epsilon \approx \frac{0.2}{r} \tag{2.41}$$

For this model it is argued that entrainment works through the boundary area of the cloud but the air is redistributed throughout the complete cloud volume. Larger areas ($\sim r^2$) have relatively smaller perimeters ($\sim r$), and therefore the entrainment fractional rate should inversely depend on r.

In order to match this size dependent model with the literature estimates of ϵ from Gerber et al. (2008) and Siebesma et al. (2003) given above, the sizes of the clouds from the literature studies should be mentioned. Measurements of small trade-wind cumuli with average diameters of 550 m were analyzed in Gerber et al. (2008). The corresponding average ϵ following Equation 2.41 is $0.73\,\mathrm{km}^{-1}$. The clouds in the study by Siebesma et al. (2003) had mostly sizes < 1 km (Neggers et al., 2003) which corresponds to $\epsilon = 0.4\,\mathrm{km}^{-1}$. This shows that the proportionality coefficient (0.2) in Equation 2.41 might not be a universal constant (Takahashi et al., 2021).

Chapter 3

Methods

3.1 The specMACS instrument and field campaigns

Parts of this text were published in Pörtge et al. (2023).

The specMACS instrument was developed at the Meteorological Institute of the Ludwig-Maximilians-Universität München and originally consisted of two hyperspectral line cameras sensitive in the wavelength range from 400 to 2500 nm (Ewald et al., 2016). Prior to the EUREC^{4}A measurement campaign in 2020, this set of cameras was, for the first time, complemented by two identical polarization-sensitive imaging cameras. All four cameras are built into a pressurized, temperature-stabilized, and humidity-controlled housing with a window in front of the cameras. The whole camera system was flown in a nadir-looking perspective aboard the German research aircraft HALO (Krautstrunk and Giez, 2012). In the past, the hyperspectral cameras have been successfully used to derive cloud droplet radius profiles (Ewald et al., 2019; Polonik et al., 2020) or to retrieve cloud geometry from oxygen-A-band observations (Zinner et al., 2019). In this work, the focus will be on the polarization cameras.

Statement about the camera names

The two polarization cameras were initially named *polA* and *polB*. These names were also used in Pörtge et al. (2023). For 2024, an upgrade of the specMACS system is planned which will include two additional sideward looking polarization cameras. For better differentiation, we decided to rename the old (nadir looking) cameras to *polLL* and *polLR*, where "LL" and "LR" stand for "lower left" and "lower right". The new cameras will have the names *polUL* and *polUR* where "UL" and "UR" stand for "upper left" and "upper right".

3.1.1 specMACS polarization cameras

The polarimeters are Phoenix polarization RGB cameras (Phoenix 5.0 MP Polarization Model), which come with Sony IMX250MYR CMOS polarized 2448 × 2048 pixels (along track × across track) sensors (LUCID Vision Labs Inc., 2022b). They are accompanied by a Cinegon 1.8/4.8 lens (Schneider Kreuznach). The aperture is set to 5.6. The two cameras are installed in a partly overlapping perspective resulting in a combined maximum field of view of about $\pm 45^\circ \times \pm 59^\circ$ (along track × across track). The horizontal pixel size at the ground is 10–20 m at a cruise altitude of about 10 km. The cameras are synchronized and measure at an acquisition frequency of 8 Hz. Furthermore, an automatic exposure control system based on the method described in Ewald et al. (2016) is used to adjust the measurements to varying illuminations.

The sensor accomplishes the measurement of polarization with on-chip directional polarizing filters (Fig. 3.1a). The 2448 × 2048 pixels are split up into blocks of 4 × 4 adjacent pixels. These blocks are further divided into four 2 × 2 pixel blocks for each color of the color filter array (RGGB – red, green, green, blue). The spectral channels have center wavelengths (bandwidths) of 620 nm (66 nm), 546 nm (117 nm), and 468 nm (82 nm) (determined by a Gaussian fit), and the normalized spectral response functions of each color channel are shown in Fig. 3.1b. Polarizing filters (0, 45, 90, 135°) are placed on top of each pixel (pixelated wire-grid polarizer). This enables the retrieval of three components (I, Q, and U) of the Stokes vector of the light. The last component of the Stokes vector (V), which cannot be measured by specMACS, specifies the circular polarization. However, circular polarization does not play a role in cloud remote sensing because it is orders of magnitude smaller than linear polarization (e.g., Emde et al., 2015; Hansen and Travis, 1974).

Figure 3.2 displays a specMACS measurement from 2 February 2020. Panels (a) and (b) show the measurements of the polLL camera, which observes clouds slightly to the left in the flight direction, and panels (c) and (d) correspond to the polLR camera, which observes clouds to the right in the flight direction. Figure 3.2a and c show the measured total intensities of the two cameras. Dashed lines indicate lines of constant scattering angle. The corresponding DOLP is shown in Fig. 3.2b and d. Most parts of the measurement have a small DOLP (blue in the image). The cloudbow region (scattering angle 135 to 165°) and the backscatter glory (scattering angle 170 to 180°) stand out due to their high DOLP (red). To avoid interpolation errors, we use the original data from the two individual cameras here, instead of projecting the data onto a common mapping/figure. The yellow box is defined by along-track lines tangent to the 165° scattering angle contourline. This box indicates the approximate region to which the retrieval can be applied.

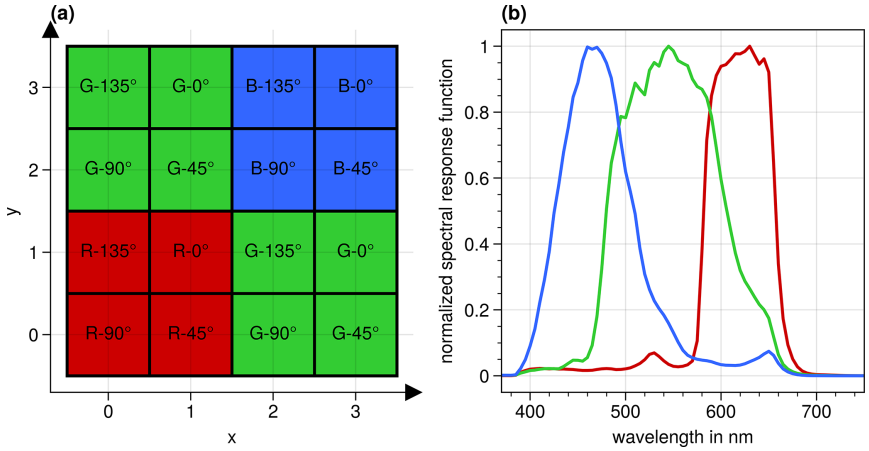

Figure 3.1: (a) Structure of a 4×4 pixel block of the polarization cameras. Each 4×4 block is subdivided into four blocks of 2×2 pixels for the different colors: red (R), green (G), and blue (B). On the 2×2 pixel blocks, four differently angled polarizers are placed. Figure adapted from the datasheet of the camera (LUCID Vision Labs Inc., 2022a). (b) Normalized spectral response functions of the three color channels averaged over the four polarization directions, considering the effect of the camera lens and of the window of the specMACS housing on the spectral response function.

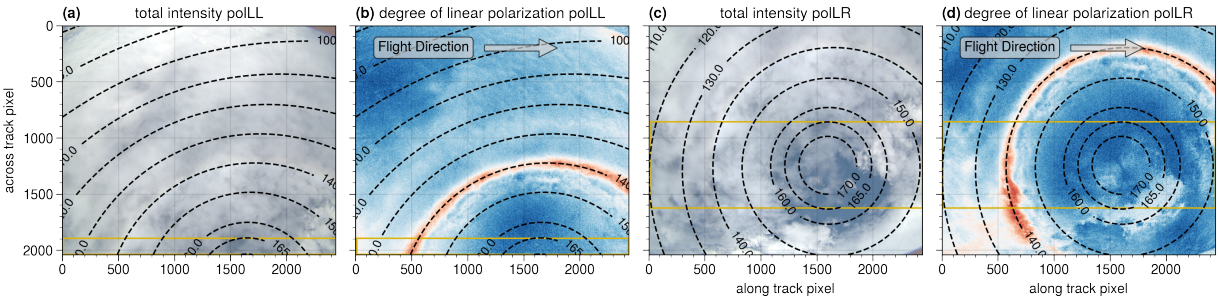

Figure 3.2: Example of measurements of both polarization cameras (2 February 2020, 16:47:45.07 UTC): (a, b) measurements from the first polarization camera (polLL), which looks slightly to the left in the flight direction; (c, d) measurements from the second polarization camera (polLR), which looks slightly to the right in the flight direction. The field of view of the two cameras overlaps. Panels (a) and (c) show the total intensity, and panels (b) and (d) show the DOLP. The dashed black lines indicate lines of constant scattering angles in degrees. The primary bow of the cloudbow is visible in the DOLP as a red ring at a scattering angle of about 140°. The yellow box indicates the approximate region that is suitable for the retrieval (along-track lines tangent to 165° scattering angle). Figure adapted from Pörtge et al. (2023) with small modifications.

3.1.2 Data processing

As already stated, a Stokes vector is defined with respect to a plane of reference. In the case of the measurements, the original reference plane is the x–z plane of the camera coordinate system. The x axis of the camera coordinate system points into the flight direction, which is also the polarizing axis of the 0° filter. The z axis points in the direction of the optical axis of the camera. For further analysis, each measured Stokes vector is rotated into its scattering plane which is unique for each pixel (Hansen and Travis, 1974; Eshelman and Shaw, 2019), and we only evaluate Q since $U \approx 0$ for single scattering which is the dominant contribution to the cloudbow signal. The window in front of the polarization cameras affects the polarization state of the measurements. To correct for this, the window is handled as a linear diattenuator, and the Müller matrix of a linear diattenuator is applied to the measurements (Bass et al., 1995). A geometric calibration of the cameras was carried out using the chessboard calibration method described in Kölling et al. (2019) which is based on Zhang (2000), but we exchanged the thin prism model (used in Kölling et al. (2019)) with the rational model. Both camera models come from the OpenCV library (Bradski, 2000). In order to calculate the pixel coordinates of specific 3-D points, the location and orientation of the camera with respect to a fixed world coordinate system have to be determined. The required precise information about the position and attitude of the aircraft is part of the Basic HALO Measurement and Sensor system (BAHAMAS) dataset. A high-precision inertial reference system aided by data from a Global Navigation Satellite System (GNSS) delivers the data at 100 Hz. The accuracy of the data is further increased by GNSS post-processing after the flight (Giez et al., 2021).

The camera location and orientation relative to the airframe is determined from the measured aircraft position and the location of distinct features, like rivers or roads, in the images once after installation. In 2021, a laboratory calibration of the polarization cameras was performed at the Calibration Home Base of the Remote Sensing Technology Insitute of the German Aerospace Center (DLR) in Oberpfaffenhofen (Gege et al., 2009). The results of this calibration are published in Weber et al. (2024). From the laboratory calibration, a full radiometric calibration of the data is possible. Together with the geometric calibration described above, it is now possible to determine absolute calibrated Stokes vectors rotated into the scattering plane from the measured raw data.

3.1.3 Field campaigns

In the last years, the specMACS instrument has been operated in several different measurement campaigns. The first deployment of the current setup including the polarization cameras was the EUREC^{4}A campaign in 2020 which aimed at studying clouds in the wintertime trade-wind region from ground based, airborne and shipborne measurements (Stevens et al., 2021). In 2021, the CIRRUS-HL campaign took place

which focused on measuring cirrus clouds both by remote sensing instruments such as specMACS and in situ instruments. The HALO-(AC)^3 campaign took place in 2022 and studied arctic clouds from different research airplanes. In the same year, the specMACS instrument has been operated in the CoMet 2.0 Arctic campaign in Canada where the focus has been on the study of greenhouse gas emissions both from anthropogenic sources as well as from natural sources such as wetlands. This shows that a huge dataset of polarimetric and spectral observations of clouds at different geographic locations and seasons was generated over the last four years which allows to study many different properties of clouds.

In this work, the main goal will be to evaluate the specMACS observations from the EUREC^{4}A campaign. During EUREC^{4}A, the HALO aircraft was mostly flying on a circular pattern. To facilitate identifying different parts of the flights, the flights were segmented into a subset of hierarchical identifiers with different kinds or categories (Prange et al., 2021; Konow et al., 2021). Typical segment names are, for example, "HALO-0202_c5", which is an abbreviation of the fifth circle ("c5") of the HALO on 2 February 2020 or HALO-0205_sl2 which is the second straight leg ("sl") on 5 February 2020. These abbreviations will also be used in the following chapters.

3.2 Retrieval of cloud droplet size distributions

In Subsection 2.2.2, the cloudbow was presented, and how its structure and shape depend on the cloud droplet size distribution were discussed. The following section explains how this property of the cloudbow is used by the cloudbow retrieval. The different steps of the method are demonstrated based on a case study, and uncertainties of the method are explained.

3.2.1 Retrieval description

Parts of this subsection were published in Pörtge et al. (2023).

The goal of our algorithm is to determine the size distribution of cloud droplets from angularly resolved cloudbow measurements. An average cloudbow signal could be extracted from a cross section of a single measurement (e.g., from Fig. 3.2). This method can easily be applied to any cloudbow observations, including those from commercial cameras, but the signal comes from a large area. The method presented in this paper is based on co-located along-track observations, allowing for the acquisition of the cloudbow signature of individual targets. As a result, distributions are obtained at a high spatial resolution, as this method does not involve averaging over a large area.

With HALO, we fly over the clouds at a speed of about $200\,\mathrm{m\,s^{-1}}$, observing the

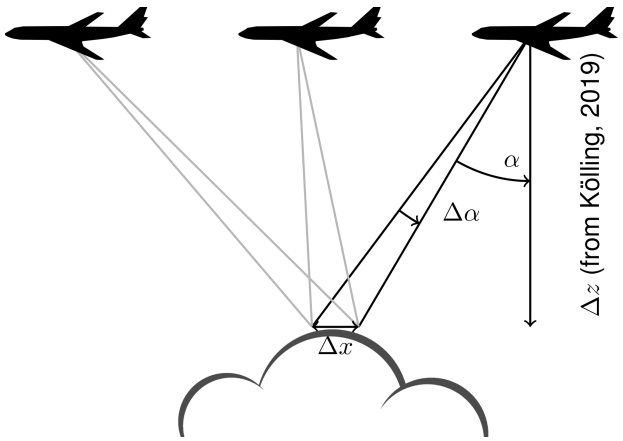

Figure 3.3: Observation geometry: the same target on the cloud (indicated by Δx) is observed from different viewing angles (α). The cloud top height information needed to calculate the distance Δz between the target and camera is retrieved using the method described in Kölling et al. (2019). The single measurements are then aggregated into one radiance measurement of the target.

same cloud from different viewing directions. Instead of evaluating the cloudbow in individual images, different viewing directions are sampled for each target on the cloud as specMACS images the scene (illustrated in Fig. 3.3). Similar approaches have also been applied to measurements of other airborne and spaceborne instruments (e.g., Bréon and Goloub, 1998; Alexandrov et al., 2015; McBride et al., 2020). The retrieval consists of three steps. First, cloud surface locations ("cloud targets") in the real-world 3-D space and their trajectory caused by the wind are determined. For this purpose, we combine each 10×10 block of pixels from the specMACS images into target pixels. Such a target pixel typically has a size of about $100\,\text{m} \times 100\,\text{m}$, but the actual size depends on the distance to the cloud. We decided to use this target pixel size because it matches our geolocation accuracy (see Subsection 3.2.2). Second, for each cloud target, the pixels of all images observing the same location are collected. The individual measurements of one target are aggregated into a combined radiance measurement for the entire range of the viewing directions. In a final step, a lookup table (LUT) based on Mie calculations of polarized phase functions for different DSD values is fitted to the angular distributions to retrieve the best-fitting DSD values.

The flowchart in Figure 3.4 summarizes the technical steps of the method. The algorithm is split up into two parts. In the first part (Fig. 3.4 a), the possible cloud targets are identified and the corresponding 3-D locations are determined. Since targets are observed in subsequent images, we identify possible cloud targets only every 15 s. The second part loops through all measurements and performs the aggregation of the individual measurements of all identified targets. If the aggregation of a target is finished, the fit is performed. The particular steps of the aggregation process and the retrieval are described in the following.

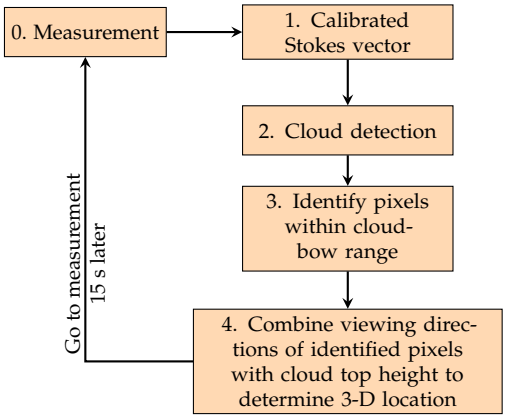

(a) Initial target identification

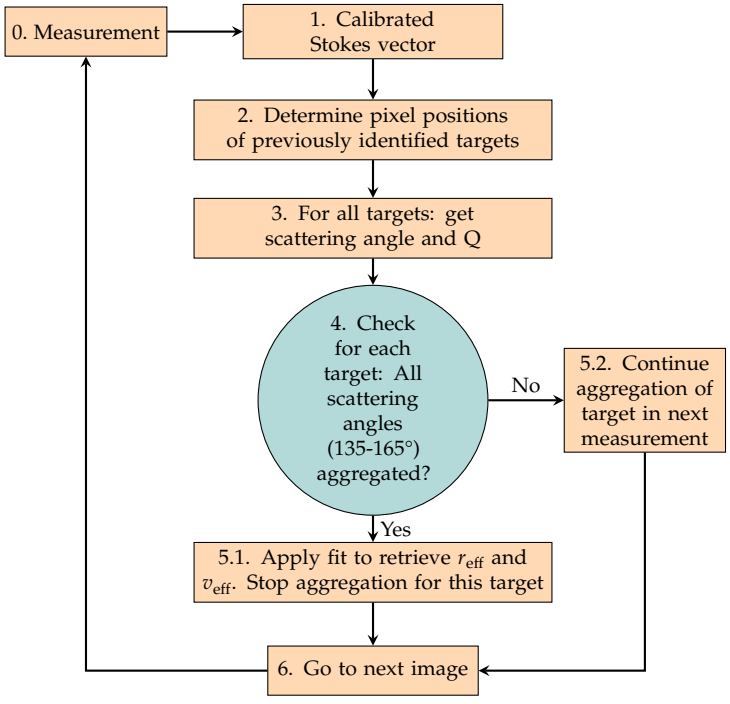

(b) Aggregation of measurements and fit

Figure 3.4: Flowchart of the cloudbow retrieval based on two successively executed algorithms. The upper part (a) explains the initial target identification and the lower part (b) explains the aggregation of the measurements followed by a fitting algorithm.

Cloud detection

The first step of the algorithm consists of detecting clouds in the measurements (Fig. 3.4 panel (a)). The specMACS cloud detection method was developed in Scheiderer (2021) and was later extended for observations above land surfaces in Ma (2022). As most EUREC^{4}A measurements were taken above the ocean, the measurements are often contaminated with the sunglint, which appears due to the specular reflection of sunlight from the ocean surface. Cloud detection algorithms based on the brightness of the image often wrongly identify this bright sunglint as clouds. To (partially) overcome this problem, we use the parallel component of the polarized light for cloud detection. In the parallel component, the reflectance of the sunglint is significantly reduced. At the Brewster angle ($\theta_B \approx 53.1^\circ$ for an air–water interface) reflected light is even completely perpendicularly polarized (Bass et al., 1995). In the case of a scene with medium cloud coverage, the algorithm chooses the red channel of the parallel component for further processing. For scenes with high cloud coverage, the normalized red (r) to blue (b) ratio ($\mathrm{nrbr} = (b_\parallel - r_\parallel)/(b_\parallel + r_\parallel)$) is calculated. Based on a brightness histogram of the selected data, a threshold value that distinguishes between cloudy and cloud-free pixels is determined using the method described in Otsu (1979). A good cloud mask is beneficial for the retrieval since it filters cloud-free observations which reduces the amount of data that are processed and, therefore, computational time. However, a perfect cloud mask is not needed for the retrieval. After the retrieval is performed, the results are filtered again based on the results of the fit and the shape of the cloudbow signal (see Subsection 3.2.1). This process filters out targets that were incorrectly identified as clouds from the final results.

A cloudy pixel is suitable for the cloudbow algorithm if it is observed within all scattering angles from 135° to 165° during the measurement sequence (for the choice of the range, see, e.g., Alexandrov et al., 2012a, or McBride et al., 2020). This, of course, depends on the solar geometry and the camera's viewing direction. Therefore, the next step is to identify the cloud targets that meet this criterion which is shown in the flowchart in panel (a/3). In the case of Fig. 3.2, the yellow box approximately indicates the region that is eligible for the retrieval. Outside the yellow box, the observations do not cover the full cloudbow scattering angle range while the aircraft is flying above the cloud and these observations cannot be used for the retrieval. The flight direction is to the right, as indicated by the arrow in Fig. 3.2, and the scattering angles are shown as dashed circular lines.

Geolocating the cloud targets

In order to identify the same target in different observations, we first use the geometric calibration of the camera to determine the viewing angle of the target (see Sect. 3.1). To fully localize the target (flowchart: panel (a/4)), we need to know the distance between

the aircraft and the target (Δz in Fig. 3.3). The altitude of the aircraft and, thus, of the camera is measured by the BAHAMAS system. The cloud top height is derived using a stereographic reconstruction method which determines the cloud geometry from specMACS measurements. This was demonstrated for measurements of the previous 2-D RGB camera in Kölling et al. (2019), and is now operationally applied to the RGB images of the polarization cameras with slight modifications. The method identifies pixels with prominent features that are detected in the following images by a matching contrast gradient. To correct for horizontal displacements of the cloud, the method was extended in Volkmer et al. (2024), and now includes data of the horizontal wind from the ERA5 reanalysis dataset (Hersbach et al., 2020, 2018). The ERA5 dataset has an hourly temporal resolution, a $0.25^\circ \times 0.25^\circ$ horizontal resolution, and 37 vertical levels from the surface to 1 hPa. During EUREC^{4}A, clouds were typically observed at an altitude of 1–2 km, where the ERA5 dataset has a vertical grid spacing of about 250 m.

First, the stereo method is performed without additional wind information, and the 3-D coordinates of the points identified on the cloud surface (stereo points) are retrieved. The ERA5 data are then interpolated to these coordinates to extract the corresponding wind data. The stereo method is performed again, but this time the wind data are taken into account. The whole process is iteratively repeated five times; each time the wind data are updated with the ERA5 wind interpolated to the heights and locations of the previously found stereo points. Further increasing the number of iterations did not notably change the results.

Figure 3.5a shows an example of the derived cloud top height of the polLR camera using the stereographic method for the scene shown in Fig. 3.2c and d (2 February 2020, 16:47:45 UTC). Although the method has difficulties in homogeneous regions of the cloud due to a lack of contrast (e.g., in the lower right), large parts of the cloud are analyzed successfully. The cloud top heights from the single points of the stereographic method are interpolated to the entire image (Fig. 3.5c). The interpolation process first consists of a linear interpolation of the stereo points onto all image pixels inside the convex hull of the stereo points. Then, the regions outside the convex hull of the original stereo points are filled by a nearest-neighbor interpolation. The resulting cloud top heights are assigned to the selected cloud targets of the cloudbow retrieval.

The WAter vapour Lidar Experiment in Space (WALES) lidar system was also operated aboard HALO during EUREC^{4}A (Wirth et al., 2009; Konow et al., 2021). The stereographically derived cloud top height is close to the measured cloud top height from the WALES lidar (Wirth, 2021) which is projected onto the specMACS RGB image in Fig. 3.5b. Figure 3.5c plots the WALES track on top of the interpolated specMACS cloud top height map. Within the high cloud on the left, the WALES data agree very well with the specMACS cloud top height, and it is hard to distinguish the WALES data from the stereo data. The two datasets differ significantly for the cloud on the right, where the stereo result is approximately 1000 m lower than the lidar measurement. From the

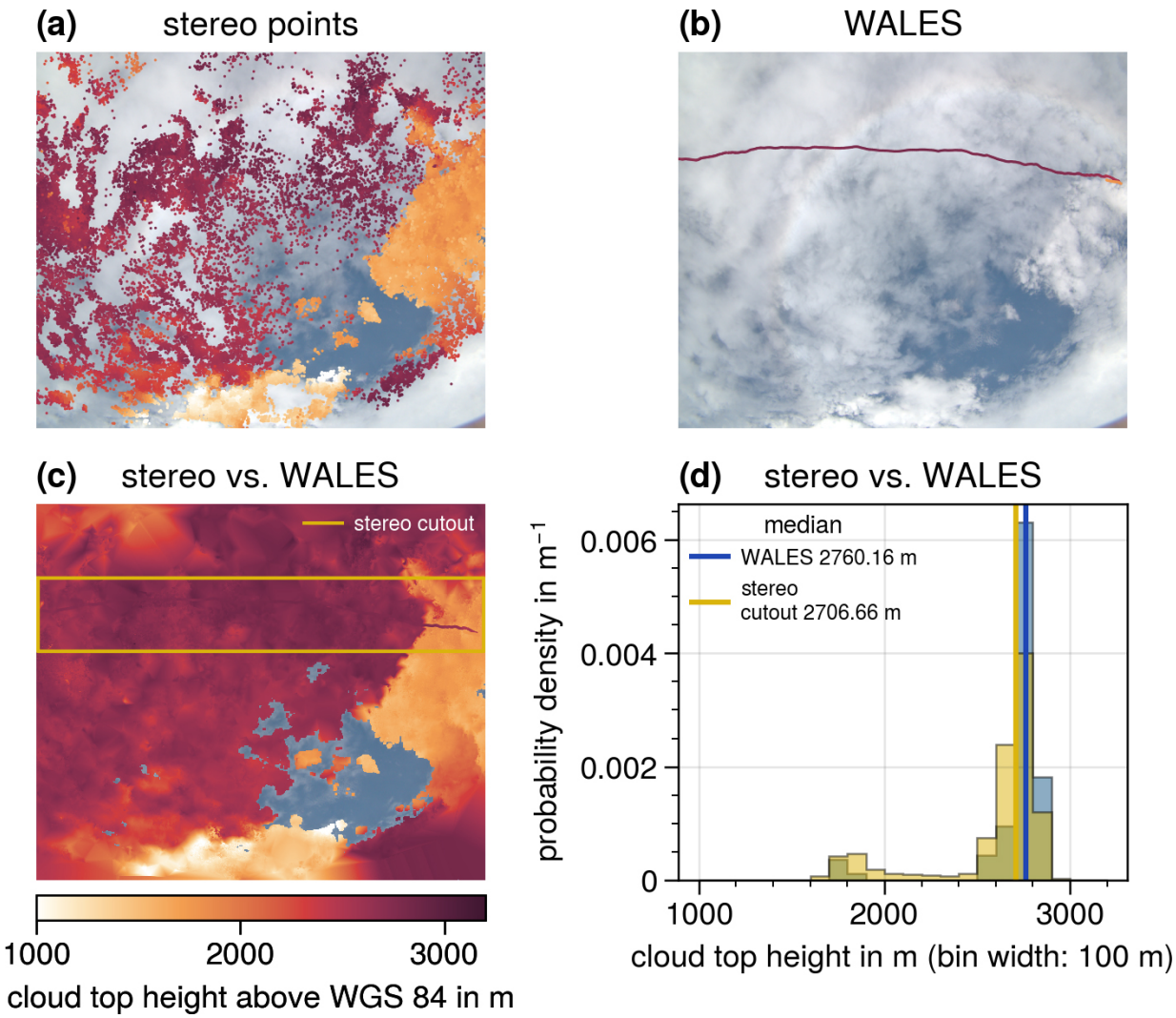

Figure 3.5: Cloud top height (CTH) information of the cloud field shown in Fig. 3.2 (2 February 2020, 16:47:45.07 UTC). Panel (a) shows the CTH of stereo points from the stereographic reconstruction method, panel (b) presents the CTH from the WALES lidar system, and panel (c) shows the interpolated CTH based on the stereo points. The WALES CTH is plotted on top (hardly visible due to the similarity to the CTH from the stereo points). The stripe marked by the yellow lines in panel (c) indicates a specMACS cutout surrounding the WALES track. Panel (d) shows the probability densities of the CTHs of the specMACS cutout (yellow) and the WALES measurements (blue). The RGB measurement of the cloud field is shown in the background of panels (a), (b), and (c). The color bar below panel (c) corresponds to all cloud top height measurements shown in panels (a), (b), and (c).

videos of the specMACS measurements it can be seen that the two cloud layers slightly overlap here. specMACS detects the lower cloud layer due to greater contrasts, whereas WALES is sensitive to the upper cloud layer. This behavior was also observed in Kölling et al. (2019) for measurements of the NARVAL-II campaign. Such cases with a thin cloud layer above a second cloud layer are difficult for the application of the cloudbow retrieval because, the cloudbow signal might be a mixture of the cloudbow signals of the two cloud layers depending on their optical thicknesses. A precise assignment of the contributions of the two layers to the total cloudbow signal is not possible and in general the evaluation of such multi-layer cloud scenes should be avoided.

The stripe marked by the yellow lines in Fig. 3.5c roughly surrounds the WALES track and defines the area for which the yellow histogram of specMACS data in Fig. 3.5d is derived. The cloud top heights of the two respective cloud layers are at approximately 1700 m and 2700 m (Fig. 3.5d). The distribution of the interpolated stereo points is quite similar to the distribution of the WALES data (shown in blue), even though the two datasets differ for the cloud on the right.

Even a small error of a few hundred meters in the cloud top height will result in an erroneous localization of the cloud in subsequent images. An incorrect localization particularly affects targets close to cloud edges, where it will cause non-cloud regions to be aggregated into the final cloudbow signal. Luckily, the stereographic method can very accurately determine the cloud geometry at cloud edges due to high contrasts. By combining the cloud top height with the viewing directions, the locations of the cloud targets in the real-world 3-D space are determined (flowchart: panel (a/4)). The whole process of detecting suitable target locations is then repeated for a measurement 15 s later. Since targets are observed in measurements at different times, it is not necessary to perform the target identification for all measurements.

Size distribution retrieval

From a technical point of view, the actual size distribution retrieval (flowchart: panel (b)) is performed after all potential cloud targets of a certain time range have been identified (flowchart: panel (a)). For the actual retrieval, the 3-D locations of the identified cloud targets are used to calculate the pixel coordinates of the targets in successive measurements (Fig. 3.3), again considering the shift in the targets' locations with the wind based on the ERA5 dataset (flowchart: panel (b/2)). The individual measurements of the same target of the Stokes parameter Q are combined to generate the aggregated polarized radiance measurement (flowchart: panel (b/3) & (b/4)). For further processing, the aggregated measurement is binned onto a scattering angle grid with a step size of 0.3°. It should be noted that, although specMACS has two polarization cameras with a partly overlapping field of view, we have not combined the measurements of the two cameras but rather decided to keep the original pixels of each camera to prevent interpolation artifacts. The results presented in the following are based on measurements of a single

camera only.

For evaluating the aggregated angular radiance measurement with regard to the cloud droplet size properties (see Fig. 2.3), a LUT of polarized phase functions (P_{12}) for different r_{eff} and different v_{eff} was created for each of the three spectral color channels of the camera. All calculations were carried out with the Mie tool (Wiscombe, 1980) included in the library for radiative transfer (libRadtran) (Mayer and Kylling, 2005; Emde et al., 2016). An example input file for the Mie tool is given in Appendix E. We assume that the DSD has the shape of a monomodal gamma distribution. This is an extensively used assumption (Alexandrov et al., 2015) that is, for example, confirmed by in situ measurements of liquid water DSDs (e.g., Miles et al., 2000).

Polarized phase functions are calculated for a logarithmic grid of 77 different r_{eff} ranging from 1 µm to 40 µm ($r_{\text{eff,i+1}} = r_{\text{eff,i}} \cdot 1.05$). The v_{eff} range between 0.01 and 0.325, with a small step size of 0.01 for $v_{\text{eff}} \leq 0.05$ and a larger step size (0.02 to 0.028) for $v_{\text{eff}} > 0.05$. This choice is similar to other publications, such as Alexandrov et al. (2012a) and McBride et al. (2020). In total, the LUT includes 16 different v_{eff}. To account for the different spectral sensitivities of the three color channels, the polarized phase functions are initially calculated for the whole wavelength range of the spectral response functions with a step size of 10 nm and are then weighted by each spectral response function (Fig. 3.1b). For the calculation of the phase functions, a wavelength- and temperature-dependent refractive index is used. We use the approximation formula of the IAPWS (International Association for the Properties of Water and Steam; Wagner and Pruß, 2002) for a temperature of $T = 15\,^{\circ}\text{C}$, which, according to dropsonde measurements, corresponds to the approximate cloud top temperature of the typical EUREC^{4}A clouds with a cloud top height of 1700 m.[1]

The LUT of polarized phase functions ($P_{12}[r_{\text{eff}}, v_{\text{eff}}]$) is fitted to the aggregated radiance distributions (Q_{meas}) using the following equation (flowchart: panel (b/5)):

$$Q_{\text{fit}}(\theta) = A \cdot P_{12}[r_{\text{eff}}, v_{\text{eff}}](\theta) + B \cdot \cos^2(\theta) + C. \tag{3.1}$$

Here, A, B, and C are fitting parameters, and θ is the scattering angle. Parameter A is needed to compare the radiometrically uncalibrated measurements with the simulated LUT, and, in addition, it scales with the cloud fraction of the target consisting of 10×10 pixels (Bréon and Goloub, 1998). The fitting parameters B and C account for any remaining effects that are not considered in the single-scattering assumption. For example, these could be contributions by multiple scattering. The term $\cos^2(\theta)$ corrects for Rayleigh-scattering contributions (Alexandrov et al., 2012a). Other studies do not rely

[1] In the original version of this text and of the plots in Pörtge et al. (2023), a temperature of $T = 10\,^{\circ}\text{C}$ was used for the calculation of the refractive index which is then used for the calculation of the phase functions. This was a mistake, and in fact, the use of $T = 15\,^{\circ}\text{C}$ is appropriate. However, the difference in the phase functions is small, and therefore, also the retrieved CDSDs are very similar. Nevertheless, for all analyses shown in the results chapter of thesis (Chapter 4), the phase functions with $T = 15\,^{\circ}\text{C}$ were used.

on the cosine term and instead use a correction term linear in θ plus a constant (e.g., Bréon and Goloub, 1998; Bréon and Doutriaux-Boucher, 2005). In the cloudbow range, however, this is similar to $\cos^2(\theta)$ (Alexandrov et al., 2012a). A further contribution, beyond single scattering, could be a thin cirrus cloud above the cloud that generates the cloudbow. In Riedi et al. (2010), it was shown that the polarization signal of ice particles depends linearly on the scattering angle in the rainbow region. Furthermore, Alexandrov et al. (2012a) showed that the magnitude of a cloudbow signal is attenuated by an overlying aerosol layer, but the aerosol layer does not change the structure of the cloudbow signal. The fitting parameters B and C also account for these two effects of cirrus and aerosol.

To determine P_{12} (and thus the r_{eff} and v_{eff} of the DSD), a least-squares approach is used to invert Eq. 3.1. In the inversion process, not only the grid points of the LUT are allowed but also values in between. This is realized by a linear interpolation of the LUT. The root-mean-square error (RMSE) is calculated for the scattering angle range from 135° to 165° where the cloudbow structure is most prominent:

$$\text{RMSE} = \sqrt{\frac{1}{n}\sum_{i=1}^{n}(Q_{\text{fit}}(\theta_i) - Q_{\text{meas}}(\theta_i))^2}. \tag{3.2}$$

The smallest RMSE reveals the r_{eff} and v_{eff} of the DSD. In addition, the RMSE serves as a measure of accuracy, and we filter out all fits with RMSE > 2.5. As a second quality measure, we calculate the quality index "Qual", as in Eq. 3.3 (first defined by Bréon and Doutriaux-Boucher, 2005). This is the ratio between the variability in the measurement, which corresponds to the squared amplitude of the cloudbow ($A \cdot P_{12}$), and the RMSE of the fit. Measurements with a low quality index (Qual < 4) are filtered out of any further processing. This excludes, for example, "cloudbow signals" of ocean areas that have been incorrectly identified as clouds from the result.

$$\text{Qual}^2 = \frac{A^2(\langle P_{12}^2\rangle - \langle P_{12}\rangle^2)}{\text{RMSE}^2} \tag{3.3}$$

Figure 3.6 shows three examples of aggregated cloudbow measurements for the green channel binned into a 0.3° resolution in the scattering angle (black dots with standard deviation and connecting black line). Each corresponding model fit is plotted as a solid yellow line. The model fit matching the example shown in Fig. 3.6a has $r_{\text{eff}} = 33.37\,\mu\text{m}$ and $v_{\text{eff}} = 0.16$. The example in Fig. 3.6b has several secondary minima which indicate a narrow size distribution. This is confirmed by the fit result of $v_{\text{eff}} = 0.02$. The effective radius is 12.51 µm. The cloudbow minimum is shifted to slightly larger scattering angles in Fig. 3.6c, and the amplitude of the cloudbow is smaller than the amplitudes of the targets in panel (a) and (b). According to our expectations from the simulations (Fig. 2.3), this corresponds to a smaller r_{eff}, which is confirmed by the fit ($r_{\text{eff}} = 8.68\,\mu\text{m}$). The existence of the secondary minima indicates a narrow size distribution which is verified

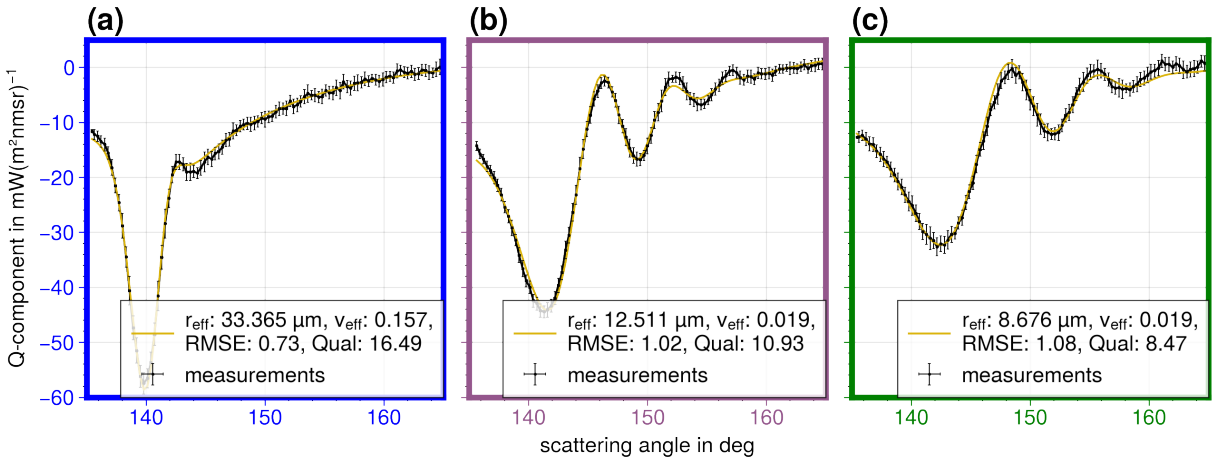

Figure 3.6: The aggregated polarized radiance measurements of the green channel of the locations shown in Fig. 3.7 were binned to a 0.3° resolution in the scattering angle (black dots connected by black lines). The error bars represent the standard deviations of all original data points within a 0.3° bin. The yellow lines indicate the best-fitting simulations. The parameters r_{eff}, v_{eff}, RMSE, and Qual of the best-fitting simulations are shown in the boxes in the lower right.

by the small v_{eff} of the fit ($v_{\text{eff}} = 0.02$). All three measurements have little noise as indicated by the error bars.

Application of cloudbow retrieval to stratocumulus cloud system

In the following, we demonstrate the polarimetric technique based on two case studies from specMACS measurements of this day. The first case study shows a part of a (stratiform) cloud field and is used to discuss the individual steps of the retrieval in detail. In Subsection 3.2.2, we analyze small trade-wind cumuli that were connected to a cold pool that formed during the dissipation of the stratiform cloud. This example serves to analyze the possible spatial resolution in the case of small clouds. We limit the presentation of the retrieval results to the green channel, as the results from the red and blue channels are very similar.

First, the cloud field observed at 16:47:45 UTC is presented. This measurement has already been introduced in Sect. 3.2.1 and is shown in Fig. 3.2. At this time, HALO was flying at an altitude of about 10 km, and the solar zenith angle was 31.15°. The cloudbow technique is applied to the measurements. The time required to sample the angular range from 135° to 165° is 40 s. Figure 3.7g shows the RGB image of the measurement from the polLR camera. The labels on the four sides of the image indicate the distances between the neighboring corners of the image. It is noticeable that the side lengths of the top (14.44 km) and bottom (27.02 km) differ greatly. This happens because the camera is installed at a slight angle in the across-track direction. Therefore, the lower part of the image covers a much larger distance in the along-track direction. This is also the case for

the measurements of the polLL camera, but the upper part of the image covers a larger distance here.

The retrieval results of the individual cloud targets are combined into maps of r_{eff} and v_{eff} (Fig. 3.7a and b, respectively). The maps in Fig. 3.7 contain indicators of the three particular cloud targets (colored circles) that were presented in Figure 3.6. About one-third of the image can be evaluated, as only the targets inside this area are observed from all necessary scattering angles during the overpass. The map of r_{eff} (Fig. 3.7a) is a consequence of the vertical distribution of the cloud field with two cloud layers at different cloud top heights (Fig. 3.5 and Fig. 3.7h). The upper cloud deck at a height of about 2700 m has a large r_{eff} ranging between 15 and 40 µm. Distinct patches of very large r_{eff} values up to 40 µm are observed. These patches occur in regions where the cloud is optically thick (Fig. 3.7g). The spatial distribution of r_{eff} for the lower cloud deck (cloud top height of 1700 m) is more homogeneous, and the absolute values are much smaller ($r_{\text{eff}} \approx 6$ µm). Figure 3.7d shows the frequency distribution of r_{eff}, and the two r_{eff} peaks of the two cloud decks are very easily distinguished.

The retrieved r_{eff} values of the higher cloud are very large. To better understand the cloud field and the large r_{eff} values, we evaluated radar measurements of the polarimetric K_{a}-band MIRA-35 cloud radar of the HAMP (HALO Microwave Package) instrument aboard HALO (Mech et al., 2014; Konow et al., 2021). The radar measurements from 16:47:00 to 16:48:30 UTC are shown in Fig. 3.8 as well as a push-broom-like image of the specMACS measurements and an indication of the HAMP radar field of view within the specMACS image. Within the high cloud from 16:47:00 to 16:48:15 the radar shows bands of enhanced reflectivity > 0 dBz and positive fall speeds (not shown). This likely corresponds to sedimenting droplets. Along with our observation of droplet sizes clearly larger than the usual cloud droplet size range (< 15 µm), this points to drizzle development, and we may see impacts of precipitation formation deeper in the cloud within the polarimetric signal originating from cloud top. Although our technique is not able to observe the precipitation droplet range (> 100 µm) directly, it is still sensitive to the intermediate size range below a possible drizzle droplet mode. A recent study by Sinclair et al. (2021) discussed the correlation between large cloud droplets detected by the RSP polarimeter and rain observed with a radar in great detail and found that the estimated cloud top precipitation rates from the RSP are strongly correlated with radar-derived precipitation rates and rainwater paths.

The spatial distribution of v_{eff} in Fig. 3.7b does not show a clear separation of the two cloud decks. Small patches of both very high and very low v_{eff} can be seen. At the boundary between the two cloud decks, large v_{eff} values are observed over several pixels. These are the result of a mixing of the signals of the two different cloud decks with different DSDs. Similar effects have been seen in RSP observations of multilayer clouds (Alexandrov et al., 2015, 2016). The resulting oscillating signal cannot be reproduced by a monomodal polarized phase function, and the outcoming fit has a large v_{eff}. The

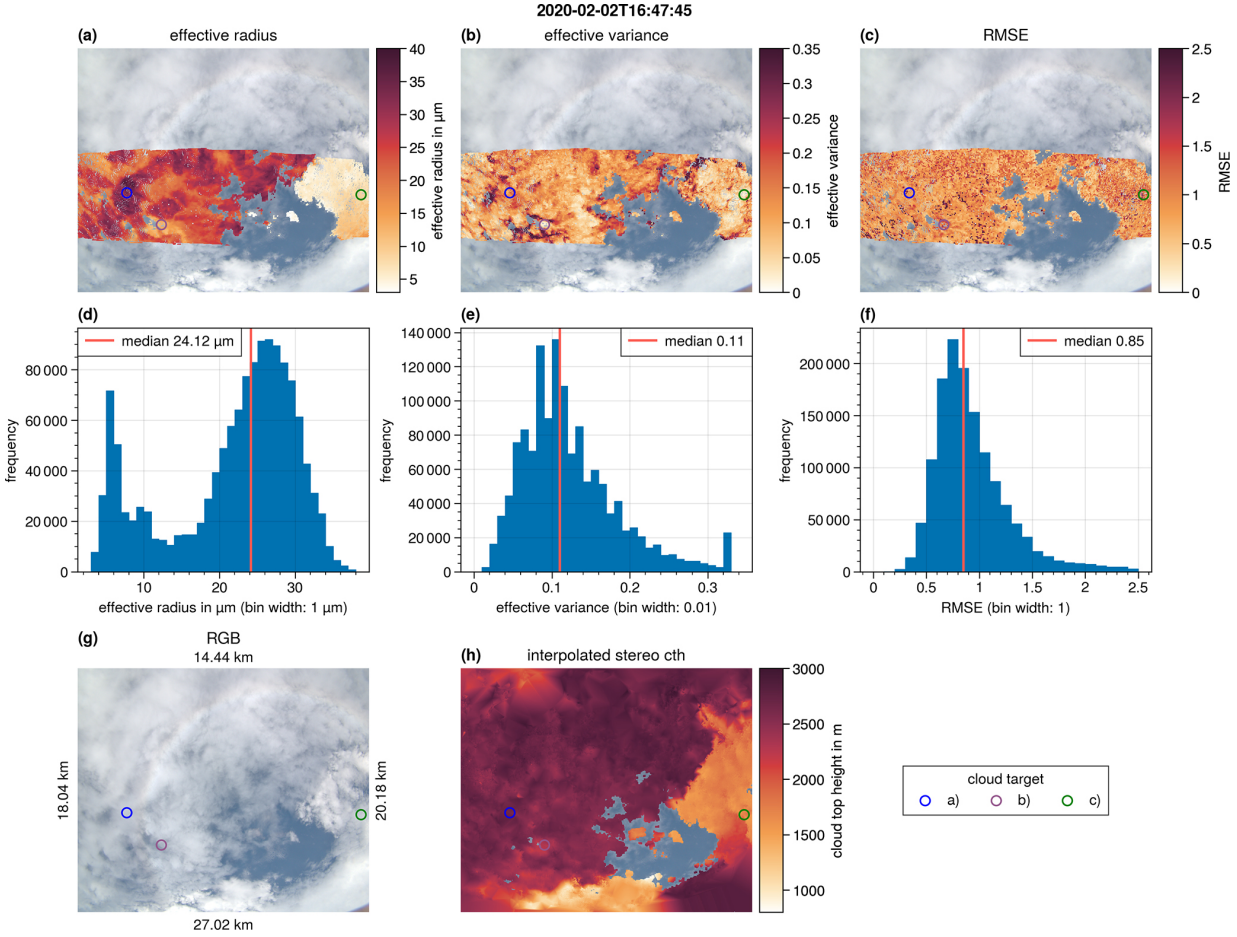

Figure 3.7: Spatial distributions of r_{eff} (a), v_{eff} (b), and RMSE (c) for the case study presented in Fig. 3.2. Panels (d)–(f) show the corresponding frequency distributions. Panel (g) shows the RGB image of the measurement. The labels on the four sides of the RGB image indicate the distances between neighboring corners of the image. Panel (h) shows the cloud top height from the stereo method interpolated onto the whole pixel grid of the image. The three cloud targets from Fig. 3.6 are indicated by colored circles on the maps.

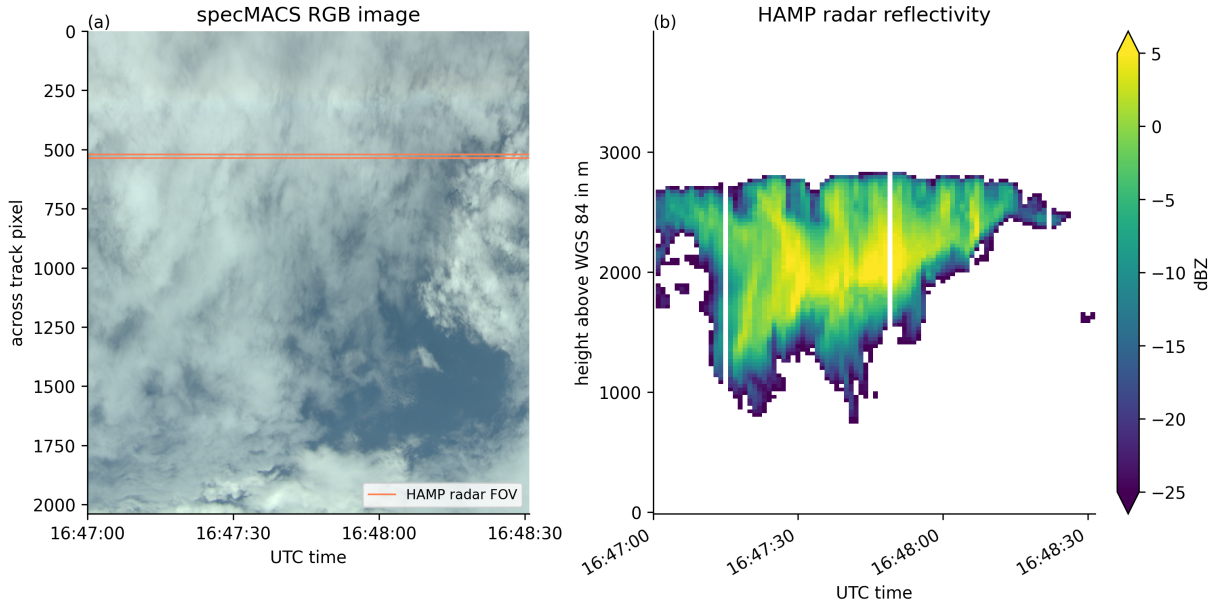

Figure 3.8: Temporal evolution of specMACS measurement (a) and HAMP radar reflectivity (b) for the scene presented in Fig. 3.7. The specMACS measurements are stacked together from individual images to generate a push-broom-like image with a time axis. The HAMP radar field of view is marked within the specMACS image. Figure adapted from Pörtge et al. (2023) with small modifications.

frequency distribution of v_{eff} is shown in Fig. 3.7e, and v_{eff} has a median value of 0.11.

Figure 3.7c and f show the spatial distribution and the frequency distribution of the RMSE. The RMSE has a median value of 0.85, and there is no noticeable difference between the RMSE of the lower cloud with small r_{eff} and the upper cloud with large r_{eff}. Small cracks are visible within the spatial distributions of r_{eff}, v_{eff}, and the RMSE due to the reprojection of the targets onto the RGB image of the measurement. This is due to small discontinuities within the interpolated stereo cloud top height. This, in turn, results in discontinuities within the locations of the reprojected targets.

3.2.2 Uncertainty assessment

In the following, the impact of various instrumental characteristics and technical aspects on the retrieval uncertainty are studied, including:

- angular resolution
- spectral resolution
- geolocation accuracy
- the assumption of monomodal CDSDs for the LUT of polarized phase functions

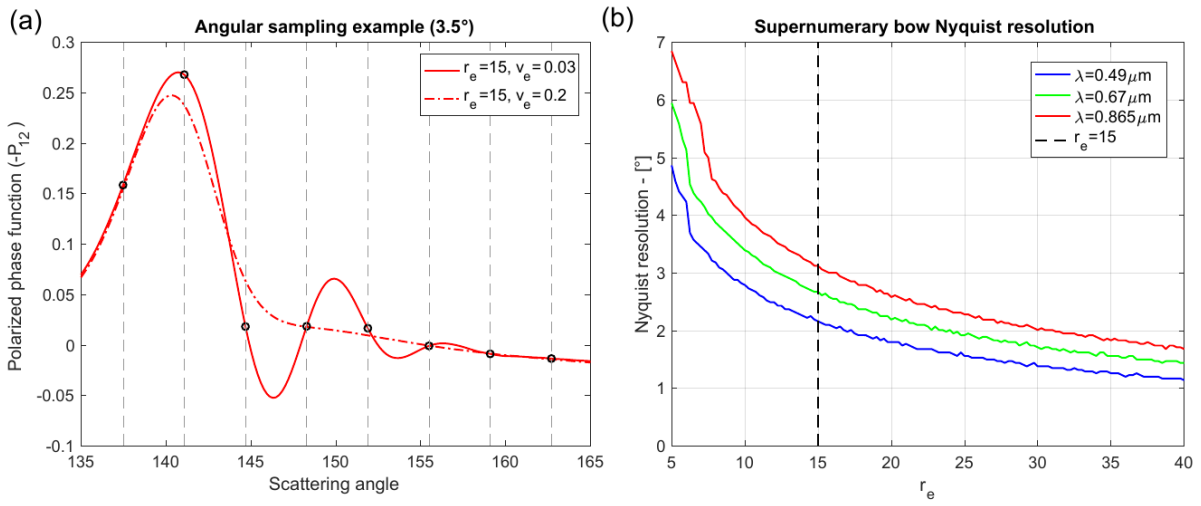

Figure 3.9: Reproduced from Figure 13 from Miller et al. (2018) (CC BY 4.0 license). Panel (a): Polarized phase function ($-P_{12}$) for two different CDSDs and sampling at 3.4° angular resolution (black circles). Panel (b): Nyquist resolution as a function of r_{eff} (in µm) and λ as obtained by measuring the peak-to-peak distance of the supernumerary bow osciallations divided by two.

- the effect of an overlying cirrus

Especially the effect of the geolocation accuracy is discussed based on a case study of small cumulus clouds.

Angular resolution

The angular resolution of a measurement of a target at a distance of 10 km is determined by the data acquisition frequency, which is set to 8 Hz, and the velocity of the aircraft, which is typically 200 m s^{-1}. The resulting angular resolution is approximately 0.14° (Weber et al., 2024). As already explained, the current setup of the retrieval determines an average polarization signal of a target of 10 by 10 pixels. For this purpose, all individual measurements of the target area at different times are first collected and are then gridded onto a regular grid with an angular resolution of 0.3°. This is a coarser resolution compared to the resolution defined by the data acquisition frequency (0.14°). The choice of the angular resolution of 0.3° was motivated by the previous development of a similar retrieval but for measurements of the backscatter glory which has a very fine angular structure (Pörtge, 2019). Although the cloudbow is more smooth, we still kept the angular resolution required for the glory measurements.

Figure 3.9, adapted from Miller et al. (2018), shows that in the case of large droplets, a high angular resolution is required for a precise retrieval. In panel (a), two cloudbow signals with different v_{eff} are sampled at an angular resolution of 3.5°. The given angular sample grid would almost provide the same values for both size distributions, and

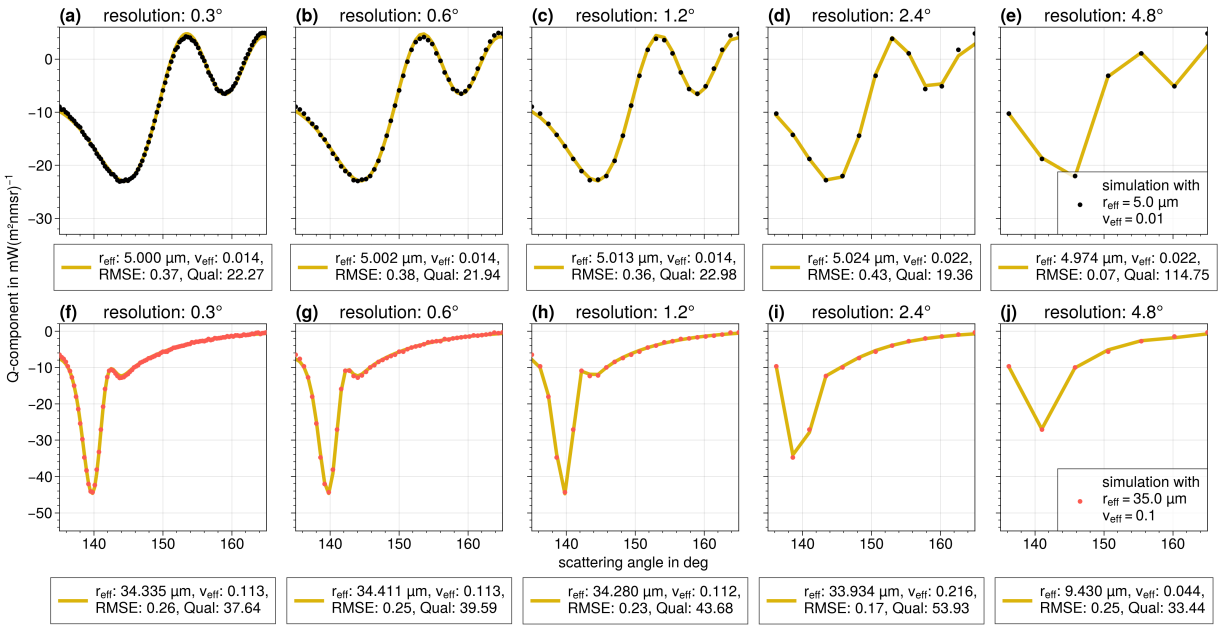

Figure 3.10: Simulation of a 1-D cloud for the red channel of the specMACS cameras for five different angular resolutions. Upper row: $r_{\text{eff}} = 5\,\mu\text{m}$ and $v_{\text{eff}} = 0.01$. Lower row: $r_{\text{eff}} = 35\,\mu\text{m}$ and $v_{\text{eff}} = 0.1$.

the angular resolution clearly does not allow to distinguish between the two effective variances. The distance between the peaks of the oscillations in supernumerary bows can be regarded as the Nyquist resolution. This defines the maximum sampling resolution to still resolve all supernumerary bow oscillations of the angular distribution. Panel (b) shows how the Nyquist resolution depends on the r_{eff} for three different spectral channels. For higher r_{eff} as well as for smaller wavelengths a finer angular resolution is needed. For the extreme values ($r_{\text{eff}} = 40\,\mu\text{m}$ and $\lambda = 0.49\,\mu\text{m}$) an angular resolution of approximately 1.2° is needed to fully resolve the signal. This means choosing 0.3° as angular resolution is more than sufficient for the cloudbow retrieval and the sampling frequency could even be decreased in order to, e.g., save data storage space.

To analyze the effect of a potential coarser resolution, radiative transfer simulations of a 1-D cloud were performed at different angular resolutions using the MYSTIC solver included in libRadtran. The standard tropical atmosphere of libRadtran was used, with Rayleigh scattering and molecular absorption turned on by default. The results are shown in the Figure 3.10 for two clouds with different CDSDs. The upper row shows a simulation of a cloud with $r_{\text{eff}} = 5\,\mu\text{m}$ and $v_{\text{eff}} = 0.01$. In the lower row a cloud with $r_{\text{eff}} = 35\,\mu\text{m}$ and $v_{\text{eff}} = 0.1$ was simulated. The dots are the simulated Q values. The lookup table of polarized phase functions is fitted to these simulated data and plotted as a yellow line. The corresponding retrieved r_{eff} and v_{eff} values are given in the legend of each subplot. Figure 3.10 shows that even with the coarsest resolution of 4.8° in panel (e), the r_{eff} is predicted quite accurately. All five angular resolutions show a deviation

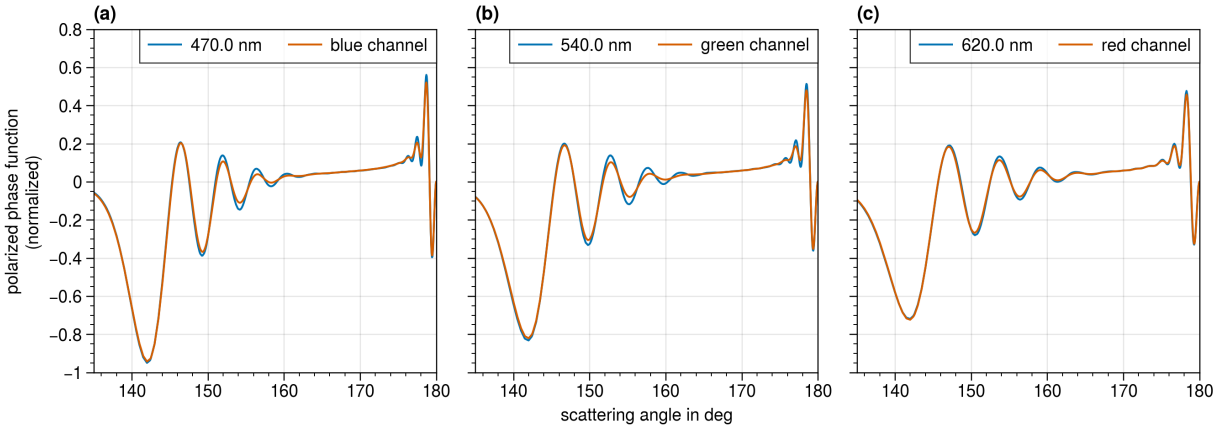

Figure 3.11: Effect of spectral response functions of specMACS polarization cameras on cloudbow signal

of less than 0.1 µm from the actual r_{eff} value. The coarsest resolution has the largest deviation in v_{eff} (0.021 versus 0.1). For the second simulation in Figure 3.10 in the lower row, with much larger droplet size and CDSD width, the retrieved r_{eff} deviates strongly from the actual value for the simulation with a resolution of 4.8°. However, for all other angular resolutions the retrieved r_{eff} are very similar to the actual r_{eff} with deviations of less than 0.45 µm. The v_{eff} deviates most for the case with an angular resolution of 2.4°. The simulations confirm the results from the Nyquist analysis shown in Figure 3.9, and illustrate that a coarser angular resolution than 0.3° is sufficient for the cloudbow retrieval.

Spectral response

As shown in Figure 3.1, the camera's three color channels are relatively wide. The green channel is the widest with a width of approximately 120 nm. This can be an issue for the cloudbow retrieval since the cloudbow signal and especially the position of the cloudbow minima (see Figure 2.3c) depend on the wavelength of the radiation. The features of the cloudbow may be smoothed out for wide channels. Figure 3.11 shows normalized polarized phase functions for the three specMACS color channels and for the corresponding center wavelengths. The signals of the color channels are very similar to the signals of the center wavelengths, and the deviations are smallest for the narrowest channel (red). The primary and supernumerary bows are clearly visible in the spectrally integrated signals. This indicates that the spectral response functions do not significantly smooth the signal.

Geolocation accuracy

The aggregation of the polarized cloudbow signal is a critical step in the retrieval. It relies heavily on a precise initial identification of the target's 3-D location, and on the

process of re-identifying the target in different images. The whole aggregation process is influenced by the following characteristics:

- the position and attitude of the aircraft
- the geometric camera calibration which defines the viewing angles of the pixels
- the orientation of the instrument relative to the airplane
- the determined cloud top height
- the ambient horizontal wind

In the following, the first four points are assessed based on two approaches using targets on the ground. In the next section, the retrieval is applied to measurements of small cumulus clouds which illustrates the expected accuracy of the operational retrieval and also considers the fourth point (wind movement).

In the first approach, the pixel position of a specific ground target in a specMACS measurement is manually identified and the corresponding location (in latitude and longitude) is calculated from the pixel position, and compared with the true latitude and longitude coordinates that are found from Google Earth. The pixel position of the target is shown in Figure 3.12 for the images of the two cameras. The upper left panel shows the image captured by the polLL camera, and the upper right panel shows the image of the polLR camera. A yellow rectangle marks the region, which is shown as a closeup in the lower panels. Here, the target (the corner of a big building) is marked by a pink cross. Due to the large distance of the camera to the target (about 10 km), the corner is quite blurry and determining the exact pixel position of the corner is difficult. By combining the viewing direction of the pixel with the aircraft's position and attitude data from the BAHAMAS measurement and the true ground height of the target[2], the corresponding latitude and longitude coordinates are calculated (see legend of Figure 3.12). The calculated position is then compared with the target's actual location in Google Earth as shown in Figure 3.13. The offset is approximately 20 m for the polLL camera and 10 m for the polLR camera.

The second approach uses the same data in the inverse way. First, the actual coordinates of the building's corner are determined from Google Earth, and then the corresponding pixel positions using the camera model are calculated. Figures 3.14 and 3.15 show measurements at five different times zoomed into the region of interest (panels (b)–(f)). Panel (a) of both figures shows the dimension of the whole specMACS

[2]The true ground height of the target is determined from Google Earth data. The latitude and longitude coordinates in Google Earth are given with respect to the WGS 84 ellipsoid, while the heights refer to the EGM96 geoid (Wilson, 2008). Since the processing of specMACS data is generally done in the WGS 84 ellipsoid coordinate system, the Google Earth height (in this case 480 m) is converted to WGS 84 by adding the geoid undulation (in this case: 47 m) to the Google Earth height.

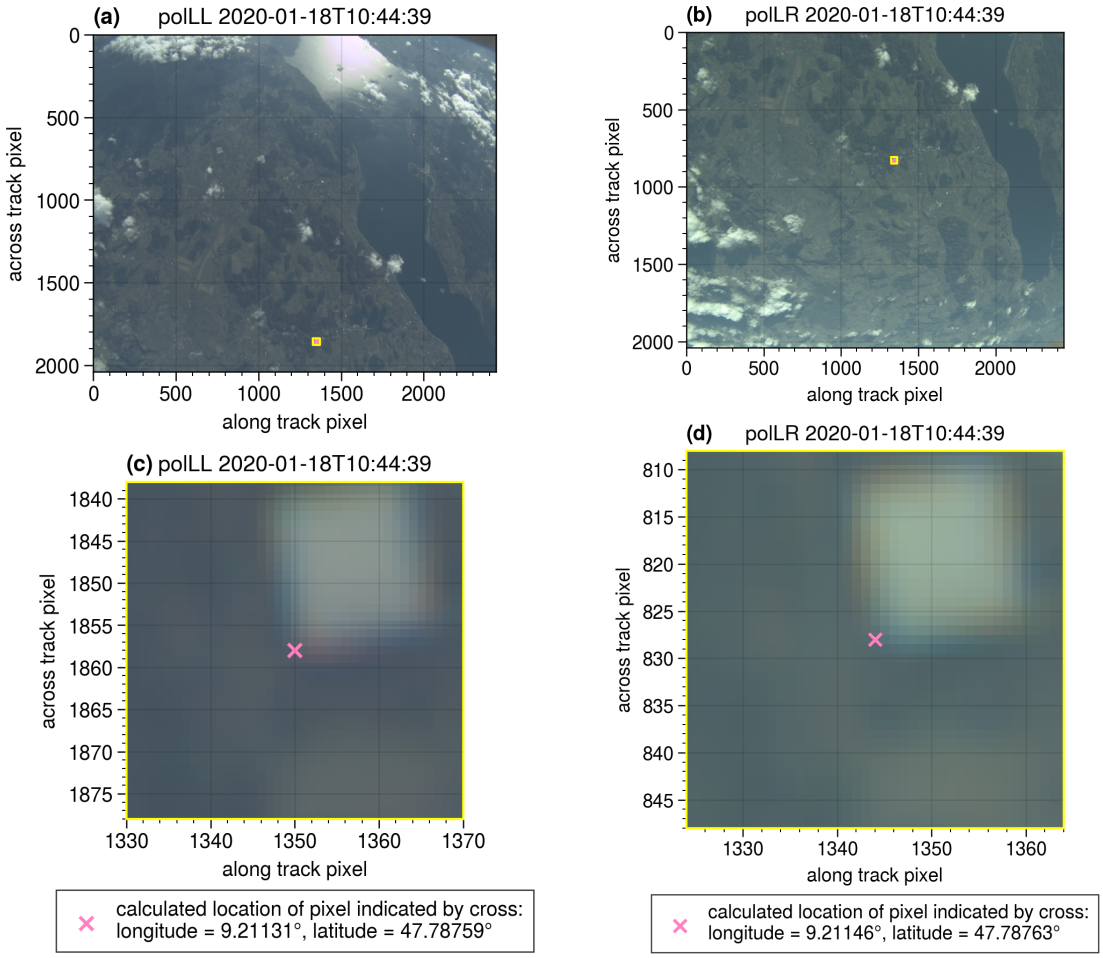

Figure 3.12: The pink crosses mark the manually determined pixel positions of a building's corner in the specMACS images of the two cameras (left: polLL, right: polLR). A zoom into the region of interest is shown in the lower two panels. The corresponding calculated locations are given in the legend.

image and marks the pixel position of the target corresponding to the individual times. This illustrates where the zoomed areas are located within the overall field of view (FOV). Deviations are expected to be smaller in the center regions of the FOV than in the edge regions because the center areas were better characterized during the geometric calibration. For both cameras, the calculated pixels seem to be a bit too far on the left side of the actual corner, and the position of the marked pixel relative to the actual corner slightly moves from image to image. The offset is approximately two to three pixels which corresponds to approximately 20 m, which is similar to the deviation found using the first approach (Figure 3.13).

The different sources that affect the geolocation of the target are discussed in the following. One factor is the accuracy of the position and attitude of the airplane measured by the BAHAMAS system. The accuracy of the BAHAMAS data is stated in Giez

Figure 3.13: Google Earth image showing the same ground target as in Figure 3.12 and the corresponding offsets to the calculated positions from manually identifying the corner pixel in images of the polLL (red) and polLR (blue) cameras.

et al. (2021) in Table 2. They determined a very good accuracy of 0.05 m in the aircraft position data, 0.003° in the roll and pitch angles, and 0.007° in the true heading data. The reference point of the BAHAMAS system is at the aircraft nose boom, and the specMACS instrument is located at a distance of approximately 23 m to the BAHAMAS measurement unit in the back of the airplane. During a flight, the airplane fuselage might experience deformations, which limits the accuracy of the BAHAMAS data with respect to specMACS.

A further uncertainty arises from the geometric calibration (Weber et al., 2024). For this purpose, images of a known chessboard were taken across the entire field of view of the cameras. The calibration method (Zhang, 2000) detects the corners of the chessboards in the images to determine the viewing directions of the pixels. The results of this calibration are affected by the 2 cm thick window in front of the cameras. This window introduces a shift of the viewing directions, especially for large incident angles. Weber et al. (2024) found an average uncertainty of the geometric calibration of 10 m at a typical flight altitude of 10 km which corresponds to an angular uncertainty of 0.04°. A further uncertainty emerges from the position and orientation of the camera relative to the airplane. This is determined by projecting specMACS measurements onto Google Earth satellite images as described in Weber et al. (2024). An error in the camera's orientation results in a constant pointing offset which could be the reason for the offset observed in the polLL camera in Figure 3.14. As stated in Weber et al. (2024), the uncertainty of the orientation angles is 0.05°.

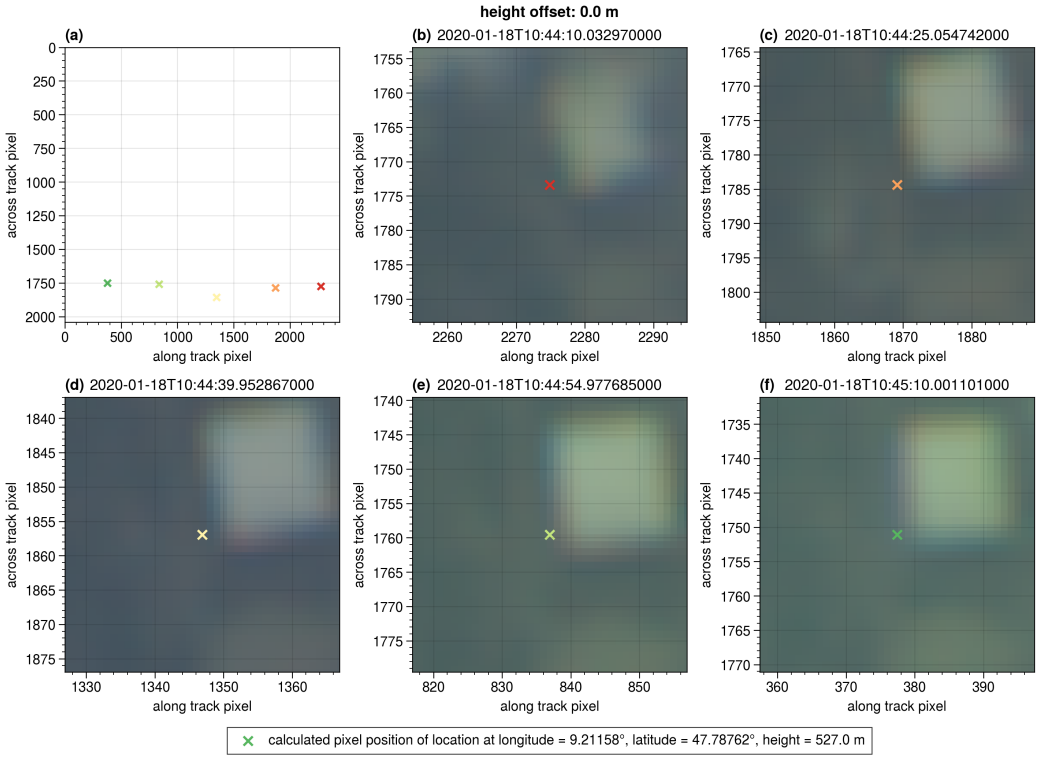

Figure 3.14: Calculated pixel positions of specific location for different specMACS images of the polLL camera. Panel (a) indicates the positions of the target inside the whole specMACS image marked by a cross. (b)–(f) show a zoom into the region of interest for the different times and the target marked by a cross.

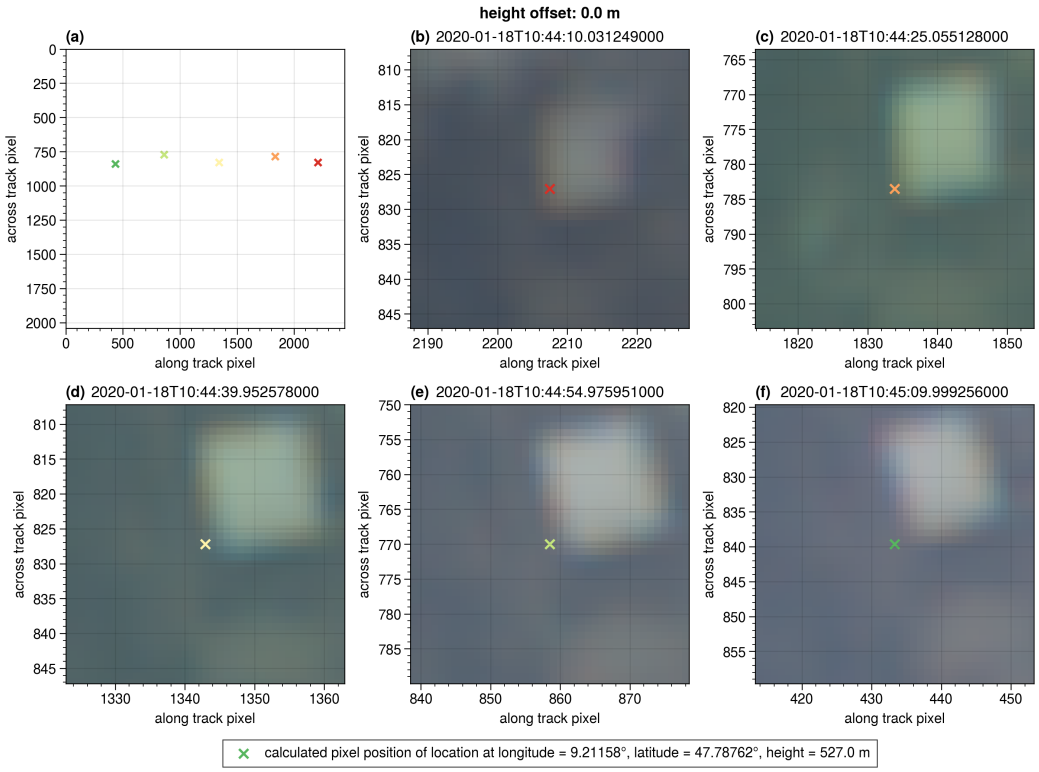

Figure 3.15: Calculated pixel positions of specific location for different specMACS images of the polLR camera. Panel (a) indicates the positions of the target inside the whole specMACS image marked by a cross. (b)–(f) show a zoom into the region of interest for the different times and the target marked by a cross.

The cloud top height determined from the stereographic retrieval is a further factor that influences the geolocation. An uncertainty of approximately 100 m in the derived cloud top height was found from both a validation with observational data (Kölling et al., 2019) and a model study (Volkmer et al., 2023). The effect of an offset in the retrieved cloud top height on geolocating the target is smallest close to the nadir looking direction and increases for larger viewing angles. Assuming an incorrect height of 627 m instead of 527 m in the ground target study in Fig. 3.14 and Fig. 3.15 leads to an along track offset of approximately 80 m for large viewing angles.

In the case of real cloud measurements, re-identifying the same target in different measurements is even more difficult since the target moves with the ambient (mainly horizontal) wind. Typical horizontal wind speeds in the cloud layer are in the order of $5\,\mathrm{m\,s^{-1}}$ to $10\,\mathrm{m\,s^{-1}}$. During the flight, it usually takes about 35 s to 40 s to sample the targets in the necessary scattering angle range from 135° to 165°. During this aggregation process, a target cloud shifts by 200 m to 400 m for typical wind speeds, and a wind correction is applied to the initial location of the target to account for any displacement due to the wind.

Based on the presented analysis of known ground targets and considering the uncertainty introduced by the cloud top height, we used cloud targets of approximately 100 m × 100 m in size in the current study. In the following, we will refer to this size of 100 m as "target unit". In summary, the uncertainties of the geometric calibration (0.04°) and of the orientation of specMACS relative to the airplane (0.05°) as stated in Weber et al. (2024) could already explain the observed deviation of the calculated locations to the actual locations based on the study of ground targets in Figure 3.13. In real cloud measurements, the determination of the cloud top height and the ambient horizontal wind are additional uncertainties. The next section shows that the geolocation accuracy is sufficient to analyze a more complicated case study of small cumulus clouds where a precise pointing is needed.

Spatial resolution discussed in the context of small cumulus clouds

Parts of the following section were published in Pörtge et al. (2023).

In the following subsection, a second case study is discussed. The observations were taken from 18:28:15 to 18:31:30 UTC with the polLR camera. HALO was flying at an altitude of 10 345 m, and the solar zenith angle was 46.1°. The measurement shows a cloud field of small trade-wind cumulus clouds with diameters of about 1 km to 2 km (Fig. 3.16b). This example is chosen to demonstrate that the retrieval is capable of generating good results, even in the case of more heterogeneous cloud scenes and especially for small cumulus clouds. In such scenes, the traditional bispectral retrieval has issues with 3-D radiative transfer effects (Marshak et al., 2006; Zhang et al., 2012).

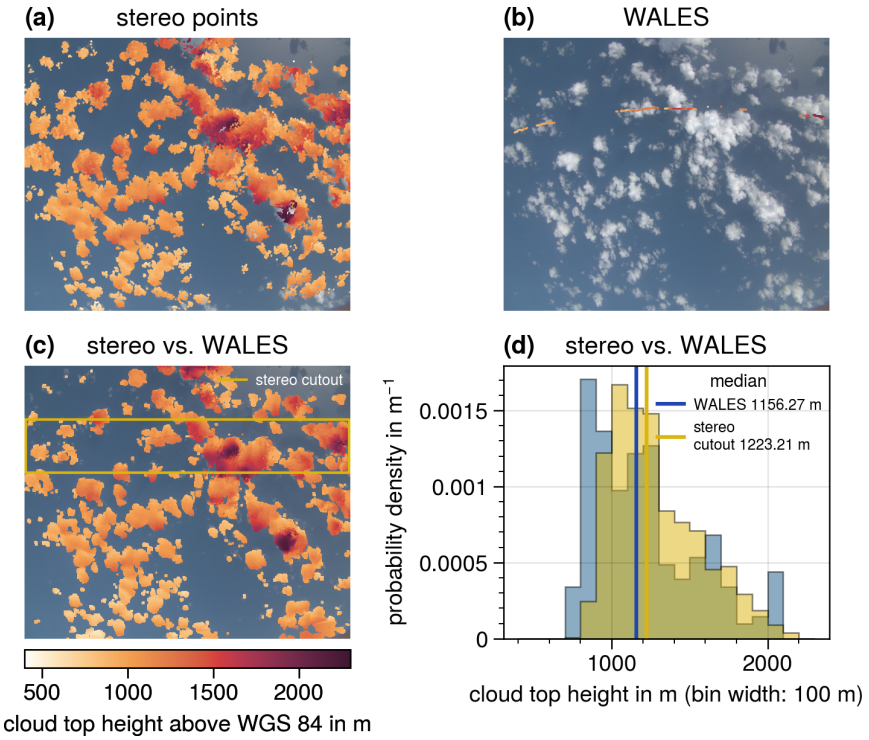

Figure 3.16: Cloud top height (CTH) data of the case study of small cumulus clouds (2 February 2020, 18:29:30 UTC). Panel (a) shows the CTH of stereo points from the stereographic reconstruction method, panel (b) presents the CTH from the WALES lidar system, and panel (c) shows the interpolated CTH based on the stereo points. The WALES CTH is plotted on top. The stripe marked by the yellow lines indicates a specMACS cutout surrounding the WALES track. Panel (d) shows the probability densities of the CTHs of the specMACS cutout (yellow) and the WALES measurements (blue). The RGB measurement of the cloud field is shown in the background of panels (a), (b), and (c). The color bar below panel (c) corresponds to all cloud top height measurements shown in panels (a), (b), and (c).

These are shadowing or illumination effects, which are normally not accounted for in standard radiance lookup tables.

The stereographic cloud geometry retrieval is very applicable to this cloud field because of the strong contrasts between the clouds and the ocean. The resulting cloud top height (shown in Fig. 3.16a) is relatively constant across the whole cloud field with a median value of about 1200 m. Some (diameter-wise) larger and more developed clouds also have higher cloud tops up to 2200 m. Cloud top height data derived from WALES lidar measurements are projected onto the specMACS RGB image and are shown in Fig. 3.16b. The lidar measurements are also plotted on top of the stereo points, which were interpolated onto the whole image (Fig. 3.16c). The stereographic result is again similar to the WALES measurements. This is also evident in Fig. 3.16d, where the probability density of the stereo data in the surroundings of the WALES track (yellow rectangle in Fig. 3.16c) is plotted along with the WALES cloud top height data (blue).

For a successful cloudbow retrieval, we rely on an accurate aggregation of the mea-

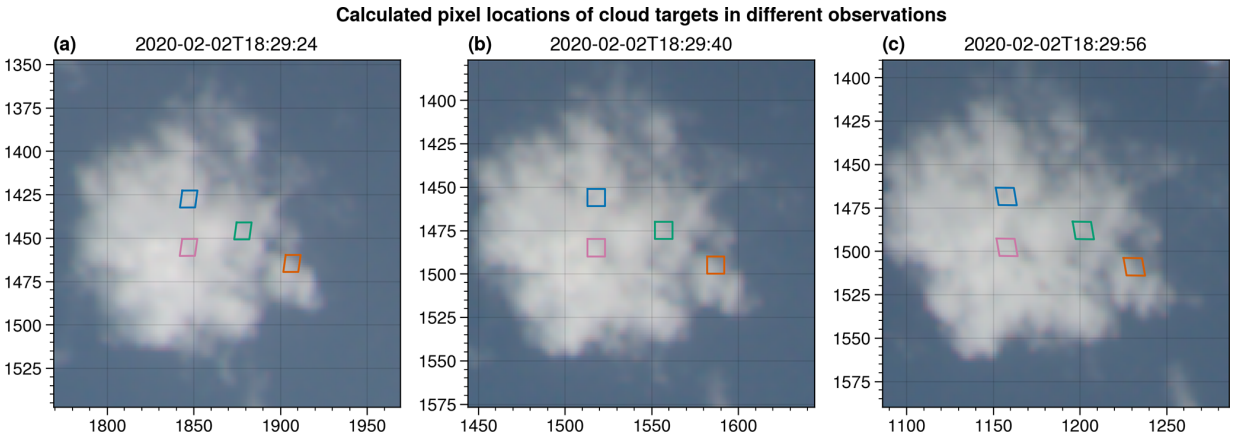

Figure 3.17: Calculated pixel positions of cloud targets, indicated by different colors, in observations at different times during the overflight.

surements by mapping from the known viewing angles to the image pixel location corresponding to the same cloud target as discussed in the last section. We manually verified the tracking of cloud targets with distinctive features during the overflight. One such example is shown in Fig. 3.17. Based on the location of the targets and the ambient wind at 18:29:40 UTC (panel (b)), the pixel positions of the targets in a previous (panel (a)) and a later (panel (c)) image are calculated. A visual comparison of the identified targets in the different images shows that the targets are successfully tracked: the colored markers in Fig. 3.17 highlight the same areas of the cloud in all three images. Due to camera distortions, the originally rectangular cloud targets (at 18:29:40 UTC) increasingly take the shape of a trapezoid when they approach the edge of the entire image. Please note that each panel in Fig. 3.17 shows only a small part of the entire image.

The retrieved r_{eff}, v_{eff}, and RMSE results are projected onto the RGB image and shown in Fig. 3.18a–c. The corresponding frequency distributions are presented in Fig. 3.18d–f. Figure 3.18g and h display the RGB image of the measurement as well as an indication of the dimension of the image and the interpolated cloud top height, respectively. Compared with the first case study (Fig. 3.7), r_{eff} is much smaller (median of 7.0 µm) and has a more narrow distribution. Values of r_{eff} larger than 12 µm are not observed. The spatial distribution of r_{eff} is homogeneous and has few outliers.

The v_{eff} (Fig. 3.18b and e) is small (median v_{eff} of 0.08) and consistent within the inner part of the clouds. There are some cloud targets with $v_{\mathrm{eff}} = 0.32$ (the upper limit of the LUT) that occur mainly at the edge of the cloud. At the cloud edge, a small offset in the geolocation can have a significant impact on the aggregated observations. The offset between the assumed location and the actual location may increase during the aggregation process and could even include cloudless parts for targets at the cloud edge. In this case, the aggregated measurements originate from different regions, and the cloudbow signal broadens or vanishes completely. We tried to ensure that the RMSE and

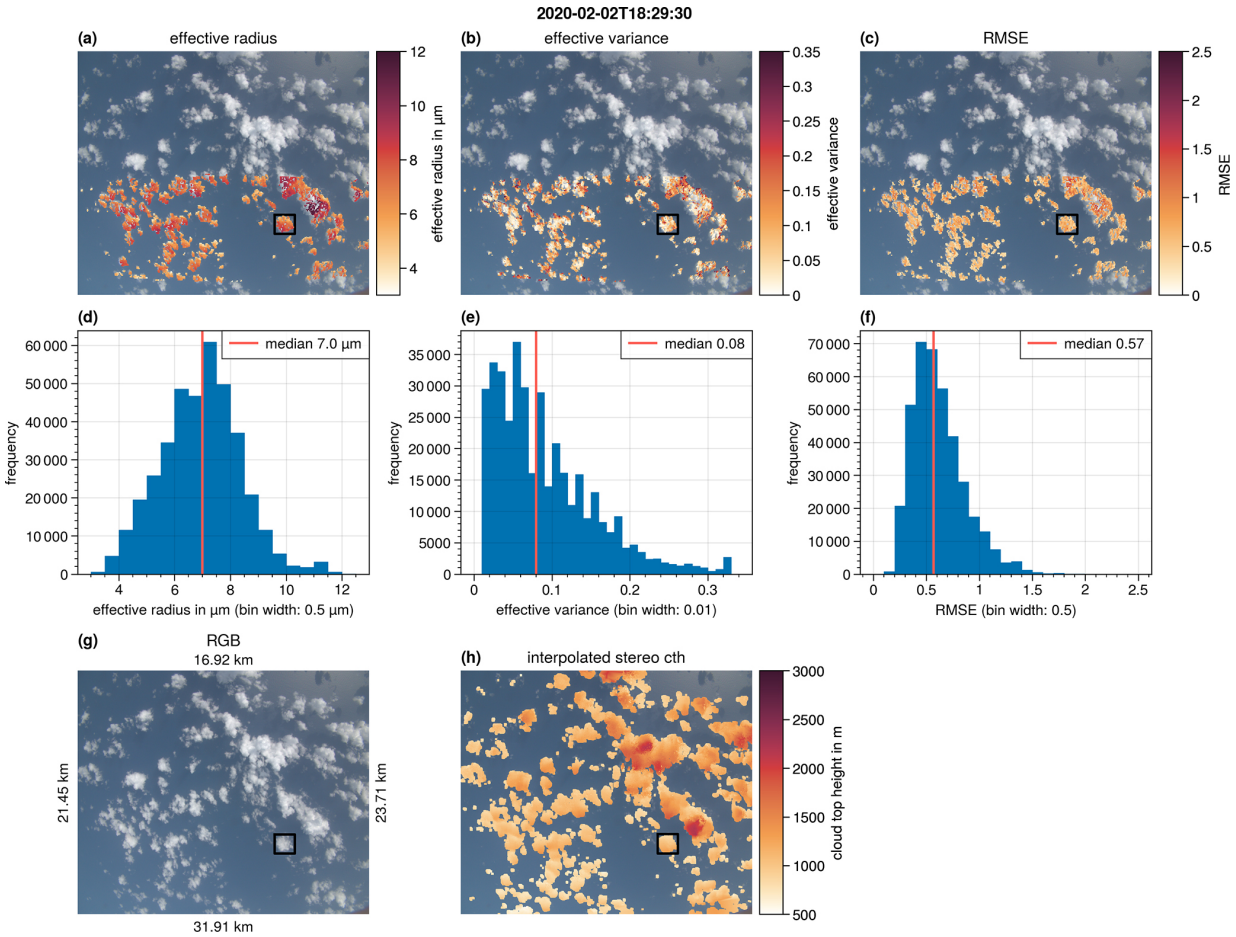

Figure 3.18: Same as in Fig. 3.7 but for the second case study presented in Fig. 3.16. The black rectangle marks a single cloud that is presented in Fig. 3.19.

Qual criteria successfully filter out such cases. Furthermore, the high values in v_{eff} could also be a physical effect related to entrainment and (inhomogeneous) mixing of dry air in the cloud. In this case, modeling studies predict a broadening (increase in v_{eff}) of the DSD (Pinsky et al., 2016).

The black rectangle in Fig. 3.18 marks a single cloud (diameter of 1.5 km) that is presented in more detail in Fig. 3.19. In Fig. 3.19, maps of the r_{eff}, v_{eff}, and the cloud top height are shown along with the frequency distributions of r_{eff} and v_{eff} of the single cloud. The Qual and RMSE criteria filter out some of the cloud targets inside the cloud, which mainly appear in shadowed or optically thin parts of the cloud. The high spatial resolution of the measurements reveals small-scale structures of the DSD, especially regarding the v_{eff}, which is, for example, increased along a line from the top left to the center of the cloud.

Three targets of the cloud are selected (marked by circles on the maps). The targets (a) and (b) have a similar r_{eff} but differ with respect to the v_{eff}. Target (c) lies within the region of increased cloud top height, where the r_{eff} is also large. The difference in these three targets is visible in the aggregated cloudbow observations presented in Fig. 3.20, which especially vary regarding the number and visibility of secondary minima. The observations are more noisy compared with the observations of the first case study (Fig. 3.6), and the absolute values of the cloudbow signals are smaller. This indicates that, even within one target, the variability in the cloudbow signal is relatively large. A reduction in the size of a target would be helpful, but this comes with the need for a further increase in the precision of the geolocation. Although the observations are more noisy, the primary cloudbow is still very pronounced, indicating that the retrieval of r_{eff} is robust. Furthermore, r_{eff} is relatively small for all three targets (6.54–9.2 µm). In this size range, the cloudbow signal depends strongly on r_{eff} (see Fig. 2.3). The result of v_{eff} is more difficult to interpret. The structure of the supernumerary bows (which mainly defines v_{eff}) can become smoothed out while averaging the signals of different DSDs within the averaging target, and the resulting DSD is, in the worst-case, different from any of the actual sub-pixel distributions. A sensitivity analysis of the cloudbow algorithm based on different resolutions of AirHARP data was presented in McBride et al. (2020) to identify effects of sub-pixel variability. This analysis showed that, in the case of a wide spread of the DSDs within the sub-pixels, the coarse-resolution result may not reflect the mean of the sub-pixels, as the combination of different gamma size distributions from the sub-pixels is not another gamma size distribution (Shang et al., 2015).

Shape of cloud droplet size distribution

For generating the lookup table of simulated cloudbow signals, it is assumed that the CDSD has the shape of a modified gamma distribution. This is usually a good assumption since it is also observed from in situ measurements (Miles et al., 2000). To support this

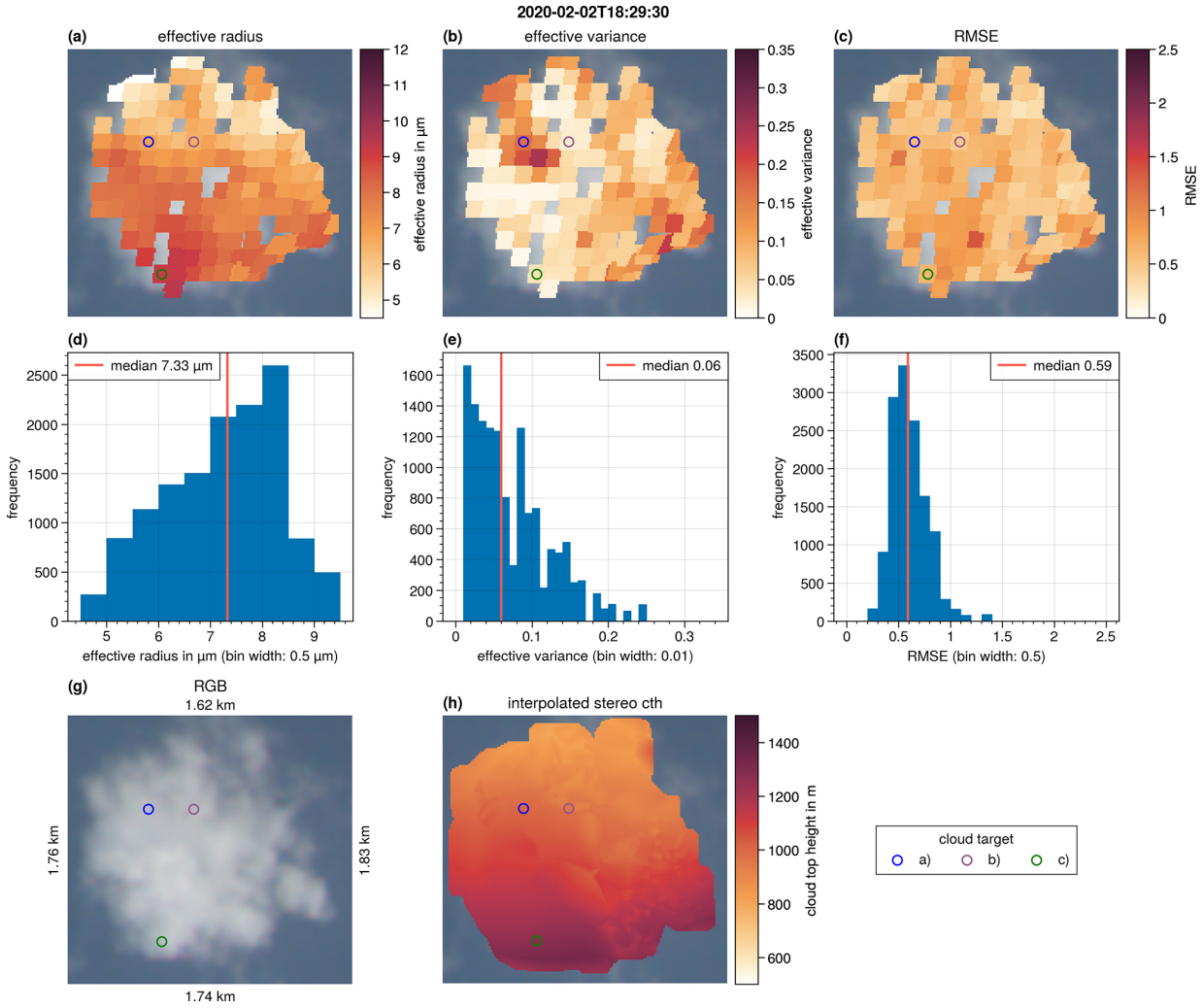

Figure 3.19: Same as in Fig. 3.7 but for a zoom into a single cloud shown in the second case study (Figs. 3.16 and 3.18). Three specific cloud targets are indicated by colored circles on the maps.

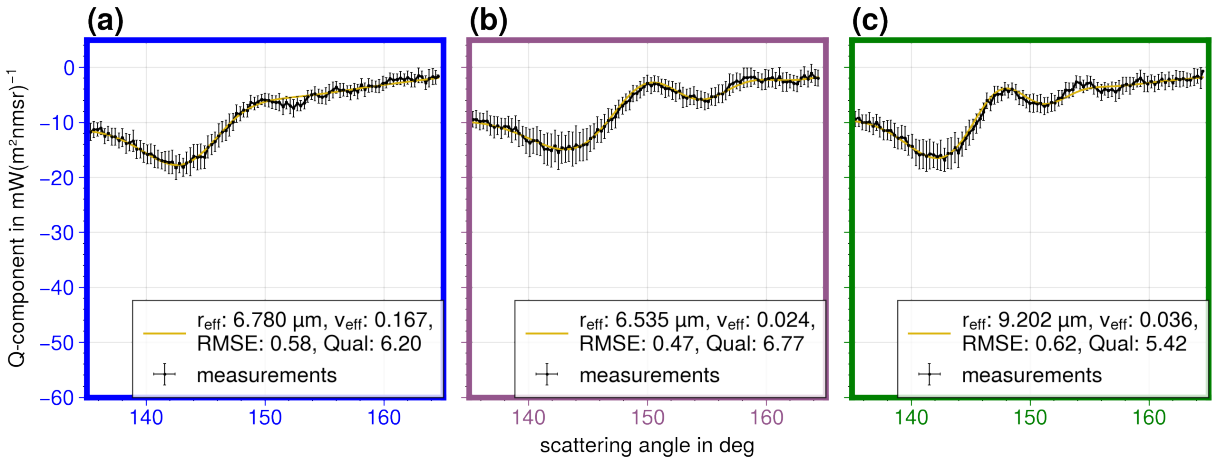

Figure 3.20: The aggregated polarized radiance measurements of the green channel of the locations shown in Fig. 3.19 were binned to a 0.3° resolution in the scattering angle (black dots connected by black lines). The error bars represent the standard deviations of all original data points within a 0.3° bin. The yellow lines indicate the best-fitting simulations. The parameters r_{eff}, v_{eff}, RMSE, and Qual of the best-fitting simulations are shown in the boxes in the lower right. For better visual comparison with the aggregated measurements of the first case study, the y axis covers the same range as in Fig. 3.6.

assumption, three in situ CDSD measurements from the ATR dataset (Coutris, 2021) from different days of the EUREC^{4}A campaign are shown in Figure 3.21. A modified gamma distribution is fitted to the data, and r_{eff} and v_{eff} are determined both from the fit and calculated directly from the definitions of r_{eff} and v_{eff} (Equations 2.14 and 2.15). In general, the data shown in Figure 3.21 are noisy, but the modified gamma distribution appears to represent the size distribution's shape. Furthermore, the calculated r_{eff} and v_{eff} are similar to the parameters fitted by the gamma distribution fit.

It is also possible to extract information about the shape of the size distribution from the cloudbow measurements. The method is called Rainbow Fourier Transform (RFT) and was developed by Alexandrov et al. (2012b). The idea of the method is that the polarization signal of the cloudbow is a superposition of the cloudbow signals that are generated by all individual droplets within the cloud. A single droplet with size r generates a cloudbow signal, which can be approximated by the polarized phase function for the size r (again neglecting multiple scattering). In Alexandrov et al. (2012b) it is shown that the polarization signal can be approximately decomposed into the contributions of the individual droplets, allowing the true size distribution to be retrieved. The phase functions for specific radii are used as basis functions for an integral transform similar to the sine Fourier transform. A limitation of the method is that the basis functions are only weakly orthogonal and therefore, a loop transform, where the forward and backward transformation are applied consecutively, is not an identity operator. Some artifacts remain after application of a transform and complex corrections must be applied to reduce the artifacts (Alexandrov et al., 2012b). The method has been

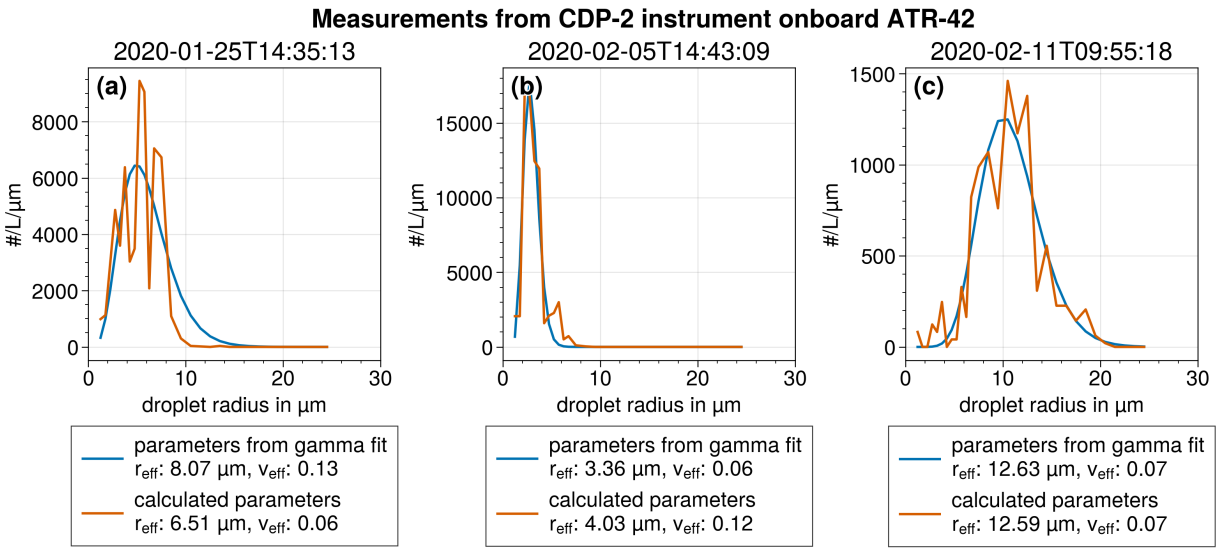

Figure 3.21: Measured droplet size distributions (orange) from the CDP-2 instrument onboard the ATR aircraft on different days of the EUREC^{4}A campaign and fit of a modified gamma distribution to the data (blue). The parameters r_{eff} and v_{eff} as calculated from the size distribution are also given.

successfully applied to RSP data and showed good agreement to in situ measurements (e.g. Alexandrov et al., 2015, 2016, 2018).

In Bernlochner (2023) it was shown that the RFT method can also be applied to specMACS data. Again, the retrieved size distributions often exhibit the shape of a gamma distribution (Bernlochner, 2023). Figure 3.22 shows six examples of CDSD retrieved using the RFT method as shown in Bernlochner (2023). The gamma distribution fits of both the RFT results and the parametric cloudbow are very similar. Nevertheless, in Bernlochner (2023), only a few selected cases were examined. Future work should extend this analysis to more case studies and ultimately to entire measurement campaigns. In summary, these two approaches support the assumption that the modified gamma distribution is a good model for the CDSDs typically observed during the EUREC^{4}A campaign. However, for observations that include precipitation, the gamma distribution is not expected to be a good model for the CDSD, and the parametric cloudbow retrieval results will be biased.

Effect of cirrus cloud above

The cloudbow feature does not appear in ice clouds because it is formed through scattering of light by liquid cloud droplets. However, if an optically thin ice cloud is above a liquid cloud, it may still be possible to see the cloudbow signal from the lower cloud. This section investigates up to which cirrus optical thickness the observation is possible. A similar study can be found in Riedi et al. (2010). In the following, two simulations are dis-

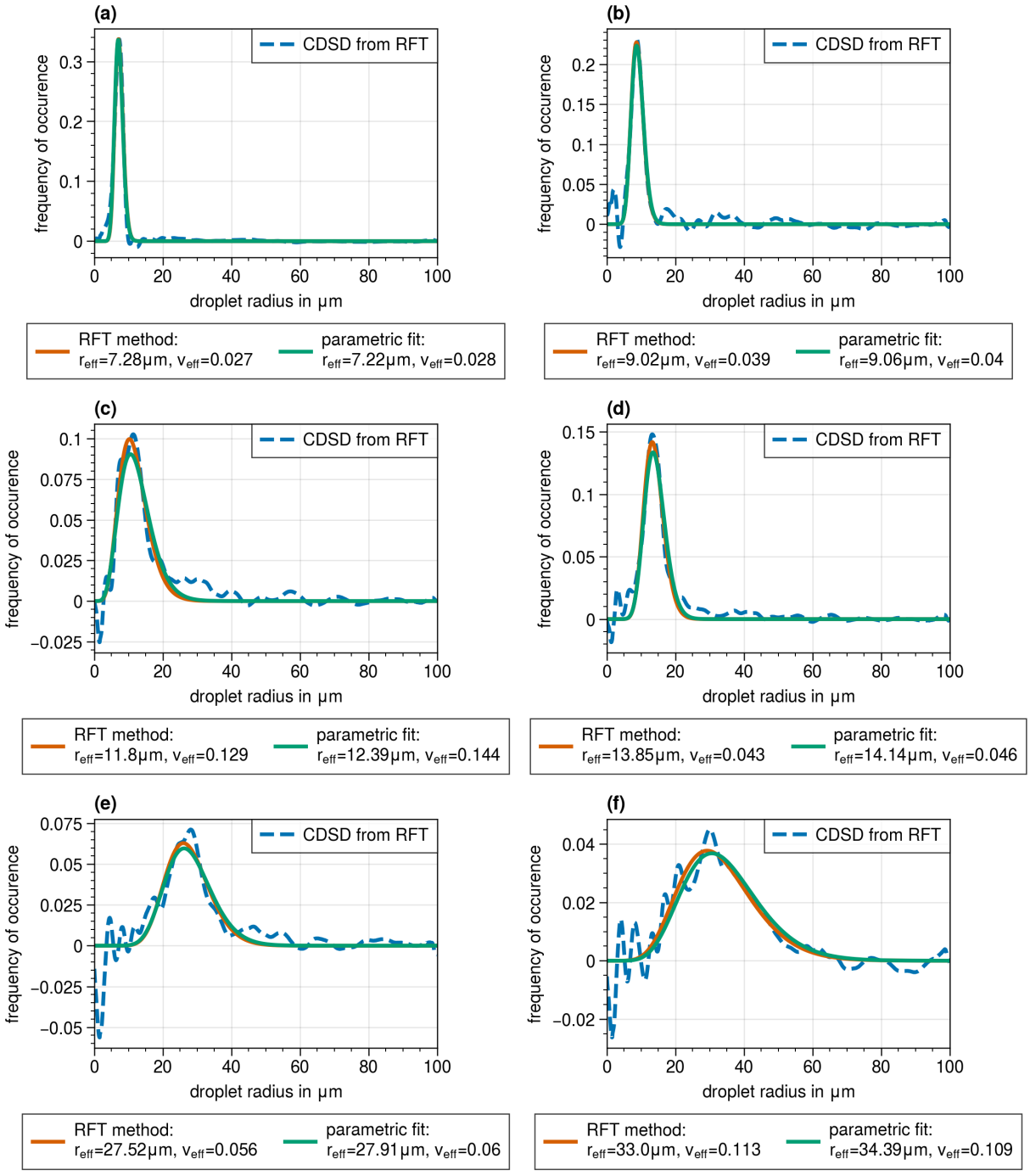

Figure 3.22: As Figure 25 from Bernlochner (2023) but translated to English. The CDSD retrieved from the RFT method is shown as blue, dashed line. The corresponding gamma distribution from r_{eff} and v_{eff} fitted to the RFT-CDSD is shown in orange. Furthermore, the CDSD according to r_{eff} and v_{eff} from the parametric fit is plotted in green.

cussed. specMACS is located at a height of 10 km and the liquid cloud is at 2 km to 3 km with $\tau_c = 10$ and $r_{eff} = 5\,\mu m$. In the first simulation the cirrus is located below specMACS within the height range 7 km to 7.5 km and it is above specMACS (10.5 km to 11.0 km) in the second simulation. The cirrus has $r_{eff} = 50\,\mu m$ and the `baum_v36` ice cloud parameterization (Heymsfield et al., 2013; Yang et al., 2013; Baum et al., 2014) included in libRadtran is used with the general habit mixture (`ghm`).

The main difference between the two simulations is that the radiation passes twice through the cirrus cloud in the first simulation, and only once in the second case where specMACS is located between the two cloud layers. The angular signals of the two simulations are shown in Fig. 3.23 and Fig. 3.24 for the green channel of the specMACS camera. Panel (a) shows I, panel (b) shows Q, and panel (c) shows Q but normalized to its absolute value of the primary cloudbow at 145° scattering angle. The cirrus optical depth is varied from 0 to 8. Both figures illustrate that the visibility of the cloudbow signal reduces if the cirrus optical depth increases. The smoothing is stronger in the first simulation where specMACS is above the cirrus than in the second simulation. If specMACS is below the cirrus, the cloudbow signal is still visible in Q for a cirrus optical depth of 2. Panel (c) illustrates that an optically thin cirrus does not significantly affect the position of the cloudbow minima, which mainly determines r_{eff} in the cloudbow retrieval. This analysis shows that for future measurement campaigns, it is recommended to fly below the cirrus if the cloudbow signal is to be studied.

3.2.3 Validation

Observation-based evaluation of retrieval uncertainty

In the following, the CDSDs from specMACS measurements will be compared to data from in situ instruments. The comparison is based on work done by Stefan Koppenhofer as part of his Master's thesis which he will submit in 2024 (Koppenhofer, 2024). During the EUREC^{4}A field campaign, many different measurement platforms were operated. This included research vessels, ground-based measurements on Barbados at the Barbados Cloud Observatory (BCO), and research aircraft (Stevens et al., 2021). Furthermore, different satellite instruments (GOES-ABI, MODIS on Terra and Aqua satellite, ...) frequently observed the region around Barbados.

In general, the most direct comparison is to compare the specMACS derived CDSD with in situ measurements at the same time and location. Especially, the height within the cloud is essential for such a comparison. For this reason, a comparison with in situ measurements from the ATR aircraft is made. However, the design of the ATR and HALO flight tracks makes a direct comparison very difficult. Most of the time, the HALO airplane was flying a circular pattern East of Barbados. The ATR was flying a rectangular pattern (at cloud base or cloud top) measuring clouds inside the HALO circle. Therefore, spatially coincident measurements are already very rare. Furthermore, the cloudbow

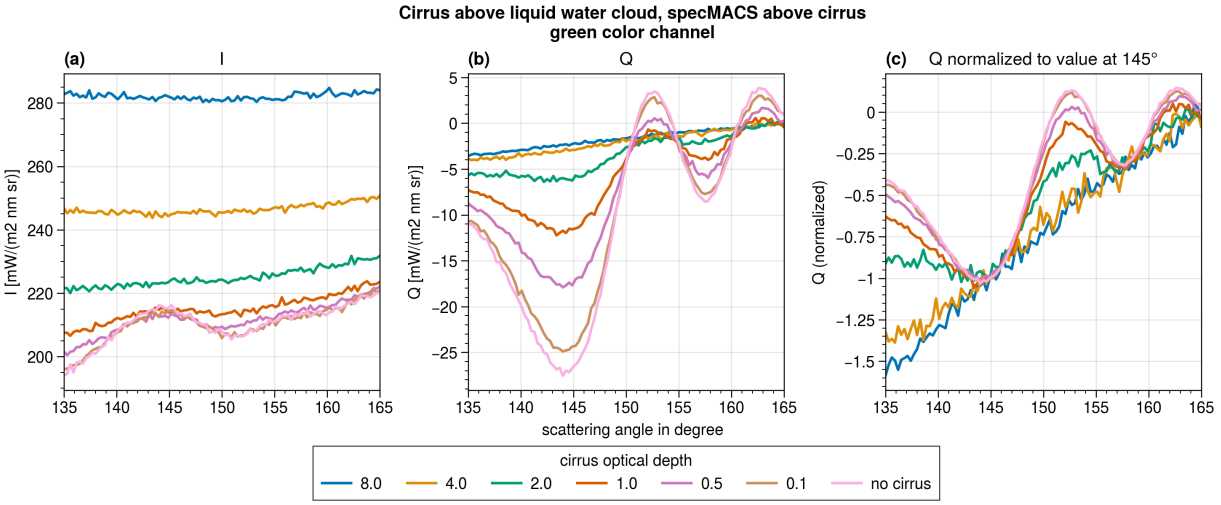

Figure 3.23: Simulated cloudbow signals for a scene where a cirrus is above a liquid cloud and specMACS is above both clouds. The optical thickness of the cirrus is varied to determine the effect of the cirrus. The green channel of specMACS is simulated.

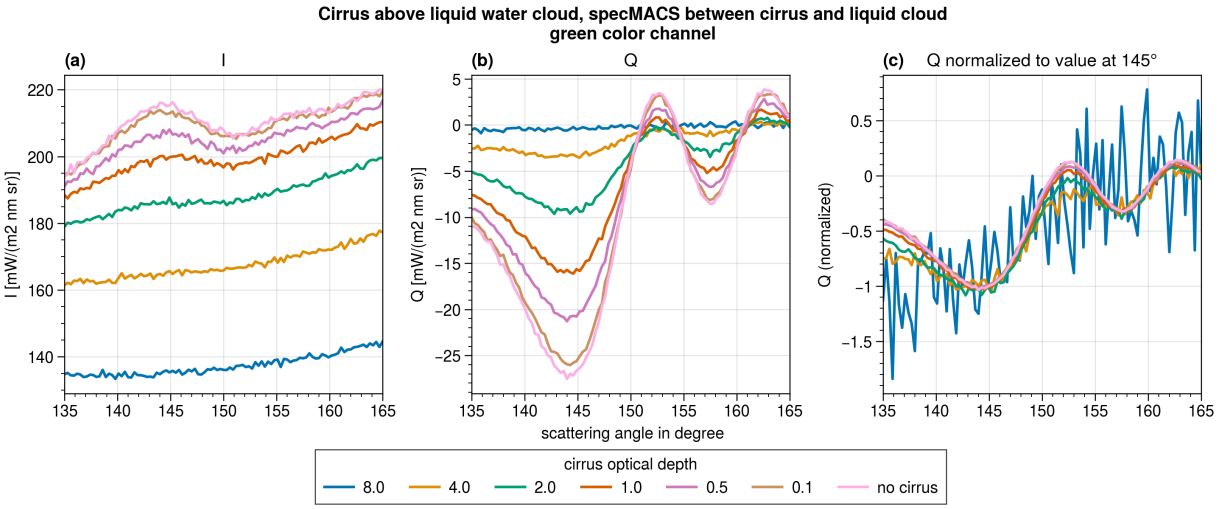

Figure 3.24: Simulated cloudbow signals for a scene where a cirrus is above a liquid cloud and specMACS is between both clouds. The optical thickness of the cirrus is varied to determine the effect of the cirrus. The green channel of specMACS is simulated.

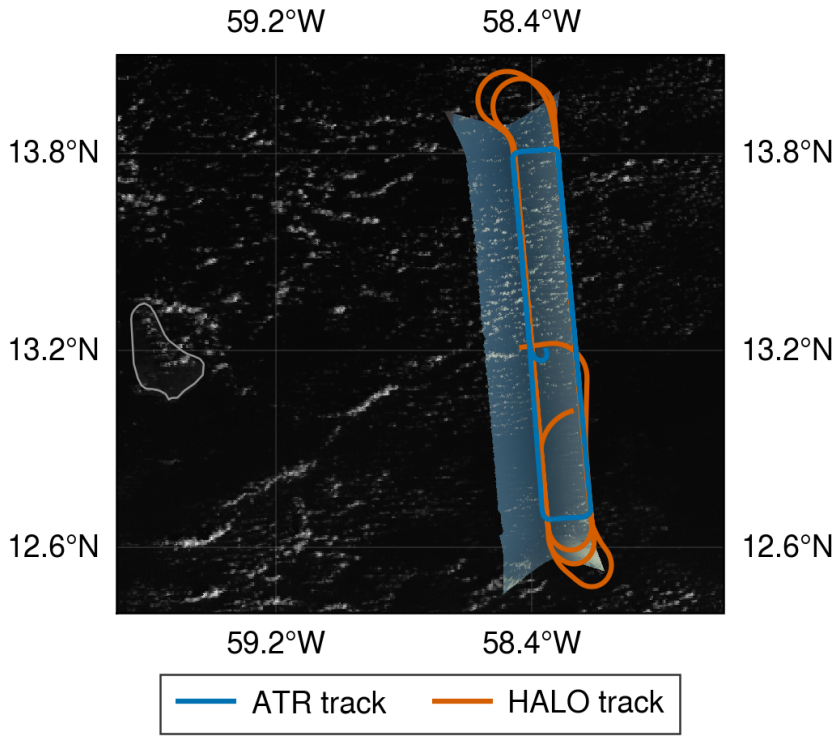

Figure 3.25: Case study for in situ comparison on 30 January 2020. The specMACS map of the flight segment HALO-0130_sl3 is shown on top of the GOES satellite image at 12:10:00 UTC. The orange track marks the path flown by HALO (11:45 to 12:38 UTC) and the blue track corresponds to the ATR flight track (11:45 to 13:00 UTC). Barbados is indicated in the center left.

retrieval cannot be applied to nighttime measurements or in general, when the sun is too low. And of course, there were also periods where no clouds were measured at all. All of these points significantly reduce the amount of usable data for the comparison.

One day with simultaneous cloud observations was 30 January 2020 where a field of shallow cumulus clouds was observed by specMACS (11:45 to 12:38 UTC) and the ATR during a similar time (11:45 to 13:00 UTC). Figure 3.25 shows the GOES satellite observation at 12:10 UTC together with the specMACS RGB measurements of the third straight leg of this measurement day. The clouds are really small and are not resolved in the satellite image which has a spatial resolution of 500 m. The HALO and ATR tracks are plotted as orange and blue lines respectively.

Two in situ instruments onboard the ATR measured the CDSD. The first one was the CDP-2 instrument which measured droplets in the size range from 2 µm to 50 µm with a resolution of 1 µm to 2 µm at a data acquisition frequency of 1 Hz. A second instrument (called 2D-S) measured cloud, drizzle and rain particles (size range: 10 µm to 1280 µm). The particle size distributions were calculated at 1 Hz. A combined dataset of the measurements of the two instruments is published in Coutris (2021) which is used for

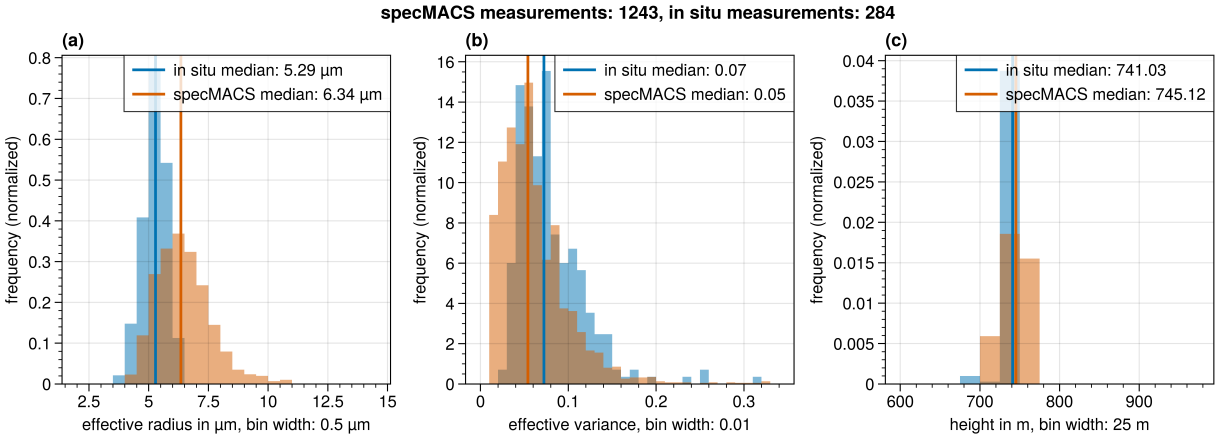

Figure 3.26: Comparison of r_{eff} (panel (a)) and v_{eff} (panel (b)) from ATR in situ measurements with results from the polarimetric cloudbow retrieval. Panel (c) shows the height distribution of the measurements. The total number of measurements are given in the title.

the comparison in Figure 3.26 that shows r_{eff} (panel (a)) and v_{eff} (panel (b)) from the in situ (blue) and the specMACS dataset (orange) of the case study on 30 January 2020. It should be stated that the figure does not show a direct comparison of individual clouds since there were just too few exactly simultaneous measurements. Instead, it is a comparison of the CDSD of the whole cloud field. For this comparison, the specMACS data are filtered to only include the data within $\pm 25\,\text{m}$ from the median flight height of the ATR (around 740 m). The medians of the two r_{eff} and v_{eff} distributions differ by approximately 1 µm in the effective radius and 0.02 in the effective variance. In general, the r_{eff} distribution is broader for specMACS than for the in situ measurements, and the v_{eff} distribution is shifted to smaller v_{eff} in the case of specMACS. These differences could firstly arise from the fact that the two datasets are not perfectly coincident, and that the two instruments measured the clouds at slightly different places and times. Due to such temporal differences, the clouds might have evolved which could change their CDSD. Furthermore, the higher r_{eff} in specMACS data could come from a slightly incorrect height assignment. Since r_{eff} typically increases with height (see Subsection 2.3.3), it could be that the actual height of the cloud is slightly underestimated. The ATR dataset of this time range does not offer any information about the vertical profile of the CDSD which would help in interpreting the observed differences.

Stefan Koppenhofer was able to carry out similar statistical comparisons, but a thorough simultaneous comparison of individual clouds is still missing due to the unsuitable flight patterns. Other in situ measurements of the EUREC^{4}A campaign have a similar issue with not being measured at the same place as the specMACS measurements (P3 aircraft), and/or not being published yet (Twin Otter aircraft). For flight planning in future measurement campaigns, specifically designed flight patterns that allow a more direct comparison of in situ and remote sensing data could improve such comparisons.

Model-based evaluation of retrieval uncertainty

As discussed in the last section, finding good observational data for validating the cloudbow retrieval is difficult. Therefore, it was decided to conduct a model-based validation which allows a more flexible investigation of the retrieval's accuracy. The study is published in Volkmer et al. (2023), and the main points are discussed in the following. The study used the PALM model (Raasch and Schröter, 2001) to simulate a field of shallow cumulus clouds (Jakub and Volkmer, 2023). The simulation was initialized by dropsonde measurements of the EUREC^{4}A campaign of a day with typical shallow cumulus clouds (28 January 2020). In the PALM model, cloud microphysical processes are described by the bulk two-moment liquid-phase cloud microphysics scheme of Seifert and Beheng (2001, 2006). This scheme provides the cloud droplet number concentration and specific liquid water content. Since we are interested in comparing the effective radius of the droplet size distribution, r_{eff} is calculated following Martin et al. (1994) from the cloud droplet number concentration N_{d}, the liquid water content LWC, and the k-factor. The formula was already discussed in Subsection 2.3.3, but is repeated here for better readability:

$$r_{\text{eff}} = \left(\frac{3\text{LWC}}{4\pi k N_{\text{d}} \rho_w} \right)^{1/3} \tag{3.4}$$

To calculate r_{eff} from this formula, a k-factor of $k = 0.80$ was chosen, which according to Martin et al. (1994), is representative of maritime air masses. Using the 3-D radiative transfer model MYSTIC (Mayer, 2009; Emde et al., 2010, 2016), realistic radiance simulations of an overflight over the modeled cloud field were performed. For the radiative transfer simulations, the calculated r_{eff} were combined with an effective variance of $v_{\text{eff}} = 0.1$ and it was assumed that the CDSDs have gamma distribution shapes. Furthermore, realistic aerosol distributions were used (Volkmer et al., 2023). The radiative transfer simulations were tuned to replicate the measurements of the specMACS polarization cameras as much as possible. This means that each individual 4×4 pixel block of the polLR camera defined by the viewing direction and average opening angle of a pixel block was simulated. Furthermore, the effect of the spectral response functions of the specMACS cameras was considered. A comparison of a typical measurement of shallow cumulus clouds and one timestep of the simulated overflight is shown in Figure 3.27. The simulated data (panel (b)) look qualitatively very realistic. A more quantitative validation of the simulation's representativeness for actual measurements is discussed in Volkmer et al. (2023).

The study applies two algorithms to the simulated data of the overflight. First, the stereographic retrieval (Kölling et al., 2019) is performed and compared to the cloud top height of the radiative transfer simulations. Determining the cloud top height of the simulations was not a straightforward task. Since the main goal was to assess the

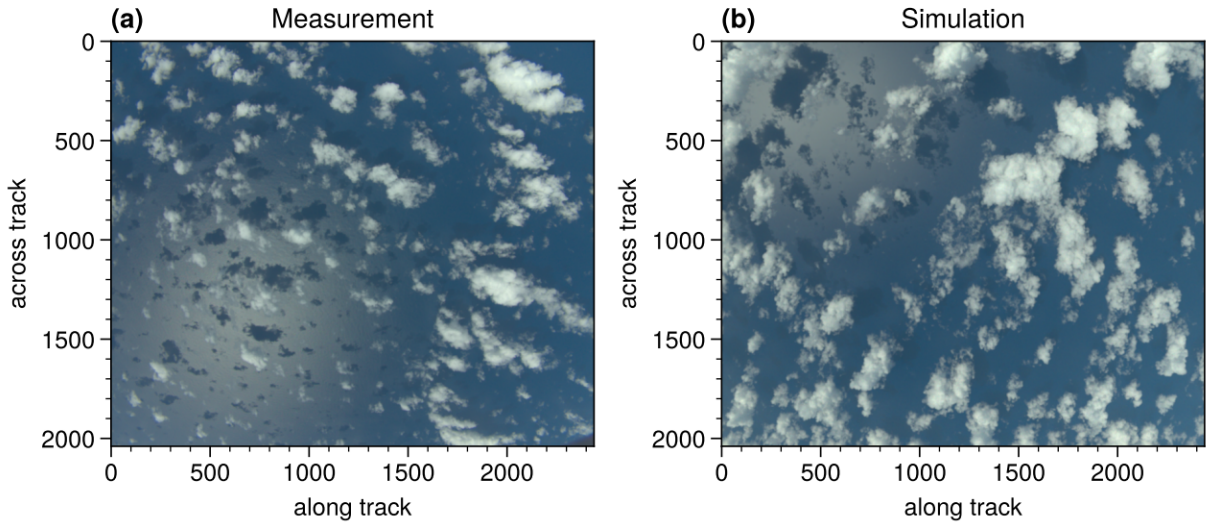

Figure 3.27: Measurement of a shallow cumulus field during EUREC^{4}A (left) and simulation of a shallow cumulus field (right). Figure from Volkmer et al. (2023) modified to only include panels (a) and (b) (CC BY 4.0 license).

uncertainty of the cloudbow retrieval relying on polarization measurements, we decided to use the height most representative of the origin of the (singly-scattered) polarization signal. For this, a second simulation was carried out, where each photon experienced only one scattering event. The height, where this scattering event happened on average, is assumed to be the cloud top height expected from the model. When comparing the model heights with the heights retrieved using the stereographic algorithm, an absolute mean difference of less than 70 m with a standard deviation of about 130 m was found. The mean bias was further reduced to 15 m (standard deviation: 133 m) by considering the background wind field (Volkmer et al., 2024).

In the second step, a comparison of the model-CDSD and the retrieved CDSD using the cloudbow algorithm was done. The data acquisition frequency of the simulated data is lower (1 Hz) than of actual specMACS measurements (8 Hz). Apart from this, the retrieval was applied to the simulations in the same way as to real measurements (see the flowchart in Figure 3.4). An intermediate step is required to compare the model input with the retrieved CDSD because the signal measured by single pixels of the detector originates from scattering events in different model grid boxes with different CDSDs. These CDSDs are superimposed to obtain a CDSD representative for the cloudbow signal of this pixel. By fitting a modified gamma distribution to the obtained CDSD, the parameters r_{eff} and v_{eff} are obtained. Finally, the cloud targets evaluated by the cloudbow retrieval have approximately a size of 10 by 10 pixels and the average polarization signal of these pixels is used for the retrieval. To account for this, the model-based r_{eff} and v_{eff} are brought to the same spatial resolution.

The model-based and retrieved r_{eff} are shown in Figure 3.28, which is taken from

Volkmer et al. (2023). Panel (a) and (b) show the spatial distribution and frequency distribution of the model-based r_{eff}. Panel (c) and (d) display the same for the r_{eff} retrieved by applying the cloudbow algorithm to the simulated data. Panel (e) shows the spatial distribution of the difference between retrieved and model-based r_{eff}, and panel (f) shows the point-wise comparison of the model input and the retrieved results. On average, a slight underestimation of the retrieved r_{eff} of approximately 0.2 µm is found with a standard deviation of 1.3 µm.

Figure 3.29 displays the same comparison for v_{eff}. The retrieved v_{eff} is mostly higher than the model-based v_{eff} and contains patches of really high v_{eff}, which are not observed in the model-based v_{eff}. The average difference is 0.02 with a standard deviation of 0.05. This deviation is probably caused by large variability in the simulated cloud data from the PALM simulations, which causes large sub-grid variability in the simulated radiance signals. This leads to a smoothing of the supernumerary bows when combining the simulations of multiple pixels into cloud targets. Since the supernumerary bows contain the information about the v_{eff}, an increase of v_{eff} for smoothed supernumerary bows is expected. Furthermore, multiple scattering also smoothes the signal, again leading to an increased v_{eff} as stated in Alexandrov et al. (2012a).

In summary, the presented model study showed a very good agreement in r_{eff}. For v_{eff}, a bias towards higher v_{eff} in the retrieval results was found but the results were still very similar to the model-v_{eff}. Although there is a small bias, the measurements of v_{eff} from polarized observations of the cloudbow are still very useful since no other method exists that allows to retrieve v_{eff} from remote sensing observations.

3.2.4 Discussion with respect to related work

The following section was published in Pörtge et al. (2023).

Similarities and differences to other retrievals

In the past, similar methods have been applied to the measurements of other instruments such as POLDER (POLarization and Directionality of the Earth's Reflectances; Bréon and Goloub, 1998; Bréon and Doutriaux-Boucher, 2005; Shang et al., 2019), RSP (Research Scanning Polarimeter; Cairns et al., 1999; Alexandrov et al., 2012a) or AirHARP (Airborne Hyper-Angular Rainbow Polarimeter; Martins et al., 2018; McBride et al., 2020). To situate specMACS in the scope of the preexisting instruments, we summarize the main features of specMACS and compare them to the technical details of the RSP and the AirHARP instruments, which are also airborne instruments. The main differences between the instruments are listed in Table 3.1 based on Alexandrov et al. (2012a) and McBride et al. (2020). The outcome of the retrieval techniques of all three instruments are angularly

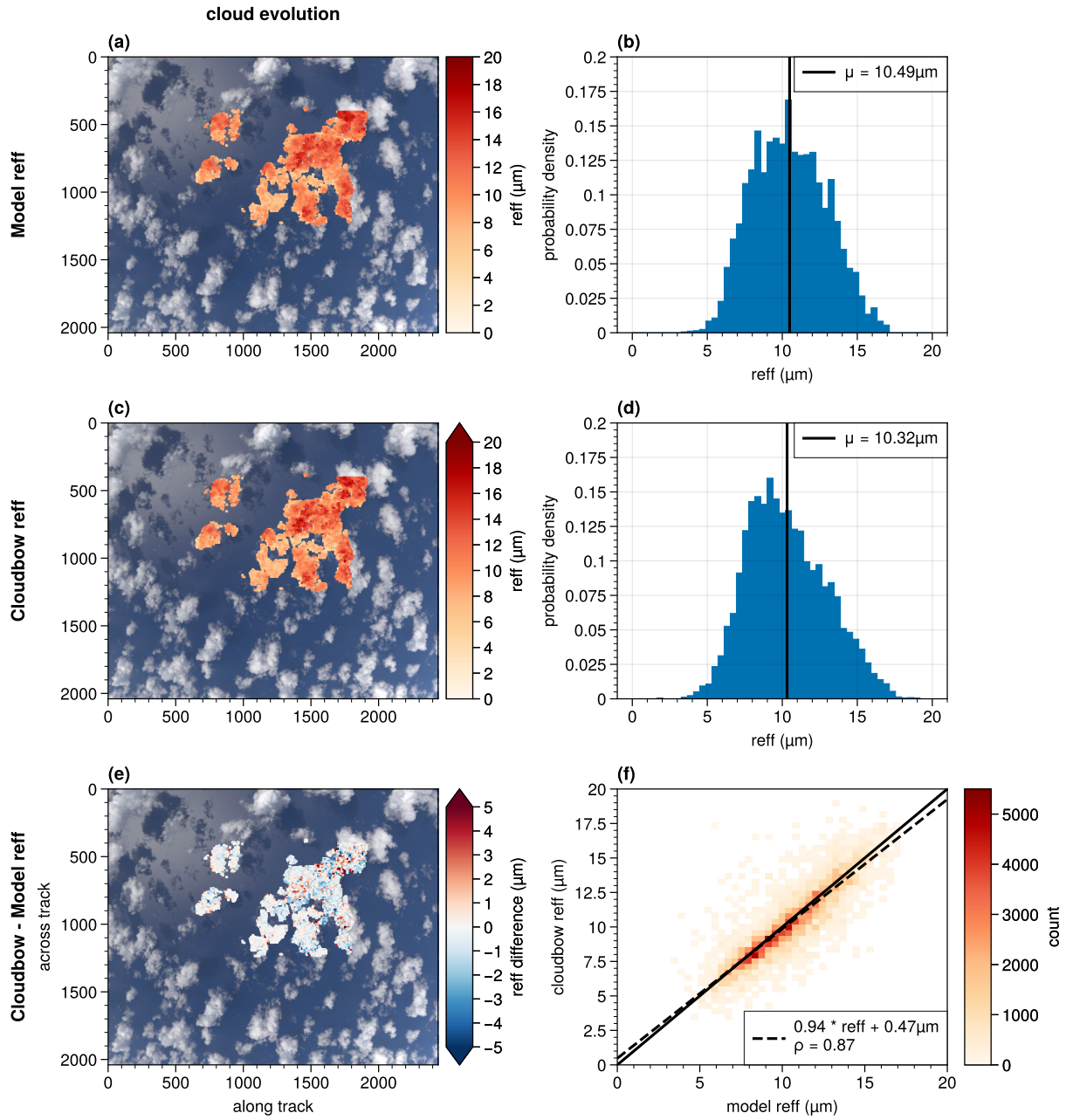

Figure 3.28: Adapted from Volkmer et al. (2023) (CC BY 4.0 license); Comparison of r_{eff} of the model (first row) with r_{eff} retrieved using the cloudbow retrieval (second row). The last row displays the point-wise differences of the two datasets.

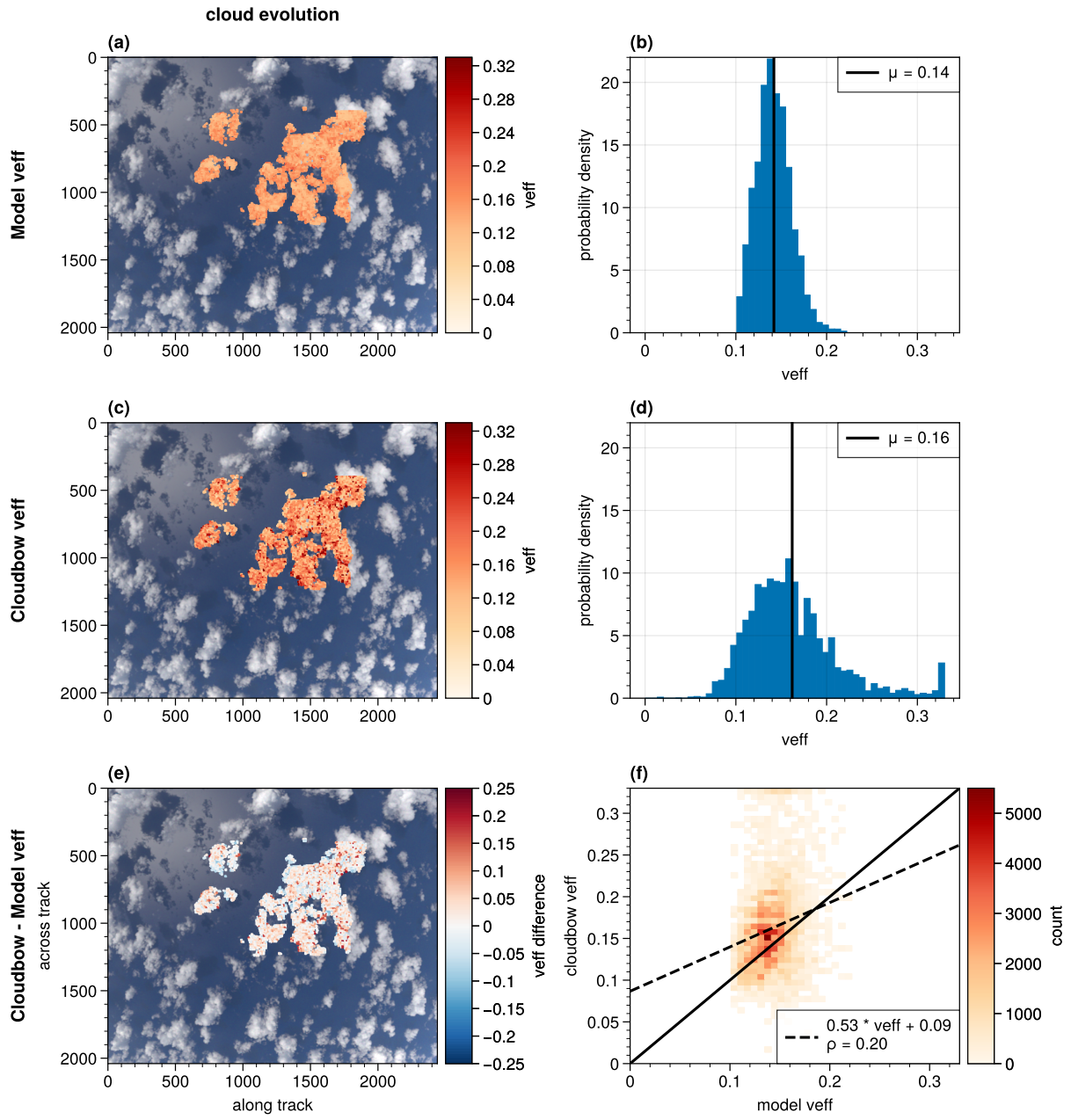

Figure 3.29: Adapted from Volkmer et al. (2023) (CC BY 4.0 license); Comparison of v_{eff} of the model (first row) with v_{eff} retrieved using the cloudbow retrieval (second row). The last row displays the point-wise differences of the two datasets.

resolved measurements of the Stokes parameters: I, Q, and U. However, the way these measurements are generated differs:

- Each observation of the specMACS instrument is a 2-D image. Individual clouds are identified in successive images from different viewing directions, and the subsequent observations are combined to generate angularly resolved cloudbow signals of each cloud. The cloudbow signals are exploited for the complete theoretical possible area concerning the flight direction.

- The AirHARP instrument is also an imaging instrument with a similar field of view to that of specMACS. There are 120 view sectors in the along-track direction, which all have a unique average viewing angle. The individual measurements of a single view sector are combined to generate a 2-D push-broom image where all pixels are observed from the same viewing direction. Targets that are observed in multiple view sectors during the overflight can be used to generate angularly resolved reflectance measurements.

- RSP is an along-track scanner with only a single pixel in the across-track direction. During each RSP scan, about 150 measurements are taken at 0.8° intervals. Data from all individual scans are aggregated into "virtual scans" which provide the full angular reflectance measurement at a single target. As already mentioned, in addition to the common parametric fit retrieval, the RSP data can also be used to retrieve the DSD from the rainbow Fourier transform (RFT) technique, which does not rely on an assumption regarding the number of modes of the DSD (Alexandrov et al., 2012b).

The major advantage of the specMACS and AirHARP instruments is their imaging capability with a large field of view. This not only increases the information content of the data but also makes it easier to measure the cloudbow because the cloudbow is observed within the field of view of the cameras for a large range of solar zenith angles. specMACS enables an even more detailed representation of the spatial distribution of the DSD, due to the higher spatial resolution (100 m) compared with AirHARP (200 m). RSP has the highest number of spectral channels (nine), including SWIR channels and can, therefore, simultaneously retrieve the r_{eff} based on the bispectral technique without any alignment errors. specMACS also offers the possibility for a bispectral retrieval because of its additional two spectrometers, but these have a smaller field of view compared with the polarization cameras. Furthermore, RSP and AirHARP have narrower spectral channels compared with specMACS, which sharpens the cloudbow signal and improves the sensitivity of the retrieval, especially for large droplets. However, the specMACS measurements have the highest angular resolution.

Table 3.1: Technical details of specMACS, AirHARP (McBride et al., 2020), and RSP (Alexandrov et al., 2012a).

	specMACS	AirHARP	RSP
Field of view	Maximum: $\pm 45^\circ \times \pm 59^\circ$	$\pm 57^\circ \times \pm 47^\circ$	$\pm 60^\circ$ (along-track only)
Spectral channels	Three color channels (468, 546, and 620 nm)	Four narrow spectral channels (440, 550, 670, and 870 nm)	Nine narrow spectral channels (410, 470, 555, 670, 865, 960, 1590, 1880, and 2260 nm)
Angular resolution	Binned to 0.3°	2° for 670 nm channel, 6° for all other channels	0.8°
Typical resolution of retrieval results (depends on distance to cloud)	Approximately 100 m × 100 m	200 m × 200 m	120 m in Fu et al. (2022)

Literature review on validation studies

The retrieval technique has already been validated in several studies. Alexandrov et al. (2018) compared in situ data to r_{eff} and v_{eff} results from the parametric fit of RSP measurements and found a good agreement of better than 1 µm for r_{eff} and, in most cases, better than 0.02 for v_{eff}. Painemal et al. (2021) compared the r_{eff} and optical thickness of airborne data (polarimetric and bispectral retrieval based on RSP measurements and in situ measurements from the cloud droplet probe) with satellite retrievals (MODIS and the ABI instrument of the GOES-13 satellite) over the midlatitude North Atlantic. The comparison showed good correlations for the r_{eff}; however, the satellite-based results were systematically higher than the aircraft measurements, and the bias was larger for GOES-13 (5.3 µm) than for MODIS (2.6 µm).

Recently, another comparison study was published by Fu et al. (2022) in which data collected during the Cloud, Aerosol and Monsoon Processes Philippines Experiment (CAMP2Ex) in 2019 were analyzed. One goal of the field campaign was to comprehensively compare r_{eff} retrievals of cumulus clouds from different platforms (MODIS, RSP, and in situ). As mentioned, RSP data can provide a bispectral and a polarimetric r_{eff} from the same cloud target because of the spectral coverage from the visible to shortwave-infrared, and the along-track, co-located, multi-angle sampling. The study evaluated the r_{eff} statistics of all research flight segments of the campaign that were suited for a co-location of the different instruments and platforms, and showed that the

median r_{eff} from the polarimetric RSP retrieval (9.6 µm), from the in situ data (11.0 µm) and from the bias-adjusted MODIS (Fu et al., 2019) (10.4 µm) are in good agreement but are much smaller than the bispectral median r_{eff} from MODIS (17.2 µm) and RSP (15.1 µm). For shallow clouds, these differences are primarily caused by 3-D radiative transfer and cloud heterogeneity. There are several other studies, such as Bréon and Doutriaux-Boucher (2005), Di Noia et al. (2019), and Alexandrov et al. (2015), that have compared the r_{eff} obtained from polarized measurements with bispectral results, and these publications reported similar biases. The differences could largely be attributed to the different penetration depths of the shortwave-infrared band compared with the polarized signal, to differences in retrieval resolution, and to 3-D radiative transfer effects.

3.3 Retrieval of cloud optical depth

So far, the polarimetric cloudbow retrieval was presented which determines the CDSD from the specMACS measurements. To further retrieve information about the cloud optical depth, a modified version of the bispectral technique of Nakajima and King (1990) is used. The traditional bispectral technique simultaneously retrieves r_{eff} and τ_c from reflectance measurements in the visible and near-infrared (NIR) spectral range, and was already mentioned in the introduction of this work (Section 1.1). In the following, a slightly modified implementation of this method is introduced. Instead of using a NIR channel measurement, the effective radius is provided by the cloudbow retrieval described above (Section 3.2). The total visible reflectance measurement of the polarization camera is then used as additional information to retrieve the cloud optical thickness.

A lookup table of reflectance measurements for clouds with different cloud optical depths and effective radii was computed. The algorithm was provided by Dennys Erdtmann (personal communication, 2023) following the approach in Erdtmann (2023) adapted for liquid water clouds. For the EUREC^{4}A measurements, a horizontally uniform atmosphere with a cloud between 1 km to 2 km was simulated using the DIScrete ORdinate Radiative Transfer solvers (DISORT) (Stamnes et al., 1988) part of the libRadtran software package (Mayer and Kylling, 2005). Further details on the generation of the lookup table are given in Erdtmann (2023). The simulated reflectances are weighted with the spectral response functions (Figure 3.1) of the three channels of the polarization cameras to replicate the measurement. The reflectance measurement is then combined with r_{eff} retrieved from the cloudbow algorithm to determine τ_c from the lookup table. This method is prone to uncertainties from 3-D radiative transfer effects, as the lookup table does not take into account the 3-D geometry of the clouds. This is an inherent limitation of this widely-used method, and leads to retrieval inaccuracies, especially for large solar zenith angles.

As a rough validation of the retrieved τ_c, a comparison with τ_c from MODIS measurements on 5 February 2020 is shown in Figure 3.30. On this day, the HALO flight pattern

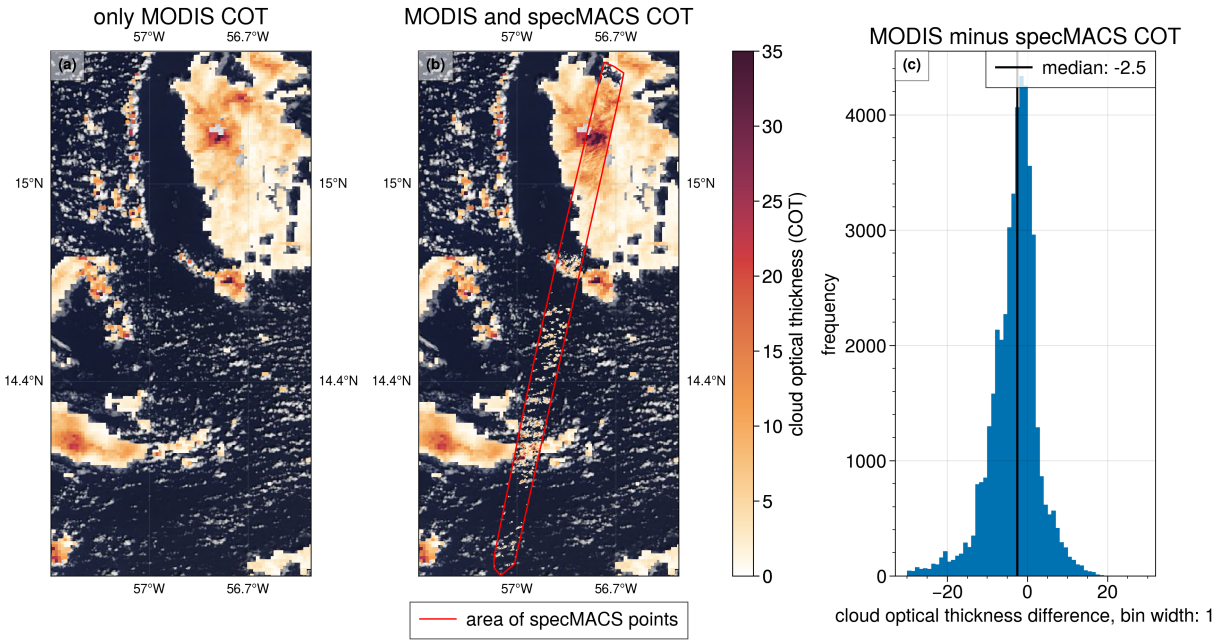

Figure 3.30: Cloud optical thickness τ_c from MODIS (panel (a)), from MODIS with overlaid specMACS results (panel (b)) and the difference in panel (c) on 5 February 2020.

was specifically designed to include this coordinated underflight under MODIS. Panel (a) shows a map of τ_c from the MODIS instrument onboard Terra, and in panel (b) the specMACS τ_c is plotted on top. For better visibility, the area containing the specMACS measurements is marked with a red line. Comparing the panels (a) and (b) highlights the fact that specMACS has a much higher resolution than MODIS. There are many small clouds located in the center of the figure, for which MODIS cannot retrieve an optical thickness. However, for the large cloud in the North of the map, the specMACS τ_c agrees with the MODIS τ_c, and the transition from smaller τ_c to larger values in the center of the cloud looks similar. However, the area of maximum τ_c is larger in specMACS compared to MODIS.

For a pointwise comparison, the MODIS data were interpolated onto the specMACS points. Of course, only the overlapping points remain, which are mostly found in the large cloud in the North of the scene. The difference between specMACS and MODIS for these points is plotted as a frequency distribution in panel (c) in Figure 3.30. In general, the distribution is slightly shifted towards negative values meaning that the MODIS τ_c is mostly smaller compared to the specMACS τ_c. The spatial resolution of MODIS is 1 km and the specMACS τ_c have a resolution of approximately 100 m. The relationship between the measured reflectance and τ_c is nonlinear. This has the effect that if subpixel variation is ignored such as in the MODIS measurements, the τ_c will be underestimated compared to the true pixel averaged values (Marshak et al., 2006). The same applies to the retrieved r_{eff} from the bispectral retrieval. Therefore, it is reasonable that the median

difference of the histogram in Figure 3.30 is negative. Overall, this comparison shows that specMACS and MODIS retrieve relatively similar cloud optical thickness values. With this additional information about the cloud optical thickness, it is now possible to also retrieve the droplet number concentration which is shown in the next subsection.

3.4 Retrieval of droplet number concentration and adiabaticity

The derivation of the droplet number concentration based on the adiabatic cloud model has already been theoretically introduced in Subsection 2.3.3. With the assumption of N_d being constant with height and LWC and r_eff increasing with height according to the adiabatic model, the Equation 2.38 was derived and is repeated here for better readability:

$$N_\mathrm{d} = \frac{\sqrt{5}}{2\pi k}\left(\frac{f_\mathrm{ad} C_\mathrm{w} \tau_\mathrm{c}}{Q_\mathrm{ext}\rho_w r_\mathrm{eff}^5}\right)^{1/2} \tag{3.5}$$

This formula is highly dependent on the effective radius of the size distribution. For most satellite applications, r_eff is usually determined from bispectral retrievals, which, as explained earlier, are subject to large uncertainties in r_eff. Besides r_eff, the parameter τ_c is also determined from the bispectral retrieval. The k-factor, which determines the relationship between r_eff and r_v (Equation 2.18), is in satellite applications typically assumed to be constant or only dependent on the cloud type (marine or continental), as it is not retrieved from the bispectral retrieval. Often, the k-factors found in the study by Martin et al. (1994) are used. C_w is only a weak function of temperature and pressure, and therefore often assumed to be constant (Grosvenor et al., 2018b). Furthermore, the adiabaticity f_ad, which describes the ratio between the actual LWC and the adiabatic LWC, is assumed to be constant. But f_ad can also be defined in terms of r_eff, τ_c, C_w, and the distance to the cloud base $(z - z_\mathrm{base})$ by combining the three Equations 2.23, 2.34, and 2.38:

$$f_\mathrm{ad} = \frac{20}{9}\frac{\rho_w \tau_\mathrm{c} r_\mathrm{eff}}{Q_\mathrm{ext} C_\mathrm{w} (z - z_\mathrm{base})^2} \tag{3.6}$$

The detailed derivation of this formula is shown in Appendix B. By inserting Equation 3.6 into Equation 3.5 the following formula is derived:

$$N_\mathrm{d} = \frac{5}{3}\frac{\tau_\mathrm{c}}{\pi k Q_\mathrm{ext} r_\mathrm{eff}^2 (z - z_\mathrm{base})} \tag{3.7}$$

This is in accordance with the formula presented in Sinclair et al. (2019) if a modified gamma distribution is assumed for the shape of the CDSD. Sinclair et al. (2019) directly retrieve the shape of the CDSD and do not have to make this assumption. They further apply the formula to RSP measurements, which shows good agreement of N_d with in situ measurements over large spatial and temporal domains. A similar f_{ad} formulation derived from the definition of the LWP is presented in Merk et al. (2016), and applied to ground based data. They estimate the uncertainty of the f_{ad} retrieval with a maximum range of $f_{ad} = 0.54$ to 1.89 for an adiabatic cloud with true $f_{ad} = 1$. Overall, they conclude that f_{ad} cannot be obtained with sufficient accuracy neither from ground-based, nor from passive satellite observations using this method, and that an independent method is desired.

In the results chapter of this thesis, N_d will be determined from Equation 3.5. For this, k is calculated from v_{eff} following Equation 2.21. r_{eff} is retrieved from the cloudbow retrieval and τ_c is determined from the modified bispectral retrieval as described in Section 3.3. C_w is calculated from Equation 2.33 with additional information about the cloud base height determined from dropsonde measurements (Equation 2.27). The adiabaticity f_{ad} is either held constant or determined from Equation 3.6.

3.4.1 Error estimation of droplet number concentration retrieval

An estimate of the error budget of the presented N_d retrieval was made in Grosvenor et al. (2018b) and presented in their Figure 8. As this assessment is particularly interesting, the information from this figure is repeated in Figure 3.31a in this section. Grosvenor et al. (2018b) investigated the uncertainty of N_d determined from satellite retrievals with typical spatial resolutions of 1 km using Gaussian error propagation. The error budget is

$$|\Delta N_d|^2 = |\tfrac{1}{2}\Delta C_w|^2 + |\tfrac{1}{2}\Delta f_{ad}|^2 + |\tfrac{1}{2}\Delta \tau_c|^2 + |\Delta k|^2 + |\tfrac{5}{2}\Delta r_{eff}|^2 + |\Delta VS|^2 \quad (3.8)$$

The estimated percentage errors ($\Delta C_w, \Delta f_{ad}, \Delta \tau_c, ...$) of each component are shown in the textbox of Fig. 3.31a and the reader is referred to Grosvenor et al. (2018b) for a detailed description of how these percentage errors were estimated. Here, only the estimated percentage error of $\Delta r_{eff} = 27\,\%$ is mentioned. This error consists of a 17 % uncertainty due to cloud heterogeneity which arises because bispectral retrievals usually assume that each cloud pixel is horizontally homogeneous, and neglect subpixel variability of the cloud. In addition, bispectral retrievals also ignore resolved cloud heterogeneities or 3-D radiative effects such as shadows. Besides the 17 % error from cloud heterogeneity, Grosvenor et al. (2018b) assume a 10 % uncertainty in r_{eff} due to instrument uncertainty. From their error budget assessment (Equation 3.8), they find an overall error of $\Delta N_d = 78\,\%$.

The contributions of each term on the right-hand side of Equation 3.8 to the overall error in N_d are calculated, and shown as bars in Fig. 3.31a. The r_{eff} contribution is for

example $|\frac{5}{2}\Delta r_{\text{eff}}|^2/|\Delta N_{\text{d}}|^2 = 76\,\%$. The individual contributions add up to 100 %. By far the largest contribution to the overall error comes from errors in r_{eff}. The second largest contribution is the vertical stratification (VS). The vertical stratification describes the problem that N_{d} retrievals usually assume a cloud following sub-adiabatic growth where r_{eff} and LWC increase with height, while operational r_{eff} and τ_{c} retrievals assume constant values of τ_{c} and r_{eff} for homogeneous cloud layers. There are bispectral retrievals that take into account the adiabatic growth within the cloud (e.g. Brenguier et al., 2000; Schüller et al., 2005), but these retrievals are not operational. Nevertheless, such retrievals could be a way to reduce the uncertainty caused by the vertical stratification assumption. The contributions found in Grosvenor et al. (2018b) from uncertainties in k, f_{ad}, C_{w} and τ_{c} are all $< 5\,\%$. Grosvenor et al. (2018b) conclude that: "Therefore, improvements in r_{eff} uncertainty characterization are the most beneficial in terms of improving N_{d} accuracy."

This is exactly the strength of the specMACS r_{eff} retrieval. From the comparison with observational data (Section 3.2.3) and the model-based evaluation (Section 3.2.3), it was concluded that the r_{eff} derived from specMACS measurements has a much smaller error than what is assumed in Grosvenor et al. (2018b). A reasonable value for the r_{eff} error from polarimetric retrievals is 10 %. Furthermore, the error associated with vertical stratification is reduced if the retrieved r_{eff} is representative of the cloud top, which is the case if it is retrieved from polarimetric observations. In the current setup, the optical thickness is determined from a LUT approach based on simulations of vertically homogeneous clouds which are combined with the r_{eff} retrieved using the cloudbow retrieval. The found r_{eff} is therefore representative of the r_{eff} at the cloud top, but for generating the LUT, it is assumed that the clouds are vertically homogeneous. Therefore, the uncertainty of the vertical stratification might still play a role in our setup although being substantially reduced compared to common bispectral retrievals. In addition, the polarimetric technique is beneficial in terms of the k-factor because the method also determines v_{eff}, from which k can be estimated assuming a modified gamma distribution. This has the potential to further reduce the associated uncertainty in the N_{d} retrieval but k has only a minor influence on the overall N_{d} error. When assuming a percentage error of $\Delta r_{\text{eff}} = 10\,\%$ and all other errors as in Grosvenor et al. (2018b), the overall N_{d} uncertainty is strongly reduced from 78 % to 46 %. The resulting individual error contributions are shown in Figure 3.31b. To illustrate the effect of an additional reduction of vertical stratification uncertainty the error budget contributions are again plotted in panel (c) but this time both the r_{eff} error and the VS error are reduced to 10 %. With this, the overall N_{d} error reduces to 36 %. If all errors are zero except for the r_{eff} percentage uncertainty which is assumed to be 10 %, the overall N_{d} error is 25 %. This illustrates that the retrieved N_{d} is strongly influenced by errors in r_{eff}.

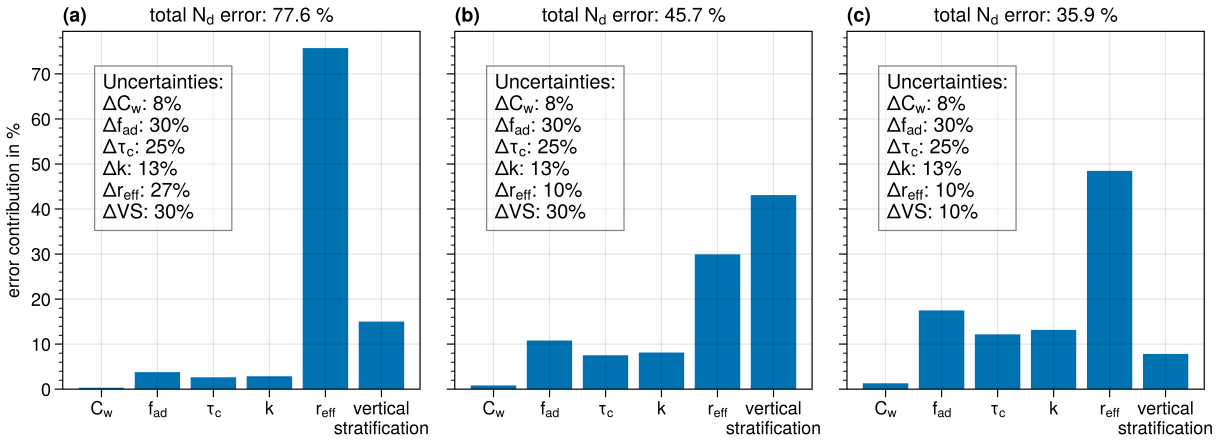

Figure 3.31: Error contribution of the individual parameters that determine N_d. Own illustration based on Grosvenor et al. (2018b) (CC BY 4.0 license). The assumed uncertainty estimates are given in the textboxes. "VS" refers to the vertical stratification uncertainty. Panel (a) shows the same information as in Figure 6 in Grosvenor et al. (2018b) on the left side. In panel (b), the assumed r_{eff} uncertainty is reduced. In panel (c), the assumed errors in r_{eff} and the vertical stratification are reduced.

3.4.2 Comparison with in situ measurements

A first validation of the retrieved N_d using specMACS data is shown in Fig. 3.32. Here, the hourly averaged in situ measurements from the ATR aircraft (Coutris, 2021) of the entire EUREC^{4}A field campaign are compared with the corresponding hourly averaged N_d retrieved from the specMACS data. Please note that although the in situ instruments measured in a similar region as the specMACS instrument, the two datasets are not exactly spatially coincident. Furthermore, the in situ data were mostly measured at the cloud base, whereas the specMACS r_{eff} and v_{eff} retrievals are representative of the situation at the cloud top. Although it is generally assumed that N_d is constant with height and that it does not substantially vary on large spatial scales, these two points could partly explain differences between the two datasets.

The assumed f_{ad} of the specMACS N_d retrieval is varied in the panels (a) and (b) of Fig. 3.32. The specMACS N_d is mostly higher than the in situ N_d for $f_{ad} = 1$ (panel (a)) and the points are closer to the line indicating perfect agreement for $f_{ad} = 0.4$ (panel (b)). The optimal f_{ad} for which $N_{d,\,\text{specMACS}} = N_{d,\,\text{in situ}}$ can be calculated for each data point. The distribution of this optimal f_{ad} is shown in panel (c) and has a median value of $f_{ad} = 0.41$. The Pearson correlation coefficient between the in situ data and the specMACS dataset is 0.61 for a constant f_{ad}, indicating a moderate positive correlation. This shows that, depending on the choice of f_{ad}, the derived number concentrations from specMACS are representative of corresponding in situ measurements. However, a detailed investigation based on case studies is still pending, owing to the poor spatial agreement of the in situ and specMACS measurements. The presented data will be

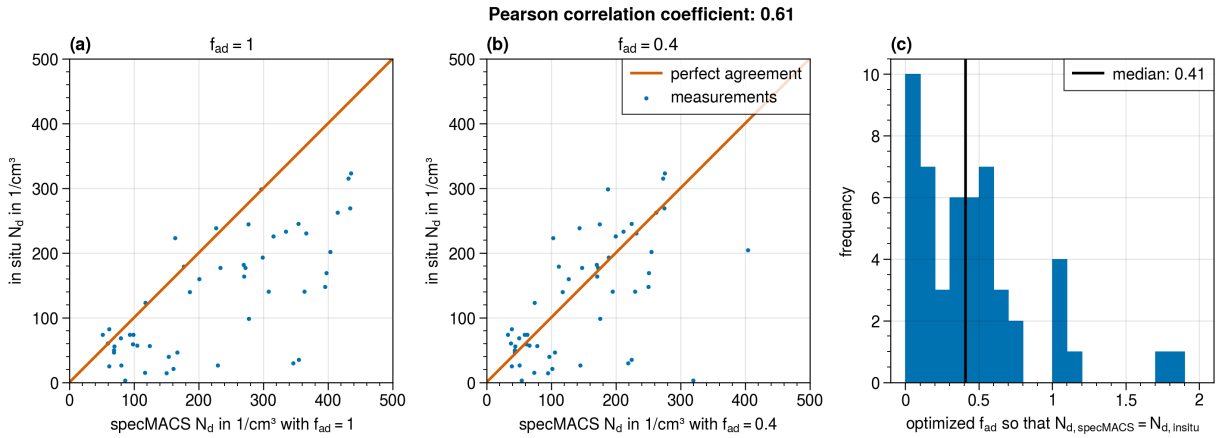

Figure 3.32: Comparison of hourly averaged N_d measured with in situ instruments onboard ATR-42 (y-axis) and hourly averaged N_d retrieved from specMACS (x-axis). Panel (a): $f_{ad} = 1.0$; Panel (b): $f_{ad} = 0.4$; Panel (c): optimized f_{ad} for which $N_{d,\,specMACS} = N_{d,\,in\,situ}$.

further analyzed as a time series in Section 4.1.2. In Section 4.3.2, the droplet number concentrations of a field of shallow cumulus clouds are analyzed with respect to the adiabaticity of the clouds.

3.5 Separation into cloud edge and cloud center

The boundary of the cloud is an interesting region, since here, entrainment and mixing of ambient dry air into the cloud take place which might affect the droplet size distribution (see Section 2.3.4). In the following, a method that was developed for specMACS measurements is presented, which separates points that belong to the edge of a cloud from points that are from the center of the cloud. This separation will be applied to the specMACS measurements in Chapter 4.3 to study the difference between the droplet size distributions of central parts of the cloud and the edge.

First of all, note that we are not looking at the 3-D center volume of a cloud, which will be called "cloud core" in the following, but rather at the horizontal center and edge of the cloud when looking at the cloud from above. For separating the points into edge and center, the following steps are carried out, which are illustrated in Figure 3.33. First, the individual points are grouped into points that belong to the same cloud. This is done by the DBSCAN clustering algorithm which is implemented in the 'sklearn.cluster' Python package.[3] In our algorithm, a point is defined to be in the neighborhood of another point, if the distance between the two points is less than 150 m, and a cluster consists of at least three individual points. The algorithm then groups the points based on these input parameters. This is shown in panel (b) where pixels that belong to the

[3] `https://scikit-learn.org/stable/modules/clustering.html` (accessed on 19-03-2024)

same cloud have the same color.

As a second step, the horizontal edge that encloses the individual points of a cloud is determined. For this, the alphashape algorithm is used which finds a concave hull of a set of 2-D or 3-D points based on the parameter α (Akkiraju et al., 1995). The definition of α is that for any two edge members of a set of points, an edge of a disk of radius $1/\alpha$ can be drawn and the disk still contains all points. The convex hull of a set of points is an alphashape with $\alpha = 0$. Again, the Python implementation is utilized.[4] The next step is to calculate the perpendicular distance of each point to the edge defined by the concave hull found. Additionally, the cloud diameter is estimated by the distance between the points on the concave hull that are furthest apart. The boundaries of the clouds which are found via the alphashape algorithm are shown as white lines in Figure 3.33c together with the minimum distance of each point to the corresponding boundary.

As a last step, the points are separated into center and edge points. The separation criterion identifies edge points as points with a maximum horizontal distance of 40 m from the edge. For center points, the center of mass of all points of one cluster and the distance of each point to the center of mass are calculated. Center points are then defined as points where the ratio of the distance to center to the cloud diameter is less than 0.15. Moreover, a point cannot be classified as both center and edge. The final classification into center (yellow) and edge (black) points is shown in panel (d) of Figure 3.33. The purple points are neither center nor edge. These separation criteria and thresholds were determined empirically. Especially the criterion of the center points is only a good approximation in the case of relatively circular clouds. For instance, consider an elongated cloud primarily extending in the x-direction. In such cases, points near the center of mass along the x-axis could be close to the cloud's edge in the y-direction while still meeting the center criterion (ratio of distance to the center of mass relative to the cloud's diameter being less than 0.15).

For most points, the separation looks reasonable. Nevertheless, there are some points that are identified as center points although they are located at the edge of the cloud. This has two causes. First, it can happen that the initial clustering (panel (b)) is too large. For example, the large cloud formation in the center of the image could be split up into several single clouds. Furthermore, in some cases, the concave hull found by the alphashape algorithm is not strict enough and too close to the convex hull of the points. This also appears for the large cloud in the middle. In addition, the CDSD dataset has a maximum swath of approximately 8 km, and therefore, points at the edge of the swath are identified as edge points although they might be located in the center of a cloud which is cut off.

One further aspect of this approach of separating points into center and edge points based on the 2-D view on the clouds should be discussed. The polarization signal originates from the cloud top, specifically within an optical depth of 1 within the cloud.

[4] `https://pypi.org/project/alphashape/` (accessed on 19-03-2024)

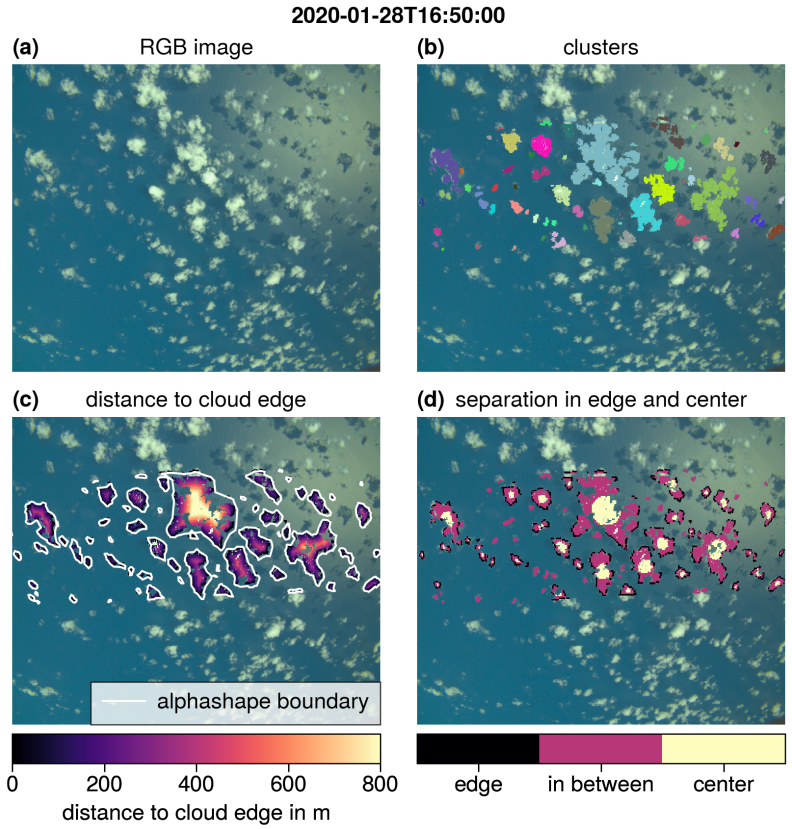

Figure 3.33: Example of classification of points into center and edge points. Panel (a): RGB image; panel (b): pixels of the CDSD dataset are grouped into clouds; panel (c): the boundary of each cloud is shown in white and the minimum distance of each point to the boundary is color coded; panel (d): final separation into edge and center points.

Consequently, both the edge points and center points are close to the vertical/upper boundary of the cloud, and therefore, likely to be affected by entrainment and mixing. Nevertheless, the center points are expected to be less influenced by entrainment due to the circulation inside a cloud which is characterized by a strong updraft region in the core of the cloud. When categorizing the specMACS CDSD into center and edge points as discussed, it is expected that droplets that belong to center points, have experienced this updraft in the cloud. Therefore, these points should be more representative of the conditions inside the core of the cloud (Eytan et al., 2021; Lim and Hoffmann, 2023a). CDSDs of edge points experienced more entrainment and mixing during their lifetime. This process is further studied in Chapter 4.3.

Chapter 4

Results

In the following chapter, the scientific results of the CDSD analysis of the EUREC^{4}A campaign are discussed. First, an overview of the CDSDs from the whole EUREC^{4}A campaign is given (Section 4.1). The r_{eff} and v_{eff} are analyzed in terms of vertical profiles where the retrieved CDSD collected over a whole day are plotted against the corresponding altitude similar to Rosenfeld and Lensky (1998). Of course, these vertical profiles do not represent the actual vertical profile inside a cloud. It is assumed, that clouds at different stages of their development are observed in the specMACS measurements, and that these individual observations are representative of the actual CDSD inside a typical cloud. This is only valid in the case of non-precipitating clouds. Furthermore, an overview of the estimated droplet number concentration is presented and compared with in situ measurements. In Section 4.2, variations of the observed CDSDs with the predominant mesoscale cloud pattern are observed. For this analysis, the specMACS data are coupled with a classification dataset from Schulz (2022a). The case study of 2 February 2020 is studied in more detail. On this day, a so-called flower cloud system was observed, which is connected to precipitation with specMACS consistently observing large r_{eff}. The specMACS results are also discussed with regard to the recently published study by Cui et al. (2023), where the same measurement day was evaluated from the satellite perspective. In the last section (Section 4.3), the high spatial resolution CDSDs of specMACS are evaluated in terms of entrainment and mixing in which r_{eff}, v_{eff}, and N_{d} of points from the center of the cloud are compared to the retrieval results from edge points. In addition, the adiabaticity is derived and its vertical variation is analyzed. The presented cloud droplet size distribution dataset is published in Pörtge et al. (2023).

4.1 EUREC^{4}A campaign overview results

To begin with, an overview of the specMACS observations during the EUREC^{4}A campaign is given. Figure 4.1 shows snapshots of the measurement domain from GOES-16 ABI satellite images. The snapshots correspond to a time in the middle of the HALO

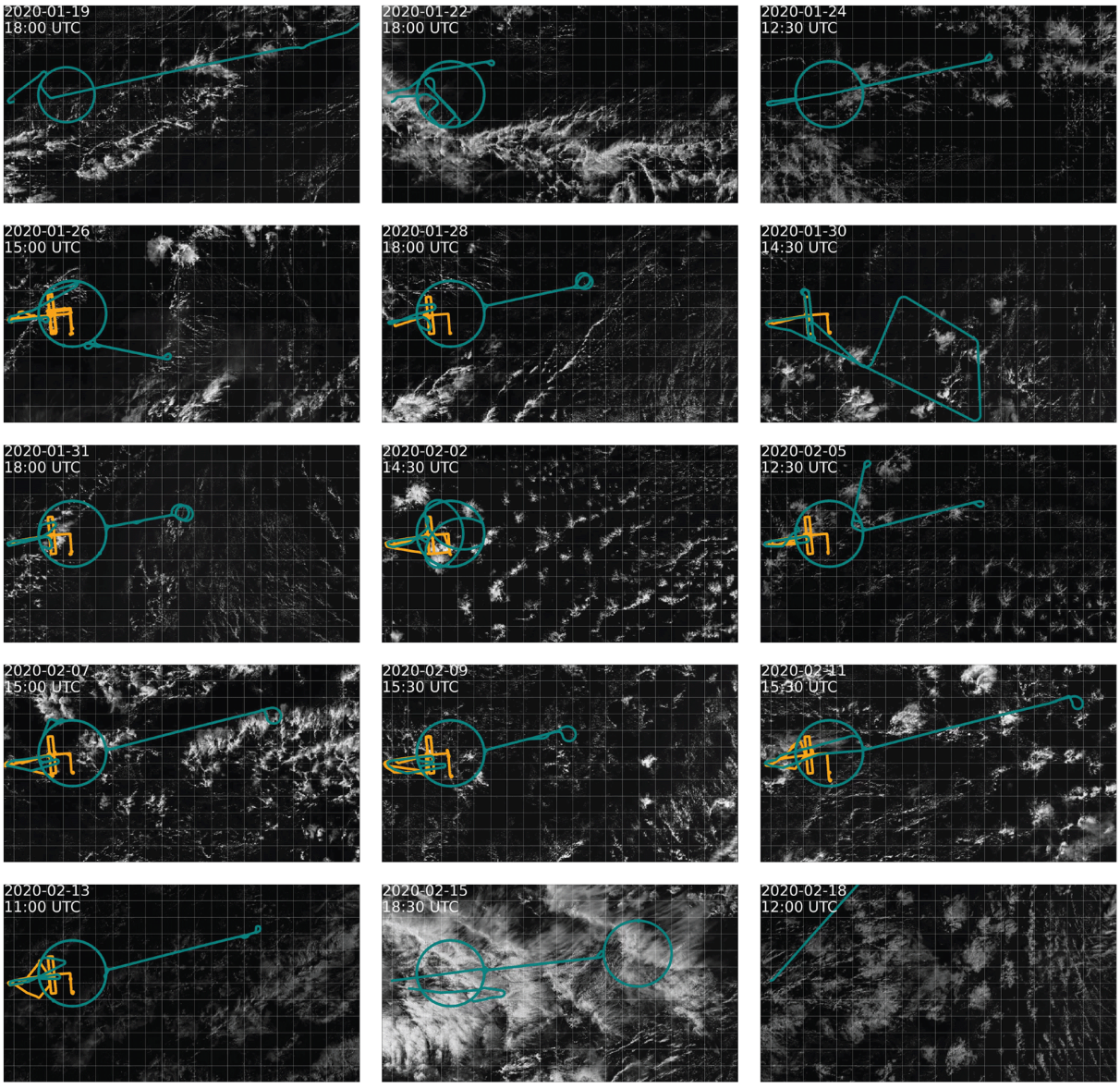

Figure 4.1: Reproduced from Konow et al. (2021) (CC BY 4.0 license). Snapshots of GOES satellite observations with HALO (teal blue) and ATR (orange) flight tracks for all HALO flight days during EUREC^{4}A.

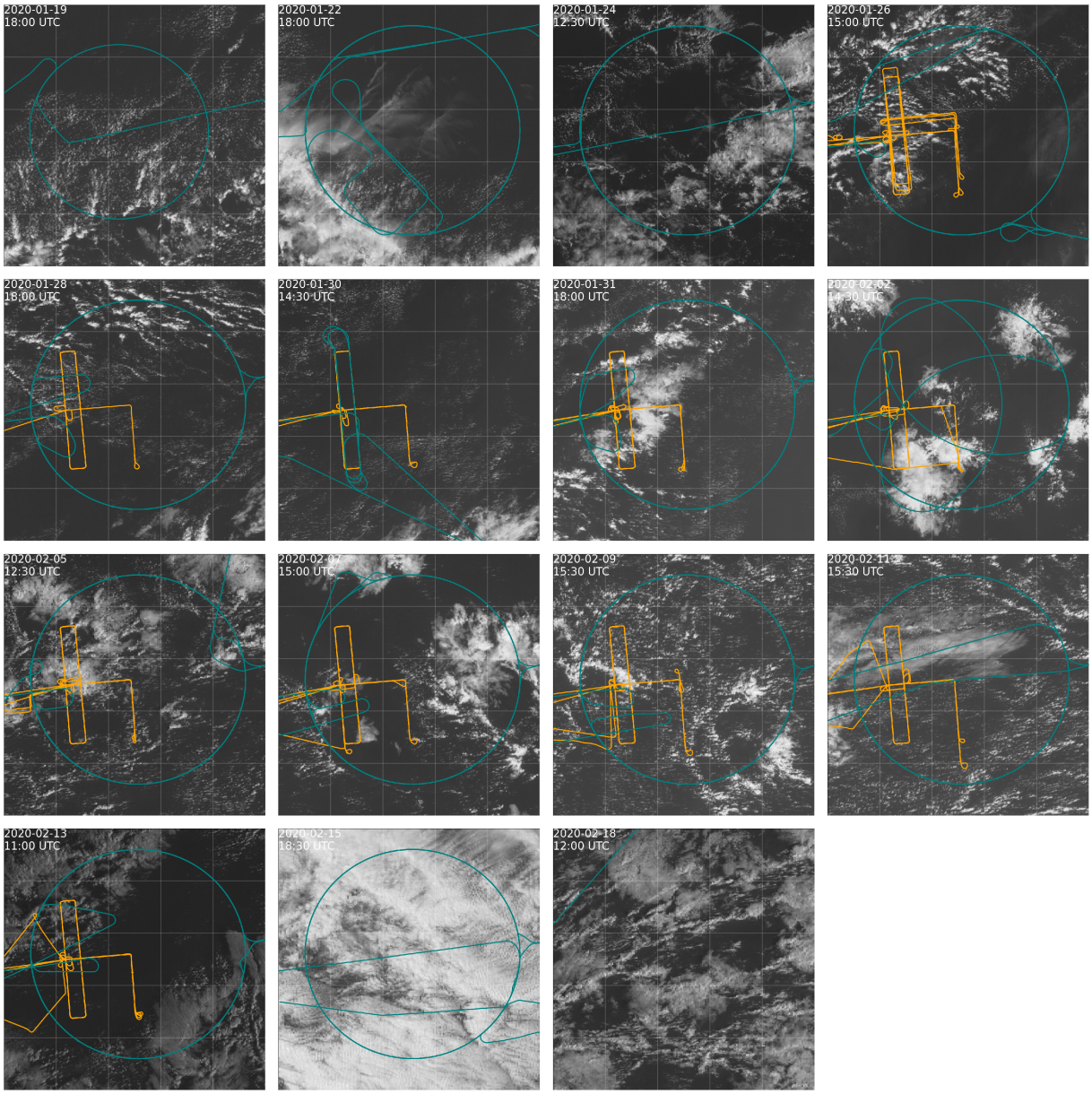

Figure 4.2: Snapshots of GOES-16 ABI (channel 2 at 0.64 µm) satellite observations with HALO (teal blue) and ATR (orange) flight tracks for all HALO flight days during EUREC^{4}A as in Figure 4.1 but zoomed into the region of the HALO circle. The plot was generated using `https://github.com/bfildier/EUREC4A_movies` with slight modifications concerning the brightness of the images. Please note that all subplots show the same area, but the circle flown on 19 January was smaller compared with all other circles.

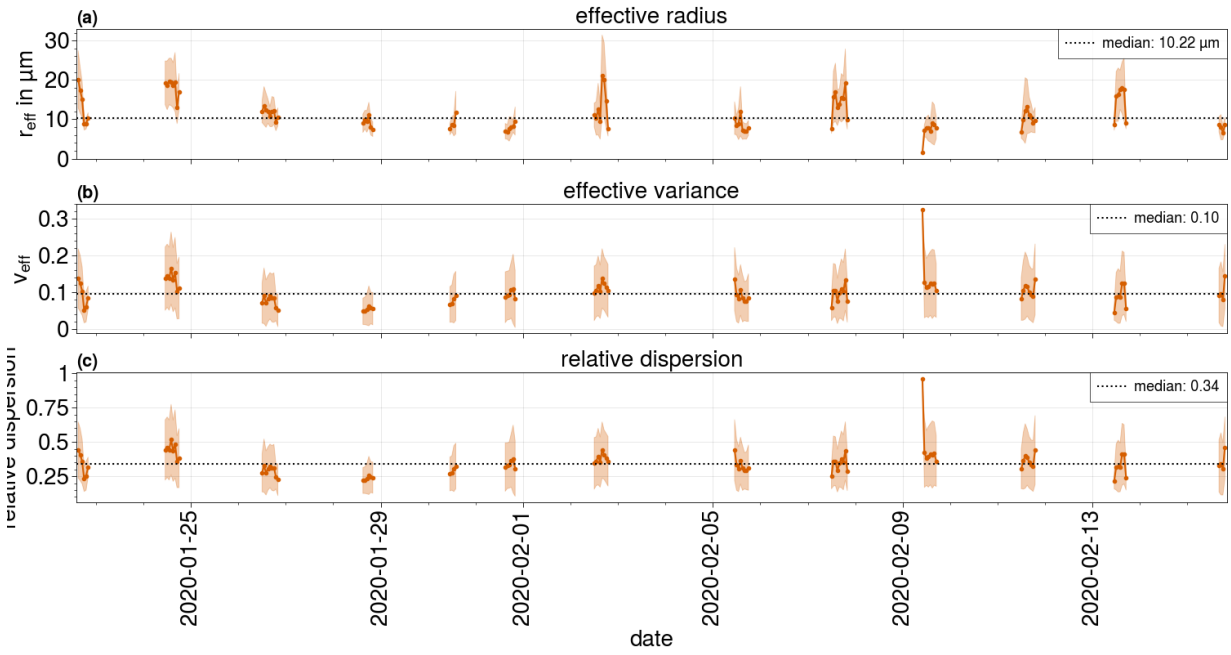

Figure 4.3: r_{eff} (a), v_{eff} (b) and corresponding relative dispersion (c) shown as hourly averaged time series of retrievals of polLR camera. The median values of the hourly averages are indicated as dashed line.

flight of each measurement day. The tracks of the HALO and ATR aircraft are indicated in teal blue and orange respectively. Many different cloud types occurred during the campaign in the measurement area. Some days were mainly characterized by small cumulus clouds (e.g. 26 January or 13 February) while on others, more clustered cloud systems (e.g. 2 February) or an almost continuous cloud cover was present (15 February). Furthermore, also the concentration of ambient aerosol changed during the campaign. It is worth mentioning, that there was a strong Saharan dust event from 30 January to 2 February (Gutleben et al., 2022; Chazette et al., 2022) which could have had a modulating effect on the observed CDSDs. In the following, the retrieval results from the 15 February are often excluded from the analysis. On this day, the HALO airplane frequently changed its flight altitude to also fly below the highest cloud level, and in such cases, the cloudbow cannot be analyzed, and it was decided to not analyze this measurement day in as much detail as the other days. In addition, the transfer flights to and from Barbados were not processed.

4.1.1 Cloud droplet size distribution

Figure 4.3 shows time series of r_{eff} (top), v_{eff} (middle) and corresponding relative dispersion (bottom) (Equation 2.22) of the whole EUREC^{4}A campaign. For this plot, the whole CDSD dataset of the polLR camera was resampled to hourly values. These are shown as orange dots which are connected by a line. The shaded regions around this line indicate

the standard deviation of the values within the hourly window. The campaign median values are shown as dashed lines. On most days the measured r_{eff} was below 15 µm which is often seen as a threshold for the start of precipitation formation. Still, on certain days (22 January, 24 January, 2 February, 7 February, 15 February) the hourly averaged values exceeded this threshold. The median r_{eff} was 10.2 µm ± 4.2 µm.

The v_{eff} distribution in the middle panel had in general a higher relative standard deviation within the hourly values than r_{eff} but the average v_{eff} was relatively constant during the whole campaign. The median v_{eff} of the hourly averaged time series is 0.1 ± 0.04. This corresponds to a k-factor of 0.73 (Equation 2.21). As already stated, the study by Martin et al. (1994) found a typical value of $k = 0.80 \pm 0.07$ within maritime air masses. Panel (c) shows the result of converting v_{eff} into relative dispersion following Equation 2.22 which yields a median relative dispersion of 0.34, and could be of interest for readers that are more familiar with the relative dispersion than with v_{eff}.

Figure 4.4 shows the vertical profiles of r_{eff} from the cloudbow dataset for each measurement day as a 2-D frequency histogram plot. The colors of the histogram boxes indicate the frequency of measurements within each box. The red line represents the average r_{eff} for each height bin. On all measurement days, an increase of r_{eff} with height is observed as expected from the adiabatic model. On some days (e.g., 28 January, 31 January, 5 February, 11 February), the clouds were mainly very shallow. Only few data points were captured above the height of approximately 1500 m. Moreover, the vertical profiles show considerable differences in their slopes. On 22 January, 7 February and 13 February, a steep increase of the r_{eff} is observed and values of 20 µm were frequently observed. Such differences can be assigned to different cloud types which will be discussed in Section 4.2.

In Figure 4.5 the vertical profiles of v_{eff} are presented. The average values do not show a significant increase or decrease with height, and the average v_{eff} seems to be relatively constant with height on most days. One exception is 22 January in which an increase of v_{eff} with height is observed. On this day, also r_{eff} shows a steep increase with height (Figure 4.4). The generally higher variability that was observed in the time series in Figure 4.3 in v_{eff} is also visible in the vertical profile plots, and most points have $v_{\text{eff}} < 0.1$. Besides, there is an accumulation at $v_{\text{eff}} = 0.32$, which is the upper limit of the lookup table used in the polarimetric cloudbow retrieval (Section 3.2).

4.1.2 Cloud droplet number concentration

The aerosol and droplet number concentrations measured with the in situ instruments onboard the ATR aircraft (Coutris, 2021) are shown in Figure 4.6 in blue. For this plot, the data were resampled to generate the hourly time series shown in the panels (a) and (b). There were two aerosol outbreak events during the campaign. The first one took place from 31 January to 2 February where Saharan dust was observed (Chazette et al., 2022). During the second event on 11 February the analysis in Chazette et al. (2022) indicates a

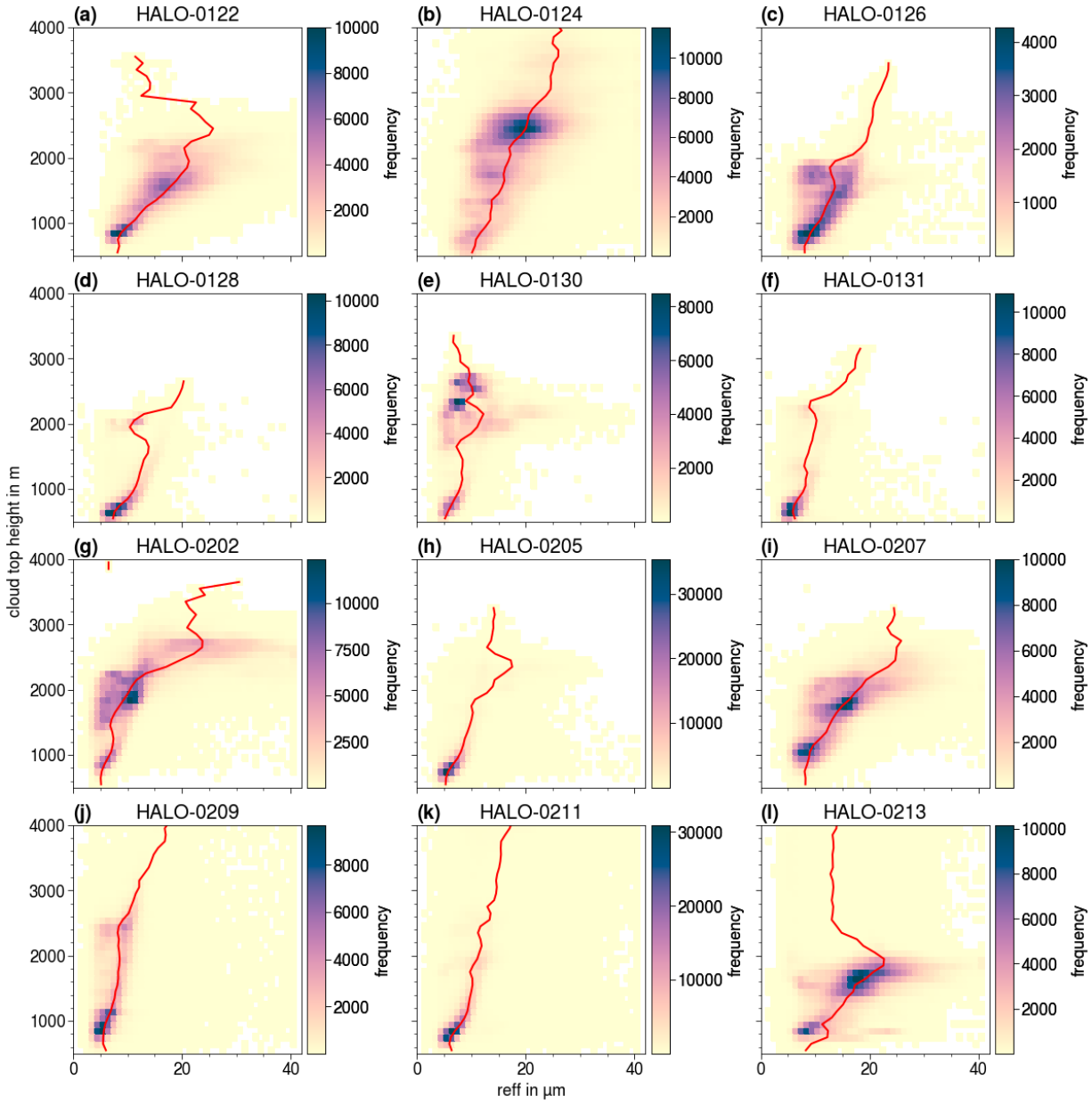

Figure 4.4: Vertical profiles of r_{eff} for all measurement days of the EUREC^{4}A campaign (except 15 February)

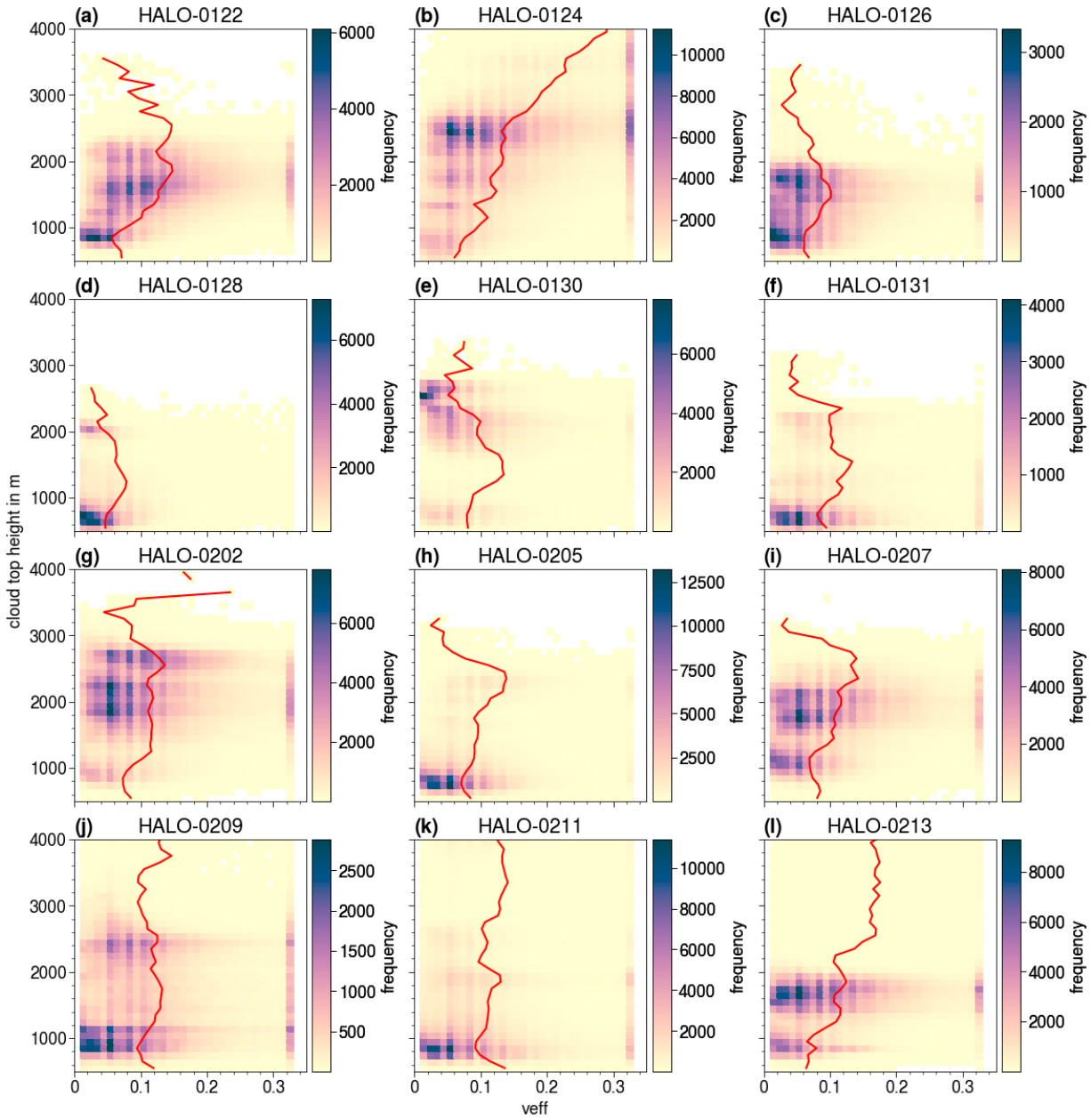

Figure 4.5: Vertical profiles of v_{eff} for all measurement days of the EUREC^{4}A campaign (except 15 February)

dust source located in northwest Africa. The aerosol number concentration is shown in panel (a), and the droplet number concentration from the in situ instruments in panel (b) of Figure 4.6 in blue. An increase in N_d during the aerosol outbreak events is visible. This relationship is visualized in panel (c) in which the two quantities (droplet number concentration and aerosol number concentration) are plotted against each other.

Furthermore, an estimate of the droplet number concentration retrieved from the specMACS CDSD dataset as described in Section 3.4 is shown in panel (b) in orange. From the average air temperature (292.6 K) and pressure (926.6 hPa) of dropsonde measurements at the typical cloud base height of 800 m, the adiabatic condensation rate of $C_w = 2.5 \times 10^{-3}\,\mathrm{g\,m^{-3}}$ was determined, which is required for the N_d equation (see Equation 3.5). Moreover, for calculating N_d from the specMACS CDSD dataset, an adiabaticity of $f_{ad} = 0.66$ is assumed as in Grosvenor et al. (2018b). At this point it was decided to use a constant f_{ad} and C_w similar to what is commonly used in satellite retrievals (e.g. Grosvenor et al., 2018a; Grosvenor and Wood, 2018). The error budget analysis presented in Section 3.4.1 showed that the uncertainty in N_d related to typical uncertainties in C_w and f_{ad} is minor compared to other contributions. However, the choice of the constant f_{ad} and C_w could be responsible for an offset in the retrieved N_d.

Any sample points of the CDSD dataset where a corresponding $\tau_c > 50$ was retrieved are discarded for the analysis in Fig. 4.6 because the uncertainty of the τ_c retrieval becomes too large for such high optical depths and often the retrieval returns the upper limit of the τ_c lookup table. Furthermore, a qualitative analysis of the retrieved τ_c showed that such large τ_c are often observed in cloud side regions illuminated by the sun. This is a common retrieval error of the used bispectral retrieval in which the orientation of the cloud surface is not considered. In addition, retrievals with $v_{eff} = 0.32$, which is the upper limit of the cloudbow LUT, are also excluded from the analysis. Retrievals with $v_{eff} = 0.32$ (which corresponds to $k = 0.25$) are often a result of a mixing of cloudbow signals from two different cloud layers with different CDSDs. In general, the cloudbow retrieval should not be applied to such multi layer cloud scenes since an exact assignment of the signal to the cloud is not possible. Although τ_c and k have only a minor impact on N_d compared to r_{eff} ($N_d \sim \tau_c^{1/2} k^{-1} r_{eff}^{-5/2}$), the combination of both too large τ_c and too small k results in unrealistically large N_d which are excluded if these filters are applied. This process removes about 8 % of the initial data points.

The orange line in panel (b) of Figure 4.6 shows N_d from specMACS. Note that the two datasets are not exactly spatially coincident. Nevertheless, the analysis shows that the two datasets agree well in a statistical sense. For example, the change of N_d with time from specMACS looks similar to the change in the situ data, and an increase in N_d during the two aerosol outbreak events is also observed within the specMACS data. Nevertheless, the median specMACS N_d is slightly higher than the in situ N_d. Two things need to be considered. First, the presented time series does not show a comparison of simultaneous observations but a comparison of the overall picture of two datasets

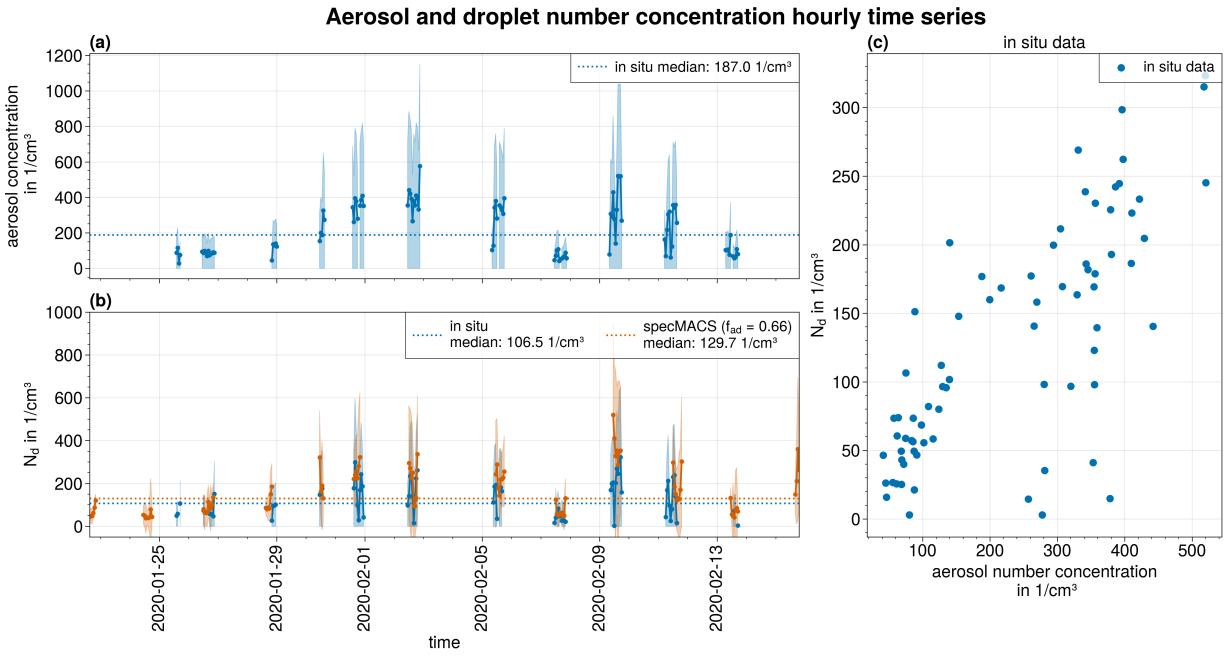

Figure 4.6: Panel (a): Aerosol number concentration from in situ measurements onboard the ATR aircraft; Panel (b): Droplet number concentration from ATR in situ measurements and estimate of droplet number concentration from specMACS CDSD with $f_{ad} = 0.66$; Panel (c): Relationship between aerosol and droplet number concentration of in situ dataset. For this plot, all measurements were resampled to hourly bins.

that were measured in the same region. Second, it is assumed that $f_{ad} = 0.66$ for the specMACS N_d derivation. Other observational studies found different f_{ad} values (e.g. 0.8 in Gryspeerdt et al. (2022) or 0.9 in Painemal and Zuidema (2013)), and modeling studies show even much smaller f_{ad} and a decrease of f_{ad} with height (e.g. Eytan et al., 2021; Lim and Hoffmann, 2023a) which would then lead to a N_d decreasing with height. The use of a constant f_{ad} is therefore not necessarily correct and this could easily explain the observed differences in N_d.

In summary, the very accurate knowledge of the CDSD (especially of r_{eff}) from the cloudbow retrieval benefits the droplet number concentration retrieval substantially (see Section 3.4.1) and the presented observational analysis shows that the retrieved N_d is comparable to in situ measurements. Nevertheless, a higher accuracy of the other input parameters for the droplet number concentration retrieval, namely the cloud optical thickness and the adiabaticity, is desired. The retrieval of the cloud optical thickness might be improved by considering the cloud geometry as in Kölling (2020), but this is very complex, and only moderately improves the result ($N_d \sim \tau_c^{1/2}$).

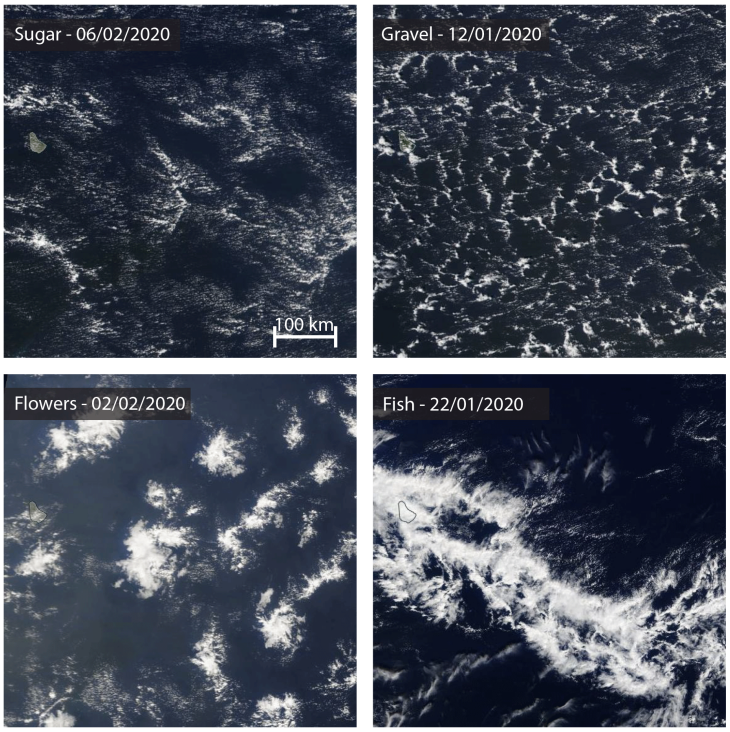

Figure 4.7: Reproduced from Schulz (2022b) (CC BY 4.0 license). Examples of the four named mesoscale cloud patterns as observed in satellite images. Top row: reflectance measurement from MODIS onboard Terra satellite; Bottom row: reflectance measurement from VIIRS onboard NPP satellite.

4.2 CDSD in different mesoscale cloud patterns

It has been observed that tradewind clouds often exhibit typical spatial structures. In order to have a common language when talking about these structures, four terms for mesoscale cloud patterns have been agreed upon: sugar, gravel, flowers and fish (Stevens et al., 2020). The four categories as observed in satellite imagery are shown in Figure 4.7 (adapted from Schulz (2022b)). The patterns differ not only in their visual appearance, e.g., in the degree of cloud clustering, but are also characterized by the amount of precipitation associated with each pattern (Schulz et al., 2021). A classification of the EUREC^{4}A campaign is published in the C^{3}ONTEXT (a Common Consensus on Convective OrgaNizaTion during the EUREC4A eXperimenT) dataset (Schulz, 2022a,b). For the creation of this dataset, satellite images from the GOES-16, Aqua and Terra satellites were manually labeled by 50 scientists. The scientists were asked to mark rectangular areas in the images, and to decide which pattern matched the cloud situation inside the marked area. They could also attribute more than one classification to a single pixel. Furthermore, if a scientist did not label a certain region in the satellite image, this region was marked as “unclassified”.

An example of the classification dataset is shown in Fig. 4.8 (adapted from Schulz

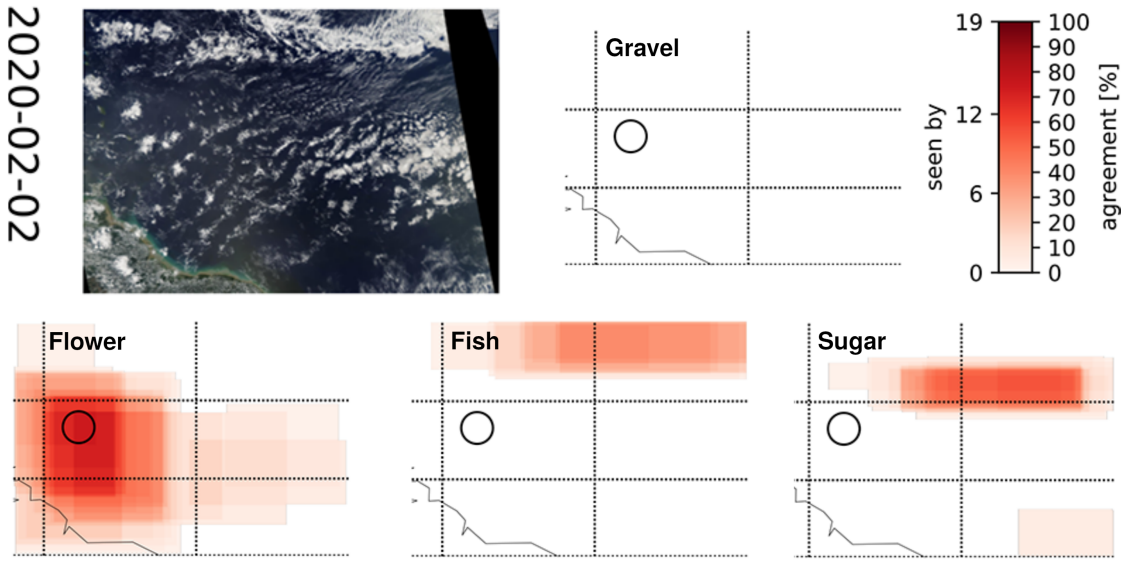

Figure 4.8: Example of daily averaged classification of the C^{3}ONTEXT dataset on 2 February. The corrected reflectance from MODIS Aqua measurements is shown on the top left. The other four panels show the classification for the four mesoscale patterns for the same region as shown in the satellite image. The circles inside the plots indicate the location of the HALO circle. Reproduced from Schulz (2022b) (CC BY 4.0 license) in a cropped version to only include images from 2 February. Note that the "instantaneous" dataset is used in the following analysis and this figure shows the daily average.

(2022b)) where the agreement between the scientists for the four patterns is plotted next to the MODIS image. On this day, most scientists classified the region as flowers. The "unclassified" category is not shown in the Figure but it is implicitly visible, for example, in the lower region of the plots. Here, the classification agreement in all four patterns is zero which means that none of the scientists applied a classification to this region. The corresponding "unclassified" agreement would be 100 %. In the following analysis, the "instantaneous" (two hourly) dataset of C^{3}ONTEXT based on the visible satellite images is used. The dataset has a two hourly temporal resolution and a spatial resolution of around 1 km. Furthermore, it covers a relatively large domain from 5° to 20°N and 62° to 40°W. For the presented analysis, the classification dataset is linearly interpolated in time and space onto each data point of the specMACS CDSD dataset. As a result, each CDSD data point receives a corresponding pattern probability. This way, typical characteristics of the pattern types with respect to the CDSD are analyzed.

4.2.1 Relating specMACS CDSD data to mesoscale patterns

Figure 4.9 shows an example of the values in the classification dataset for the times and positions of specMACS derived CDSDs for the HALO-0202_c5 segment. The background (grey colors) is the GOES-16 ABI measurement (channel 2 at 0.64 µm) at the time ap-

proximately in the middle of the flight segment. The island Barbados is visible in the left part of the satellite images. The high-resolution specMACS radiance data from the two polarization resolving cameras are plotted on top of the low resolution GOES-16 ABI data as true-color RGB images. Furthermore, the individual positions of the CDSD retrievals are plotted as points colored according to the classification frequency for the four classes. In this case, the scene was mostly not classified at all ("unclassified", panel (e)) followed by a classification as "flowers" (panel (b)). It should be mentioned that the region shown in this figure is only a small part of the whole scene classified by the users. Figure 4.8 shows the total size of the classification area and the HALO circle is indicated in black in each panel. If there are more prominent cloud structures in the larger scene, there is a high probability that these parts of the scene will be classified by the user and other parts that are less clear will not be classified. In my opinion, the classification "flowers" is certainly correct for the large cloud structures that are visible in Figure 4.9. However, between the large clouds, there are many small clouds (e.g., in the southern part of the HALO circle) with diameters of only a few km. These are hardly visible in the satellite images and have therefore not been specifically classified by the users. Such clouds could probably be categorized as "sugar" but a classification at such small scales is not what the C^{3}ONTEXT dataset intends to provide and the dataset should better be used in the mesoscale context. In this respect, the whole scene including the small-scale context is interpreted as clouds of the flower type. This example should highlight the potential ambiguities of coupling the C^{3}ONTEXT dataset to the local specMACS CDSD due to the large size of the classified region and the relatively low spatial resolution of the C^{3}ONTEXT dataset.

Figure 4.10 shows the time series of daily averages of the classification frequencies assigned to all CDSD data points. It is clear that the category "unclassified" is dominant. There are only two days (22 January and 2 February) where a single other classification was observed more frequently than the "unclassified" category. As just shown, it is well possible to assume that the second most frequent classification is appropriate for the scene if the most frequent classification of the scene is "unclassified". Therefore, the category "unclassified" is not considered for the following analysis. Furthermore, data points where the classification frequency of the most frequent pattern was less than 10 % were excluded from the following analysis. Applying the frequency threshold filter reduces the number of datapoints for the analysis by about 12 %.

The CDSDs are evaluated with regard to the corresponding mesoscale patterns. For each sample of the CDSD dataset the corresponding most frequent mesoscale pattern neglecting the "unclassified" category is found. Figure 4.11 shows histograms of the r_{eff} (top) and v_{eff} (bottom) of the individual data points separated into the four patterns. According to this figure, sugar has the smallest median r_{eff} (approximately 7 µm), followed by gravel and flowers (approximately 10 µm). The fish category has by far the largest median r_{eff} (approximately 17 µm). Furthermore, the r_{eff} histograms of flowers and gravel

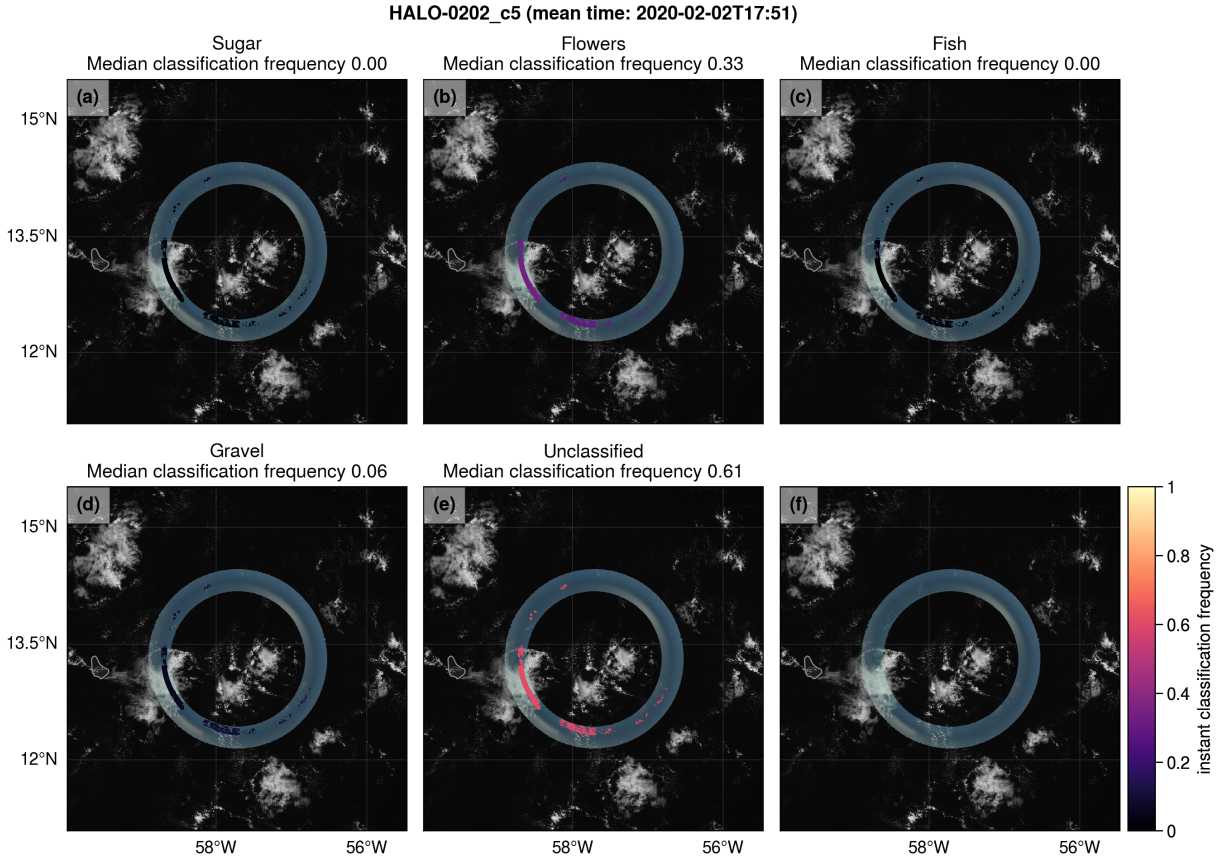

Figure 4.9: specMACS RGB image on top of GOES-16 ABI image in the background of a time during the HALO-0202_c5 segment. The positions of retrieved CDSDs of this flight segment are plotted and colored according to their classification frequency of the C^{3}ONTEXT dataset for the four mesoscale patterns (panels (a)–(d)) and the "unclassified" category (panel (e)). The last panel (f) shows only the satellite measurement and the specMACS image.

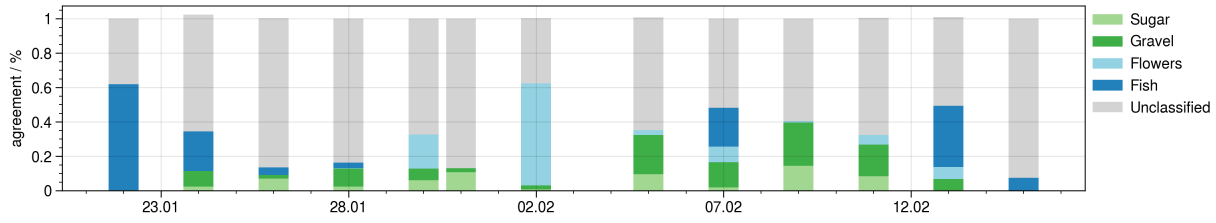

Figure 4.10: Daily averages of classification frequencies of mesoscale patterns assigned to data points of CDSD dataset. Figure as in `https://howto.eurec4a.eu/c3ontext.html`

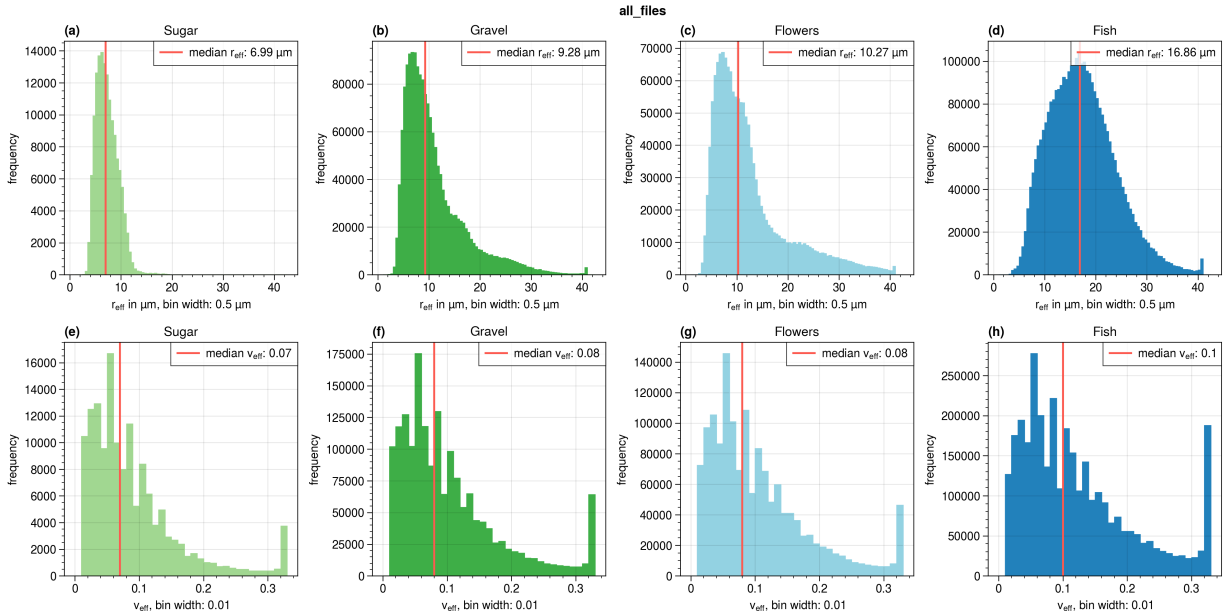

Figure 4.11: Frequency distribution of r_{eff} (top) and v_{eff} (bottom) for the four different mesoscale patterns. The median values are indicated as red lines.

exhibit a similar structure with a peak at around 8 µm and a tail with larger droplets up to 30 µm. Since gravel and flower are also associated with similar rain amounts (Schulz et al., 2021) these larger effective droplet sizes could be an indication for rain formation. According to Schulz et al. (2021), the fish pattern has the highest precipitation amount and the analysis here shows that fish is also characterized by the largest droplet effective radii. Sugar pattern clouds are mostly non-precipitating (Schulz et al., 2021) and the r_{eff} distribution does not indicate precipitation either. The frequency distributions of v_{eff} (bottom) do not show much difference between the individual mesoscale patterns but one thing to note is that the fish pattern has the highest number of retrievals with $v_{\text{eff}} = 0.32$ (the largest value in the LUT) which could originate from multi-layer cloud scenes or scenes with precipitation, which are problematic for the retrieval.

The vertical profiles of r_{eff} and v_{eff} for the four categories are shown in Figure 4.12. As before, the 2-D frequency histograms are calculated and are plotted as colored boxes. The averages for each height bin are connected with a solid line for each pattern. The last column (panels (e) and (j)) compares the averages of all four pattern types. The vertical axis was cut at 3000 m as most cloud tops are below this height. Sugar and gravel appear to be shallow clouds having geometrical cloud depths mostly smaller than 1 km but gravel also includes some higher points. Flowers and fish comprise clouds with higher cloud tops (up to 2.5 km). These observations are mostly in line with Schulz et al. (2021).

The average r_{eff} vertical profiles of sugar, gravel and flowers in panel (e) are relatively similar, and only fish stands out with much higher r_{eff}. The 2-D frequency distributions

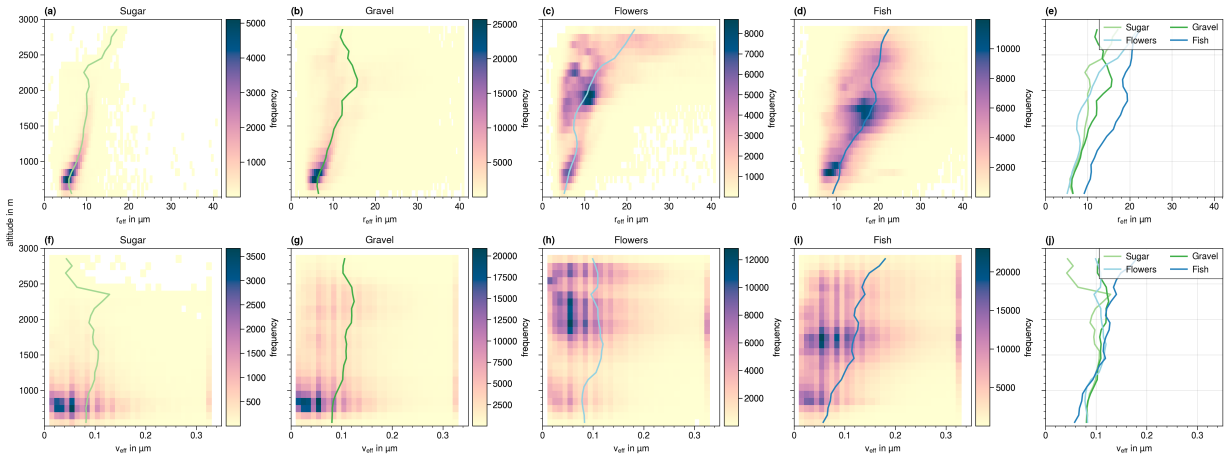

Figure 4.12: Vertical distributions of r_{eff} (top) and v_{eff} (bottom) for the four different mesoscale patterns. The average values of each height bin are indicated as colored lines and are compared in the last column.

show that although the average profiles are similar, flowers seem to reach much higher cloud top heights much more frequently. In the case of flowers, there is an agglomeration at a height of approximately 1900 m with $r_{\text{eff}} \approx 10\,\mu\text{m}$. Most of these retrievals are data from 2 February (compare Figure 4.4 g). The flower pattern consists of a relatively small updraft region with a large anvil (Schulz et al., 2021). Since the presented vertical profiles are created from signals from the cloud top, we mostly see the anvil of the flowers in our measurements and the observations at lower cloud heights are not necessarily representative of the actual updraft area of the flower but are probably associated with other cumulus clouds in the vicinity. This difference between the four patterns in terms of cloud height is also visible in the v_{eff} plots at the bottom of Figure 4.12. The average vertical profile of v_{eff} (panel (j)) does not strongly depend on the pattern type, and v_{eff} seems to be relatively constant with height except for fish where a slight increase of v_{eff} with height is observed. As already seen before, v_{eff} is much more variable than r_{eff}.

This analysis shows that although the four patterns were originally defined from their visual appearance in satellite images which was mainly based on the cloudiness and degree of cloud clustering, they also differ with regard to the CDSD especially for sugar (small r_{eff}) and fish (large r_{eff}). This result nicely adds to the study by Schulz et al. (2021) in which differences of the patterns in cloud geometry, precipitation amount and corresponding atmospheric environments were studied.

4.2.2 Microphysical view on the mature stage of a flower cloud system

In Subsection 3.2.1 and 3.2.2, the flower cloud system of the 2 February was already discussed in two case studies. There are already a number of publications dealing with this specific measurement day of the EUREC^{4}A campaign (e.g. Narenpitak et al., 2021; Dauhut et al., 2022; Touzé-Peiffer et al., 2022), which shows that the measurements of

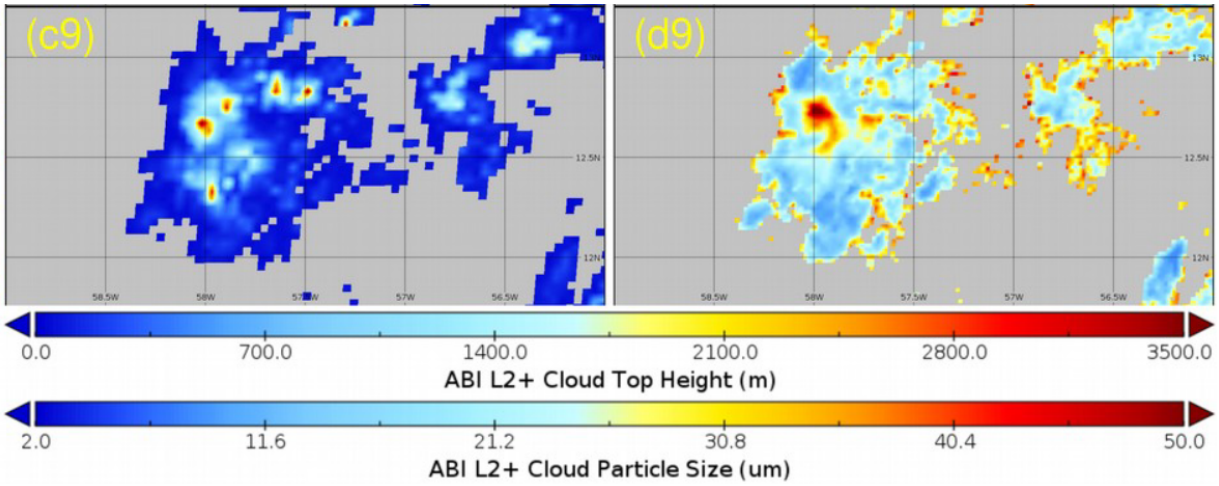

Figure 4.13: Cloud top height (c9) and cloud particle size (d9) of GOES-16 satellite measurements on 2 February 2020 13:40 UTC. Figure adapted from Cui et al. (2023) to only show the panels (c9) and (d9) (used under CC BY 4.0). The comma shaped region of large droplet sizes is clearly visible.

this day are of high interest for the scientific community. Therefore, also our analysis will be extended in the following.

The life cycle of this flower cloud system was analyzed in Cui et al. (2023) based on GOES satellite measurements, ATR in situ measurements, and dropsonde measurements. They show that two cloud systems merged at around 1 UTC and the flower cloud system started to develop. From 10:30 to 12:00 UTC, a rapid increase of the cloud area of the flower cloud was observed during which the cloud top was rising above 2.5 km for large regions of the cloud. Figure 4.13 shows a subset of Figure 8 from Cui et al. (2023) where the cloud top height is shown on the left and the cloud particle size on the right from GOES-16 ABI measurements at 13:40 UTC. This figure shows the formation of a comma shaped area with $r_{\text{eff}} > 30\,\mu\text{m}$ which is interpreted as the region of precipitation formation in Cui et al. (2023). Such large r_{eff} were also seen in the specMACS data in Subsection 3.2.1, where we could support the hypothesis of precipitation formation by radar observations onboard HALO which showed regions of enhanced reflectivity and positive fall speeds. The satellite measurements in Cui et al. (2023) show that this area of large r_{eff} increased until about 16 UTC and afterwards, droplet sizes started to decrease as precipitation particles sedimented. Furthermore, cold pools formed around the flower cloud system. A cold pool is created through evaporation underneath precipitating clouds, which cools the atmosphere. This leads to a strong downdraft which radially spreads outwards resulting in a cloud free area. New convection can be triggered at the gust front of the downdraft and a circular cloud arc of smaller cumulus clouds is formed around the cloud free area. From 19 - 21 UTC, the total area of the cloud decreased and the cloud system slowly decayed.

The same flower cloud was also observed by specMACS. In total, there were eight

overflights of specMACS in the time range from 12:20 to 18:45 UTC. In the following, these specMACS observations are discussed with regard to the satellite observations described in Cui et al. (2023). The eight individual occurrences of the flower cloud in the southern part of the HALO circle are shown in Figure 4.14 for all HALO flight segments. In the background, corresponding GOES-16 ABI images are shown and the specMACS RGB image as well as the retrieved r_{eff} indicated by color are displayed in the foreground. All maps cover the same area. specMACS observed the cloud system mainly in its mature stage during which the comma shaped area of high r_{eff} developed (Cui et al., 2023) but the swath of the specMACS CDSD is not wide enough to capture the comma shape. Nevertheless, in the segments HALO-0202_cl3 and HALO-0202_c4 (panels (e) and (f)), the retrieved CDSD are approximately located within the region of highest r_{eff} as seen in the satellite retrievals shown in Cui et al. (2023). specMACS also retrieves r_{eff} larger than 30 µm there. In the two segments HALO-0202_c4 and HALO-0202_c5, the formation of the cold pool is visible which creates cloud arcs to the north and to the south of the flower. After HALO-0202_c5, the flower cloud slowly dissolves. Approximately one hour after the last specMACS observation, the flower cloud is already quite fragmented, and no longer recognisable as a typical flower cloud (Cui et al., 2023). Figure 4.16a shows a time series of the retrieved r_{eff} plotted as a 2-D frequency distribution. The highest r_{eff} values were observed at around 16 UTC, and afterwards r_{eff} decreased. Please note that different parts of the flower cloud were sampled by specMACS during the individual HALO overflights. For example, HALO-0202_cl1 observed a part of the cloud close to the edge of the cloud and in HALO-0202_c4 the center part of the cloud was observed (see Figure 4.14). From these measurements it is therefore not possible to analyze the time evolution of a certain part of the cloud.

Figure 4.15 shows the corresponding v_{eff} maps. The maps display a very heterogeneous v_{eff} distribution similar to that seen in the case study in Subsection 3.2.1. Some parts of the flower cloud are associated with very large v_{eff}, and just next to it v_{eff} can be very small. It is hard to find a trend in v_{eff} during the course of the day which is shown in Figure 4.16b. Again, a wider swath and temporally longer observations of the same cloud would help in analyzing the flower cloud in more detail.

To summarize, this study showed that the specMACS observations clearly provide similar results as seen in the satellite observations in terms of r_{eff}, but with a significantly higher spatial resolution. The presented example of the flower cloud impressively shows how large the small-scale spatial variability of the microphysical parameters is. Further studies of this flower cloud could involve, for example, a sophisticated, statistical analysis of the r_{eff} and v_{eff} distributions in combination with the radar observations from HALO from which downdraft locations can be estimated. This approach has already been tested in the case study shown in Section 3.2.1 but would require considerable extension.

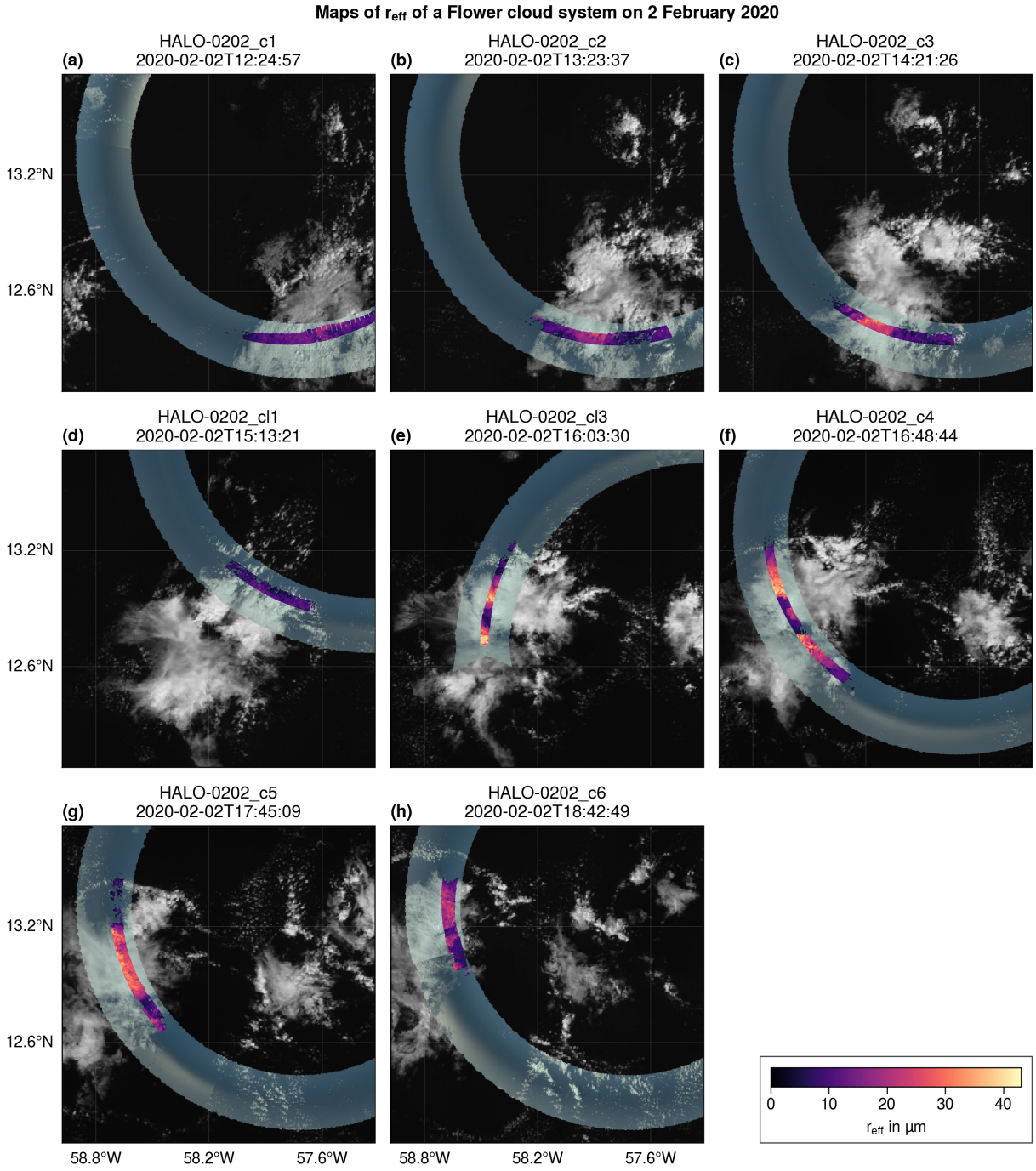

Figure 4.14: Maps of r_{eff} of specMACS observations on top of specMACS RGB and GOES-16 ABI image of a flower cloud on 2 February 2020.

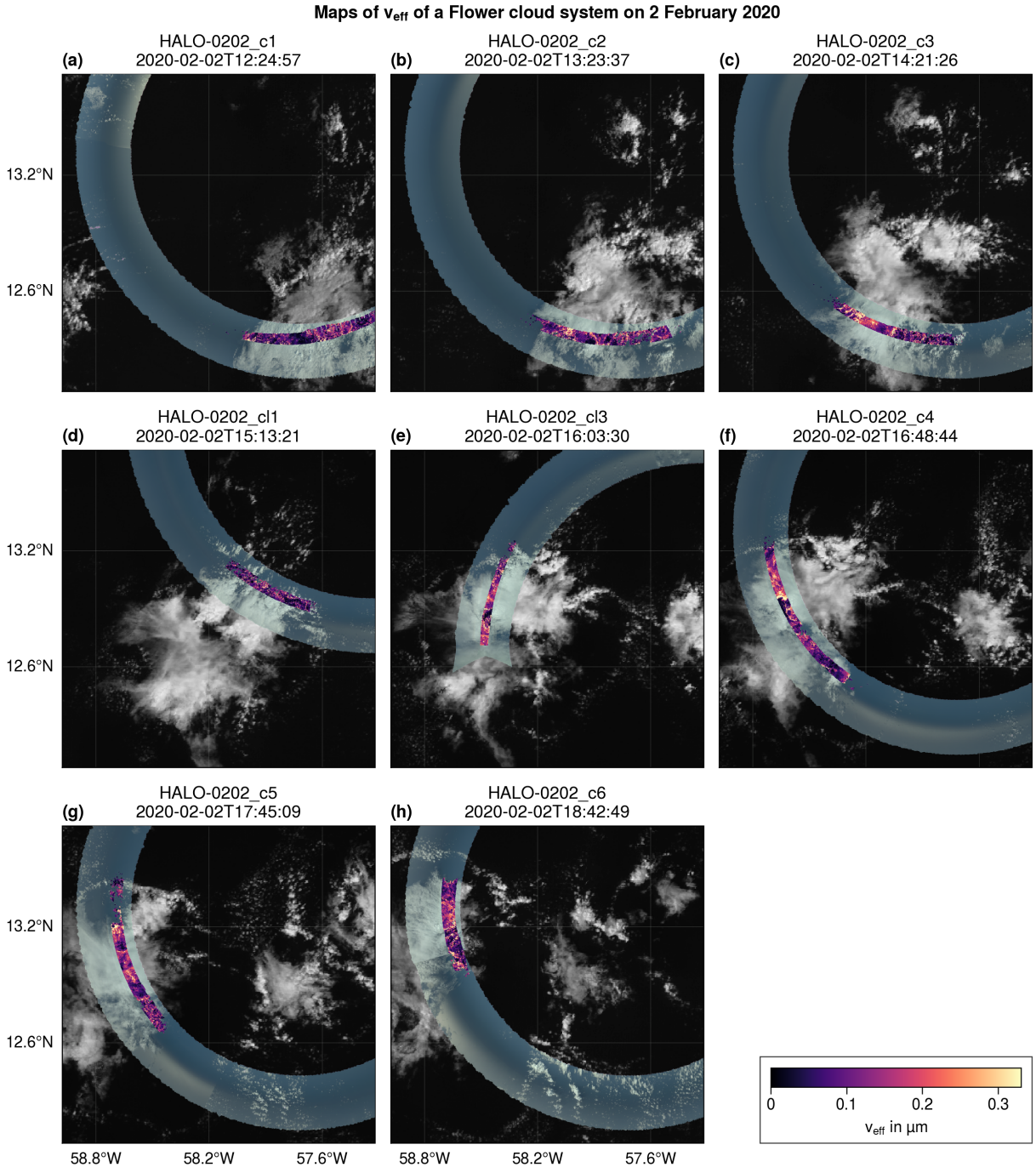

Figure 4.15: Maps of v_{eff} of specMACS observations on top of specMACS RGB and GOES-16 ABI image of a flower cloud on 2 February 2020.

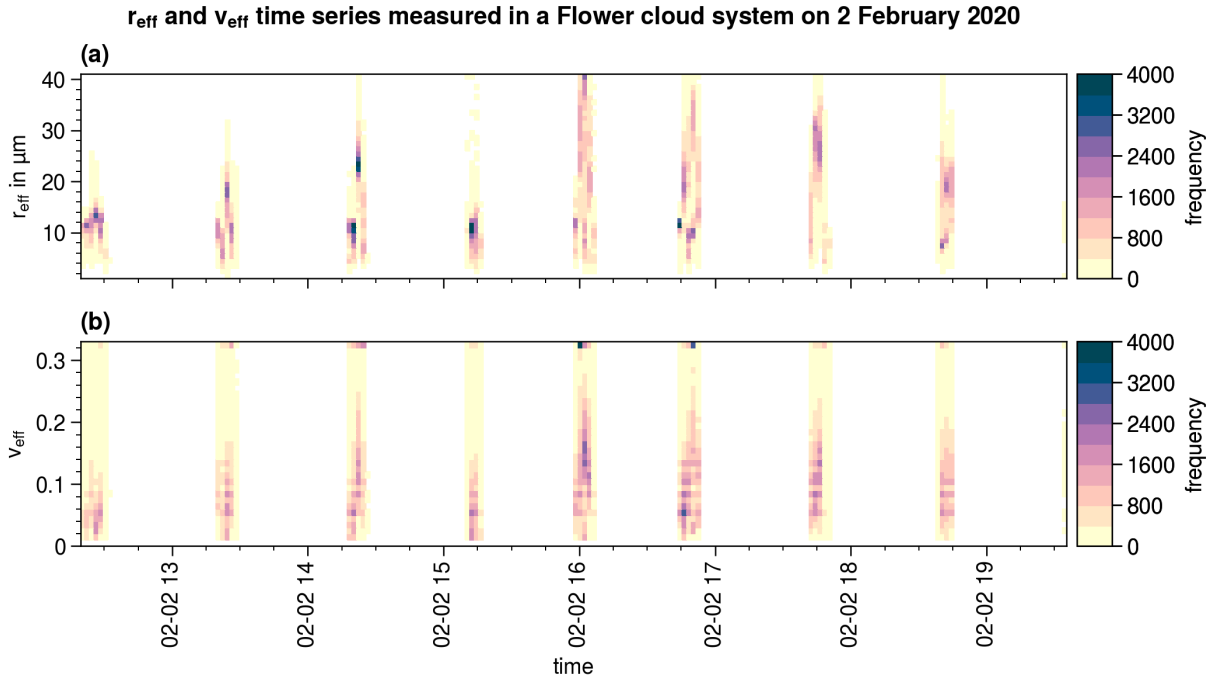

Figure 4.16: Time series shown as 2-D frequency distribution of r_{eff} (panel (a)) and v_{eff} (panel (b)) of specMACS observations of a flower cloud on 2 February 2020.

4.3 Effects of entrainment and mixing on the CDSD

As explained in Subsection 2.3.4, entrainment and mixing affect the CDSD in the extreme cases by either reducing the droplet number concentration (inhomogeneous mixing) or by reducing the overall sizes of the droplets (homogeneous mixing). So far, these effects have mainly been studied through in situ observations of clouds (e.g. Gerber et al., 2008). In the following section, it is analyzed whether effects of entrainment and mixing might be observable in the specMACS CDSD dataset. In contrast to in situ measurements, specMACS offers a 2-D picture of the cloud allowing to localize measurements with respect to the cloud edge. Some tendency of increased v_{eff} at the cloud edges was already observed in the case study presented in Subsection 3.2.2. This increase could be related to entrainment and mixing which will be investigated in the following.

First, the CDSDs are separated into points near the edge of the cloud and points from the center of the cloud following the method presented in Section 3.5. Afterwards, the CDSDs of the two groups (center and edge) are compared on the basis of vertical profiles of the two groups. In a last step, the droplet number concentrations and computed adiabaticities are compared.

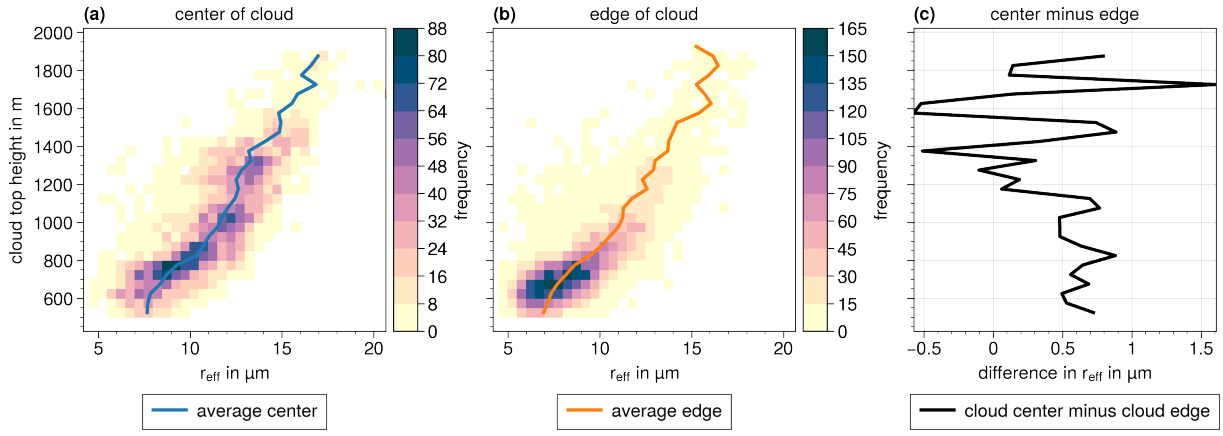

Figure 4.17: Comparison of vertical profile of r_{eff} for center (panel (a)) and edge (panel (b)) points. Panel (c) shows the difference of the average r_{eff} indicated by the blue and orange lines in panels (a) and (b).

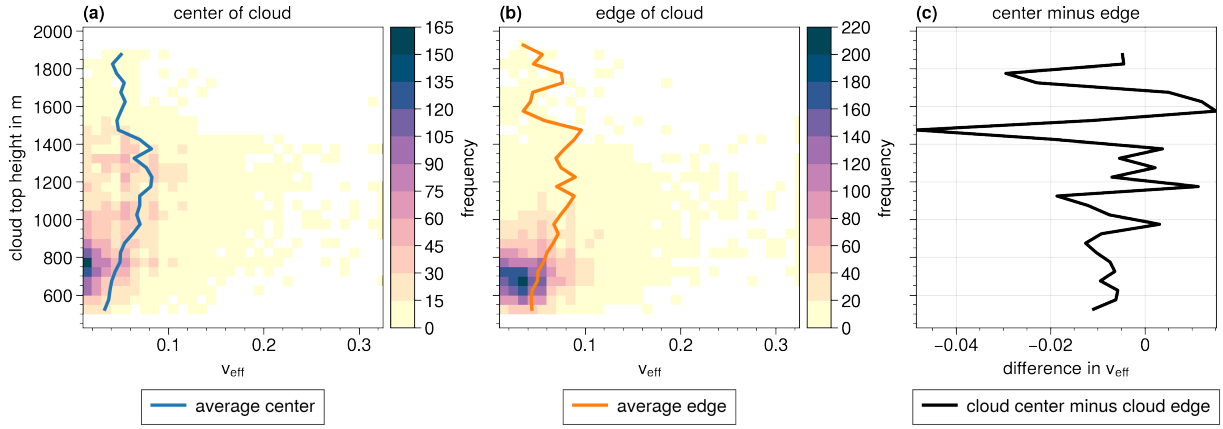

Figure 4.18: Comparison of vertical profile of v_{eff} for center (panel (a)) and edge (panel (b)) points. Panel (c) shows the difference of the average r_{eff} indicated by the blue and orange lines in panels (a) and (b).

4.3.1 Vertical profiles of the CDSD of cloud core and cloud edge

In the following, a case study of a one hour overflight above shallow cumulus clouds is presented from the flight segment "HALO-0128_c2". One scene of the segment was shown in Figure 3.33 where the separation into edge and center points was presented. Now, the CDSDs from center points are compared with the CDSDs from edge points. To decouple the increase of r_{eff} with altitude from any mixing effects, vertical profiles of the CDSDs are constructed by plotting the retrieved r_{eff} and v_{eff} of all individual clouds of a certain scene against the corresponding cloud top heights (as in Rosenfeld and Lensky, 1998). The vertical profiles of r_{eff} and v_{eff} categorized into edge and center points are shown in the Figures 4.17 and 4.18 respectively. The two plots show 2-D frequency distributions for the center points in panel (a) and the edge points in panel (b) with the average values for each height layer as blue or orange line. The difference of these

average lines is plotted in panel (c). Most points are located below 1500 m. In general, edge points accumulate at lower altitudes compared to center points. A classical school book view on a cloud would support this: Without any vertical wind shear, the highest part of the cloud is in the horizontal center.

Figure 4.17c shows that below a height of 1500 m, r_{eff} is slightly higher for center points than for edge points. The opposite is true for v_{eff} where values at the center are slightly smaller on average compared to the ones near the edge (Figure 4.18c). The absolute differences are less than 1 µm in r_{eff} and less than 0.02 in v_{eff}. From theory, a smaller droplet size at the edge and an increased effective variance could be related to homogeneous mixing (Baker and Latham, 1979; Lim and Hoffmann, 2023a).

Figure 4.19 shows the corresponding vertical profiles of N_{d} computed with a theoretical perfect adiabaticity of $f_{\text{ad}} = 1$ using Equation 3.5 for center and edge points. This figure illustrates that N_{d} is relatively constant with height and only shows a small decrease in the lower cloud layers. Furthermore, N_{d} in the center of the cloud is on average slightly higher than N_{d} at the cloud edge. Below 1500 m altitude where most points are, this difference is in the order of 20 cm^{-3}. Such a reduction in N_{d} at the cloud edge could be related to inhomogeneous mixing. However, the retrieved N_{d} strongly depends on what is assumed for f_{ad}. At this point, $f_{\text{ad}} = 1$ is assumed but in reality f_{ad} is expected to be smaller at the edge than at the center, and a smaller f_{ad} value would further reduce N_{d} at the edge. The dependency of N_{d} on f_{ad} will be studied in the next section.

Other measurement days with shallow cumulus clouds that were analyzed in the same way showed very similar findings with center points having on average larger r_{eff}, smaller v_{eff}, and larger N_{d} than edge points. The results of these other days are not presented due to the large similarities but they support the confidence in the findings presented here. To discuss the statistical significance of the presented results, the average vertical profiles are shown in Figure 4.20 together with the variability (one standard deviation σ) of r_{eff} in each height layer (panel (a)). This illustrates the offset in the average curves in the lower layers but also shows that the error bars overlap due to the relatively broad distributions.

Panel (b) shows the standard error of the mean (SEM $= \frac{\sigma}{\sqrt{n}}$, with sample size n), which quantifies uncertainties in estimates of the sample mean. The SEM is small and the error bars of the two groups do not overlap in the lower height layers up to approximately 1200 m which increases confidence in the representativenesses of the means. It is required to have independent sample points for calculating SEM. This is not necessarily true here since all datapoints were used, including points located just next to each other, which might not be independent. Thus, the same analysis was done with a subset of the data points where only one random point of center and edge was considered for each cloud. The found SEM distribution was very similar and is therefore not presented here.

In addition to this analysis of the standard deviation and the standard error of the

mean, a first quantitative analysis of the statistical significance of the findings is presented using a bootstrapping approach which, in contrast to other statistical significance tests, does not require any assumption about the shape of the distribution. Different bootstrapping methods are described in detail in Efron and Tibshirani (1994) and the adapted approach is based on Algorithm 16.2 in Efron and Tibshirani (1994). The null hypothesis regarding the analysis of r_{eff} is: "The mean r_{eff} of the center points is equal to that of the edge points." And the alternative hypothesis (that we want to confirm using the bootstrapping technique) is: "The mean r_{eff} of the center points is greater than that of the edge points." First, the observed test statistic t is calculated as in Efron and Tibshirani (1994) from the two datasets with, in our case, n_x center points (x_i) with average $\overline{x}$ and standard deviation σ_x, and n_y edge points (y_i) with average $\overline{y}$ and standard deviation σ_y.

$$t = \frac{\overline{x} - \overline{y}}{\sqrt{\sigma_x^2/n_x + \sigma_y^2/n_y}} \tag{4.1}$$

In the next step, the two original datasets are changed such that both datasets are centered around the overall mean ($\overline{z}$) of the combined dataset with sample points z_i, and the null hypothesis is true:

$$X_i = x_i - \overline{x} + \overline{z} \tag{4.2}$$

The same transformation is applied to the edge points which are then called Y_i. Then, B bootstrap datasets are created by randomly sampling with replacement n_x data points from X_i and n_y data points from Y_i of each height layer. The points of the bootstrap datasets are called X_i^* and Y_i^*. The test statistic t^* is calculated for each bootstrap dataset:

$$t^* = \frac{\overline{X}^* - \overline{Y}^*}{\sqrt{\sigma_X^{*2}/n_x + \sigma_Y^{*2}/n_y}} \tag{4.3}$$

In the next step, the test statistic of the randomly sampled datasets is compared to the observed test statistic, where $S_i = 1$ if $t^* > t$, and $S_i = 0$ otherwise. This process is repeated $B = 10000$ times, each time determining S_i. The p–value is then calculated via the average of S_i over all bootstrap samples:

$$p = \frac{1}{B}\sum_{i=1}^{B} S_i \tag{4.4}$$

A significance level of $\alpha = 5\,\%$ is chosen and the null hypothesis is rejected if $p < \alpha$. Figure 4.20c shows the result of this bootstrapping method. It illustrates that the null hypothesis is mostly rejected in the height range up to 1200 m, which shows that the

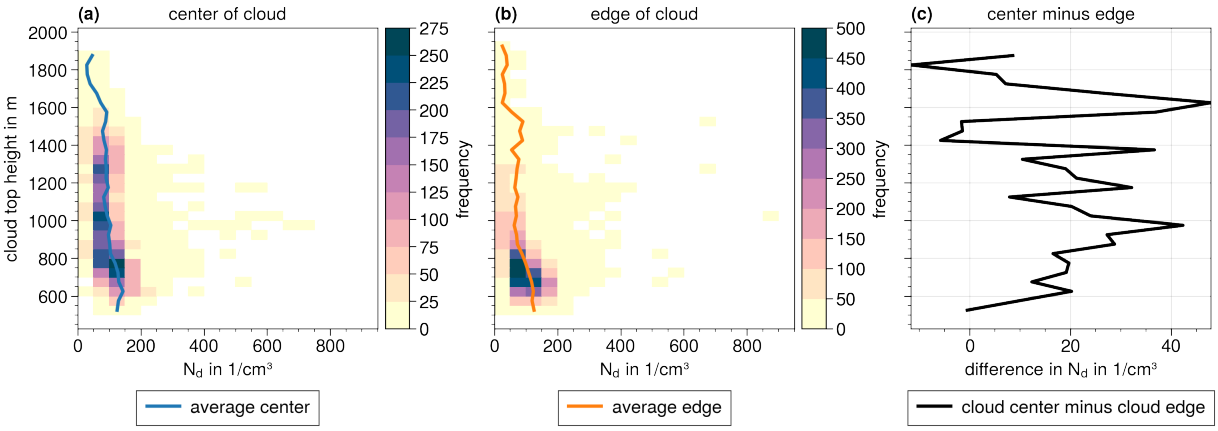

Figure 4.19: Comparison of vertical profile of N_d computed with $f_{ad} = 1$ for center (panel (a)) and edge (panel (b)) points. Panel (c) shows the difference of the average N_d indicated by the blue and orange lines in panels (a) and (b).

finding that center points have on average larger r_{eff} than edge points is statistically significant in this height range. The null hypothesis cannot be rejected in higher layers. The results for v_{eff} and N_d are shown in the Figures 4.21 and 4.22. The presented statistical analysis points at a correct interpretation of the results, and, as discussed, we additionally trust the findings based on the fact that similar differences between center and edge were seen on all measurement days that were analyzed.

From the results up to this point it can be concluded that signatures of both inhomogeneous and homogeneous mixing were visible in the analyzed CDSDs. The recent study by Lim and Hoffmann (2023a) based on Lagrangian cloud model simulations showed similar results. They found that in a single cloud, inhomogeneous mixing can even appear just next to homogeneous mixing. A comparison with their results is given in Subsection 4.3.3.

4.3.2 Droplet number concentration and adiabaticity

In the following, the same measurement data are analyzed as in the last section but this time with a focus on the droplet number concentration N_d and possible applications in terms of the adiabaticity. Overall, the adiabaticity is expected to be reduced at the cloud edges compared to the cloud center. Therefore, the data are again separated into edge and center points, and a third classification "all points" is introduced that includes edge points, center points and points that were neither classified as center nor edge. The use of the "all points" class is justified to increase the overall number of sample points.

First, the adiabaticity is calculated using Equation 3.6. This will be referred to as the "retrieved f_{ad}" in the following, as opposed to the "constant f_{ad}" which is also used. Figure 4.23 shows the retrieved f_{ad} as a vertical profile in the panel (a) and as a frequency distribution in panel (d) using the "all points" class. The corresponding N_d using the

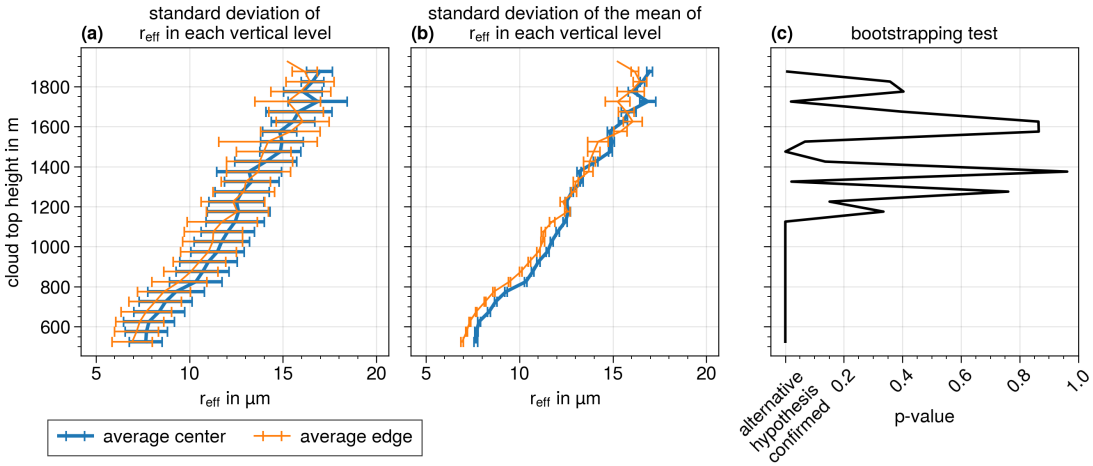

Figure 4.20: Average r_{eff} with standard deviation (a), with SEM (b), and bootstrapping result (c).

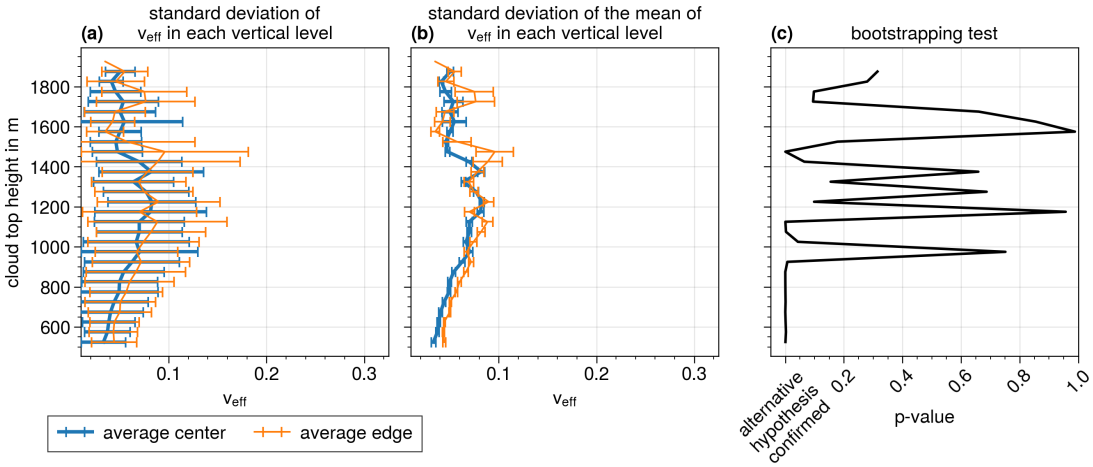

Figure 4.21: Average v_{eff} with standard deviation (a), with SEM (b), and bootstrapping result (c).

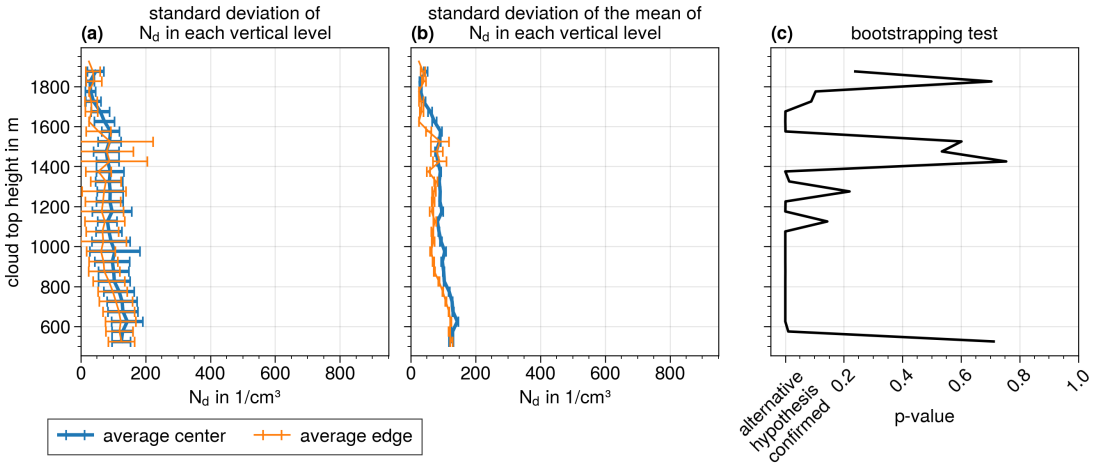

Figure 4.22: Average N_{d} with $f_{\text{ad}} = 1$ with standard deviation (a), with SEM (b), and bootstrapping result (c).

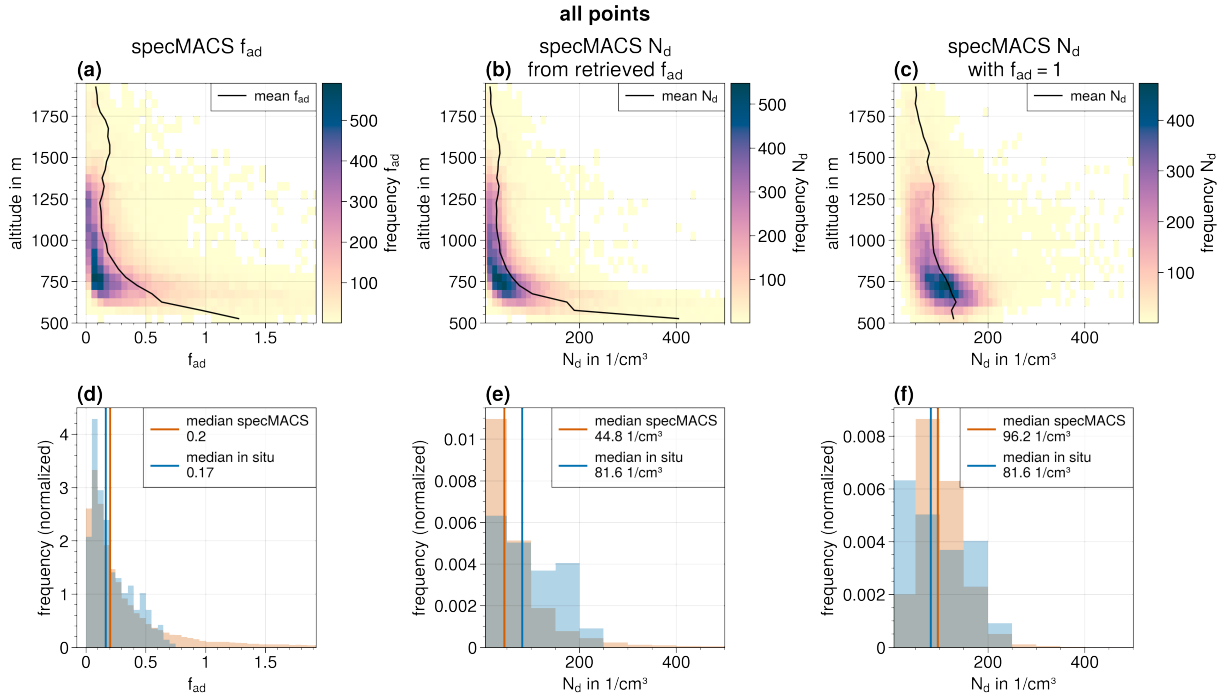

Figure 4.23: Vertical profiles of retrieved f_{ad} (a), corresponding N_d (b), and N_d assuming a constant f_{ad} (c) from specMACS plotted as 2-D density distributions. The black lines indicate the mean of each height bin. The corresponding frequency distributions are plotted in (d), (e) and (f). In situ distributions from the same day and region are also plotted in the panels (d), (e), and (f). The x-axis in (b), (c), (e) and (f) is limited to 500 cm^{-3}.

retrieved f_{ad} is shown in the panels (b) and (e). N_d calculated using a constant $f_{ad} = 1$ is shown in the panels (c) and (f). Again, the vertical profiles are plotted as 2-D frequency plots together with the averages for each height bin as black curves. The largest f_{ad} and N_d values are observed at the cloud base, and both parameters decrease towards the cloud top. However, they are fairly constant above a vertical height of 750 m.

The corresponding frequency distributions in the lower panels of Figure 4.23 show the specMACS measurements in orange and in situ measurements in blue from the same measurement day in a similar region. For the in situ measurements f_{ad} was found by relating the measured LWC to the computed adiabatic LWC_{ad} at the corresponding height level according to $LWC = f_{ad}LWC_{ad}$ (Equation 2.35). As with the specMACS f_{ad} retrieval, one difficulty is deriving the distance to the cloud base which is needed to estimate LWC_{ad}. The f_{ad} distributions of the two datasets (Figure 4.23 (d)) are relatively similar with a similar median of $f_{ad} \approx 0.17$ from the in situ data and $f_{ad} \approx 0.21$ from specMACS. Close to the cloud base, specMACS retrieves $f_{ad} > 1$ which is unrealistic. Overall, the retrieved f_{ad} are quite small for both specMACS and in situ data, and the median value is much smaller than typical literature values (e.g. 0.63 ± 0.22 in Merk et al. (2016) or 0.71 ± 0.18 in Kim et al. (2012) both based on ground-based remote sensing measurements). It should be mentioned that on other measurement days (for example

on 2 February), the specMACS f_{ad} were also very small (median 0.1) while the in situ f_{ad} were larger (median 0.49).

There is a substantial difference between the N_d using the retrieved f_{ad} (Figure 4.23 (b) and (e)) versus the N_d computed with a constant f_{ad} (Figure 4.23 (c) and (f)). In the first case (retrieved f_{ad}), N_d decreases sharply with height and overall, N_d is small through most vertical layers except for the cloud base layer where it is exceptionally large due to the large f_{ad}. In the second case (constant f_{ad}), N_d is relatively constant with height, but a small decrease of N_d with height is observed in the lower cloud levels. The comparison with the in situ measurements in Figure 4.23 (e) and (f) shows that N_d computed with $f_{ad} = 1$ is more similar to the in situ data than N_d computed with the retrieved f_{ad}. Note that the specMACS data were measured at different altitudes and the in situ data are mainly representative of the situation at the cloud base. If the decrease of N_d with height as observed in the specMACS data is true, then it is clear that a comparison of the in situ N_d from cloud base with the specMACS N_d from different altitudes will show differences.

The corresponding figures using only edge points and only center points are shown in the Figures 4.24 and 4.25. As expected, f_{ad} and N_d are reduced in the analysis using only edge points compared to the analysis based on only center points which is expected since entrainment and mixing should have a larger effect at the cloud edge. This again indicates that the presented method to separate points into edge and center points might be meaningful. The overall picture that was observed in the "all points" category is also visible in the analysis using only edge and only center points. This means, the retrieved f_{ad} is overall very small and the corresponding N_d sharply decreases with height and is also very small.

Overall, the unrealistically large f_{ad} at cloud base and small f_{ad} in higher vertical levels, and the correspondingly large N_d at the cloud base and small N_d at higher altitudes all indicate that the results of the presented coupled f_{ad} and N_d retrieval are questionable. Especially since, for example, the N_d retrieved from CDSD data measured with the RSP polarimeter in Reid et al. (2023) are based on a constant f_{ad} and do show good agreement with in situ data. These retrievals mostly assume $f_{ad} = 0.6$ to 0.8 which is much larger than the retrieved f_{ad} from specMACS. In addition, the statistical analysis of specMACS N_d presented in Section 4.1.2 was also based on a constant $f_{ad} = 0.66$ and compared relatively well with in situ measurements of N_d.

There could be several reasons for these findings. First, small errors in CBH translate to large errors in f_{ad} and N_d close to cloud base ($f_{ad} \sim (z - z_{base})^{-2}$). This most likely explains the $f_{ad} > 1$ close to cloud base. Second, one of the other parameters of Equation 3.6 (τ_c, r_{eff}, C_w) could be subject to uncertainties which could be the reason for the very small f_{ad} values in higher vertical layers. Since C_w is relatively constant (Grosvenor et al., 2018b) and the accuracy of the retrieved r_{eff} is known to be very high, the accuracy of the optical thickness should be called into question although its effect is

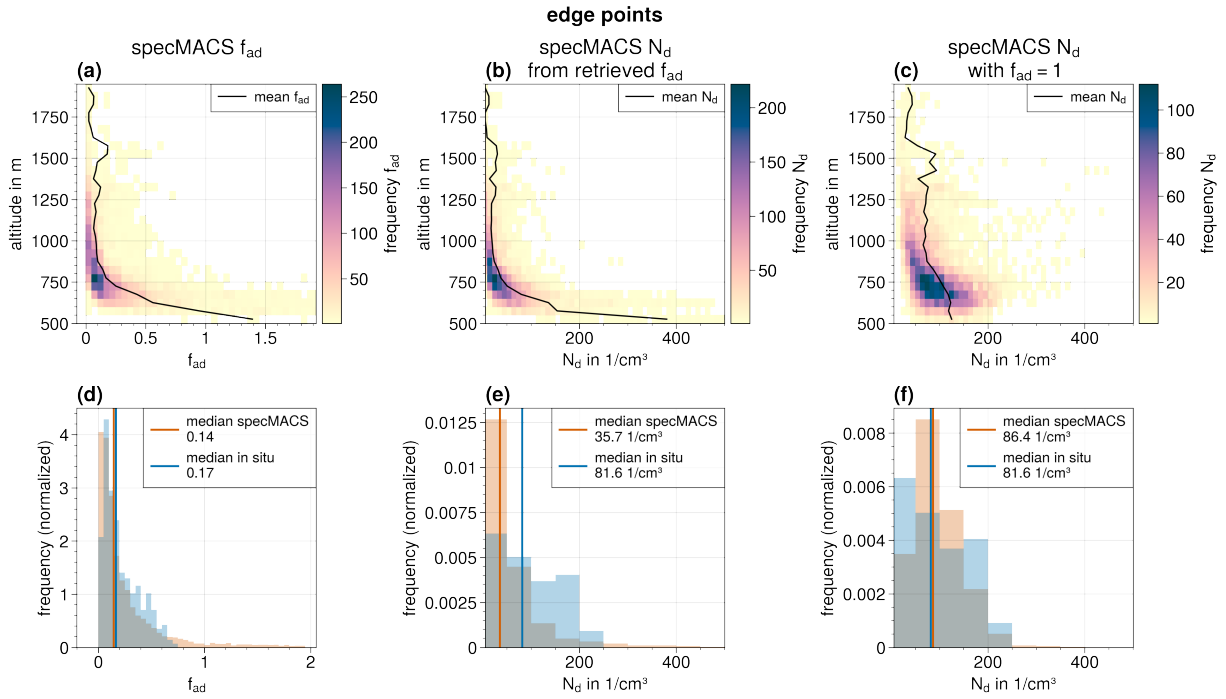

Figure 4.24: Same as Fig. 4.23 but only edge points.

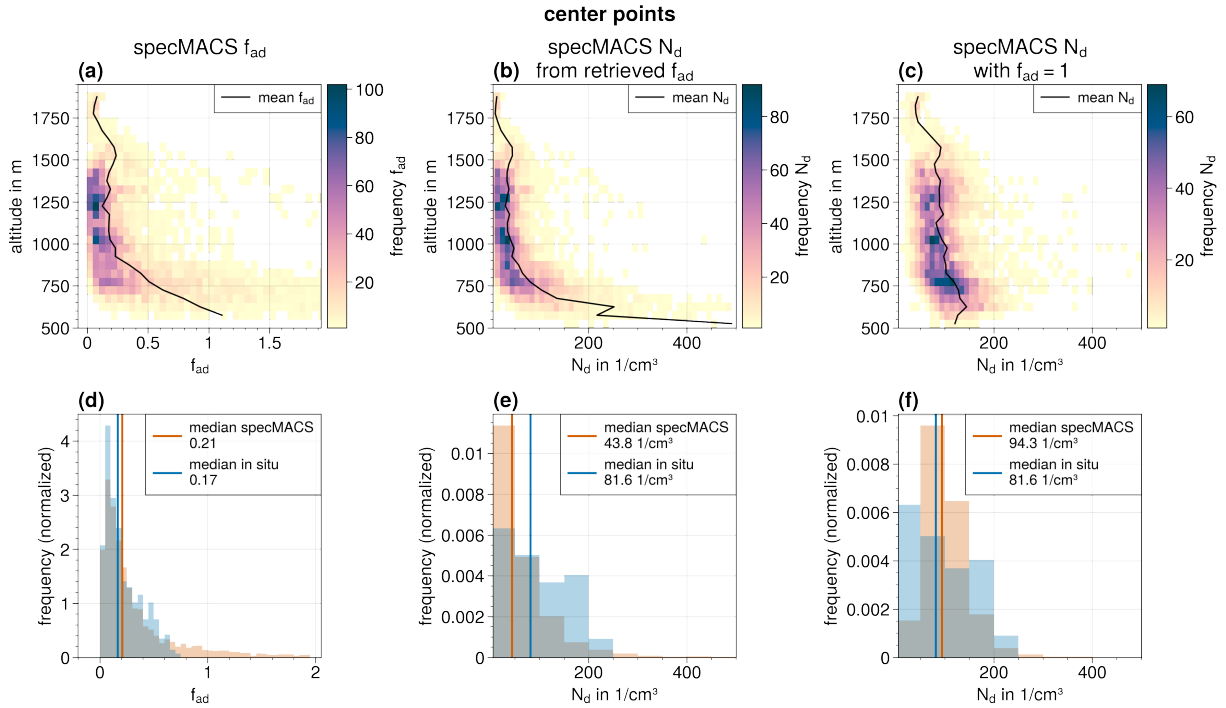

Figure 4.25: Same as Fig. 4.23 but only center points.

smaller than the effect of the cloud base height ($f_{ad} \sim \tau_c$). The current τ_c retrieval is a 1-D retrieval which assumes a homogeneous cloud layer. This might lead to a significant underestimation of the true τ_c as shown in Cornet and Davies (2008) which could partly explain the derivation of small f_{ad} (except for the cloud base).

Based on the presented results using the retrieved f_{ad}, there is an exciting possible application concerning the fractional rate of entrainment, which will be presented below. The fractional rate of entrainment ϵ is usually derived from the height change of conserved quantities such as the equivalent potential temperature or the total water mixing ratio (see Section 2.3.4). There are no information about these quantities from the spec-MACS measurements. However, there is the information about the adiabaticity's vertical change. Although f_{ad} is not a conserved quantity, the change of f_{ad} with height should also be related to the entrainment fractional rate. The adiabaticity (= ratio of observed LWC to LWC_{ad}) depends non-linearly on the conserved quantities (equivalent potential temperature and total water mixing ratio). Therefore, f_{ad} is a good qualitative indicator of entrainment but cannot be used for quantifying ϵ. Theoretical models suggest that the entrainment fractional rate should be inversely related to the cloud radius which was already introduced in the theory chapter of this thesis (Chapter 2.3.4, see Equation 2.41). This assumption is tested on the derived adiabaticity with the model

$$f_{ad}(z) = \exp[-\epsilon(z - z_b)], \tag{4.5}$$

with $\epsilon = \frac{\eta}{R}$ (Morton et al., 1956).

Figure 4.26 shows the results of applying this model to the data. The first column shows the results for all points and the other two columns for the edge and center points respectively. As in Figure 4.23, the vertical profiles of f_{ad} are shown here in the first row, but this time the individual data points are displayed and the color indicates the cloud diameter. The cloud diameter was estimated when grouping the individual CDSD data points into clouds (see description in Section 3.5), based on the distance between the most distant points on the concave hull of one cloud cluster. There is a relatively smooth transition from large clouds at higher altitudes having larger f_{ad} to smaller clouds which is best observed in the left column were all points of the sample dataset are used. The individual scatterpoints overlap meaning that there could be large clouds in areas where mostly small clouds appear in the visualization as shown in the first row. This could distort the interpretation, and therefore, the individual points were binned into boxes weighted with the diameter of the cloud the point belongs to. The resulting figures are shown in the second row. The transition from large clouds to smaller clouds is also visible in these figures.

The colored lines in the first two rows show the fits to the points according to the cloud size dependent model (Equation 4.5) for three cloud sizes (500 m, 1000 m and 4000 m). The last row shows the corresponding entrainment fractional rates ϵ which are found from the three fitting curves. The smallest clouds have the largest entrainment fractional

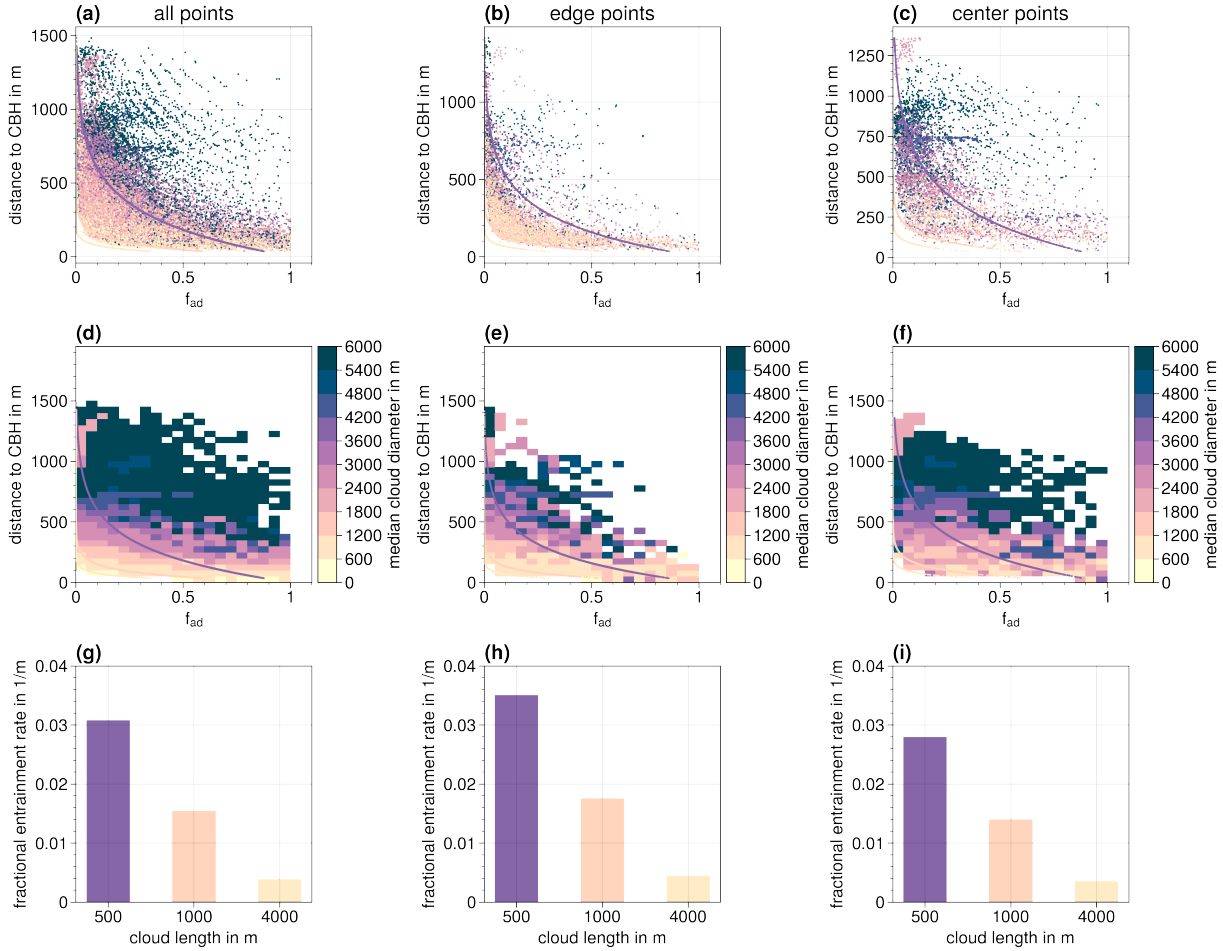

Figure 4.26: Entrainment study with cloud size using all points (first column), only edge points (second column) and only center points (last column). For all three categories, the vertical profile of retrieved f_{ad} are shown plotted as individual points (first row), and plotted as 2-D binning (second row). The colors indicate the corresponding cloud size. In addition, the fits for three cloud sizes are plotted. The corresponding entrainment fractional rate ϵ for the fits corresponding to the three different cloud sizes is shown in the bottom row.

rate (purple), and ϵ is highest in the analysis using the edge points (panel (h)). The range of retrieved ϵ ($0.005\,\mathrm{m}^{-1}$ to $0.03\,\mathrm{m}^{-1}$) is slightly higher than typical literature values (e.g. $0.002\,\mathrm{m}^{-1}$ in Siebesma et al. (2003)). As already stated, f_{ad} is not a conserved quantity and a quantitative interpretation of the retrieved ϵ is debatable. Still, the qualitative result showing that a higher ϵ is found in specMACS observations of smaller clouds is interesting.

These results show that at least the information contained in the vertical profile of the retrieved f_{ad} can be further evaluated, although the validity of the absolute values of f_{ad} may be subject to large uncertainties especially due to uncertainties related to the estimation of the distance to the cloud base. For future work, targeted flights with

simultaneous in situ observations of vertical profiles could be extremely helpful to obtain a better quantification of f_{ad} that could be used to validate the specMACS f_{ad}. Until this is done, it is difficult to comment on the accuracy and scientific value of this method.

4.3.3 Model perspective on entrainment and mixing

The results of the last two sections will be discussed and compared with findings from the recent studies by Lim and Hoffmann (2023a) and Lim and Hoffmann (2023b). This section should be considered as a discussion section, which is used to put the observations into the context of the results from the model studies.

The two studies investigated entrainment and mixing in a single cumulus congestus (Lim and Hoffmann, 2023a) and in a shallow cumulus field (Lim and Hoffmann, 2023a). For this purpose, they used the L3 model (LES-LCM-LEM) developed by Hoffmann et al. (2019). The L3 model couples a large eddy simulation (LES) with a Lagrangian cloud model (LCM) and the linear eddy model (LEM), a statistical turbulence model. The basic concept of this coupling is explained in the following, and the reader is referred to Hoffmann et al. (2019) for a more detailed description.

Large eddy simulations are commonly used to simulate boundary layer meteorological processes at relatively high spatial resolutions for sufficiently large domains to also allow mesoscale cloud organizations to be included. Sub-grid scale processes are usually parameterized in LES simulations (Guichard and Couvreux, 2017). There are numerous studies where LES simulations have been used to study cumulus cloud dynamics, and entrainment and mixing processes (de Rooy et al., 2013). In Lim and Hoffmann (2023a) and Lim and Hoffmann (2023b), the LES setup had a spatial resolution of about 50 m. The Lagrangian cloud model (LCM) tracks individual particles or super-droplets which represent a certain number of identical aerosol particles or droplets (Hoffmann et al., 2019). The model allows to consider various cloud microphysical processes that impact the particles (e.g. interactions between the particles, diffusional growth or evaporation). The last model of the L3 model is the linear eddy model which is used to describe subgrid scale turbulent mixing processes. It predicts turbulence fluctuation of supersaturation. Lim and Hoffmann (2023a) and Lim and Hoffmann (2023b) use a spatial resolution of 40 cm for the LEM. By coupling the LES to the LCM and the LEM, the representation of small scale mixing processes is greatly improved in the simulations, and the L3 model setup is ideally suited to study entrainment and mixing processes. Hoffmann et al. (2019) showed that especially the process of inhomogeneous mixing is accurately predicted using the L3 model which is not the case for common LES.

The difference between the CDSDs of edge and center regions of the cloud can also be studied with the simulations from the L3 model. This is shown in Figure 4.27a where the vertical profile of r_{eff} inside typical shallow cumulus clouds is displayed. The figures were provided by Jung-Sub Lim (personal communication, 2024) based on the model setup published in Lim and Hoffmann (2023b). In Fig. 4.27a, the cloud core (solid lines)

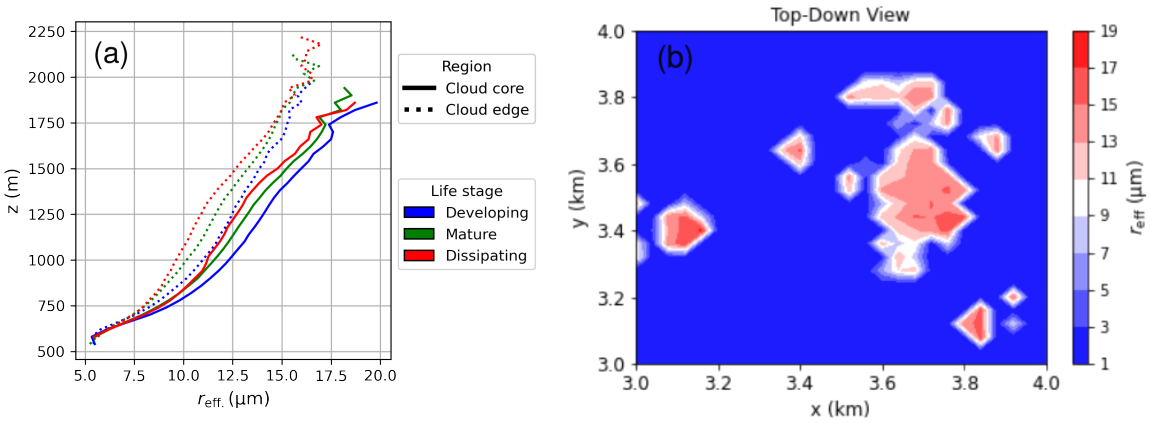

Figure 4.27: (a): Vertical profile of r_{eff} of the L3 model simulation of shallow cumulus clouds. (b): Top down view on parts of the simulated cloud field. The figures were provided by Jung-Sub Lim (personal communication, 2024) based on the model setup described in Lim and Hoffmann (2023b).

is defined as the region where both the vertical velocity and the buoyancy are positive, and in the edge region (dashed lines) they are negative. The r_{eff} profile is shown at three different life stages of the cumulus cloud indicated by the color (developing, mature and dissipating). Overall, the model results show that the core region has higher r_{eff} compared to the CDSDs of the edge region at the same altitude with differences of approximately 2 µm caused by entrainment and mixing at the cloud edge. The panel (b) in Figure 4.27 illustrates a top-down view on the modeled r_{eff} field showing the highest cloud layer from above. This figure shows that the transition region where r_{eff} decreases at the edge of the cloud is often very thin. With the current specMACS CDSD spatial resolution of approximately 100 m it is not possible to accurately capture this transition region. Furthermore, the highest r_{eff} are not located in the geometric center of the cloud.

Figure 4.28 shows another model view of entrainment in shallow cumulus clouds and reproduces Figure 1 from Lim and Hoffmann (2023a) (used under CC BY 4.0). The figure displays a cross-section of the adiabaticity distribution in a cumulus congestus cloud simulated with the L3 model. f_{ad} is close to one at the cloud base and decreases towards the top. In addition, it reduces approaching the edges of the cloud. Moreover, there are streams of high adiabaticity running through almost the whole cloud but they are not necessarily in the actual (horizontal) center of the cloud. A similar picture is shown in the model study by Eytan et al. (2021).

Overall this comparison demonstrates that the results from the specMACS observations confirm the findings from the model study, and the observations can be used to study mixing processes in more detail. Nevertheless, the presented analysis of the specMACS data in Section 4.3.1 could be improved. First, entrainment and mixing occur on very small scales as shown in the model simulations. The spatial resolution of approximately 100 m in the specMACS CDSD dataset should be increased to more

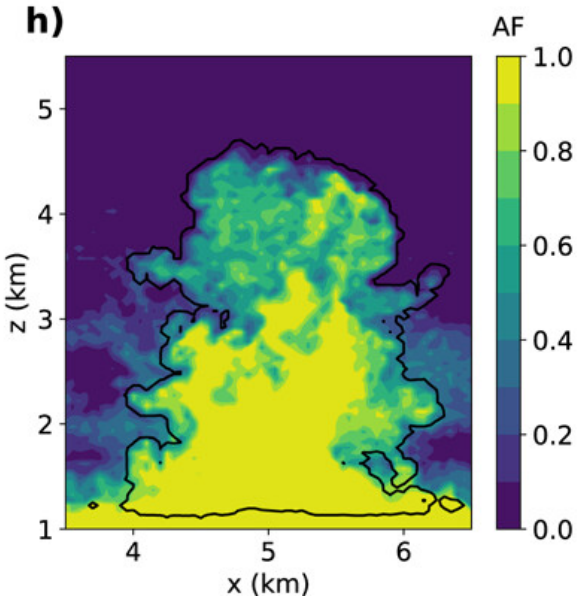

Figure 4.28: Adiabatic fraction (f_{ad}) inside a shallow cumulus cloud of a simulation of the L3 (LES-LCM-LEM) model. Reproduced from Figure 1 in Lim and Hoffmann (2023a) (CC BY 4.0 license). The original figure was cropped to only include panel (h).

accurately observe the change in the CDSD due to entrainment. Moreover, the separation into edge and center points based mainly on the geometric center of the clouds is not robust since the model results show that the regions in the cloud that are unaffected by entrainment and mixing are not necessarily located in the geometric center. As already stated, Lim and Hoffmann used the vertical velocity and buoyancy data to separate the cloud core from the cloud edge in Fig. 4.27a. Applying the same criterion to the specMACS observations would be useful. For this purpose, the HAMP doppler radar measurements could be used to estimate possible updraft and downdraft regions in the clouds but the radar signal of the EUREC^{4}A measurements is only available below the aircraft track and usually very weak for such shallow cumulus clouds due to the large distance of the airplane to the clouds. In addition, it has a much lower resolution compared with the specMACS resolution. Furthermore, a study of radiative transfer simulations similar to Volkmer et al. (2023) but based on the cloud simulations from Lim and Hoffmann (2023b), where up- and downdrafts are known, could be used to study and compare different separation criteria. Finally, comparisons with high-resolution in situ measurements such as in Gerber et al. (2008) would help in interpreting our measurements. Vertical profiles of in situ data would be particularly helpful here.

Nevertheless, the analysis from Section 4.3.1 shows that differences in the CDSDs between edge and center regions of clouds are visible in the specMACS data, and they are comparable to the differences seen in the model data by Lim and Hoffmann (2023b). This shows that the specMACS observations provide information about mixing processes,

and proves that such processes, which have previously been studied mainly from in situ measurements, can also be studied from passive remote sensing measurements but a high spatial resolution is necessary.

Chapter 5

Summary and outlook

5.1 Summary

Uncertainties of climate models are mostly caused by the representation of clouds. This is partly due to the poor spatial resolution of climate models that cannot capture the processes taking place in clouds, but also caused by the fact that many of these processes are not yet fully understood. An essential property of clouds is their droplet size distribution, which determines the radiative properties of clouds and is important for precipitation formation. Observations of the cloud droplet size distribution (CDSD) are either rare (in situ measurements) or subject to large uncertainties (satellite observations) because retrievals rely on many assumptions. In recent years, the use of polarimetric observations both from airborne as well as space-borne instruments has become popular. Polarized measurements have the advantage of reducing retrieval uncertainties through minimization of multiple-scattering contributions in the signal. A sophisticated method is the polarimetric cloudbow retrieval which retrieves the CDSD of liquid water clouds from multi-angle measurements of the cloudbow (e.g. Bréon and Goloub, 1998; Alexandrov et al., 2012a; McBride et al., 2020). This thesis focused on liquid water clouds, although ice clouds of course also play an important role in Earth's climate.

The goal of this work was to study the CDSDs of shallow cumulus clouds from airborne observations of the specMACS instrument onboard the German research airplane HALO. For this purpose, a polarimetric cloudbow retrieval was developed for the observations of the specMACS polarization cameras. The cloudbow forms through single-scattering by liquid cloud droplets at cloud top and its signal is sensitive to the effective radius (r_{eff}), and to the effective variance (v_{eff}) of the size distribution in the scattering angle range from 135° to 165°. The r_{eff} is an area-weighted mean radius, thus giving greater weight to larger droplets which contribute more significantly to scattering processes, and v_{eff} determines the width of the size distribution. The specMACS polarization cameras measure 2-D polarized radiance distributions in which the same cloud is observed from different viewing angles during an overflight. These individual mea-

surements of the same cloud are aggregated into polarized radiance measurements from different scattering angles. This produces a multi-angle measurement of the cloudbow. The aggregation process includes a precise geolocation of the cloud targets which defines the 3-D coordinates of the approximately 100 m × 100 m targets. For this purpose, the viewing directions of the individual pixels are combined with cloud top height data which are determined using an existing stereographic approach (Kölling et al., 2019; Volkmer et al., 2024). A lookup table of pre-calculated cloudbow signals for different CDSDs is fitted to the aggregated signal to determine r_{eff} and v_{eff} of the cloud target. The retrieved CDSD parameters are combined into spatial maps which allow to study the spatial distribution of the CDSD.

The retrieval method introduced in detail in the first part of the thesis, and published in Pörtge et al. (2023), was first validated based on a comparison with in situ measurements. Good agreement was found, but limitations due to temporally and spatially not perfectly coincident measurements became apparent. This observational comparison is extended in Koppenhofer (2024) using available operational satellite data with similar results. To further validate the retrieval results, an evaluation based on synthetic test data was carried out by Volkmer et al. (2023). To this end, measurements were simulated with the radiative transfer model MYSTIC using cloud model data of shallow cumulus clouds generated with the PALM LES model. It allowed a more flexible investigation of the method's accuracy in which the full cloudbow retrieval was tested, including the determination of the cloud geometry using the stereographic approach, the aggregation of the cloudbow signal, and the fit of the pre-calculated LUT to the aggregated signal. The results showed very good agreement between the derived and modeled ("true") r_{eff} with an average deviation of 0.2 µm (standard deviation: 1.3 µm), and an average deviation of 0.02 in v_{eff} (standard deviation: 0.05). This evaluation provided additional confidence in the retrieval results, and showed that the cloudbow retrieval is highly applicable to small cumulus clouds, where traditional bispectral retrievals (Nakajima and King, 1990) have large uncertainties due to multiple-scattering caused by 3-D radiative transfer effects that are usually not considered.

In addition, a retrieval of the droplet number concentration N_{d} was presented, which is a crucial parameter for estimating the effect of aerosol–cloud interactions. The retrieval is based on the (satellite) retrieval presented in Grosvenor et al. (2018b) assuming a sub-adiabatic cloud model which provides a theoretical framework for understanding how clouds evolve vertically. This model is based on the theoretical adiabatic cooling during the vertical ascent of the air inside a cloud and the related increase of liquid water content. However, real-world conditions involve the mixing of dry air into the cloud, causing the actual liquid water content to deviate from the theoretically predicted adiabatic values. This deviation is quantified by the parameter known as adiabaticity (f_{ad}).

In order to derive N_{d} using the thus sub-adiabatic model, the cloud optical thickness τ_{c} is required. For this purpose, the r_{eff} retrievals from the cloudbow technique were

combined with the corresponding unpolarized reflectance measurements of the camera in the visible wavelength range, and a LUT of pre-calculated reflectances was fitted to the measurements to determine τ_c. In a next step, the adiabatic N_d was determined which most strongly depends on r_{eff}. It was demonstrated that the retrieved N_d have a lower uncertainty compared with similar satellite retrievals because of the highly accurate r_{eff} retrievals using the cloudbow technique. The deviation of the derived N_d from the theoretical adiabatic model was analyzed. In addition, a method to derive f_{ad} was presented which depends on r_{eff}, τ_c and the distance to the cloud base height.

Three scientific studies based on the developed methods were presented. First, the variation of the CDSD and droplet number concentration during the EUREC^{4}A campaign was evaluated. The campaign median r_{eff} is 10 µm and the median v_{eff} is 0.1. The droplet number concentrations showed a moderate correlation to in situ measurements although the retrieved N_d are affected by uncertainties in the cloud optical thickness and the assumed cloud's adiabaticity. The analysis showed that r_{eff} increased with height, as expected from the adiabatic cloud theory. However, the strength of the increase varied from day to day. Overall, the effective variance showed a higher variability than the effective radius at all vertical levels. The vertical profiles of v_{eff} showed no clear trend with height.

Second, the CDSDs were analyzed in the context of the cloud organization, which is commonly categorized into four different mesoscale patterns (fish, flower, gravel and sugar) (Stevens et al., 2020). The C^{3}ONTEXT dataset (Schulz, 2022a,b) was presented which provides information about the pattern classification probability based on the outcome of a manual labeling process done by 50 scientists. The scientists analyzed the satellite images from the campaign period to determine the dominant mesoscale pattern. The resulting classification probability from the C^{3}ONTEXT dataset was used to identify the prevailing mesoscale pattern for the time and position of each data point of the specMACS CDSD dataset, providing valuable insights into the relationship between cloud microphysical properties and mesoscale organization. Previous studies (e.g. Schulz et al., 2021) showed that the mesoscale patterns differ in terms of precipitation amount and cloud coverage. The analysis of the CDSD showed that patterns associated with precipitation (especially fish) also have large effective radii. The sugar pattern consists mostly of shallow cumulus clouds in which precipitation is usually not observed and the analysis indicated small $r_{eff} < 15$ µm. No significant differences were found between the four patterns regarding v_{eff}.

Finally, it was analyzed whether effects caused by entrainment and mixing of ambient dry air into the cloud are visible in the retrieved CDSDs. Entrainment and mixing affect the formation and growth of cloud droplets which in turn impacts the evolution of the cloud itself. To study these effects, the points of the CDSD dataset of a scene of shallow cumulus clouds were separated into points that are located at the edges of the clouds, which are highly affected by entrainment, and points from the less affected center regions.

The analysis showed small but clear differences in r_{eff} and v_{eff} between the two groups with slightly higher r_{eff} in the center than at the edge (less than 1 µm deviation) and vice versa for v_{eff} (deviation of less than 0.02). In addition, it indicated a slight reduction of the droplet number concentration at the edge compared to the center. This observation is consistent with theoretical considerations investigating the effects of entrainment and mixing on the droplet size distribution which predict a reduced r_{eff} in the case of extreme homogeneous mixing and a reduced N_{d} in the case of extreme inhomogeneous mixing. The findings from the specMACS dataset were discussed with regard to the sophisticated cloud physics model study by Lim and Hoffmann (2023b) which showed slightly higher deviations in r_{eff} of approximately 2 µm between edge and center but also demonstrated that entrainment and mixing occur on very small spatial scales (< 50 m). Therefore, the current spatial resolution (about 100 m) of the CDSD dataset from specMACS data should be increased in future investigations to more accurately capture the effect of entrainment and mixing on the droplet size distribution.

The adiabaticity was retrieved from the same specMACS dataset of shallow cumulus clouds. Very small adiabaticities were found with an average $f_{\text{ad}} = 0.2$. This is not in accordance with literature values ($f_{\text{ad}} = 0.6$ to 0.8, e.g. Grosvenor et al. (2018b)), and could be related to uncertainties of the estimated τ_{c} or cloud base height. Nevertheless, a decrease of f_{ad} with height was observed which was also seen in the model study by Lim and Hoffmann (2023a). A theoretical relationship between the entrainment fractional rate and the size of the cloud was introduced (Morton et al., 1956). This was combined with the observed vertical profiles of f_{ad} in which also a cloud-size dependent f_{ad} was observed.

5.2 Suggested technical improvements of the cloudbow retrieval

Although the results from the cloudbow retrieval are already very accurate, a number of future development steps seem necessary based on this thesis' results.

- First, the polarization calibration was found to have unrealistic artifacts in the corners of the images. These artifacts disturb measurements at high solar zenith angles, such as during the high latitude HALO-(AC)^3 measurements, where the cloudbow appeared in the image corners. An example is shown in Figure 5.1, where the Q and U components relative to the scattering plane are shown in (b) and (c). In the region of the supernumerary bows, which mainly determines v_{eff}, a change from positive values (red) to negative values (blue) along one scattering angle contourline (e.g. along the 155° line) is apparent and the absolute values in U are similar to the values in Q although U should be considerably smaller since the Stokes vector is given relative to the scattering plane. This calibration artifact can

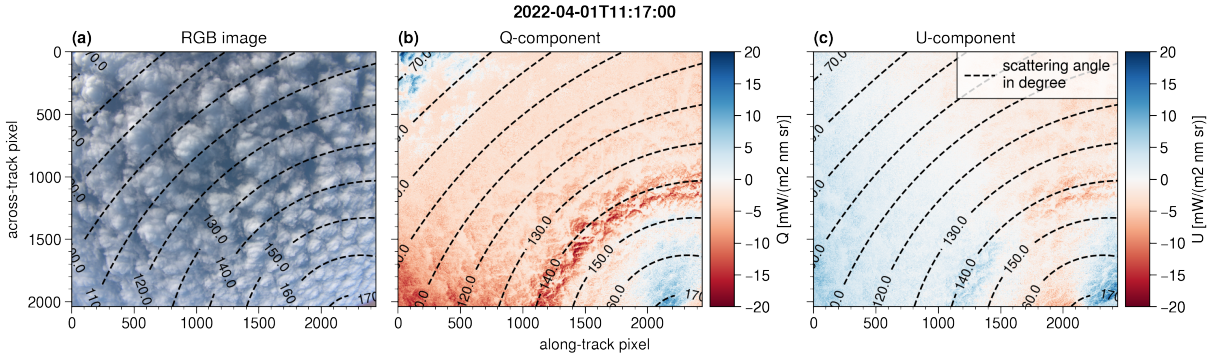

Figure 5.1: Measurement of the polLR camera taken during the HALO-(AC)^3 campaign. Panel (a): RGB image; (b): Calibrated Q-component of the measured Stokes vector rotated into the scattering plane; (c): Calibrated U-component of the measured Stokes vector rotated into the scattering plane; The dashed lines indicate lines of constant scattering angle in degree.

interfere with the retrieval of v_{eff}. The artifact arises because only the central parts of the field of view were measured during the laboratory calibration in 2021 (Weber et al., 2024). It should be investigated which polarization measurements could be feasible that would improve the calibration. In addition, two sideward-looking polarization cameras will be added to the specMACS instrument in 2024. For cases with high solar zenith angles, the cloudbow will then be visible in the central parts of the images of the sideward-looking cameras where the polarization calibration yields good results.

- Often, it was found that the model fit was smoother than the actual measurement especially in the region of the supernumerary bows of the cloudbow (e.g. in Figure 3.6). The cause of this smoothing is not understood and should be investigated further. One effect that could modify the signal is Rayleigh scattering but this would smooth the measurement and not the model fit as observed. Still, it could modify the signal in a way that the calculated LUT does not perfectly fit the measurements, and in the end, a smoother fit is preferred. Nevertheless, an approximate correction for the viewing angle dependent Rayleigh scattering contribution could be implemented.

- The parametric cloudbow retrieval assumes that the size distribution can generally be represented by a monomodal modified gamma distribution. However, this assumption may not always hold true. To overcome this assumption, the Rainbow Fourier Transform (RFT) can be used which retrieves the actual CDSD without relying on assumptions about its shape. The RFT was developed in Alexandrov et al. (2012b), and was for the first time applied to specMACS data in Bernlochner (2023). Obtaining the actual DSD is also beneficial in retrieving the droplet number concentration as shown in Sinclair et al. (2019). Therefore, an operational implementation

of the RFT is recommended for specMACS measurements.

- A further possible improvement concerns the aggregation of the polarization signal which requires a precise geolocation. This is influenced by the horizontal movement of the clouds due to the ambient wind that is currently considered using wind data from the global ERA5 weather model reanalysis dataset. The ERA5 dataset has a relatively coarse spatial resolution compared to the specMACS data. To improve geolocation precision, the integration of a wind dataset with higher spatial resolution is worth exploring. One such dataset is the wind data derived from the stereographic matching (Kölling et al., 2019). Barbara Damböck is currently investigating the scientific significance, accuracy, and usability of the stereographic wind dataset in her Bachelor's thesis (Damböck, 2024).

- The presented analysis of entrainment and mixing effects suggests increasing the spatial resolution of specMACS retrievals for future studies. For cloud measurements, the spatial resolution is impacted by the accuracy of the retrieved cloud top height. The CTH accuracy of approximately 100 m can lead to geolocation errors of about 80 m for large viewing angles. An improved geometric calibration which also reduces uncertainties in the CTHs could potentially achieve a resolution of the cloudbow retrievals of < 50 m compared to the current resolution of 80 m to 100 m. Alternatively, flying closer to the clouds would increase spatial resolution, albeit with reduced coverage.

- A further point where the cloudbow retrieval could be improved is related to cloud shadows. The cloudbow is not visible or at least reduced in shadowed regions of the cloud depending on the optical thickness of the cloud that generates the shadow (see Fig. 5.1b). Most of the time, such shadowed regions are filtered from the final results based on the fit criteria but they could also be excluded from the processing using the geometric shadow mask determined from the stereographic points developed in Kölling (2020).

- A similar retrieval technique as presented for the cloudbow measurements can be applied to measurements of the backscatter glory. The glory has the disadvantage of covering a much smaller area but is therefore also sampled in a much shorter time. The shorter sampling time reduces the impact of a movement of the target due to the ambient wind, and mitigates changes of the CDSD due to cloud evolution which is beneficial for the retrieval.

- The last two points that are presented are not related to technical aspects of the cloudbow retrieval but to improvements regarding the method of retrieving droplet number concentrations. Due to the high accuracy of the r_{eff} retrieved using the cloudbow technique, the presented droplet number concentrations (which strongly depend on r_{eff}) already have a lower uncertainty than similar satellite retrievals.

As shown in this thesis, the first comparison of the retrieved N_d with in situ data looked promising. Nevertheless, the actual accuracy of the specMACS N_d retrievals should be studied in the future in more detail. For this purpose, the model-based evaluation study of Volkmer et al. (2023) could be extended to also carry out a comparison of the retrieved and modeled cloud optical thickness and the corresponding droplet number concentration.

- The retrieved adiabaticities exhibited small average values, but close to the cloud base unrealistically large values. A key factor affecting adiabaticity that was discussed is the cloud base height (CBH). The CBH is estimated from an approximate method using dropsonde measurements, since none of the instruments of the EUREC^{4}A-HALO payload is capable of providing a better estimate. However, the CBH is a frequently requested parameter for different scientific purposes, so the development of new retrieval methods is recommended. For this purpose, the sideward-looking cameras may be useful to determine the typical lower boundary of the clouds from the images using the stereographic technique. Although such a retrieval might have relatively large uncertainties due to the viewing geometry, it is still a new source of CBH data that would be particularly useful for measurement campaigns when dropsonde measurements are unavailable.

5.3 Future work

specMACS offers great potential for further evaluations of clouds going beyond the study of liquid water clouds. In future, the measurements of the different specMACS cameras (polarimetric and hyperspectral) will be combined to, for example, retrieve information about the vertical variation of cloud microphysical properties inside the cloud or to identify the thermodynamic phase of the observed clouds. First steps to create a coupled polarimetric and hyperspectral method to retrieve the ice crystal r_{eff}, τ_c and habit type were presented in Erdtmann (2023). Furthermore, preliminary results by Anna Weber show that the polarimetric signal can be successfully exploited to retrieve the ice fraction of mixed phase clouds (personal communication, 2024). In addition, the HALO remote sensing payload makes it possible to deepen the understanding of clouds by combining the measurements of the different instruments. For example, the aerosol retrievals of the WALES instrument (e.g. Gutleben et al., 2020; Groß et al., 2016) could be combined with the specMACS CDSD retrievals to study the relationship between aerosol particles and cloud droplets. Although there are also methods that retrieve aerosol properties directly from multi-angle polarimetric observations (Hasekamp et al., 2011; Wu et al., 2015), these are probably not applicable to the specMACS observations because the absolute calibration of specMACS is not accurate enough. Nevertheless, a feasibility study would be interesting. Further HALO observations that could be combined with

the specMACS products include the HAMP radar observations which could be used to study the relationship between the cloud droplet size distribution and the occurrence of precipitation in more detail. For the development of new retrievals it is recommended to also continue working on observational comparisons of the retrieval results. Future comparisons could be based on the in situ data of other HALO measurement campaigns where specMACS participated (CIRRUS-HL and HALO-(AC)^3). In these campaigns, also ice and mixed-phase clouds were measured.

The newly launched PACE satellite with two polarimeters onboard is an exciting opportunity where the high-spatial resolution specMACS measurements could help to validate the satellite retrievals. Recently, the specMACS data were also used at a reduced spatial resolution to imitate satellite measurements (Emde et al., 2024). This work showed that the multi-angle polarized signal not only contains information about the CDSD and the phase of the cloud, but can also be exploited to simultaneously determine the (subpixel) cloud fraction and cloud optical thickness. This could be useful for satellite measurements with typical pixel sizes of approximately 2.5 km.

Finally, the upcoming PERCUSION/ORCESTRA HALO-campaign[1] in August and September 2024 in Cape Verde and Barbados offers great potential for studying deep convective clouds near the equator in which both liquid cloud droplets and ice particles are present. The instruments onboard HALO will be the same as during EUREC^{4}A with the difference that the specMACS camera system is extended by the two sideward-looking polarization cameras. These measurements will enable the observation of the cloudbow at cloud sides which allows the retrieval of vertical profiles of the CDSD within a single cloud similar to Ewald et al. (2019). Concerning the specMACS measurements, the scientific objectives of the campaign are to deepen the observational understanding of entrainment and mixing processes, to study ice particle formation, and to investigate the microphysical properties of cumulus clouds at different stages of their development. The influence of a cloud's development stage on the dominant mixing mechanism has been investigated in a recent study (Lim and Hoffmann, 2023b), and it would be interesting to study this effect from observations as well. The multi-platform (aircraft, research vessel, ground-based stations, and satellites) and multi-location (Cape Verde and Barbados) measurement approach allows a broad investigation of cloud properties, which will certainly improve the overall understanding of clouds.

[1] `https://orcestra-campaign.org` (accessed on 19-03-2024)

Appendix A

Derivation of the droplet number concentration equation

In this appendix, the equation that determines N_d will be derived similar to Grosvenor et al. (2018b):

$$N_\mathrm{d} = \frac{\sqrt{5}}{2\pi k}\left(\frac{f_\mathrm{ad} C_\mathrm{w} \tau_c}{Q_\mathrm{ext}\rho_\mathrm{w} {r_\mathrm{eff,top}}^5}\right)^{1/2} \tag{A.1}$$

For this, we will first introduce the effective radius r_eff:

$$r_\mathrm{eff} = \frac{\int_0^\infty r\pi r^2 n(r)\mathrm{d}r}{\int_0^\infty \pi r^2 n(r)\mathrm{d}r}; \tag{A.2}$$

r_eff is connected to the volume-mean droplet radius via the empirical factor k (Martin et al., 1994):

$$r_\mathrm{v}^3 = k r_\mathrm{eff}^3 \tag{A.3}$$

The LWC of spherical particles is defined as:

$$\mathrm{LWC} = \frac{4\pi\rho_\mathrm{w}}{3}\int_0^\infty r^3 n(r) dr = \frac{4}{3}\pi k r_\mathrm{eff}^3 N_\mathrm{d}\rho_\mathrm{w} \tag{A.4}$$

r_eff can also be expressed in terms of LWC and we assume that the LWC is a fraction of its adiabatic value ($\mathrm{LWC} = f_\mathrm{ad} C_\mathrm{w}(z - z_\mathrm{base})$):

$$r_\mathrm{eff}(z) = \left(\frac{3\mathrm{LWC}(z)}{4\pi\rho_\mathrm{w} k N_\mathrm{d}(z)}\right)^{1/3} = \left(\frac{3 f_\mathrm{ad} C_\mathrm{w} z}{4\pi\rho_\mathrm{w} k N_\mathrm{d}(z)}\right)^{1/3} \tag{A.5}$$

For a distribution of spherical particles, β_{ext} can be expressed as:

$$\beta_{\text{ext}} = \pi \int_0^\infty Q_{\text{ext}}(r) r^2 n(r) dr \tag{A.6}$$

The vertical integral of β_{ext} between the cloud base (z_{base}) and the cloud top (z_{top}) is the cloud optical thickness τ_c:

$$\tau_c = \int_{z_{\text{base}}}^{z_{\text{top}}} \beta_{\text{ext}}(z) dz \tag{A.7}$$

Q_{ext} can be approximated by 2. Combining Equation A.4 together with Equation A.2 shows that β_{ext} can also be expressed in terms of r_{eff} and LWC:

$$\beta_{\text{ext}}(z) = \frac{3 Q_{\text{ext}} \text{LWC}(z)}{4 \rho_{\text{w}} r_{\text{eff}}(z)} \tag{A.8}$$

This can be further reformulated into the following equation using Equation A.5:

$$\begin{aligned} \beta_{\text{ext}}(z) &= \frac{3 Q_{\text{ext}} \text{LWC}(z) (4\pi \rho_{\text{w}} k N_{\text{d}}(z))^{1/3}}{4 \rho_{\text{w}} (3\text{LWC}(z))^{1/3}} = \\ &= Q_{\text{ext}} \left(\frac{3 f_{\text{ad}} C_{\text{w}}}{4 \rho_{\text{w}}} \right)^{2/3} (N_{\text{d}} \pi k)^{1/3} (z - z_{\text{base}})^{2/3} \end{aligned} \tag{A.9}$$

Inserting this into Equation A.7 yields:

$$\tau_c = \int_{z_{\text{base}}}^{z_{\text{top}}} \beta_{\text{ext}}(z) dz = \int_{z_{\text{base}}}^{z_{\text{top}}} Q_{\text{ext}} \left(\frac{3 f_{\text{ad}} C_{\text{w}}}{4 \rho_{\text{w}}} \right)^{2/3} (N_{\text{d}} \pi k)^{1/3} (z - z_{\text{base}})^{2/3} dz \tag{A.10}$$

If we assume that N_{d} is constant with height and if we introduce the cloud geometrical depth H, this equation can be reformulated as:

$$\tau_c = \frac{3 Q_{\text{ext}}}{5} \left(\frac{3 f_{\text{ad}} C_{\text{w}}}{4 \rho_{\text{w}}} \right)^{2/3} (N_{\text{d}} \pi k)^{1/3} H^{5/3} \tag{A.11}$$

$$N_{\text{d}} = \left(\frac{5 \tau_c}{3 Q_{\text{ext}}} \right)^3 \left(\frac{4 \rho_{\text{w}}}{3 f_{\text{ad}} C_{\text{w}}} \right)^2 \frac{1}{\pi k H^5} \tag{A.12}$$

We then define the effective radius at cloud top $r_{\text{eff,top}}$ using Equation A.5:

$$r_{\text{eff,top}} = \left(\frac{3 f_{\text{ad}} C_{\text{w}} H}{4 \pi \rho_{\text{w}} k N_{\text{d,top}}} \right)^{1/3} \tag{A.13}$$

$$H = {r_{\text{eff,top}}}^3 \frac{4\pi\rho_{\text{w}} k N_{\text{d,top}}}{3 f_{\text{ad}} C_{\text{w}}} \tag{A.14}$$

Then, Equation A.11 is reformulated as:

$$\begin{aligned} \tau_c &= \frac{3Q_{\text{ext}}}{5}\left(\frac{3 f_{\text{ad}} C_{\text{w}}}{4\rho_{\text{w}}}\right)^{2/3} (N_{\text{d}}\pi k)^{1/3} H^{5/3} = \\ &= \frac{3Q_{\text{ext}}}{5}\left(\frac{3 f_{\text{ad}} C_{\text{w}}}{4\rho_{\text{w}}}\right)^{2/3} (N_{\text{d}}\pi k)^{1/3} \left({r_{\text{eff,top}}}^3 \frac{4\pi\rho_{\text{w}} k N_{\text{d,top}}}{3 f_{\text{ad}} C_{\text{w}}}\right)^{5/3} = \\ &= \frac{Q_{\text{ext}}}{5}\frac{\rho_{\text{w}}}{f_{\text{ad}} C_{\text{w}}} {r_{\text{eff,top}}}^5 (2N_{\text{d}}\pi k)^2 \end{aligned} \tag{A.15}$$

This can be rearranged to the equation that determines N_{d}:

$$N_{\text{d}} = \frac{\sqrt{5}}{2\pi k}\left(\frac{f_{\text{ad}} C_{\text{w}} \tau_c}{Q_{\text{ext}} \rho_{\text{w}} {r_{\text{eff,top}}}^5}\right)^{1/2} \tag{A.16}$$

Appendix B

Derivation of the adiabaticity equation

In this appendix, we will derive the formula for the f_{ad} retrieval:

$$f_{\mathrm{ad}} = \frac{20\rho_{\mathrm{w}}\tau_c r_{\mathrm{eff}}}{9C_{\mathrm{w}}Q_{\mathrm{ext}}(z - z_{\mathrm{base}})^2} \tag{B.1}$$

First, the LWC is defined:

$$\mathrm{LWC} = \frac{4\pi\rho_{\mathrm{w}}}{3}\int_0^\infty r^3 n(r)dr = \frac{4}{3}\pi r_{\mathrm{eff}}^3 k N_{\mathrm{d}}\rho_{\mathrm{w}} \tag{B.2}$$

And we assume that the LWC is a fraction of its adiabatic value

$$\mathrm{LWC}(z) = f_{\mathrm{ad}}C_{\mathrm{w}}(z - z_{\mathrm{base}}) \tag{B.3}$$

From these two equations, the droplet number concentration can be expressed as:

$$N_{\mathrm{d}} = \frac{3}{4\pi r_{\mathrm{eff}}^3 k\rho_{\mathrm{w}}} f_{\mathrm{ad}}C_{\mathrm{w}}(z - z_{\mathrm{base}}) \tag{B.4}$$

The droplet number concentration defined in terms of r_{eff} and τ_c was already defined:

$$N_{\mathrm{d}} = \frac{\sqrt{5}}{2\pi k}\left(\frac{f_{\mathrm{ad}}C_{\mathrm{w}}\tau_c}{Q_{\mathrm{ext}}\rho_{\mathrm{w}}r_{\mathrm{eff}}^5}\right)^{1/2} \tag{B.5}$$

Combining Equation B.4 and Equation B.5 yields:

$$\frac{3}{4\pi r_{\mathrm{eff}}^3 k\rho_{\mathrm{w}}} f_{\mathrm{ad}}C_{\mathrm{w}}(z - z_{\mathrm{base}}) = \frac{\sqrt{5}}{2\pi k}\left(\frac{f_{\mathrm{ad}}C_{\mathrm{w}}\tau_c}{Q_{\mathrm{ext}}\rho_{\mathrm{w}}r_{\mathrm{eff}}^5}\right)^{1/2} \tag{B.6}$$

$$\frac{3}{2r_{\text{eff}}^3\rho_{\text{w}}}\sqrt{f_{\text{ad}}C_{\text{w}}}(z-z_{\text{base}}) = \sqrt{5}\left(\frac{\tau_c}{Q_{\text{ext}}\rho_{\text{w}}r_{\text{eff}}^5}\right)^{1/2} \tag{B.7}$$

$$\sqrt{f_{\text{ad}}} = \frac{2\sqrt{5}}{3\sqrt{C_{\text{w}}}(z-z_{\text{base}})}\left(\frac{\tau_c r_{\text{eff}}\rho_{\text{w}}}{Q_{\text{ext}}}\right)^{1/2} \tag{B.8}$$

$$f_{\text{ad}} = \frac{20\rho_{\text{w}}\tau_c r_{\text{eff}}}{9C_{\text{w}}Q_{\text{ext}}(z-z_{\text{base}})^2} \tag{B.9}$$

This is the same equation as for example used in Merk et al. (2016) but they derived this formula coming from the LWP.

Appendix C

Derivation of the adiabatic liquid water content variation with height

The change of the adiabatic liquid water content with height is derived in the following. First, the mixing ratio w and the saturation mixing ratio w_s are defined:

$$w = \epsilon \frac{e}{p-e} \quad \text{and} \quad w_\mathrm{s} = \epsilon \frac{e_\mathrm{s}}{p-e_\mathrm{s}} \tag{C.1}$$

We want to analyze the change of w_s with height z and apply the chain rule for this:

$$\frac{\mathrm{d}w_\mathrm{s}}{\mathrm{d}z} = \frac{\partial w_\mathrm{s}}{\partial e_\mathrm{s}} \frac{\mathrm{d}e_\mathrm{s}}{\mathrm{d}z} + \frac{\partial w_\mathrm{s}}{\partial p} \frac{\mathrm{d}p}{\mathrm{d}z} \tag{C.2}$$

The contribution related to the change of saturation vapor pressure e_s with height is expressed as:

$$\frac{\partial w_\mathrm{s}}{\partial e_\mathrm{s}} \frac{\mathrm{d}e_\mathrm{s}}{\mathrm{d}z} \tag{C.3}$$

The first part $\dfrac{\partial w_\mathrm{s}}{\partial e_\mathrm{s}}$ is reformulated as follows:

$$\frac{\partial w_\mathrm{s}}{\partial e_\mathrm{s}} = \frac{\partial (\epsilon \frac{e_\mathrm{s}}{p-e_\mathrm{s}})}{\partial e_\mathrm{s}} = \epsilon \left(\frac{1}{p-e_\mathrm{s}} + \frac{e_\mathrm{s}}{(p-e_\mathrm{s})^2} \right) = \epsilon \frac{p}{(p-e_\mathrm{s})^2} \tag{C.4}$$

For the second part $\left(\dfrac{\mathrm{d}e_\mathrm{s}}{\mathrm{d}z} \right)$, the Clausius-Clapeyron equation is introduced, which specifies the temperature dependence of pressure:

$$\frac{\partial e_\mathrm{s}}{\partial T} = \frac{l_\mathrm{v} e_\mathrm{s}}{R_\mathrm{v} T^2} \tag{C.5}$$

The Clausius-Clapeyron equation and the adiabatic lapse rate $-\frac{\mathrm{d}T}{\mathrm{d}z} = \Gamma_\mathrm{S}$ are inserted:

$$\frac{\mathrm{d}e_\mathrm{s}}{\mathrm{d}z} = \frac{\partial e_\mathrm{s}}{\partial T}\frac{\mathrm{d}T}{\mathrm{d}z} = \frac{l_\mathrm{v} e_\mathrm{s}}{R_\mathrm{v} T^2}(-\Gamma_\mathrm{S}) \tag{C.6}$$

With $R_\mathrm{v} = \frac{R_\mathrm{d}}{\epsilon}$, this leads us to:

$$\begin{aligned}\frac{\partial w_\mathrm{s}}{\partial e_\mathrm{s}}\frac{\mathrm{d}e_\mathrm{s}}{\mathrm{d}z} &= -\epsilon\frac{p}{(p-e_\mathrm{s})^2}\frac{e_\mathrm{s} l_\mathrm{v}}{R_\mathrm{v} T^2}\Gamma_\mathrm{S} = -\epsilon\frac{e_\mathrm{s}}{p-e_\mathrm{s}}\frac{p}{p-e_\mathrm{s}}\frac{l_\mathrm{v}\epsilon}{R_\mathrm{d} T^2}\Gamma_\mathrm{S} = \\ &= -w_\mathrm{s}\frac{p\epsilon}{p-e_\mathrm{s}}\frac{l_\mathrm{v}}{R_\mathrm{d} T^2}\Gamma_\mathrm{S} = -w_\mathrm{s}\frac{p}{e_\mathrm{s}}\frac{\epsilon e_\mathrm{s}}{p-e_\mathrm{s}}\frac{l_\mathrm{v}}{R_\mathrm{d} T^2}\Gamma_\mathrm{S} = \\ &= -w_\mathrm{s}^2\frac{p}{e_\mathrm{s}}\frac{l_\mathrm{v}}{R_\mathrm{d} T^2}\Gamma_\mathrm{S} = -w_\mathrm{s}^2\left(\frac{\epsilon}{w_\mathrm{s}}+1\right)\frac{l_\mathrm{v}}{R_\mathrm{d} T^2}\Gamma_\mathrm{S} = -w_\mathrm{s}(\epsilon + w_\mathrm{s})\frac{l_\mathrm{v}}{R_\mathrm{d} T^2}\Gamma_\mathrm{S}\end{aligned} \tag{C.7}$$

For the second part of Equation C.2 $\left(\frac{\partial w_\mathrm{s}}{\partial p}\frac{\mathrm{d}p}{\mathrm{d}z}\right)$, the hydrostatic equation together with the ideal gas law are used:

$$\frac{\mathrm{d}p}{\mathrm{d}z} = -\rho g = \frac{-pg}{R_\mathrm{d} T} \tag{C.8}$$

In this step, it is assumed that the vapor contribution to the density (ρ_v) can be neglected and $\rho = \rho_\mathrm{d} + \rho_\mathrm{v} \approx \rho_\mathrm{d}$. Inserting this into the second part of Equation C.2 leads to:

$$\begin{aligned}\frac{\partial w_\mathrm{s}}{\partial p}\frac{\mathrm{d}p}{\mathrm{d}z} &= \frac{\partial w_\mathrm{s}}{\partial p}\frac{(-pg)}{R_\mathrm{d} T} = \frac{\partial(\epsilon\frac{e_\mathrm{s}}{p-e_\mathrm{s}})}{\partial p}\frac{(-pg)}{R_\mathrm{d} T} = \frac{\epsilon e_\mathrm{s}}{(p-e_\mathrm{s})^2}\frac{pg}{R_\mathrm{d} T} = \\ &= \epsilon\frac{e_\mathrm{s}}{p-e_\mathrm{s}}\frac{1}{p-e_\mathrm{s}}\frac{pg}{R_\mathrm{d} T} = \frac{w_\mathrm{s}}{p-e_\mathrm{s}}\frac{pg}{R_\mathrm{d} T}\end{aligned} \tag{C.9}$$

Combining Equation C.7 with Equation C.9:

$$\frac{\mathrm{d}w_\mathrm{s}}{\mathrm{d}z} = \frac{\partial w_\mathrm{s}}{\partial e_\mathrm{s}}\frac{\mathrm{d}e_\mathrm{s}}{\mathrm{d}z} + \frac{\partial w_\mathrm{s}}{\partial p}\frac{\mathrm{d}p}{\mathrm{d}z} = \frac{-w_\mathrm{s}(\epsilon + w_\mathrm{s}) l_\mathrm{v}}{R_\mathrm{d} T^2}\Gamma_\mathrm{S} + \frac{w_\mathrm{s} pg}{(p-e_\mathrm{s}) R_\mathrm{d} T} \tag{C.10}$$

This is identical to the equation presented in Albrecht et al. (1990). Now, the change of liquid water content with height is calculated:

$$\frac{\mathrm{dLWC}}{\mathrm{d}z} = \frac{\mathrm{d}(w_\mathrm{l}\rho_\mathrm{d})}{\mathrm{d}z} = \frac{\mathrm{d}w_\mathrm{l}}{\mathrm{d}z}\rho_\mathrm{d} + w_\mathrm{l}\frac{\mathrm{d}\rho_\mathrm{d}}{\mathrm{d}z} \tag{C.11}$$

The second part of the equation ($w_\mathrm{l}\frac{\mathrm{d}\rho_\mathrm{d}}{\mathrm{d}z}$) is zero at the cloud base ($w_\mathrm{l} = 0\,\mathrm{g\,kg^{-1}}$) and overall much smaller than the first part. It is therefore usually neglected to simplify the

equation (see also below). The condensate rate C_w which defines the change of LWC with height consists of only the first part:

$$C_w = \rho_d \frac{dw_l}{dz} = \rho_d \left[-\frac{dw_s}{dz} \right] = \rho_d \left[\frac{(\epsilon + w_s) w_s l_v}{R_d T^2} \Gamma_S - \frac{w_s p g}{(p - e_s) R_d T} \right] \tag{C.12}$$

In literature, the change of LWC with height is sometimes also formulated as follows (e.g. Grosvenor et al., 2018b):

$$C_w = \rho_d \frac{c_{p,d}}{l_v} (\Gamma_S(T, p) - \Gamma_d) \tag{C.13}$$

Here, $\Gamma_d = \frac{g}{c_{p,d}}$ is the dry adiabatic lapse rate. Curry and Webster (1999) show in Chapter 6.5 how this equation is derived from the adiabatic enthalpy equation:

$$0 = c_{p,d} dT - l_v dw_l - v dp \tag{C.14}$$

This equation is solved for dw_l and the hydrostatic equation is used. A comparison of the two equations (C.12 and C.13) is shown in Figure C.1 for a cloud with cloud base temperature $T = 283.15\,\text{K}$ and pressure $p = 900\,\text{hPa}$. This shows that the two equations are very similar but the formulation from Albrecht et al. (1990) yields slightly higher values than the formulation from Grosvenor et al. (2018b). The formula from Albrecht et al. (1990) but including the correction term $\left(w_l \frac{d\rho_d}{dz} \right)$ is shown in green. This shows that although the impact of the correction term increases with height, its overall impact is small. C_w including the correction term is approximately 10 % smaller than without the correction term. Note that in literature usually only the final equation is shown without derivation. Especially the argumentation concerning the second term is not mentioned in the literature that I found concerning this topic.

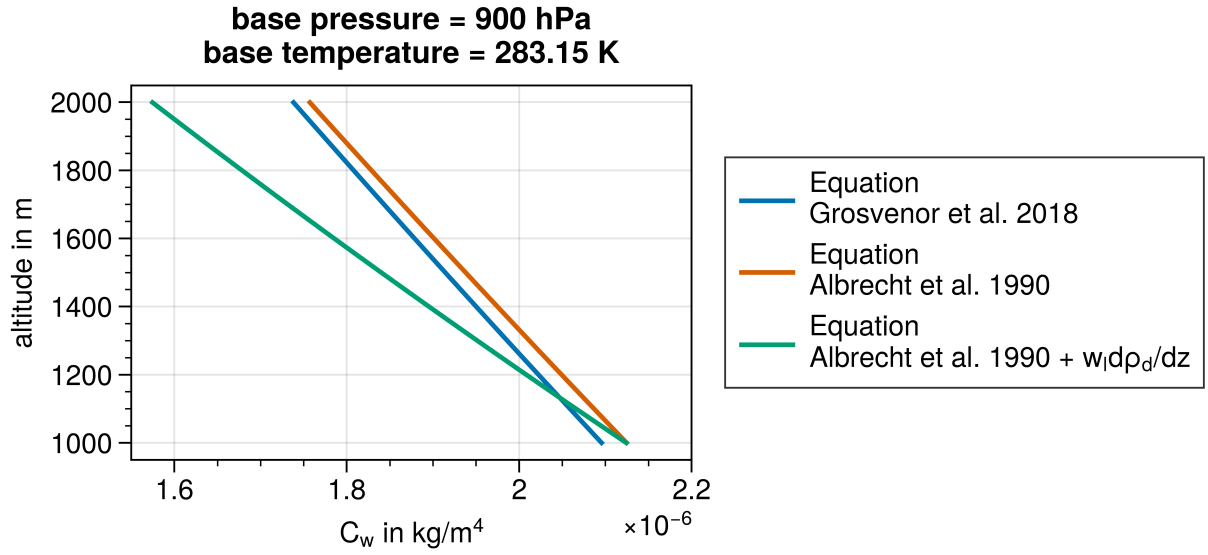

Figure C.1: Comparison of C_w equations as given in Albrecht et al. (1990) and Grosvenor et al. (2018b).

Appendix D

Derivation of the k-factor

The factor k relates the effective radius r_{eff} to the volume-mean droplet radius r_{v}:

$$r_{\text{v}}^3 = k r_{\text{eff}}^3 \tag{D.1}$$

In the following it is shown that in the case of a size distribution having the shape of a modified gamma distribution, the k-factor depends on the effective variance v_{eff}:

$$k = (1 - v_{\text{eff}})(1 - 2v_{\text{eff}}) \tag{D.2}$$

The k-factor is defined as:

$$k = \frac{r_{\text{v}}^3}{r_{\text{eff}}^3} \tag{D.3}$$

And the modified gamma distribution is defined as:

$$n_\gamma(r) = n_0 r^{(1-3v_{\text{eff}})/v_{\text{eff}}} \exp^{[-r/(r_{\text{eff}}v_{\text{eff}})]}, \tag{D.4}$$

where

$$n_0 = N_{\text{d}} \frac{(r_{\text{eff}}v_{\text{eff}})^{[(2v_{\text{eff}}-1)/v_{\text{eff}}]}}{\Gamma\left(\frac{1-2v_{\text{eff}}}{v_{\text{eff}}}\right)}. \tag{D.5}$$

The gamma distribution can be rewritten as:

$$n_\gamma(r) = n_0 r^{(1-3v_{\text{eff}})/v_{\text{eff}}} \exp\left[-r/(r_{\text{eff}}v_{\text{eff}})\right] = n_0 r^\alpha \exp(-\beta r) \tag{D.6}$$

with $\alpha = \frac{1-3v_{\text{eff}}}{v_{\text{eff}}}$ and $\beta = \frac{1}{r_{\text{eff}}v_{\text{eff}}}$. Using the gamma function we can show:

$$\int_0^\infty n_\gamma(r)dr = \int_0^\infty n_0 r^\alpha \exp(-\beta r)dr = n_0\beta^{-\alpha-1}\Gamma(\alpha+1) \tag{D.7}$$

$$\int_0^\infty n_\gamma(r)rdr = \int_0^\infty n_0 r^{\alpha+1} \exp(-\beta r)dr = n_0\beta^{-\alpha-2}\Gamma(\alpha+2) \tag{D.8}$$

$$\int_0^\infty n_\gamma(r)r^2dr = \int_0^\infty n_0 r^{\alpha+2} \exp(-\beta r)dr = n_0\beta^{-\alpha-3}\Gamma(\alpha+3) \tag{D.9}$$

$$\int_0^\infty n_\gamma(r)r^3dr = \int_0^\infty n_0 r^{\alpha+3} \exp(-\beta r)dr = n_0\beta^{-\alpha-4}\Gamma(\alpha+4) \tag{D.10}$$

With this knowledge, and using the definition of the Gamma function ($\Gamma(n+1) = n!$), we can rewrite the volume-mean droplet radius r_{v} to:

$$\begin{aligned}
r_{\text{v}} &= \left(\frac{\int_0^\infty n_0 r^3 n(r)dr}{\int_0^\infty n_0 n(r)dr}\right)^{1/3} = \left(\frac{\beta^{-\alpha-4}\Gamma(\alpha+4)}{\beta^{-\alpha-1}\Gamma(\alpha+1)}\right)^{1/3} = \\
&= \left(\frac{\beta^{-3}\Gamma(\alpha+4)}{\Gamma(\alpha+1)}\right)^{1/3} = \left(\frac{\beta^{-3}(\alpha+3)(\alpha+2)(\alpha+1)\alpha!}{\alpha!}\right)^{1/3} = \\
&= \left(\beta^{-3}(\alpha+3)(\alpha+2)(\alpha+1)\right)^{1/3} = \\
&= \left((r_{\text{eff}}v_{\text{eff}})^3(v_{\text{eff}}^{-1}-3+3)(v_{\text{eff}}^{-1}-3+2)(v_{\text{eff}}^{-1}-3+1)\right)^{1/3} = \\
&= \left((r_{\text{eff}}v_{\text{eff}})^3(v_{\text{eff}}^{-1})(v_{\text{eff}}^{-1})(1-v_{\text{eff}})v_{\text{eff}}^{-1}(1-2v_{\text{eff}})\right)^{1/3} = \\
&= r_{\text{eff}}\left((1-v_{\text{eff}})(1-2v_{\text{eff}})\right)^{1/3} = r_{\text{eff}}k^{1/3}
\end{aligned} \tag{D.11}$$

This shows that $k = (1-v_{\text{eff}})(1-2v_{\text{eff}})$ for a size distribution with the shape of a modified gamma distribution.

Appendix E

Input file for Mie simulations

An example file that was used to generate the phase functions with the Mie Tool included in libRadtran is shown in the following:

```
#Example file for calculation of phase functions
mie_program MIEV0 # Select Mie code by Wiscombe
water_properties iapws # Calculate refractive index of water
temperature 283.15
refrac water # refractive index of water

r_eff 1 40 1.05 log # Specify effective radius grid
distribution gamma 7 # Specify gamma size distribution (alpha=7)
alpha_file alpha_file.txt
wavelength LAMBDA LAMBDA # Define wavelength
nstokes 4 # Calculate all phase matrix elements

nmom 5000 # Number of Legendre terms to be computed
nmom_netcdf 5000 # Number of Legendre terms to be stored in netcdf file
nthetamax 1000
dx_max 0.003
n_r_max 8
accuracy_phase 0.01
basename ./FOLDERNAME/phase_function_ALPHA
output_user netcdf # Write output to netcdf file
verbose # Print verbose output
```

Glossary

$Q_{\mathbf{ext}}$ extinction efficiency factor.

$\beta_{\mathbf{ext}}$ extinction coefficient.

$r_{\mathbf{eff}}$ effective radius.

$v_{\mathbf{eff}}$ effective variance.

C^{3}ONTEXT a Common Consensus on Convective OrgaNizaTion during the EUREC4A eXperimenT.

CCN cloud condensation nucleus.

CDSD cloud droplet size distribution.

CIRRUS-HL Measurement campaign: Cirrus in High Latitudes.

CoMet 2.0 Arctic Measurement campaign: Carbon dioxide and Methane 2.0 Arctic.

DSD droplet size distribution.

EUREC^{4}A ElUcidating the RolE of Cloud-Circulation Coupling in ClimAte.

HALO High Altitude and LOng range research aircraft.

HALO-(AC)^3 Measurement campaign: HALO-(AC)^3.

LWC liquid water content.

polLL lower left specMACS polarization camera.

polLR lower right specMACS polarization camera.

specMACS spectrometer of the Munich Aerosol Cloud Scanner.

Bibliography

Akkiraju, N., Edelsbrunner, H., Facello, M., Fu, P., Mucke, E., and Varela, C.: Alpha shapes: definition and software, in: Proceedings of the 1st international computational geometry software workshop, vol. 63, 1995.

Albrecht, B. A.: Aerosols, Cloud Microphysics, and Fractional Cloudiness, Science, 245, 1227–1230, doi:10.1126/science.245.4923.1227, 1989.

Albrecht, B. A., Fairall, C. W., Thomson, D. W., White, A. B., Snider, J. B., and Schubert, W. H.: Surface-based remote sensing of the observed and the Adiabatic liquid water content of stratocumulus clouds, Geophysical Research Letters, 17, 89–92, doi:https://doi.org/10.1029/GL017i001p00089, 1990.

Alexandrov, M. D., Cairns, B., Emde, C., Ackerman, A. S., and van Diedenhoven, B.: Accuracy assessments of cloud droplet size retrievals from polarized reflectance measurements by the research scanning polarimeter, Remote Sens. Environ., 125, 92–111, doi:10.1016/j.rse.2012.07.012, 2012a.

Alexandrov, M. D., Cairns, B., and Mishchenko, M. I.: Rainbow Fourier transform, Journal of Quantitative Spectroscopy and Radiative Transfer, 113, 2521–2535, doi:10.1016/j.jqsrt.2012.03.025, electromagnetic and Light Scattering by non-spherical particles XIII, 2012b.

Alexandrov, M. D., Cairns, B., Wasilewski, A. P., Ackerman, A. S., McGill, M. J., Yorks, J. E., Hlavka, D. L., Platnick, S. E., Thomas Arnold, G., van Diedenhoven, B., Chowdhary, J., Ottaviani, M., and Knobelspiesse, K. D.: Liquid water cloud properties during the Polarimeter Definition Experiment (PODEX), Remote Sensing of Environment, 169, 20–36, doi:10.1016/j.rse.2015.07.029, 2015.

Alexandrov, M. D., Cairns, B., van Diedenhoven, B., Ackerman, A. S., Wasilewski, A. P., McGill, M. J., Yorks, J. E., Hlavka, D. L., Platnick, S. E., and Arnold, G. T.: Polarized view of supercooled liquid water clouds, Remote Sens. Environ., 181, 96–110, doi:10.1016/j.rse.2016.04.002, 2016.

Alexandrov, M. D., Cairns, B., Sinclair, K., Wasilewski, A. P., Ziemba, L., Crosbie, E., Moore, R., Hair, J., Scarino, A. J., Hu, Y., Stamnes, S., Shook, M. A., and Chen, G.:

Retrievals of cloud droplet size from the research scanning polarimeter data: Validation using in situ measurements, Remote Sensing of Environment, 210, 76–95, doi:10.1016/j.rse.2018.03.005, 2018.

Baker, M. B. and Latham, J.: The Evolution of Droplet Spectra and the Rate of Production of Embryonic Raindrops in Small Cumulus Clouds, Journal of Atmospheric Sciences, 36, 1612 – 1615, doi:https://doi.org/10.1175/1520-0469(1979)036<1612:TEODSA>2.0.CO;2, 1979.

Baker, M. B., Corbin, R. G., and Latham, J.: The influence of entrainment on the evolution of cloud droplet spectra: I. A model of inhomogeneous mixing, Quarterly Journal of the Royal Meteorological Society, 106, 581–598, doi:https://doi.org/10.1002/qj.49710644914, 1980.

Bass, M., Stryland, E. W. V., Williams, D. R., and Wolfe, W. L.: Handbook of Optics Volume II Devices, Measurements, and Properties 2nd edition., Handbook of Optics Volume II Devices, 1995.

Baum, B. A., Yang, P., Heymsfield, A. J., Bansemer, A., Cole, B. H., Merrelli, A., Schmitt, C., and Wang, C.: Ice cloud single-scattering property models with the full phase matrix at wavelengths from 0.2 to 100μm, Journal of Quantitative Spectroscopy and Radiative Transfer, 146, 123–139, doi:https://doi.org/10.1016/j.jqsrt.2014.02.029, electromagnetic and Light Scattering by Nonspherical Particles XIV, 2014.

Bernlochner, S.: Bestimmung von Wolkentröpfchengrößenverteilungen mithilfe der Regenbogen-Fourier-Transformation und Anwendung auf specMACS-Daten, Bachelor's Thesis, 2023.

Betts, A. K.: Parametric Interpretation of Trade-Wind Cumulus Budget Studies, Journal of Atmospheric Sciences, 32, 1934 – 1945, doi:https://doi.org/10.1175/1520-0469(1975)032<1934:PIOTWC>2.0.CO;2, 1975.

Bohren, C. F. and Huffman, D. R.: Electromagnetic Theory, chap. 2, pp. 12–56, John Wiley & Sons, Ltd, doi:https://doi.org/10.1002/9783527618156.ch2, 1998.

Bolton, D.: The Computation of Equivalent Potential Temperature, Monthly Weather Review, 108, 1046 – 1053, doi:https://doi.org/10.1175/1520-0493(1980)108<1046:TCOEPT>2.0.CO;2, 1980.

Bony, S. and Dufresne, J.-L.: Marine boundary layer clouds at the heart of tropical cloud feedback uncertainties in climate models, Geophysical Research Letters, 32, doi:10.1029/2005GL023851, 2005.

Bony, S., Stevens, B., Ament, F., Bigorre, S., Chazette, P., Crewell, S., Delanoë, J., Emanuel, K., Farrell, D., Flamant, C., Gross, S., Hirsch, L., Karstensen, J., Mayer, B., Nuijens, L., Ruppert, J. H., Sandu, I., Siebesma, P., Speich, S., Szczap, F., Totems, J., Vogel, R., Wendisch, M., and Wirth, M.: EUREC^{4}A: A Field Campaign to Elucidate the Couplings Between Clouds, Convection and Circulation, Surveys in Geophysics, 38, 1529–1568, doi:10.1007/s10712-017-9428-0, 2017.

Bony, S., Lothon, M., Delanoë, J., Coutris, P., Etienne, J.-C., Aemisegger, F., Albright, A. L., André, T., Bellec, H., Baron, A., Bourdinot, J.-F., Brilouet, P.-E., Bourdon, A., Canonici, J.-C., Caudoux, C., Chazette, P., Cluzeau, M., Cornet, C., Desbios, J.-P., Duchanoy, D., Flamant, C., Fildier, B., Gourbeyre, C., Guiraud, L., Jiang, T., Lainard, C., Le Gac, C., Lendroit, C., Lernould, J., Perrin, T., Pouvesle, F., Richard, P., Rochetin, N., Salaün, K., Schwarzenboeck, A., Seurat, G., Stevens, B., Totems, J., Touzé-Peiffer, L., Vergez, G., Vial, J., Villiger, L., and Vogel, R.: EUREC^{4}A observations from the SAFIRE ATR42 aircraft, Earth System Science Data, 14, 2021–2064, doi:10.5194/essd-14-2021-2022, 2022.

Bradski, G.: The OpenCV Library, Dr. Dobb's Journal of Software Tools, 2000.

Brenguier, J.-L., Pawlowska, H., Schüller, L., Preusker, R., Fischer, J., and Fouquart, Y.: Radiative Properties of Boundary Layer Clouds: Droplet Effective Radius versus Number Concentration, Journal of the Atmospheric Sciences, 57, 803 – 821, doi:https://doi.org/10.1175/1520-0469(2000)057<0803:RPOBLC>2.0.CO;2, 2000.

Bréon, F.-M. and Doutriaux-Boucher, M.: A comparison of cloud droplet radii measured from space, IEEE Transactions on Geoscience and Remote Sensing, 43, 1796–1805, 2005.

Bréon, F.-M. and Goloub, P.: Cloud droplet effective radius from spaceborne polarization measurements, Geophysical research letters, 25, 1879–1882, 1998.

Bünning, M.: Flugzeug- und satellitengestützte passive Fernerkundung des Effektivradius von Wolkentröpfchen im Rahmen der EUREC^{4}A-Kampagne, Bachelor's Thesis, 2021.

Cairns, B., Russell, E. E., and Travis, L. D.: The Research Scanning Polarimeter: Calibration and ground-based measurements, in: Polarization: Measurement, Analysis, and Remote Sensing II, 18 Jul. 1999, Denver, Col., vol. 3754 of *Proc. SPIE*, p. 186, doi:10.1117/12.366329, 1999.

Chazette, P., Baron, A., and Flamant, C.: Mesoscale spatio-temporal variability of airborne lidar-derived aerosol properties in the Barbados region during EUREC^{4}A, Atmospheric Chemistry and Physics, 22, 1271–1292, doi:10.5194/acp-22-1271-2022, 2022.

Cornet, C. and Davies, R.: Use of MISR measurements to study the radiative transfer of an isolated convective cloud: Implications for cloud optical thickness retrieval, Journal of Geophysical Research: Atmospheres, 113, doi:https://doi.org/10.1029/2007JD008921, 2008.

Coutris, P.: SAFIRE ATR42: PMA/Cloud composite dataset, doi:doi.org/10.25326/237, Aeris, 2021.

Cui, Z., Blyth, A., Burton, R., Bony, S., Böing, S., Gadian, A., and Denby, L.: Life cycle of a flower cloud system during the EUREC^{4}A field campaign, EGUsphere, 2023, 1–47, doi:10.5194/egusphere-2023-1999, 2023.

Curry, J. A. and Webster, P. J.: Chapter 2 - The First and Second Laws of Thermodynamics, in: Thermodynamics of Atmospheres and Oceans, vol. 65 of *International Geophysics*, pp. 35–73, Academic Press, doi:https://doi.org/10.1016/S0074-6142(99)80024-2, 1999.

Damböck, B.: Quantifying turbulence around cloud edges from stereographically derived wind fields, Bachelor's Thesis, 2024.

Dauhut, T., Couvreux, F., Bouniol, D., Beucher, F., Volkmer, L., Pörtge, V., Schäfer, M., Ayet, A., Brilouet, P.-E., Jacob, M., and Wirth, M.: Flower trade-wind clouds are shallow mesoscale convective systems, Quarterly Journal of the Royal Meteorological Society, doi:10.1002/qj.4409, 2022.

de Rooy, W. C. and Siebesma, P.: Analytical expressions for entrainment and detrainment in cumulus convection, Quarterly Journal of the Royal Meteorological Society, 136, 1216–1227, doi:https://doi.org/10.1002/qj.640, 2010.

de Rooy, W. C., Bechtold, P., Fröhlich, K., Hohenegger, C., Jonker, H., Mironov, D., Pier Siebesma, A., Teixeira, J., and Yano, J.-I.: Entrainment and detrainment in cumulus convection: an overview, Quarterly Journal of the Royal Meteorological Society, 139, 1–19, doi:https://doi.org/10.1002/qj.1959, 2013.

Di Noia, A., Hasekamp, O. P., van Diedenhoven, B., and Zhang, Z.: Retrieval of liquid water cloud properties from POLDER-3 measurements using a neural network ensemble approach, Atmospheric Measurement Techniques, 12, 1697–1716, doi:10.5194/amt-12-1697-2019, 2019.

Diner, D. J., Xu, F., Garay, M. J., Martonchik, J. V., Rheingans, B. E., Geier, S., Davis, A., Hancock, B., Jovanovic, V., Bull, M., et al.: The Airborne Multiangle SpectroPolarimetric Imager (AirMSPI): a new tool for aerosol and cloud remote sensing, Atmospheric Measurement Techniques, 6, 2007–2025, 2013.

Diner, D. J., Boland, S. W., Brauer, M., Bruegge, C., Burke, K. A., Chipman, R., Girolamo, L. D., Garay, M. J., Hasheminassab, S., Hyer, E., Jerrett, M., Jovanovic, V., Kalashnikova, O. V., Liu, Y., Lyapustin, A. I., Martin, R. V., Nastan, A., Ostro, B. D., Ritz, B., Schwartz, J., Wang, J., and Xu, F.: Advances in multiangle satellite remote sensing of speciated airborne particulate matter and association with adverse health effects: from MISR to MAIA, Journal of Applied Remote Sensing, 12, 042 603, doi:10.1117/1.JRS.12.042603, 2018.

Dirac, P. A. M.: The Principles of Quantum Mechanics, Clarendon Press, Oxford,, 1930.

Dubovik, O., Li, Z., Mishchenko, M. I., Tanré, D., Karol, Y., Bojkov, B., Cairns, B., Diner, D. J., Espinosa, W. R., Goloub, P., Gu, X., Hasekamp, O., Hong, J., Hou, W., Knobelspiesse, K. D., Landgraf, J., Li, L., Litvinov, P., Liu, Y., Lopatin, A., Marbach, T., Maring, H., Martins, V., Meijer, Y., Milinevsky, G., Mukai, S., Parol, F., Qiao, Y., Remer, L., Rietjens, J., Sano, I., Stammes, P., Stamnes, S., Sun, X., Tabary, P., Travis, L. D., Waquet, F., Xu, F., Yan, C., and Yin, D.: Polarimetric remote sensing of atmospheric aerosols: Instruments, methodologies, results, and perspectives, Journal of Quantitative Spectroscopy and Radiative Transfer, 224, 474–511, doi:10.1016/j.jqsrt.2018.11.024, 2019.

ECMWF: IFS Documentation CY48R1 - Part IV: Physical Processes, 4, ECMWF, doi:10.21957/02054f0fbf, 2023.

Edwards, J. M. and Slingo, A.: Studies with a flexible new radiation code. I: Choosing a configuration for a large-scale model, Quarterly Journal of the Royal Meteorological Society, 122, 689–719, doi:https://doi.org/10.1002/qj.49712253107, 1996.

Efron, B. and Tibshirani, R. J.: An Introduction to the Bootstrap, Chapman and Hall/CRC, 1st edn., doi:10.1201/9780429246593, 1994.

Emde, C., Buras, R., Mayer, B., and Blumthaler, M.: The impact of aerosols on polarized sky radiance: model development, validation, and applications, Atmospheric Chemistry and Physics, 10, 383–396, doi:10.5194/acp-10-383-2010, 2010.

Emde, C., Barlakas, V., Cornet, C., Evans, F., Korkin, S., Ota, Y., Labonnote, L. C., Lyapustin, A., Macke, A., Mayer, B., and Wendisch, M.: IPRT polarized radiative transfer model intercomparison project – Phase A, Journal of Quantitative Spectroscopy and Radiative Transfer, 164, 8–36, doi:10.1016/j.jqsrt.2015.05.007, 2015.

Emde, C., Buras-Schnell, R., Kylling, A., Mayer, B., Gasteiger, J., Hamann, U., Kylling, J., Richter, B., Pause, C., Dowling, T., and Bugliaro, L.: The libRadtran software package for radiative transfer calculations (version 2.0.1), Geoscientific Model Development, 9, 1647–1672, doi:10.5194/gmd-9-1647-2016, 2016.

Emde, C., Pörtge, V., Manev, M., and Mayer, B.: Retrieval of cloud fraction and optical thickness from multi-angle polarization observations, to be submitted, 2024.

Erdtmann, D.: Remote Sensing of Arctic Cirrus Microphysics using Hyperspectral Reflectivity Measurements and Polarized Imaging, Master's Thesis, 2023.

Eshelman, L. M. and Shaw, J. A.: Visualization of all-sky polarization images referenced in the instrument, scattering, and solar principal planes, Optical Engineering, 58, 082 418, doi:10.1117/1.OE.58.8.082418, 2019.

Ewald, F., Kölling, T., Baumgartner, A., Zinner, T., and Mayer, B.: Design and characterization of specMACS, a multipurpose hyperspectral cloud and sky imager, Atmospheric Measurement Techniques, 9, 2015–2042, doi:10.5194/amt-9-2015-2016, 2016.

Ewald, F., Zinner, T., Kölling, T., and Mayer, B.: Remote sensing of cloud droplet radius profiles using solar reflectance from cloud sides – Part 1: Retrieval development and characterization, Atmospheric Measurement Techniques, 12, 1183–1206, doi:10.5194/amt-12-1183-2019, 2019.

Eytan, E., Koren, I., Altaratz, O., Pinsky, M., and Khain, A.: Revisiting adiabatic fraction estimations in cumulus clouds: high-resolution simulations with a passive tracer, Atmospheric Chemistry and Physics, 21, 16 203–16 217, doi:10.5194/acp-21-16203-2021, 2021.

Forbes, R., Tompkins, A., and Untch, A.: A new prognostic bulk microphysics scheme for the IFS, doi:10.21957/bf6vjvxk, 2011.

Forster, P., Storelvmo, T., Armour, K., Collins, W., Dufresne, J.-L., Frame, D., Lunt, D., Mauritsen, T., Palmer, M., Watanabe, M., Wild, M., and Zhang, H.: The Earth's Energy Budget, Climate Feedbacks, and Climate Sensitivity, p. 923–1054, Cambridge University Press, Cambridge, United Kingdom and New York, NY, USA, doi:10.1017/9781009157896.009, 2021.

Fougnie, B., Marbach, T., Lacan, A., Lang, R., Schlüssel, P., Poli, G., Munro, R., and Couto, A. B.: The multi-viewing multi-channel multi-polarisation imager – Overview of the 3MI polarimetric mission for aerosol and cloud characterization, Journal of Quantitative Spectroscopy and Radiative Transfer, 219, 23–32, doi:10.1016/j.jqsrt.2018.07.008, 2018.

Fu, D., Di Girolamo, L., Liang, L., and Zhao, G.: Regional Biases in MODIS Marine Liquid Water Cloud Drop Effective Radius Deduced Through Fusion With MISR, Journal of Geophysical Research: Atmospheres, 124, 13 182–13 196, doi:10.1029/2019JD031063, 2019.

Fu, D., Di Girolamo, L., Rauber, R. M., McFarquhar, G. M., Nesbitt, S. W., Loveridge, J., Hong, Y., van Diedenhoven, B., Cairns, B., Alexandrov, M. D., Lawson, P., Woods, S., Tanelli, S., Schmidt, S., Hostetler, C., and Scarino, A. J.: An evaluation of the liquid cloud droplet effective radius derived from MODIS, airborne remote sensing, and in situ measurements from CAMP^{2}Ex, Atmospheric Chemistry and Physics, 22, 8259–8285, doi:10.5194/acp-22-8259-2022, 2022.

Gege, P., Fries, J., Haschberger, P., Schötz, P., Schwarzer, H., Strobl, P., Suhr, B., Ulbrich, G., and Jan Vreeling, W.: Calibration facility for airborne imaging spectrometers, ISPRS Journal of Photogrammetry and Remote Sensing, 64, 387–397, doi:https://doi.org/10.1016/j.isprsjprs.2009.01.006, 2009.

Genthon, C.: Simulations of desert dust and sea-salt aerosols in Antarctica with a general circulation model of the atmosphere, Tellus B, 44, 371–389, doi:https://doi.org/10.1034/j.1600-0889.1992.00014.x, 1992.

George, G.: JOANNE : Joint dropsonde Observations of the Atmosphere in tropical North atlaNtic meso-scale Environments (v2.0.0), doi:https://doi.org/10.25326/246, Aeris, 2021.

Gerber, H. E., Frick, G. M., Jensen, J. B., and Hudson, J. G.: Entrainment, Mixing, and Microphysics in Trade-Wind Cumulus, Journal of the Meteorological Society of Japan. Ser. II, 86A, 87–106, doi:10.2151/jmsj.86A.87, 2008.

Ghan, S., Wang, M., Zhang, S., Ferrachat, S., Gettelman, A., Griesfeller, J., Kipling, Z., Lohmann, U., Morrison, H., Neubauer, D., Partridge, D. G., Stier, P., Takemura, T., Wang, H., and Zhang, K.: Challenges in constraining anthropogenic aerosol effects on cloud radiative forcing using present-day spatiotemporal variability, Proceedings of the National Academy of Sciences, 113, 5804–5811, doi:10.1073/pnas.1514036113, 2016.

Giancoli, D. C.: Physik Lehr- und Übungsbuch, Pearson Deutschland, URL `https://elibrary.pearson.de/book/99.150005/9783863268602`, 2019.

Giez, A., Mallaun, C., Nenakhov, V., and Zöger, M.: Calibration of a Nose Boom Mounted Airflow Sensor on an Atmospheric Research Aircraft by Inflight Maneuvers, DLR-Forschungsbericht. DLR-FB-2021-17, URL `https://elib.dlr.de/145969/`, 2021.

Grabowski, W. W. and Wang, L.-P.: Growth of Cloud Droplets in a Turbulent Environment, Annual Review of Fluid Mechanics, 45, 293–324, doi:10.1146/annurev-fluid-011212-140750, 2013.

Groß, S., Gasteiger, J., Freudenthaler, V., Müller, T., Sauer, D., Toledano, C., and Ansmann, A.: Saharan dust contribution to the Caribbean summertime boundary layer – a lidar study during SALTRACE, Atmospheric Chemistry and Physics, 16, 11 535–11 546, doi:10.5194/acp-16-11535-2016, 2016.

Grosvenor, D. and Wood, R.: Daily MODIS (MODerate Imaging Spectroradiometer) derived cloud droplet number concentration global dataset for 2003-2015, Centre for Environmental Data Analysis, https://catalogue.ceda.ac.uk/uuid/cf97ccc802d348ec8a3b6f2995dfbbff, 2018.

Grosvenor, D. P., Sourdeval, O., and Wood, R.: Parameterizing cloud top effective radii from satellite retrieved values, accounting for vertical photon transport: quantification and correction of the resulting bias in droplet concentration and liquid water path retrievals, Atmospheric Measurement Techniques, 11, 4273–4289, doi:10.5194/amt-11-4273-2018, 2018a.

Grosvenor, D. P., Sourdeval, O., Zuidema, P., Ackerman, A., Alexandrov, M. D., Bennartz, R., Boers, R., Cairns, B., Chiu, J. C., Christensen, M., Deneke, H., Diamond, M., Feingold, G., Fridlind, A., Hünerbein, A., Knist, C., Kollias, P., Marshak, A., McCoy, D., Merk, D., Painemal, D., Rausch, J., Rosenfeld, D., Russchenberg, H., Seifert, P., Sinclair, K., Stier, P., van Diedenhoven, B., Wendisch, M., Werner, F., Wood, R., Zhang, Z., and Quaas, J.: Remote Sensing of Droplet Number Concentration in Warm Clouds: A Review of the Current State of Knowledge and Perspectives, Reviews of Geophysics, 56, 409–453, doi:https://doi.org/10.1029/2017RG000593, 2018b.

Gryspeerdt, E., McCoy, D. T., Crosbie, E., Moore, R. H., Nott, G. J., Painemal, D., Small-Griswold, J., Sorooshian, A., and Ziemba, L.: The impact of sampling strategy on the cloud droplet number concentration estimated from satellite data, Atmospheric Measurement Techniques, 15, 3875–3892, doi:10.5194/amt-15-3875-2022, 2022.

Guichard, F. and Couvreux, F.: A short review of numerical cloud-resolving models, Tellus A: Dynamic Meteorology and Oceanography, 69, 1373 578, doi:10.1080/16000870.2017.1373578, 2017.

Gutleben, M., Groß, S., Wirth, M., and Mayer, B.: Radiative effects of long-range-transported Saharan air layers as determined from airborne lidar measurements, Atmospheric Chemistry and Physics, 20, 12 313–12 327, doi:10.5194/acp-20-12313-2020, 2020.

Gutleben, M., Groß, S., Heske, C., and Wirth, M.: Wintertime Saharan dust transport towards the Caribbean: an airborne lidar case study during EUREC^{4}A, Atmospheric Chemistry and Physics, 22, 7319–7330, doi:10.5194/acp-22-7319-2022, 2022.

Hansen, J. E.: Multiple scattering of polarized light in planetary atmospheres part II. Sunlight reflected by terrestrial water clouds, Journal of Atmospheric Sciences, 28, 1400–1426, 1971.

Hansen, J. E. and Travis, L. D.: Light scattering in planetary atmospheres, Space Sci. Rev., 16, 527–610, doi:10.1007/BF00168069, 1974.

Hasekamp, O. P.: Capability of multi-viewing-angle photo-polarimetric measurements for the simultaneous retrieval of aerosol and cloud properties, Atmospheric Measurement Techniques, 3, 839–851, doi:10.5194/amt-3-839-2010, 2010.

Hasekamp, O. P. and Landgraf, J.: Retrieval of aerosol properties over land surfaces: capabilities of multiple-viewing-angle intensity and polarization measurements, Appl. Opt., 46, 3332–3344, doi:10.1364/AO.46.003332, 2007.

Hasekamp, O. P., Litvinov, P., and Butz, A.: Aerosol properties over the ocean from PARASOL multiangle photopolarimetric measurements, Journal of Geophysical Research: Atmospheres, 116, doi:https://doi.org/10.1029/2010JD015469, 2011.

Hasekamp, O. P., Gryspeerdt, E., and Quaas, J.: Analysis of polarimetric satellite measurements suggests stronger cooling due to aerosol-cloud interactions, Nature Communications, 10, 5405, doi:10.1038/s41467-019-13372-2, 2019.

Hersbach, H., Bell, B., Berrisford, P., Biavati, G., Horányi, A., Muñoz Sabater, J., Nicolas, J., Peubey, C., Radu, R., Rozum, I., Schepers, D., Simmons, A., Soci, C., Dee, D., and Thépaut, J.-N.: ERA5 hourly data on pressure levels from 1959 to present., Copernicus climate change service (c3s) climate data store (cds), doi:10.24381/cds.bd0915c6, (Accessed on 23-08-2022), 2018.

Hersbach, H., Bell, B., Berrisford, P., Hirahara, S., Horányi, A., Muñoz-Sabater, J., Nicolas, J., Peubey, C., Radu, R., Schepers, D., et al.: The ERA5 global reanalysis, Quarterly Journal of the Royal Meteorological Society, 146, 1999–2049, 2020.

Heymsfield, A. J., Schmitt, C., and Bansemer, A.: Ice Cloud Particle Size Distributions and Pressure-Dependent Terminal Velocities from In Situ Observations at Temperatures from 0° to -86°C, Journal of the Atmospheric Sciences, 70, 4123 – 4154, doi:10.1175/JAS-D-12-0124.1, 2013.

Hoffmann, F., Yamaguchi, T., and Feingold, G.: Inhomogeneous Mixing in Lagrangian Cloud Models: Effects on the Production of Precipitation Embryos, Journal of the Atmospheric Sciences, 76, 113 – 133, doi:10.1175/JAS-D-18-0087.1, 2019.

Ishizaka, Y., Kurahashi, Y., and Tsuruta, H.: Microphysical Properties of Winter Stratiform Clouds over the Southwest Islands Area in Japan, Journal of the Meteorological Society of Japan. Ser. II, 73, 1137–1151, doi:10.2151/jmsj1965.73.6_1137, 1995.

Jakub, F. and Volkmer, L. S.: PALM-LES / EUREC4A shallow cumulus dataset with 3D cloud output data, Dataset, doi:10.57970/r4wfp-kp367, 2023.

Karset, I. H. H., Gettelman, A., Storelvmo, T., Alterskjær, K., and Berntsen, T. K.: Exploring Impacts of Size-Dependent Evaporation and Entrainment in a Global

Model, Journal of Geophysical Research: Atmospheres, 125, e2019JD031 817, doi:https://doi.org/10.1029/2019JD031817, e2019JD031817 10.1029/2019JD031817, 2020.

Khain, A. P. and Pinsky, M.: Physical Processes in Clouds and Cloud Modeling, Cambridge University Press, 2018.

Kim, Y.-J., Kim, B.-G., Miller, M., Min, Q., and Song, C.-K.: Enhanced aerosol-cloud relationships in more stable and adiabatic clouds, Asia-Pacific Journal of Atmospheric Sciences, 48, 283–293, doi:10.1007/s13143-012-0028-0, 2012.

Knobelspiesse, K., Cairns, B., Redemann, J., Bergstrom, R. W., and Stohl, A.: Simultaneous retrieval of aerosol and cloud properties during the MILAGRO field campaign, Atmospheric Chemistry and Physics, 11, 6245–6263, doi:10.5194/acp-11-6245-2011, 2011.

Kölling, T.: Cloud geometry for passive remote sensing, URL `http://nbn-resolving.de/urn:nbn:de:bvb:19-261616`, 2020.

Kölling, T., Zinner, T., and Mayer, B.: Aircraft-based stereographic reconstruction of 3-D cloud geometry, Atmospheric Measurement Techniques, 12, 1155–1166, doi:10.5194/amt-12-1155-2019, 2019.

Konow, H., Ewald, F., George, G., Jacob, M., Klingebiel, M., Kölling, T., Luebke, A. E., Mieslinger, T., Pörtge, V., Radtke, J., Schäfer, M., Schulz, H., Vogel, R., Wirth, M., Bony, S., Crewell, S., Ehrlich, A., Forster, L., Giez, A., Gödde, F., Groß, S., Gutleben, M., Hagen, M., Hirsch, L., Jansen, F., Lang, T., Mayer, B., Mech, M., Prange, M., Schnitt, S., Vial, J., Walbröl, A., Wendisch, M., Wolf, K., Zinner, T., Zöger, M., Ament, F., and Stevens, B.: EUREC^{4}A's *HALO*, Earth System Science Data, 13, 5545–5563, doi:10.5194/essd-13-5545-2021, 2021.

Koppenhofer, S.: Spektrale und radiometrische Kalibrierung der Polarisationskameras von specMACS, Bachelor's Thesis, 2022.

Koppenhofer, S.: Validation of specMACS microphysical products with independent aircraft and satellite observations, Master's Thesis, to be submitted, 2024.

Koren, I., Kostinski, A., Wollner, U., and Dubrovin, D.: Faint yet widespread glories reflect microphysics of marine clouds, npj Climate and Atmospheric Science, 5, 87, doi:10.1038/s41612-022-00312-z, 2022.

Krautstrunk, M. and Giez, A.: The Transition From FALCON to HALO Era Airborne Atmospheric Research, pp. 609–624, Springer Berlin Heidelberg, Berlin, Heidelberg, doi:10.1007/978-3-642-30183-4_37, 2012.

Können, G. P.: Polarized light in nature, CUP Archive, 1985.

Laven, P.: How are glories formed?, Appl. Opt., 44, 5675–5683, doi:10.1364/AO.44.005675, 2005.

Lehmann, K., Siebert, H., and Shaw, R. A.: Homogeneous and Inhomogeneous Mixing in Cumulus Clouds: Dependence on Local Turbulence Structure, Journal of the Atmospheric Sciences, 66, 3641 – 3659, doi:https://doi.org/10.1175/2009JAS3012.1, 2009.

Lim, J.-S. and Hoffmann, F.: Between Broadening and Narrowing: How Mixing Affects the Width of the Droplet Size Distribution, Journal of Geophysical Research: Atmospheres, 128, e2022JD037 900, doi:https://doi.org/10.1029/2022JD037900, e2022JD037900 2022JD037900, 2023a.

Lim, J.-S. and Hoffmann, F.: Life Cycle Evolution of Inhomogeneous Mixing in Shallow Cumulus Clouds, ESS Open Archive, doi:10.22541/essoar.170224522.28596170/v1, 2023b.

Liou, K. and Hansen, J. E.: Intensity and Polarization for Single Scattering by Polydisperse Spheres: A Comparison of Ray Optics and Mie Theory, Journal of Atmospheric Sciences, 28, 995 – 1004, doi:https://doi.org/10.1175/1520-0469(1971)028<0995:IAPFSS>2.0.CO;2, 1971.

LUCID Vision Labs Inc.: Phoenix 5.0 MP Polarized Tech Ref (PHX050S1-Q, Color, IMX264MYR), `https://thinklucid.com/downloads-hub/#tab-phoenix-tech-man` (Accessed on 19-03-2024), 2022a.

LUCID Vision Labs Inc.: Phoenix 5.0 MP Polarization Model (IMX250MZR/MYR), `https://thinklucid.com/de/product/phoenix-5-0-mp-polarized-model/` (Accessed on 19-03-2024), 2022b.

Ma, Z.: Cloud Detection based on Polarimetric specMACS Observations over Ocean and Land, Bachelor's Thesis, 2022.

Marshak, A., Platnick, S., Várnai, T., Wen, G., and Cahalan, R. F.: Impact of three-dimensional radiative effects on satellite retrievals of cloud droplet sizes, Journal of Geophysical Research: Atmospheres, 111, doi:10.1029/2005JD006686, 2006.

Martin, G. M., Johnson, D. W., and Spice, A.: The Measurement and Parameterization of Effective Radius of Droplets in Warm Stratocumulus Clouds, Journal of Atmospheric Sciences, 51, 1823 – 1842, doi:https://doi.org/10.1175/1520-0469(1994)051<1823:TMAPOE>2.0.CO;2, 1994.

Martins, J. V., Fernandez-Borda, R., McBride, B., Remer, L., and Barbosa, H. M.: The harp hype ran gular imaging polarimeter and the need for small satellite payloads with high science payoff for earth science remote sensing, in: IGARSS 2018-2018 IEEE International Geoscience and Remote Sensing Symposium, pp. 6304–6307, IEEE, 2018.

Mayer, B.: Radiative transfer in the cloudy atmosphere, EPJ Web of Conferences, 1, 75–99, doi:10.1140/epjconf/e2009-00912-1, 2009.

Mayer, B. and Kylling, A.: Technical note: The libRadtran software package for radiative transfer calculations - description and examples of use, Atmospheric Chemistry and Physics, 5, 1855–1877, doi:10.5194/acp-5-1855-2005, 2005.

Mayer, B., Schröder, M., Preusker, R., and Schüller, L.: Remote sensing of water cloud droplet size distributions using the backscatter glory: a case study, Atmospheric Chemistry and Physics, 4, 1255–1263, doi:10.5194/acp-4-1255-2004, 2004.

McBride, B. A., Martins, J. V., Barbosa, H. M., Birmingham, W., and Remer, L. A.: Spatial distribution of cloud droplet size properties from Airborne Hyper-Angular Rainbow Polarimeter (AirHARP) measurements, Atmospheric Measurement Techniques, 13, 1777–1796, 2020.

Mech, M., Orlandi, E., Crewell, S., Ament, F., Hirsch, L., Hagen, M., Peters, G., and Stevens, B.: HAMP – the microwave package on the High Altitude and LOng range research aircraft (HALO), Atmospheric Measurement Techniques, 7, 4539–4553, doi:10.5194/amt-7-4539-2014, 2014.

Merk, D., Deneke, H., Pospichal, B., and Seifert, P.: Investigation of the adiabatic assumption for estimating cloud micro- and macrophysical properties from satellite and ground observations, Atmospheric Chemistry and Physics, 16, 933–952, doi:10.5194/acp-16-933-2016, 2016.

Mie, G.: Beiträge zur Optik trüber Medien, speziell kolloidaler Metallösungen, Annalen der Physik, 330, 377–445, doi:10.1002/andp.19083300302, 1908.

Miles, N. L., Verlinde, J., and Clothiaux, E. E.: Cloud Droplet Size Distributions in Low-Level Stratiform Clouds, Journal of the Atmospheric Sciences, 57, 295 – 311, doi:10.1175/1520-0469(2000)057<0295:CDSDIL>2.0.CO;2, 2000.

Miller, D. J., Zhang, Z., Platnick, S., Ackerman, A. S., Werner, F., Cornet, C., and Knobelspiesse, K.: Comparisons of bispectral and polarimetric retrievals of marine boundary layer cloud microphysics: case studies using a LES–satellite retrieval simulator, Atmospheric Measurement Techniques, 11, 3689–3715, doi:10.5194/amt-11-3689-2018, 2018.

Min, Q., Joseph, E., Lin, Y., Min, L., Yin, B., Daum, P. H., Kleinman, L. I., Wang, J., and Lee, Y.-N.: Comparison of MODIS cloud microphysical properties with in-situ measurements over the Southeast Pacific, Atmospheric Chemistry and Physics, 12, 11 261–11 273, doi:10.5194/acp-12-11261-2012, 2012.

Mishchenko, M. I. and Travis, L. D.: Satellite retrieval of aerosol properties over the ocean using measurements of reflected sunlight: Effect of instrumental errors and aerosol absorption, Journal of Geophysical Research: Atmospheres, 102, 13 543–13 553, doi:10.1029/97JD01124, 1997.

Morton, B. R., Taylor, G., and Turner, J. S.: Turbulent Gravitational Convection from Maintained and Instantaneous Sources, Proceedings of the Royal Society of London. Series A, Mathematical and Physical Sciences, 234, 1–23, URL `http://www.jstor.org/stable/99936`, 1956.

Moteki, N.: Climate-relevant properties of black carbon aerosols revealed by in situ measurements: a review, Progress in Earth and Planetary Science, 10, 12, doi:10.1186/s40645-023-00544-4, 2023.

Nakajima, T. and King, M. D.: Determination of the Optical Thickness and Effective Particle Radius of Clouds from Reflected Solar Radiation Measurements. Part I: Theory, Journal of Atmospheric Sciences, 47, 1878 – 1893, doi:10.1175/1520-0469(1990)047<1878:DOTOTA>2.0.CO;2, 1990.

Narenpitak, P., Kazil, J., Yamaguchi, T., Quinn, P., and Feingold, G.: From Sugar to Flowers: A Transition of Shallow Cumulus Organization During ATOMIC, Journal of Advances in Modeling Earth Systems, 13, e2021MS002 619, doi:https://doi.org/10.1029/2021MS002619, e2021MS002619 2021MS002619, 2021.

Neggers, R. A. J., Jonker, H. J. J., and Siebesma, A. P.: Size Statistics of Cumulus Cloud Populations in Large-Eddy Simulations, Journal of the Atmospheric Sciences, 60, 1060 – 1074, doi:https://doi.org/10.1175/1520-0469(2003)60<1060:SSOCCP>2.0.CO;2, 2003.

Otsu, N.: A Threshold Selection Method from Gray-Level Histograms, IEEE Transactions on Systems, Man, and Cybernetics, 9, 62–66, doi:10.1109/TSMC.1979.4310076, 1979.

Painemal, D. and Zuidema, P.: The first aerosol indirect effect quantified through airborne remote sensing during VOCALS-REx, Atmospheric Chemistry and Physics, 13, 917–931, doi:10.5194/acp-13-917-2013, 2013.

Painemal, D., Spangenberg, D., Smith Jr., W. L., Minnis, P., Cairns, B., Moore, R. H., Crosbie, E., Robinson, C., Thornhill, K. L., Winstead, E. L., and Ziemba, L.: Evaluation of satellite retrievals of liquid clouds from the GOES-13 imager and MODIS over the midlatitude North Atlantic during the NAAMES campaign, Atmospheric Measurement Techniques, 14, 6633–6646, doi:10.5194/amt-14-6633-2021, 2021.

Petty, G. W.: A first course in atmospheric radiation, Sundog Publishing, 2006.

Pinsky, M., Khain, A., and Korolev, A.: Theoretical analysis of mixing in liquid clouds – Part 3: Inhomogeneous mixing, Atmospheric Chemistry and Physics, 16, 9273–9297, doi:10.5194/acp-16-9273-2016, 2016.

Platnick, S.: Vertical photon transport in cloud remote sensing problems, Journal of Geophysical Research: Atmospheres, 105, 22 919–22 935, doi:10.1029/2000JD900333, 2000.

Platnick, S., King, M., Ackerman, S., Menzel, W., Baum, B., Riedi, J., and Frey, R.: The MODIS cloud products: Algorithms and Examples From Terra, IEEE Transactions on Geoscience and Remote Sensing, 41, 459–473, doi:10.1109/TGRS.2002.808301, 2003.

Polonik, P., Knote, C., Zinner, T., Ewald, F., Kölling, T., Mayer, B., Andreae, M. O., Jurkat-Witschas, T., Klimach, T., Mahnke, C., Molleker, S., Pöhlker, C., Pöhlker, M. L., Pöschl, U., Rosenfeld, D., Voigt, C., Weigel, R., and Wendisch, M.: The challenge of simulating the sensitivity of the Amazonian cloud microstructure to cloud condensation nuclei number concentrations, Atmospheric Chemistry and Physics, 20, 1591–1605, doi:10.5194/acp-20-1591-2020, 2020.

Pörtge, V., Kölling, T., Weber, A., Volkmer, L., Emde, C., Zinner, T., Forster, L., and Mayer, B.: High-spatial-resolution retrieval of cloud droplet size distribution from polarized observations of the cloudbow, Atmospheric Measurement Techniques, 16, 645–667, doi:10.5194/amt-16-645-2023, 2023.

Prange, M., Ringel, M., George, G., Hirsch, L., Kölling, T., Konow, H., Lang, T., Mieslinger, T., Pincus, R., and Saffin, L.: EUREC4A: HALO flight phase separation: Beautiful Budgie, doi:10.5281/zenodo.4900003, 2021.

Pörtge, V.: Cloud Droplet Size Distributions from Observations of Glory and Cloudbow, Master's Thesis, 2019.

Pörtge, V., Kölling, T., Zinner, T., Mayer, B., Weber, A., Forster, L., Emde, C., and Volkmer, L.: Cloud droplet size distribution from 2-D polarization measurements of specMACS during EUREC4A, Dataset, URL `https://doi.org/10.25326/549#v1.0`, accessed: 2024-02-23, 2023.

Quaas, J., Arola, A., Cairns, B., Christensen, M., Deneke, H., Ekman, A. M. L., Feingold, G., Fridlind, A., Gryspeerdt, E., Hasekamp, O., Li, Z., Lipponen, A., Ma, P.-L., Mülmenstädt, J., Nenes, A., Penner, J. E., Rosenfeld, D., Schrödner, R., Sinclair, K., Sourdeval, O., Stier, P., Tesche, M., van Diedenhoven, B., and Wendisch, M.: Constraining the Twomey effect from satellite observations: issues and perspectives, Atmospheric Chemistry and Physics, 20, 15 079–15 099, doi:10.5194/acp-20-15079-2020, 2020.

Raasch, S. and Schröter, M.: PALM - A large-eddy simulation model performing on massively parallel computers, Meteorologische Zeitschrift, 10, 363–372, doi:10.1127/0941-2948/2001/0010-0363, 2001.

Reid, J. S., Maring, H. B., Narisma, G. T., van den Heever, S., Girolamo, L. D., Ferrare, R., Lawson, P., Mace, G. G., Simpas, J. B., Tanelli, S., Ziemba, L., van Diedenhoven, B., Bruintjes, R., Bucholtz, A., Cairns, B., Cambaliza, M. O., Chen, G., Diskin, G. S., Flynn, J. H., Hostetler, C. A., Holz, R. E., Lang, T. J., Schmidt, K. S., Smith, G., Sorooshian, A., Thompson, E. J., Thornhill, K. L., Trepte, C., Wang, J., Woods, S., Yoon, S., Alexandrov, M., Alvarez, S., Amiot, C. G., Bennett, J. R., Brooks, M., Burton, S. P., Cayanan, E., Chen, H., Collow, A., Crosbie, E., DaSilva, A., DiGangi, J. P., Flagg, D. D., Freeman, S. W., Fu, D., Fukada, E., Hilario, M. R. A., Hong, Y., Hristova-Veleva, S. M., Kuehn, R., Kowch, R. S., Leung, G. R., Loveridge, J., Meyer, K., Miller, R. M., Montes, M. J., Moum, J. N., Nenes, A., Nesbitt, S. W., Norgren, M., Nowottnick, E. P., Rauber, R. M., Reid, E. A., Rutledge, S., Schlosser, J. S., Sekiyama, T. T., Shook, M. A., Sokolowsky, G. A., Stamnes, S. A., Tanaka, T. Y., Wasilewski, A., Xian, P., Xiao, Q., Xu, Z., and Zavaleta, J.: The Coupling Between Tropical Meteorology, Aerosol Lifecycle, Convection, and Radiation during the Cloud, Aerosol and Monsoon Processes Philippines Experiment (CAMP2Ex), Bulletin of the American Meteorological Society, 104, E1179 – E1205, doi:10.1175/BAMS-D-21-0285.1, 2023.

Remer, L. A., Knobelspiesse, K., Zhai, P.-W., Xu, F., Kalashnikova, O. V., Chowdhary, J., Hasekamp, O., Dubovik, O., Wu, L., Ahmad, Z., Boss, E., Cairns, B., Coddington, O., Davis, A. B., Dierssen, H. M., Diner, D. J., Franz, B., Frouin, R., Gao, B.-C., Ibrahim, A., Levy, R. C., Martins, J. V., Omar, A. H., and Torres, O.: Retrieving Aerosol Characteristics From the PACE Mission, Part 2: Multi-Angle and Polarimetry, Frontiers in Environmental Science, 7, doi:10.3389/fenvs.2019.00094, 2019.

Riedi, J., Marchant, B., Platnick, S., Baum, B. A., Thieuleux, F., Oudard, C., Parol, F., Nicolas, J.-M., and Dubuisson, P.: Cloud thermodynamic phase inferred from merged POLDER and MODIS data, Atmospheric Chemistry and Physics, 10, 11 851–11 865, doi:10.5194/acp-10-11851-2010, 2010.

Romps, D. M.: Exact Expression for the Lifting Condensation Level, Journal of the Atmospheric Sciences, 74, 3891 – 3900, doi:https://doi.org/10.1175/JAS-D-17-0102.1, 2017.

Rosenfeld, D. and Lensky, I. M.: Satellite-Based Insights into Precipitation Formation Processes in Continental and Maritime Convective Clouds, Bulletin of the American Meteorological Society, 79, 2457 – 2476, doi:10.1175/1520-0477(1998)079<2457:SBIIPF>2.0.CO;2, 1998.

Sakurai, J. and Napolitano, J.: Modern Quantum Mechanics, Cambridge University Press, Cambridge, 3rd edn., doi:10.1017/9781108587280, 2020.

Satoh, M., Stevens, B., Judt, F., Khairoutdinov, M., Lin, S.-J., Putman, W. M., and Düben, P.: Global Cloud-Resolving Models, Current Climate Change Reports, 5, 172–184, doi:10.1007/s40641-019-00131-0, 2019.

Scheiderer, A.: Polarisationsbasierte Wolkenerkennung angewendet auf Kameradaten der EUREC4A-Kampagne, Bachelor's Thesis, 2021.

Schulz, H.: C^{3}ONTEXT: a Common Consensus on Convective OrgaNizaTion during the EUREC^{4}A eXperimenT, Earth System Science Data, 14, 1233–1256, doi:10.5194/essd-14-1233-2022, 2022a.

Schulz, H.: C³ONTEXT: A Common Consensus on Convective OrgaNizaTion during the EUREC4A eXperimenT, doi:10.5281/zenodo.5979718, 2022b.

Schulz, H., Eastman, R., and Stevens, B.: Characterization and Evolution of Organized Shallow Convection in the Downstream North Atlantic Trades, Journal of Geophysical Research: Atmospheres, 126, e2021JD034 575, doi:10.1029/2021JD034575, e2021JD034575 2021JD034575, 2021.

Schüller, L., Bennartz, R., Fischer, J., and Brenguier, J.-L.: An Algorithm for the Retrieval of Droplet Number Concentration and Geometrical Thickness of Stratiform Marine Boundary Layer Clouds Applied to MODIS Radiometric Observations, Journal of Applied Meteorology, 44, 28 – 38, doi:10.1175/JAM-2185.1, 2005.

Seifert, A. and Beheng, K. D.: A double-moment parameterization for simulating autoconversion, accretion and selfcollection, Atmospheric Research, 59-60, 265–281, doi:https://doi.org/10.1016/S0169-8095(01)00126-0, 13th International Conference on Clouds and Precipitation, 2001.

Seifert, A. and Beheng, K. D.: A two-moment cloud microphysics parameterization for mixed-phase clouds. Part 1: Model description, Meteorology and Atmospheric Physics, 92, 45–66, doi:10.1007/s00703-005-0112-4, 2006.

Shang, H., Chen, L., Bréon, F. M., Letu, H., Li, S., Wang, Z., and Su, L.: Impact of cloud horizontal inhomogeneity and directional sampling on the retrieval of cloud droplet size by the POLDER instrument, Atmospheric Measurement Techniques, 8, 4931–4945, doi:10.5194/amt-8-4931-2015, 2015.

Shang, H., Letu, H., Bréon, F.-M., Riedi, J., Ma, R., Wang, Z., Nakajima, T. Y., Wang, Z., and Chen, L.: An improved algorithm of cloud droplet size distribution from POLDER polarized measurements, Remote Sensing of Environment, 228, 61–74, doi:10.1016/j.rse.2019.04.013, 2019.

Siebesma, A. P., Bretherton, C. S., Brown, A., Chlond, A., Cuxart, J., Duynkerke, P. G., Jiang, H., Khairoutdinov, M., Lewellen, D., Moeng, C.-H., Sanchez, E., Stevens, B., and Stevens, D. E.: A Large Eddy Simulation Intercomparison Study of Shallow Cumulus Convection, Journal of the Atmospheric Sciences, 60, 1201 – 1219, doi:https://doi.org/10.1175/1520-0469(2003)60<1201:ALESIS>2.0.CO;2, 2003.

Sinclair, K., van Diedenhoven, B., Cairns, B., Alexandrov, M., Moore, R., Crosbie, E., and Ziemba, L.: Polarimetric retrievals of cloud droplet number concentrations, Remote Sensing of Environment, 228, 227–240, doi:https://doi.org/10.1016/j.rse.2019.04.008, 2019.

Sinclair, K., van Diedenhoven, B., Cairns, B., Alexandrov, M., Dzambo, A. M., and L'Ecuyer, T.: Inference of Precipitation in Warm Stratiform Clouds Using Remotely Sensed Observations of the Cloud Top Droplet Size Distribution, Geophysical Research Letters, 48, e2021GL092 547, doi:10.1029/2021GL092547, e2021GL092547 2021GL092547, 2021.

Slingo, A.: A GCM Parameterization for the Shortwave Radiative Properties of Water Clouds, Journal of Atmospheric Sciences, 46, 1419 – 1427, doi:https://doi.org/10.1175/1520-0469(1989)046<1419:AGPFTS>2.0.CO;2, 1989.

Slingo, A.: Sensitivity of the Earth's radiation budget to changes in low clouds, Nature, 343, 49–51, doi:10.1038/343049a0, 1990.

Small, J. D., Chuang, P. Y., Feingold, G., and Jiang, H.: Can aerosol decrease cloud lifetime?, Geophysical Research Letters, 36, doi:https://doi.org/10.1029/2009GL038888, 2009.

Stamnes, K., Tsay, S.-C., Wiscombe, W., and Jayaweera, K.: Numerically stable algorithm for discrete-ordinate-method radiative transfer in multiple scattering and emitting layered media, Appl. Opt., 27, 2502–2509, doi:10.1364/AO.27.002502, 1988.

Stap, F., Hasekamp, O., Emde, C., and Röckmann, T.: Influence of 3D effects on 1D aerosol retrievals in synthetic, partially clouded scenes, Journal of Quantitative Spectroscopy and Radiative Transfer, 170, 54–68, doi:10.1016/j.jqsrt.2015.10.008, 2016a.

Stap, F. A., Hasekamp, O. P., Emde, C., and Röckmann, T.: Multiangle photopolarimetric aerosol retrievals in the vicinity of clouds: Synthetic study based on a large eddy simulation, Journal of Geophysical Research: Atmospheres, 121, 12,914–12,935, doi:10.1002/2016JD024787, 2016b.

Stevens, B., Bony, S., Brogniez, H., Hentgen, L., Hohenegger, C., Kiemle, C., L'Ecuyer, T. S., Naumann, A. K., Schulz, H., Siebesma, P. A., Vial, J., Winker, D. M., and Zuidema, P.: Sugar, gravel, fish and flowers: Mesoscale cloud patterns in the trade winds, Quarterly Journal of the Royal Meteorological Society, 146, 141–152, doi:10.1002/qj.3662, 2020.

Stevens, B., Bony, S., Farrell, D., Ament, F., Blyth, A., Fairall, C., Karstensen, J., Quinn, P. K., Speich, S., Acquistapace, C., Aemisegger, F., Albright, A. L., Bellenger, H., Bodenschatz, E., Caesar, K.-A., Chewitt-Lucas, R., de Boer, G., Delanoë, J., Denby, L., Ewald, F., Fildier, B., Forde, M., George, G., Gross, S., Hagen, M., Hausold, A., Heywood, K. J., Hirsch, L., Jacob, M., Jansen, F., Kinne, S., Klocke, D., Kölling, T., Konow, H., Lothon, M., Mohr, W., Naumann, A. K., Nuijens, L., Olivier, L., Pincus, R., Pöhlker, M., Reverdin, G., Roberts, G., Schnitt, S., Schulz, H., Siebesma, A. P., Stephan, C. C., Sullivan, P., Touzé-Peiffer, L., Vial, J., Vogel, R., Zuidema, P., Alexander, N., Alves, L., Arixi, S., Asmath, H., Bagheri, G., Baier, K., Bailey, A., Baranowski, D., Baron, A., Barrau, S., Barrett, P. A., Batier, F., Behrendt, A., Bendinger, A., Beucher, F., Bigorre, S., Blades, E., Blossey, P., Bock, O., Böing, S., Bosser, P., Bourras, D., Bouruet-Aubertot, P., Bower, K., Branellec, P., Branger, H., Brennek, M., Brewer, A., Brilouet, P.-E., Brügmann, B., Buehler, S. A., Burke, E., Burton, R., Calmer, R., Canonici, J.-C., Carton, X., Cato Jr., G., Charles, J. A., Chazette, P., Chen, Y., Chilinski, M. T., Choularton, T., Chuang, P., Clarke, S., Coe, H., Cornet, C., Coutris, P., Couvreux, F., Crewell, S., Cronin, T., Cui, Z., Cuypers, Y., Daley, A., Damerell, G. M., Dauhut, T., Deneke, H., Desbios, J.-P., Dörner, S., Donner, S., Douet, V., Drushka, K., Dütsch, M., Ehrlich, A., Emanuel, K., Emmanouilidis, A., Etienne, J.-C., Etienne-Leblanc, S., Faure, G., Feingold, G., Ferrero, L., Fix, A., Flamant, C., Flatau, P. J., Foltz, G. R., Forster, L., Furtuna, I., Gadian, A., Galewsky, J., Gallagher, M., Gallimore, P., Gaston, C., Gentemann, C., Geyskens, N., Giez, A., Gollop, J., Gouirand, I., Gourbeyre, C., de Graaf, D., de Groot, G. E., Grosz, R., Güttler, J., Gutleben, M., Hall, K., Harris, G., Helfer, K. C., Henze, D., Herbert, C., Holanda, B., Ibanez-Landeta, A., Intrieri, J., Iyer, S., Julien, F., Kalesse, H., Kazil, J., Kellman, A., Kidane, A. T., Kirchner, U., Klingebiel, M., Körner, M., Kremper, L. A., Kretzschmar, J., Krüger, O., Kumala, W., Kurz, A., L'Hégaret, P., Labaste, M., Lachlan-Cope, T., Laing, A., Landschützer, P., Lang, T., Lange, D., Lange, I., Laplace, C., Lavik, G., Laxenaire, R., Le Bihan, C., Leandro, M., Lefevre, N., Lena, M., Lenschow, D., Li, Q., Lloyd, G., Los, S., Losi, N., Lovell, O., Luneau, C., Makuch, P., Malinowski, S., Manta, G., Marinou, E., Marsden, N., Masson, S., Maury, N., Mayer, B., Mayers-Als, M., Mazel, C., McGeary, W., McWilliams, J. C., Mech, M., Mehlmann, M., Meroni, A. N., Mieslinger, T., Minikin, A., Minnett, P., Möller, G., Morfa Avalos, Y., Muller, C., Musat, I., Napoli, A., Neuberger, A., Noisel, C., Noone, D., Nordsiek, F., Nowak, J. L., Oswald, L., Parker, D. J., Peck, C., Person, R., Philippi, M., Plueddemann, A., Pöhlker, C., Pörtge, V., Pöschl, U., Pologne, L., Posyniak, M., Prange, M., Quiñones Meléndez, E., Radtke, J., Ramage, K., Reimann, J., Renault, L., Reus, K., Reyes, A., Ribbe, J., Ringel, M., Ritschel, M., Rocha, C. B., Rochetin, N., Röttenbacher, J., Rollo, C., Royer, H., Sadoulet, P., Saffin, L., Sandiford, S., Sandu, I., Schäfer, M., Schemann, V., Schirmacher, I., Schlenczek, O., Schmidt, J., Schröder, M., Schwarzenboeck, A., Sealy, A., Senff, C. J., Serikov, I., Shohan, S., Siddle, E., Smirnov, A., Späth, F., Spooner, B., Stolla, M. K., Szkółka, W., de Szoeke, S. P., Tarot, S., Tetoni, E., Thompson, E., Thomson,

J., Tomassini, L., Totems, J., Ubele, A. A., Villiger, L., von Arx, J., Wagner, T., Walther, A., Webber, B., Wendisch, M., Whitehall, S., Wiltshire, A., Wing, A. A., Wirth, M., Wiskandt, J., Wolf, K., Worbes, L., Wright, E., Wulfmeyer, V., Young, S., Zhang, C., Zhang, D., Ziemen, F., Zinner, T., and Zöger, M.: EUREC^{4}A, Earth System Science Data, 13, 4067–4119, doi:10.5194/essd-13-4067-2021, 2021.

Takahashi, H., Luo, Z. J., and Stephens, G.: Revisiting the Entrainment Relationship of Convective Plumes: A Perspective From Global Observations, Geophysical Research Letters, 48, e2020GL092 349, doi:https://doi.org/10.1029/2020GL092349, e2020GL092349 2020GL092349, 2021.

Tas, E., Teller, A., Altaratz, O., Axisa, D., Bruintjes, R., Levin, Z., and Koren, I.: The relative dispersion of cloud droplets: its robustness with respect to key cloud properties, Atmospheric Chemistry and Physics, 15, 2009–2017, doi:10.5194/acp-15-2009-2015, 2015.

Touzé-Peiffer, L., Vogel, R., and Rochetin, N.: Cold Pools Observed during EUREC4A: Detection and Characterization from Atmospheric Soundings, Journal of Applied Meteorology and Climatology, 61, 593 – 610, doi:https://doi.org/10.1175/JAMC-D-21-0048.1, 2022.

Turner, J. S.: The motion of buoyant elements in turbulent surroundings, Journal of Fluid Mechanics, 16, 1–16, doi:10.1017/S0022112063000549, 1963.

Twomey, S.: Pollution and the planetary albedo, Atmospheric Environment (1967), 8, 1251–1256, doi:10.1016/0004-6981(74)90004-3, 1974.

Vogel, R., Albright, A. L., Vial, J., George, G., Stevens, B., and Bony, S.: Strong cloud–circulation coupling explains weak trade cumulus feedback, Nature, 612, 696–700, doi:10.1038/s41586-022-05364-y, 2022.

Volkmer, L., Pörtge, V., Jakub, F., and Mayer, B.: Model-based evaluation of cloud geometry and droplet size retrievals from 2-D polarized measurements of specMACS, EGUsphere, 2023, 1–22, doi:10.5194/egusphere-2023-2235, 2023.

Volkmer, L., Kölling, T., Zinner, T., and Mayer, B.: Consideration of the cloud motion for aircraft-based stereographically derived cloud geometry and cloud top heights, to be submitted, 2024.

Wagner, W. and Pruß, A.: The IAPWS formulation 1995 for the thermodynamic properties of ordinary water substance for general and scientific use, Journal of physical and chemical reference data, 31, 387–535, 2002.

Wallace, J. M. and Hobbs, P. V.: 6 - Cloud Microphysics, in: Atmospheric Science (Second Edition), edited by Wallace, J. M. and Hobbs, P. V., pp. 209–269, Academic Press, San Diego, second edition edn., doi:https://doi.org/10.1016/B978-0-12-732951-2.50011-9, 2006.

Warner, J.: The Water Content of Cumuliform Cloud, Tellus, 7, 449–457, doi:https://doi.org/10.1111/j.2153-3490.1955.tb01183.x, 1955.

Warner, J.: A Reduction in Rainfall Associated with Smoke from Sugar-Cane Fires—An Inadvertent Weather Modification?, Journal of Applied Meteorology and Climatology, 7, 247 – 251, doi:https://doi.org/10.1175/1520-0450(1968)007<0247:ARIRAW>2.0.CO;2, 1968.

Weber, A., Kölling, T., Pörtge, V., Baumgartner, A., Rammeloo, C., Zinner, T., and Mayer, B.: Polarization upgrade of specMACS: calibration and characterization of the 2D RGB polarization-resolving cameras, Atmospheric Measurement Techniques, 17, 1419–1439, doi:10.5194/amt-17-1419-2024, 2024.

Wilson, T.: OGC® KML. Version 2.2. 0., 2008.

Wirth, M.: Cloud top height derived from airborne measurements with the WALES lidar during the EUREC4A field campaign, doi:10.25326/216, Aeris, 2021.

Wirth, M., Fix, A., Mahnke, P., Schwarzer, H., Schrandt, F., and Ehret, G.: The airborne multi-wavelength water vapor differential absorption lidar WALES: system design and performance, Applied Physics B, 96, 201, doi:10.1007/s00340-009-3365-7, 2009.

Wiscombe, W. J.: Improved Mie scattering algorithms, Appl. Opt., 19, 1505–1509, doi:10.1364/AO.19.001505, 1980.

Wu, L., Hasekamp, O., van Diedenhoven, B., and Cairns, B.: Aerosol retrieval from multiangle, multispectral photopolarimetric measurements: importance of spectral range and angular resolution, Atmospheric Measurement Techniques, 8, 2625–2638, doi:10.5194/amt-8-2625-2015, 2015.

Xu, F., van Harten, G., Diner, D. J., Davis, A. B., Seidel, F. C., Rheingans, B., Tosca, M., Alexandrov, M. D., Cairns, B., Ferrare, R. A., Burton, S. P., Fenn, M. A., Hostetler, C. A., Wood, R., and Redemann, J.: Coupled Retrieval of Liquid Water Cloud and Above-Cloud Aerosol Properties Using the Airborne Multiangle SpectroPolarimetric Imager (AirMSPI), Journal of Geophysical Research: Atmospheres, 123, 3175–3204, doi:10.1002/2017JD027926, 2018.

Yang, P., Bi, L., Baum, B. A., Liou, K.-N., Kattawar, G. W., Mishchenko, M. I., and Cole, B.: Spectrally Consistent Scattering, Absorption, and Polarization Properties of Atmospheric Ice Crystals at Wavelengths from 0.2 to 100μm, Journal of the Atmospheric Sciences, 70, 330 – 347, doi:10.1175/JAS-D-12-039.1, 2013.

Yau, M. K. and Rogers, R. R.: A short course in cloud physics, Elsevier, 1996.

Zelinka, M. D., Myers, T. A., McCoy, D. T., Po-Chedley, S., Caldwell, P. M., Ceppi, P., Klein, S. A., and Taylor, K. E.: Causes of Higher Climate Sensitivity in CMIP6 Models, Geophysical Research Letters, 47, e2019GL085782, doi:https://doi.org/10.1029/2019GL085782, e2019GL085782 10.1029/2019GL085782, 2020.

Zhang, Z.: A flexible new technique for camera calibration, IEEE Transactions on Pattern Analysis and Machine Intelligence, 22, 1330–1334, doi:10.1109/34.888718, 2000.

Zhang, Z., Ackerman, A. S., Feingold, G., Platnick, S., Pincus, R., and Xue, H.: Effects of cloud horizontal inhomogeneity and drizzle on remote sensing of cloud droplet effective radius: Case studies based on large-eddy simulations, Journal of Geophysical Research: Atmospheres, 117, doi:10.1029/2012JD017655, 2012.

Zinner, T., Marshak, A., Lang, S., Martins, J. V., and Mayer, B.: Remote sensing of cloud sides of deep convection: towards a three-dimensional retrieval of cloud particle size profiles, Atmospheric Chemistry and Physics, 8, 4741–4757, doi:10.5194/acp-8-4741-2008, 2008.

Zinner, T., Schwarz, U., Kölling, T., Ewald, F., Jäkel, E., Mayer, B., and Wendisch, M.: Cloud geometry from oxygen-A-band observations through an aircraft side window, Atmospheric Measurement Techniques, 12, 1167–1181, doi:10.5194/amt-12-1167-2019, 2019.

Acknowledgements

Although my thesis started with a global pandemic, I think it was a very enjoyable time despite all the external circumstances. This is largely due to the people who supported me during this time. I would therefore like to use this opportunity to thank and mention these people.

Firstly, of course, Bernhard Mayer, whom I would like to thank for giving me the opportunity to work on this doctoral thesis. When I started with this work, I wasn't really interested in airplanes at all and, to be honest, measurement campaigns were never my long-cherished dream. Bernhard convinced me that this was an important and exciting thing to do and I have to say that I really enjoyed measuring and the way of working in the EUREC^{4}A community. In addition, Bernhard was always incredibly interested in the subject, and, since he analyzed measurements of the backscatter glory almost 20 years ago, he was totally convinced of the method. This was extremely motivating and made the collaboration very pleasant, although I have to admit that my interest in airplanes has not really grown in the last four years. :-)

Next, I would like to thank Markus Rapp. He has not only kindly agreed to be the second reviewer of my thesis but has been supporting us with the specMACS measurements for a long time. Without his support many of our past projects would not have been possible and I consider the cooperation to be very valuable.

Moreover, I would like to thank the entire specMACS team for the great time: First of all, thank you Anna for your support. Anna and I struggled through our first experiences at CIRRUS-HL. We had, at first, not too much knowledge of how the instrument actually works but in the end we learned a lot and I think we did pretty well. Anna has also been very helpful during all the other campaigns and I am sure she knows the instrument better than I do by now. The next person I would like to mention is Tobi Zinner who is always very solution-oriented, which is extremely helpful especially when time is short. Furthermore, thank you Tobi for many helpful scientific suggestions, and for proof-reading large parts of this thesis. I would also like to thank Lea for the successful collaboration during your Master's thesis. I had a very good time working with you, and I am happy to have you as my office neighbour. I am excited to see how the campaign with you in Cape Verde will be this year! Thanks also to Dennys Erdtmann for helping me with the bispectral retrieval. Although no longer a 100 percent member of the specMACS team, I would of course also like to mention Tobi Kölling who is very reliable and always

helps whenever we have problems with the instrument.

Besides the specMACS team, I also want to thank Fabian Hoffmann and Jung-Sub Lim, who were always open for scientific discussions and really helped in interpreting the results of my scientific studies. I am excited to see what the collaboration with your group will bring in the future. I would like to thank Linda Forster for helping during some measurement campaigns and Claudia Emde for always answering my questions about polarization. And thank you, Linda and Claudia, for being great female role models of working in academics in general. Thank you, Felix Gödde, for proof-reading parts of this thesis. Besides, I want to thank the rest of the institute for a friendly and inspiring working atmosphere, and especially Barbara and Markus for keeping everything running very smoothly. I had the opportunity to supervise a number of students during my doctorate and therefore, I would like to thank Alex Scheiderer, Zhoutong Ma, Matthis Bünning, Selina Bernlochner and Stefan Koppenhofer (even twice). I have learned a lot from working with you and hope that you have also learned something from me.

The various measurement campaigns would definitely not have been possible without Tommy Leder, who makes almost everything possible and always manages to create a good atmosphere. I would also like to say a big thank you to our colleagues from Leipzig who spread good humor even in stressful situations and I am very grateful for their support in situations where we were somewhat understaffed.

Next, I would like to thank my friends: Michael, Bianca, Nathalie, Nina, Fatos, Richard, and Laura. I met most of you during my first week at LMU, and I am very happy that we continued to being such good friends. Thank you, Jenny and Savi for your even longer friendship and continuous support.

I would also like to thank my close family members: Gotlind, Karl-Heinz, Ingo and Doro, as well as Martin, Ute, and Xaver for always inspiring and supporting me. Finally, thank you Max for being the only office colleague I had during the Covid time, for being a very attentive audience when I was endlessly preparing my talks, and for always being there for me.

Transparency: I used the software tools DeepL and Grammarly in this work to improve the grammar. Let's hope the AI did a good job in correcting my missing commas.